CONSTRAIN NEUTRON STAR PROPERTIES WITH SπRIT EXPERIMENT

By

Chun Yuen Tsang

A DISSERTATION

Submitted to
Michigan State University
in partial fulfillment of the requirements
for the degree of

Physics – Doctor of Philosophy

2022

ABSTRACT

CONSTRAIN NEUTRON STAR PROPERTIES WITH SπRIT EXPERIMENT

By

Chun Yuen Tsang

The study of nuclear matter is an interdisciplinary endeavor that is relevant to both astrophysics and nuclear physics. Astrophysicists need to understand the properties of nuclear matter as some astrophysical objects are made of nuclear material. Nuclear physicists also need to understand the properties of nuclear matter as they are fundamental to the understanding of the existence of nuclei, their composition and the dynamics of nuclear collisions.

Recent measurements of gravitational waves from binary neutron star mergers and precise neutron star radii from X-ray data of pulsars open a new channel for physicists to study nuclear matter. Such astronomical observations of neutron stars are sensitive to nuclear matter at high density that is usually inaccessible on earth. One of the ways physicists are able to reach such high density in laboratory is through heavy-ion collision. Transport model calculations that simulate nuclear collisions show that head-on collisions of heavy nuclei at high beam energy compress the overlapping region momentarily to densities comparable to that of the interior of neutron stars.

To study neutron star where number of neutrons far exceeds that of protons, the dependence of nuclear properties on neutron-to-proton ratio (N/Z) needs to be understood. This dependence is quantified by the symmetry energy, which describes the difference in binding energy between pure neutron matter and matter with equal amount of protons and neutrons. The latter is also known as symmetric nuclear matter (SNM) which has been fairly well constrained. The amount of internal neutron star pressure that supports itself from gravitational collapse depends on the value of symmetry energy.

Most of the existing heavy-ion collision data comes from collisions of stable isotopes. This limits the range of available N/Z in nuclear experiments. Extending results to a wider range of N/Z is one of the goals of SπRIT experiment using projectiles provided by the cutting-edge Radioactive

Isotope Beam Factory in RIKEN, Japan. SπRIT time projection chamber (TPC) is constructed to measure charged pions spectra from the collision of neutron-rich system (^{132}Sn + ^{124}Sn), neutron-poor system (^{108}Sn + ^{112}Sn) and intermediate system (^{112}Sn + ^{124}Sn) at 270 MeV/u. By comparing fragmentation patterns for reactions with different number of neutrons, symmetry energy effects can be isolated. Some results from the analysis of pion spectra have been published and will be briefly reviewed in this work before we focus on light fragment observables that are also available from the TPC data. The data analysis software, with highlights on correction of some major detector aberrations, is discussed in details. Monte Carlo simulation of the SπRIT TPC is then performed to understand the behavior of SπRIT data and validate our data analysis procedure.

Finally, Bayesian analysis is performed to compare transport model simulations with selected light fragment measurements using Markov-Chain Monte Carlo and Gaussian emulators. The observables are chosen to minimize systematic uncertainties from both the experiment and model. The posterior provides a comprehensive constraint on the symmetry energy parameters. Although previous analyses of pion spectra have already constrained the slope of symmetry energy at saturation density (L), its uncertainty can be reduced by 39% if pion results are combined with our new Bayesian posterior. The implications of symmetry energy constraint for neutron star will be discussed to demonstrate the importance of data from rare isotope heavy-ion collisions.

ACKNOWLEDGEMENTS

I have received lots of support and assistance in the writing of this dissertation. I would like to first thank my advisor, Professor ManYee Betty Tsang, whose insightful feedback pushed me to sharpen my thinking and brought my work to a higher level. I would like to acknowledge my graduate guidance committee members, Professors William Lynch, Pawel Danielewicz, Edward Brown and Tyce DeYoung, for their valuable guidance throughout my studies. In addition, I would like to thanks all previous and current HiRA group members who I worked with: Jon Barney, Justin Estee, Juan Manfredi, Adam Anthony, Chi-En Fanurs Teh, Joseph Wieske, Sean Sweany, Kyle Brown, Kuan Zhu, Rebecca Shane, Rensheng Wang, Chenyang Niu, Rohit Kumar, Giordano Cerizza, Daniele Dell'Aquila, Genie Jhang, Pierre Morfouace and Clementine Santamaria. I would also like to thank the current and previous undergraduate helpers in our group: Corinne Anderson, Hananiel Setiawan, Jacob Corsby and Thomas Ladouceur.

Special thanks to all the members of the SπRIT collaboration whose continuous efforts made the SπRIT experiment and its analysis possible: JungWoo Lee (Korea University), Masanori Kaneko (Kyoto University), Tetsuya Murakami (Kyoto University), Sherry Yennello (TAMU), Tadaaki Isobe (RIKEN), Alan McIntosh (TAMU), Mizuki Kurata-Nishimura (RIKEN).

The members of Transport Model Evaluation Project (TMEP) have also helped a lot by providing transport models necessary to interpret experimental results: Hermann Wolter, Maria Colonna, Dan Cozma, Che Ming Ko,Akira Ono, Jun Xu, Ying-Xun Zhang, YongJia Wong.

Computing resources for analysis in this work were provided by the HOKUSAI-GreatWave at RIKEN, the High Performance Computing Center (HPCC) at MSU, and the NSCL computing cluster.

Finally, I want to thank the funding sources which have made this possible: this work was supported by the U.S. DOE under Grant Nos. DE-SC0014530, DE-NA0002923, US NSF Grant No. PHY-1565546, and the Japanese MEXT KAKENHI grant No. 24105004.

TABLE OF CONTENTS

LIST OF TABLES

LIST OF FIGURES

CHAPTER 1

INTRODUCTION

1.1 Nuclear equation of state (EoS)

Unification is a general goal pursued by all physicists. Isaac Newton unified gravity on Earth with the trajectories of celestial objects and James Maxwell unified electricity and magnetism through the famous Maxwell's equations. The beauty of unification is that it ties seemingly unrelated phenomena together with a single description. In the study of nuclear equation of state (EoS), we hope to unify astronomical observations, which is the study of massive celestial objects, with heavy-ion collision measurements, which is the study of tiny invisible nucleus. The masses of interest in these two fields differ by 55 orders of magnitude, and yet they are related in a unified description of nuclear EoS.

The key is to realize that the environment in the interior of neutron star (NS) is similar to that in the core of ordinary nucleus. The properties of ordinary matter we find in our everyday life are dictated by the electromagnetic interactions between electrons and nucleus of atoms, but the gravitational pull in neutron star is so strong that electromagnetic force is not strong enough to support the material from collapsing. The extreme environment forces electrons and protons to merge and form neutrons. Such a homogeneous matter of nucleons is called *nuclear matter* and is supported by nuclear degeneracy pressure. This is similar to nucleus during a heavy-ion collision where parts of it are being compressed to supersaturation density. Our knowledge on nuclear collisions can be extrapolated to predict properties of NS.

Properties of nuclear matter are described quantitatively by nuclear EoS. It is an equation that relates various state variables such as pressure, volume and internal energy. One of the simplest yet powerful approximation to nuclear EoS is the semi-empirical mass formula (SEMF). It models

nucleus as an incompressible drop of nuclear matter [9] and yields the following formula,

$$E_B = a_V A - a_S A^{2/3} - a_C \frac{Z^2}{A^{1/3}} - a_A \frac{(N-Z)^2}{A} + \delta(N,Z). \tag{1.1}$$

Here E_B is the binding energy, Z is the number of protons, N is the number of neutrons and $A = N + Z$ is the total number of nucleons inside a nucleus. The five terms in Eq. (1.1) can be understood as follows: The first term with coefficient a_V is called the *volume* term which accounts for the increased interactions due to proportionally increased number of nucleons. The second term with coefficient a_S is called the *surface term* and is negative to account for the fact that nucleons on the surface have less neighbors to interact with, so overall strength of interaction is reduced. The third term with coefficient a_C is called the *Coulomb term* which accounts for the Coulomb repulsion between protons. This term resembles Coulomb potential once you realize that average distance between nucleons $\propto A^{1/3}$ and charge of nucleus $\propto Z$. The fourth term with coefficient a_A is called the *asymmetry term* which arises from the asymmetry in number of protons and neutrons. If the numbers of protons and neutrons are the same, they share the same Fermi energy. However if there are more neutrons than protons, some neutrons are forced to occupy higher energy levels due to Pauli exclusion principle. Although Fermi energy of protons is reduced, the overall internal energy is raised which results in a reduction of binding energy. Pauli exclusion principle alone does not fully explain the magnitude of asymmetry term due to the fact that neutrons and protons do interact with each other and the assumption that they occupy independent energy levels is not true, but it does give an intuitive understanding of the meaning of asymmetry term. The final term is called the pairing term which originates from spin-coupling. For the purposes of this thesis, the pairing term will not be discussed.

The SEMF was developed to approximately describe the mass and stability of atomic nuclei. Its agreement with measured binding energies of various nuclei is satisfactory when best fitted values of the coefficients are used [10]. Baryon density at the core of most ordinary nucleus is roughly $\rho \approx \rho_0 = 0.155\,\mathrm{fm}^{-3}$, where ρ_0 is called the *saturation density*. The parameters in SEMF are fitted with data from ordinary nucleus so the equation is only valid for nuclear matter at $\rho \approx \rho_0$. If we

naively approximate NS as one giant nucleus with $A \to \infty$, its EoS can be written as,

$$\frac{E_B}{A} = E_{is} + E_{iv}\delta^2, \tag{1.2}$$

with $E_{is} = a_V$, $E_{iv} = a_A$ and $\delta = (N - Z)/A$. The surface and Coulomb terms tend to zero as we take limit to infinite atomic mass. These terms are relabelled to emphasize that the first term is the *isoscalar term* which makes no distinction between protons and neutrons, and the second term is the *isovector term* which accounts for the effects of having an unequal numbers of protons and neutrons. Such approximated NS EoS is inaccurate because baryon density in ordinary nucleus is different from that in NS. For instance, NS density at its center can be up to multiple times the saturation density. Despite the shortcomings, it is still instructive to see how EoS decomposes into isoscalar and isovector terms.

To overcome the over-simplifications in SEMF, we incorporate density dependence to equation (1.2),

$$E(\rho, \delta) = E_{is}(\rho) + \delta^2 E_{iv}(\rho) + O(\delta^4). \tag{1.3}$$

The isovector term is often denoted as $S(\rho)$ and is sometimes referred to as the *symmetry energy term*. Measurements of collective flow and Kaon production in energetic nucleus-nucleus collisions have constrained E_{is} to densities up to $4.5\rho_0$ [11–13]. Specifically, the symmetric matter constraints on pressure vs. density were determined from the measurements of transverse and elliptical flow from ^{197}Au + ^{197}Au collisions over a range of incident energies from 0.3 to 1.2 AGeV [11]. These constraints were confirmed in an independent analysis of elliptical flow data [14]. Similar constraints from $1.2\rho_0$ to $2.2\rho_0$ were obtained from the Kaon measurements [12, 13]. These heavy-ion constraints are consistent with the Bayesian analyses of the NS mass-radius correlation when certain assumptions on the formulation of E_{iv} are made [15].

This is in stark contrast to constraints on E_{iv} as it has been constrained mainly at densities near or below ρ_0. Since NS composed mostly of neutrons, E_{iv} should play a prominent role. Indeed studies found that NS properties are sensitive to E_{iv} at $2\rho_0$ [16]. The purpose of this study is

to constrain the E_{iv} at density above saturation using heavy-ion collisions. In a medium-energy heavy-ion collision, the colliding part of the nucleus is compressed and reaches higher density than ρ_0, and when it expands afterward the density falls below ρ_0. Complete knowledge of nuclear EoS across different densities is needed for nuclear theory to accurately predict collision observables.

Nuclear EoS can be parameterized in multiple ways. For example, Skyrme [3] and polytropes [17] are two common formulations of EoS. Derivatives of EoS with at saturation density are often used as empirical parameters to characterize the density and isospin dependence of the EoS. Expanding at ρ_0 also allow us to conveniently enforce the condition that symmetric matter energy density must be a minimum at ρ_0 by simply setting the first order derivative of E_{is} to zero. Symmetric matter energy has to be minimum at ρ_0 for bound states of ordinary nucleus to exist. These derivatives are commonly expressed as coefficients in the Taylor expansion when EoS is expanded in terms of $x = (\rho - \rho_0)/(3\rho_0)$:

$$E_{is}(\rho) = E_0 + \frac{1}{2}K_{\rm sat}x^2 + \frac{1}{3!}Q_{\rm sat}x^3 + \frac{1}{4!}Z_{\rm sat}x^4 + ..., \tag{1.4}$$

and,

$$E_{iv}(\rho) = S_0 + Lx + \frac{1}{2}K_{\rm sym}x^2 + \frac{1}{3!}Q_{\rm sym}x^3 + \frac{1}{4!}Z_{\rm sym}x^4 + ... \tag{1.5}$$

For some EoS families, energy depends on density and asymmetry in a way that cannot be separated into the sum of two terms, but the isoscalar term is always well-defined:

$$E_{is}(\rho) = E(\rho, \delta = 0). \tag{1.6}$$

The isovector term can be defined instead as the second term in the Taylor expansion of $E(\rho, \delta)$ in δ around $\delta = 0$ (not to be confused with previous EoS expansion coefficients which are expanded in x),

$$E_{iv}(\rho) = \frac{1}{2}\frac{\partial^2 E(\rho, \delta)}{\partial \delta^2}\Big|_{\delta=0}. \tag{1.7}$$

S, L, K, Q, Z and any higher order terms in Taylor expansion can always be extracted from any nuclear EoS by taking derivatives. These coefficients are commonly used to compare EoSs from

different families that have continuous derivatives. Families of EoSs with discontinuous higher order derivatives, such as piece-wise Polytropes, cannot be expanded this way, but in this thesis we will focus on smooth EoSs with comparable derivatives.

1.2 Neutron Star

Neutron Star (NS) matter is one of the densest material besides black hole in the universe. This matter is so dense that it becomes energetically favorable for protons and electrons to combine and form neutrons. At densities ranging from somewhat below saturation density ($\rho_0 = 0.155\,\mathrm{fm}^{-3}$) to $3\rho_0$, it is reasonable to describe NS matter as locally uniform nuclear matter composed mostly of neutrons. Study of NS is of great relevance to nuclear physics because it provides unique information on the properties of asymmetric nuclear matter at high density. Refs. [18–20] provide more in depth discussions on this subject.

Astrophysical NS properties, when combined with constraints from heavy-ion collisions, have provided a rough understanding of nuclear EoS. Typical temperatures of NSs are low with $k_B T < 1\,\mathrm{MeV}$, thus finite temperature effect is small, but the uncertainty in the relation between the pressure and energy density of nuclear matter at various baryon densities remains large [21].

Recent gravitational wave observations from the LIGO collaboration [22] has opened a new window for understanding neutron-star matter. Specifically, the LIGO observation provides estimation for *tidal deformability*, also known as *tidal polarizability*, a quantity that bears direct relevance to nuclear EoS. When two NSs orbit around each other, both stars are deformed by tidal force. The mass quadrupole that develops in response to the external quadrupole gravitational field emerges as:

$$Q_{ij} = -\lambda E_{ij}. \tag{1.8}$$

Here E_{ij} is the external gravitational field strength and λ is the tidal deformability. The orbital period of the inspiral differs from point mass calculation because tidal deformation contributes to an overall orbital energy loss and changes the rotational phases. This difference is used to extract the dimensionless tidal deformability (Λ) of a NS [23, 24]. Throughout this thesis, tidal deformability

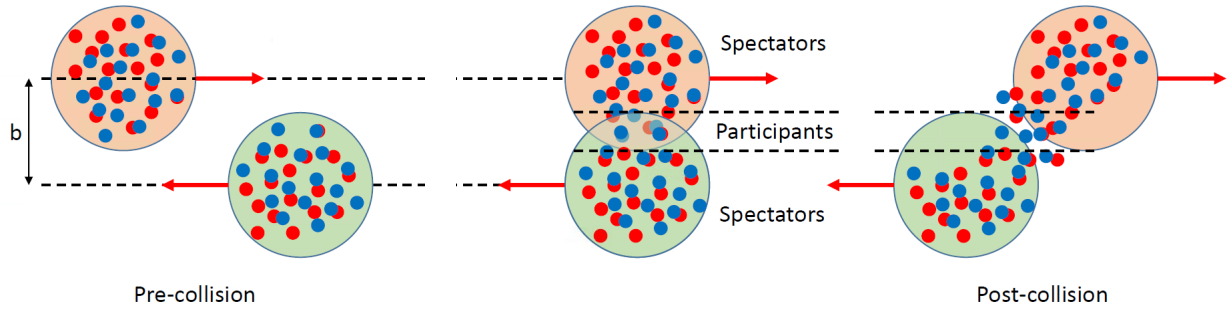

Figure 1.1: Cartoon illustration of impact parameter b, and spectator and participant nucleons. Taken from Ref. [2].

always refers to the dimensionless tidal deformability Λ defined as,

$$\Lambda = \frac{\lambda c^{10}}{G^4 M^5} = \frac{2}{3} k_2 \left(\frac{c^2 R}{GM}\right)^5, \tag{1.9}$$

where k_2 is the second Love number [25, 26]. This whole expression, including the Love number, is sensitive to the nuclear EoS [22, 27, 28]. Steps needed to calculate Λ from a given EoS are detailed in Appendix B. With the gravitational wave observation of the neutron star merger event GW170817, LIGO group first constrained this parameter to $\Lambda < 800$ [22], and later refined to $\Lambda = 190^{+390}_{-120}$ with additional assumption on the functional form of EoS [29]. The quantitative relation between Λ and EoS parameters will be explored in this thesis.

1.3 Heavy-ion collision

Another source of constraints on density dependence of the symmetry energy comes from heavy-ion collision (HIC). When two nuclei collide, part of the target and projectile nucleus overlap with each other. The collision pushes the density of the overlapping region to well above ρ_0 [2]. The nucleons in the overlapping region is commonly referred to as the *participant nucleons* whereas those not directly in the path of collision are referred to as *spectator nucleons*. The two types of nucleons are illustrated in Fig. 1.1. The emissions pattern of light fragments will shed light into the shape of nuclear EoS.

Before the advancement of Rare-Isotope (RI) beams, only stable nuclei can be studied which limits the range of neutron-to-proton ratio in a reaction. With the development of modern RI beam facilities, it is now possible to collide unstable neutron-rich or neutron-poor nuclei. By comparing results from reactions at various neutrons-to-protons ratios, the asymmetry term contribution to EoS can be studied.

The perpendicular distance between target and projectile is called the *impact parameter*, often denoted as b. Events with small b are called *central events* while those with large b are called *peripheral events*. Collision dynamics changes with impact parameter so different observables are used for central and peripheral events to study nuclear EoS [11, 30–32].

Nuclear EoS has been studied with heavy-ion collision experiments where heavy-ions are accelerated by particle accelerator(s) and guided by magnets to collide with target nucleus. Particle detector(s) records the collision fragment distributions, from which observables are constructed and compared to transport models. The properties of nucleus and constraints on nuclear EoS are then inferred.

Most of the previous analyses of heavy-ion collisions explored a few transport model input parameters at a time. For instance, Ref. [11] vary only the curvature parameter K_{sat} while keeping other parameters, such as in-medium cross-section and effective mass fixed. Different experiments have led to different one-variable constraints or two-variable correlation constraints. Ref. [33] only varies two variables, with other parameters such as in-medium cross-section or K_{sym} restricted to best fitted values from other experiments. Due to the complexity of nuclear dynamics, observables rarely depend on only one or two parameters. If certain parameters are fixed, the potential constraining power of the observable on those parameters are lost. Improvements can be made by constraining multiple parameters with multiple observables simultaneously in a high dimensional search.

Recently, pion observables on central events (will be described in details in Chapter 4.5) have been compared to a transport model to successfully constrain symmetry energy term at high density [33]. In this thesis, we will tighten the constraints from pion analysis by incorporating light

fragment observables in a high dimensional parameter space search.

1.4 Organization of Dissertation

To probe the density dependence of symmetry energy term, a set of Sn + Sn heavy-ion experiments were preformed in 2016 at RIKEN with a time projection chamber (TPC) called SπRIT TPC. It was placed inside the SAMURAI magnet which provided a near uniform magnetic field to distinguish charged particles including π^+ from π^- and measure the momentum of emitted fragments. SπRIT TPC provides a large geometrical coverage, but the analysis of TPC data is complicated as will be shown in Chapter 3.2. In this thesis I will demonstrate some of the improvements on data analysis and Monte Carlo simulation for light fragments observables, develop an efficient algorithm to search for best fits in multi-dimensional parameter space and perform correlation analysis between EoS parameters, neutron star radius R and deformability Λ. This correlation is the connection between nuclear physics, represented by EoS parameters, and astrophysics, represented by Λ and R from LIGO and NICER experiment, respectively.

The organization of the dissertation is as follows: In Chapter 2, the correlation between nuclear EoS and neutron star properties is studied. Then a brief introduction to the set up of SπRIT experiment and data analysis software are presented in Chapter 3. The results from the experiment are then shown in Chapter 4. Monte Carlo simulation of the SπRIT TPC is discussed in details in Chapter 5 to verify the accuracy of our analysis software. Bayesian analysis is then performed in Chapter 6 to translate experimental results into constraints on nuclear EoS parameters. Its implications on NS properties will be discussed. Finally a brief summary is given in Chapter 7.

CHAPTER 2

NEUTRON STAR CALCULATIONS

In this chapter, we will explore the correlation between tidal deformability and Taylor expansion parameters. Previous studies have explored the constraints on different 2D parameter planes [34], on a diverse set of models [35–37], and with Bayesian analysis on EoSs from chiral effective field theory [38]. In this chapter, we will revisit the analysis with EoSs that are commonly used in heavy-ion collision (HIC) and then explore a larger parameter space by employing a less restrictive form of EoS.

A family of theoretical EoS is needed to correlate the Taylor expansion parameters with the predicted tidal deformability (Λ). One widely used family in astrophysics is the piece-wise polytropes [17], an EoS stitched together with multiple functions of the form $P(\rho) = K\rho^{\Gamma}$ at different density ranges. In this equation, P is the pressure, ρ is the baryon number density and K and Γ are parameters that user vary. It is not suitable in this study because a Taylor expansion assumes that the EoS is analytic over the range of interest. As long as there is only one polytrope, a Taylor expansion is valid, but its validity does not extend past the point of connection between the original polytrope and the next.

A commonly used family of EoS used in nuclear physics is the Skyrme interactions [3]. It derives from simplified approximate nuclear interaction and relies on 15 free parameters in its expanded form. The mathematical formulation of Skyrme type EoS is shown in Appendix A. Many different Skyrme interactions have been developed to calculate nuclear properties and these EoSs are well documented in the literature [3, 39, 40]. Skyrme EoSs have been applied to derive ground state properties of finite nuclei and to nuclear matter under mean-field Hartree-Fock approximation [41, 42]. We will review how the new merger observable, such as the tidal deformability, correlates with parameters in nuclear EoS. The insights from this endeavor can be used to guide the nuclear physics experiments designed to constrain the symmetry energy term of the nuclear EoS.

Recently, Meta-modeling EoS [1] is proposed as an alternative EoS. Its functional form is less restrictive and would be suitable for understanding the effect from higher order terms. Due to its unique advantage, we use them to study the correlations between high order Taylor parameters and NS properties.

2.1 Structure of a NS and modifications on the nuclear EoS

Neutron stars are more than a "giant nucleus". There are structural changes at various density regions as a result of a competition between the nuclear attraction, chemical potential of various particle species and the Coulomb repulsion. The dynamics of the outermost layer of NSs is described mostly by the Coulomb repulsion and nuclear masses, where nuclei arrange themselves in a crystalline lattice. As the density increases, it becomes energetically favorable for the electrons to capture protons, and the nuclear system evolves into a Coulomb lattice of progressively more exotic, neutron-rich nuclei that are embedded in a uniform electron gas. This outer crustal region exists as a solid layer of about 1 km in thickness [28].

At intermediate densities of sub-saturation, the spherical nuclei that form the crystalline lattice start to deform to reduce the Coulomb repulsion. As a result, the system exhibits rich and complex structures that emerge from a dynamical competition between the short-range nuclear attraction and the long-range Coulomb repulsion [43].

At densities of about half of the nuclear saturation density, the uniformity in the system is restored and matter behaves as a uniform Fermi liquid of nucleons and leptons. The transition region from the highly ordered crystal to the uniform liquid core is very complex and not well understood. At these regions of the inner crust which extend about 100 meters, various topological structures are thought to emerge that are collectively referred to as "nuclear pasta". Despite the undeniable progress [44–57] in understanding the nuclear-pasta phase since their initial prediction over several decades ago [58–60], there is no known theoretical framework that simultaneously incorporates both quantum-mechanical effects and dynamical correlations beyond the mean-field level. As a result, a reliable EoS for the inner crust is still missing.

The matter in the core region of NS can be described as uniform nuclear matter where neutron, protons, electrons and muons exist in beta equilibrium [43]. Although a phase change and exotic matter such as hyperons [43, 61, 62] could appear in the inner core region, there is currently no direct evidence of their existence. In this work, we calculate the EoS in this region by assuming that the neutron-star matter is composed of nucleons and leptons only.

Due to the rich structure of NSs, the nuclear EoS needs to be contextualized before it can be used for NS properties calculation. To begin with, crustal EoS should be used at density below transition density ρ_T. Normally the determination of ρ_T requires complicated thermodynamic calculations, but some simple relationship has been found between transition densities and Taylor parameters of the EoS [63] that greatly simplifies its calculation. In this study, the following equation is used to determine ρ_T:

$$\rho_T = -(3.75 \times 10^{-4}\,\mathrm{fm}^{-3}\mathrm{MeV}^{-1})L + 0.0963\,\mathrm{fm}^{-3}. \tag{2.1}$$

Outer and inner crust exhibit different physical properties and should be described by different EoSs. For the outer crust, EoS provided by Ref. [64] is used in this analysis. For the inner crust, either a Fermi-gas EoS (used in Section 2.2) or spline interpolation (used in Section 2.3) is used. Its main purpose is to connect the outer crust and outer core. The outer crust is used in the region of $0 < \rho < 0.3\rho_T$ and the inner crust in $0.3\rho_T \leq \rho < \rho_T$. The transition density at $0.3\rho_T$ is chosen ad-hoc and this connection region cannot precisely describe crustal dynamics, but properties of the neutron star core such as tidal deformability does not appear to be sensitive to the choice of the crustal EoS [28, 65, 66].

The outer core region $\rho > \rho_T$ is characterized by the EoS of a beta equilibrated system of protons, neutrons, electrons and muons. Proton and neutrons are collectively described by nuclear EoS while electrons and muons are modeled as relativistic Fermi gases. Equilibrium is attained by minimizing the Helmholtz free energy at different densities. Beyond a certain high density threshold ρ_c, the EoS of outer core may not be applicable. To complete the description of NS EoS, polytropes (used in Section 2.2) or EoS with speed of sound equals to speed of light (used in Section 2.3) can be used to extend the EoS to the central density region of a neutron star. The

high density region mainly affects the maximum neutron star mass and does not affect the relevant properties of the 1.4 solar mass neutron stars considered here.

To summarize, EoS of the neutron-star matter is formulated as follows:

$$P(\mathcal{E}) = \begin{cases} P_{\text{outer crust}}(\mathcal{E}), & \text{if } 0 < \rho < 0.3\rho_T \\ P_{\text{connection}}(\mathcal{E}), & \text{if } 0.3\rho_T < \rho < \rho_T \\ P_{\text{outer core}}(\mathcal{E}), & \text{if } \rho_T < \rho < \rho_c \\ P_{\text{inner core}}(\mathcal{E}) & \text{if } \rho_c < \rho. \end{cases} \tag{2.2}$$

In the above equation, $\mathcal{E}$ is the energy density, $P_{\text{outer crust}}$ is the pressure from outer crustal EoS and $P_{\text{outer core}}$ is the pressure from beta-equilibrated nuclear EoS. $P_{\text{connection}}$ is the intermediate equation that connects $P_{\text{crust}}(\mathcal{E}_{\text{crust}}(0.3\rho_T))$ to $P_{\text{outer core}}(\mathcal{E}_{\text{outer core}}(\rho_T))$.

2.2 Neutron stars from Skyrme EoS

In this section, a collection of 248 Skyrme interactions from Refs. [3, 40, 67] are used to form the outer core EoS. The outer core is assumed to be valid until $\rho_c = 3\rho_0$, where a transition to inner core occurs. A polytropic EoS of the form $K'\rho^\gamma$ is used to extend the EoS to the central density region of a neutron star. The constants K' and ρ_0 are fixed by the conditions that the pressure at thrice the normal nuclear density, $P_{\text{inner core}}(\rho_c)$ matches the pressure from the Skyrme density functionals $P_{\text{outer coure}}(\rho_c)$ and that the polytrope pressure at $7\rho_0$ is such that the EoS can support a 2.17 solar-mass neutron star, the maximum neutron star mass predicted from the neutron star merger event [68]. The EoS in different density regions are presented by the different color curves in Fig. 2.1. At the lowest densities, the EoSs describing the outer crust, are represented by yellow lines. The Fermi-gas EoS that connect the crust to the inner core are represented by the green curves. As a vehicle in connecting nontrivial nuclear physics observables to 1.4 solar mass neutron-star observables, we use the Skyrme interactions (green curves) [3, 39, 40] at densities

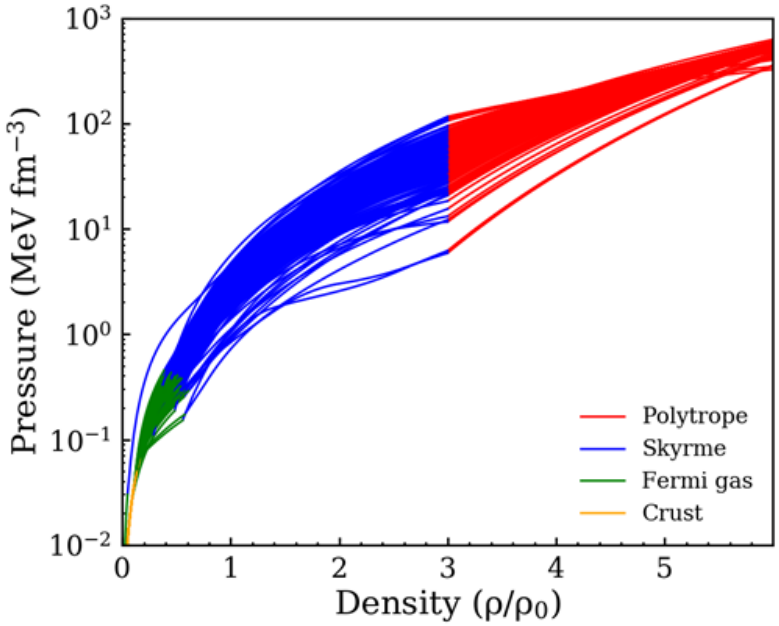

Figure 2.1: Composition of EoSs in different density regions in the neutron star. The outer crust EoS is represented by the yellow line, relativistic Fermi gas polytropic EoSs by the green lines, Skyrme EoSs by the blue lines and high density polytropes by the red lines. See text for details.

found in the outer core region (between $0.5\rho_0$ to $3\rho_0$) that represent the nuclear matter environment where such interactions can apply. The polytropic EoS above $3\rho_0$ are plotted in red. The Skyrme interactions that generate negative pressure at $3\rho_0$ or otherwise would not support a 2.17 solar mass neutron star are excluded as they are not realistic.

2.2.1 Results for a 1.4-solar mass NS

From the collection of Skyrme EoSs, only 182 of them can support a 2.17 solar mass neutron star. Each EoS, represented by an open circle in Fig. 2.2, gives rise to a unique prediction for the neutron-star radius and tidal deformability. The trend exhibited by the open circles reflects the fact that tidal deformability and neutron-star radius are correlated as described by Eq. (1.9). Tidal deformability is sensitive to pressure at density region of $0.5 - 3\rho_0$ [17, 38, 69]. If we neglect the crust in our calculations, we arrive at the blue dashed curve. Above $\Lambda > 600$, calculations including a crust produce larger radii. The phenomenon that the crust adds to the radii has also been observed in other calculations [68, 69].

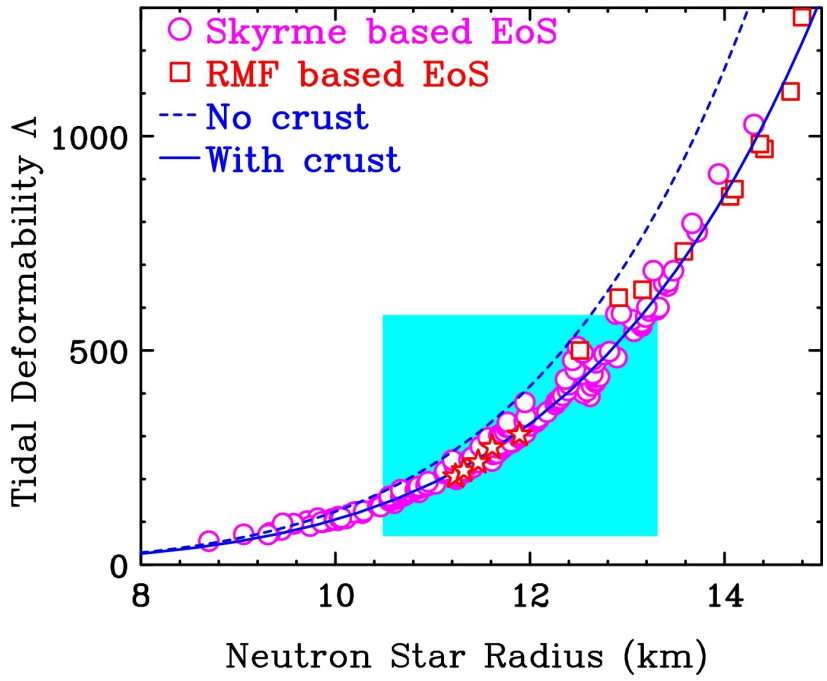

Figure 2.2: Correlation between neutron-star tidal deformability and radius from current calculations are represented by open circles and those from Ref. [3] by open squares. The light blue shaded area represents constraint from recent GW170817 analysis [4]. Five interactions, KDE0v1, LNS, NRAPR, SKRA, QMC700, deemed as the best in Ref. [3] in describing the properties of symmetric matter and calculated pure neutron matter, are plotted as red stars. The dashed curve is the best fit to our results if no crust is included in our neutron star model.

The increase in crustal thickness with neutron star radius is consistent with Ref. [70], which shows that the crust thickness increases inversely with neutron star compactness (M/R). The reason is that crust thickness contributes to the total radius but does not affect the total mass and depends little on uncertainties in the crustal EoS. In the region of large tidal deformability, our results are consistent with those from EoSs based on relativistic mean-field interactions [4] following analogous methodology and represented by the open red squares in Fig. 2.2. The range of the values $\Lambda = 70 - 580$ and $R = 10.5 - 13.3$ km obtained from the GW170817 analysis [29] is represented by the light blue-shaded square. Our calculations lie nearly diagonally across the box with about 130 interactions inside.

One advantage of Skyrme nuclear density functionals is that many different Skyrme interactions have been developed to calculate nuclear properties and these studies are well documented in the literature [3, 39, 40]. As described in Ref. [3], eleven constraints that represent the properties of

symmetric nuclear matter and pure neutron matter are used to assess 240 Skyrme interactions. Five interactions, KDE0v1, LNS, NRAPR, SKRA, QMC700, which satisfy nearly all the eleven constraints, are highlighted as red stars in all the figures in this section. The Λ values (~ 250) they yield, with the associated radii (~ 11.3 km), are well within the GW constraint.

As mentioned in Section 1.1, it is customary to expand EoS in Taylor parameters expanded at saturation density. By taking advantage of the large range of Skyrme parameters used in this work, we can explore the correlations of the set ($K_{\rm sat}$, $Q_{\rm sat}$, S_0, L, $K_{\rm sym}$, $Q_{\rm sym}$) to the neutron star properties, specifically, the tidal polarizability, Λ. Since Λ is monotonically related to the neutron star radius R, we observe similar correlation between R and the set ($K_{\rm sat}$, $Q_{\rm sat}$, S_0, L, $K_{\rm sym}$, $Q_{\rm sym}$) even though the latter correlations are not discussed below.

First we explore the connection to the parameters in E_{is}. Fig. 2.3 shows the plots of Λ vs $K_{\rm sat}$ (left panel) and $Q_{\rm sat}$ (right panel). The value of $K_{\rm sat}$, also known as compressibility, has been fairly well determined experimentally to be 230 ± 30 MeV [3]. Most of the Skyrme interactions studied here cluster around $K_{\rm sat} \sim 240$ MeV and, within this tight bound on $K_{\rm sat}$, show no obvious correlation with Λ. $Q_{\rm sat}$ values cluster around ~ -380 MeV and again show no correlation with Λ. This observation that Λ is not strongly connected to $K_{\rm sat}$ and $Q_{\rm sat}$ that characterize the symmetric matter, is consistent with conclusions of previous studies [71]. This implies that it would be difficult to extract properties of the symmetric nuclear matter from the dipole deformability of the neutron star alone.

Next we explore the importance of the parameters in symmetry energy term, S_0, L, $K_{\rm sym}$, and $Q_{\rm sym}$ in Fig. 2.4. The abscissa scales are chosen to represent the respective ranges of values found in Ref. [3] and that the correlations between the plots are comparable. The correlations between Λ and symmetry energy parameters are stronger than those for symmetric nuclear matter. The correlation is strongest in $K_{\rm sym}$ followed by L. Here L mainly characterizes the vicinity of saturation density region as it is the first derivative. Since the second-order term, $K_{\rm sym}$ impacts more at the higher densities, it is not surprising that $K_{\rm sym}$ should have stronger influence on Λ. The much weaker sensitivity to $Q_{\rm sym}$ probably reflects that it impacts density above $3\rho_0$. Different models may have

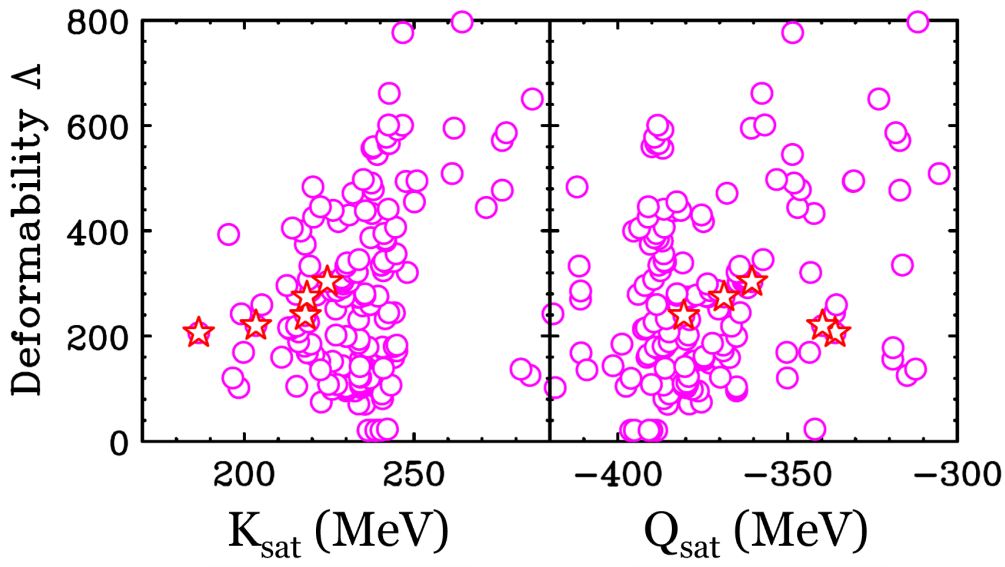

Figure 2.3: Correlation between the neutron star deformability Λ and the compressibility parameter $K_{\rm sat}$ (left panel) and skewness parameter $Q_{\rm sat}$ (right panel) defined in Eq. (1.4) for the symmetric matter EoS of Skyrme functionals used in the study. The red stars in both panels represent the five interactions, KDE0v1, LNS, NRAPR, SKRA, and QMC700 that satisfy nearly all 11 constraints of Ref. [3].

different correlations between S_0, L, $K_{\rm sym}$, and $Q_{\rm sym}$. Thus the correlations observed here may not be universal. It would be interesting to examine these correlations with other density functionals and, in particular, with interactions that have different correlations between density regions than those that are implicitly contained in the Skyrme.

2.2.2 Neutron star of different masses

Fig. 2.2 shows the power-law relationship between the tidal deformability and the radius for 1.4 solar mass neutron star. If mass of the neutron star changes, a different power law relationship is expected. The left panel of Fig. 2.5 shows the tidal deformability as a function of neutron star radius for neutron-star of mass 1 (closed violet circles), 1.2 (open violet circles), 1.4 (closed blue squares), 1.6 (open blue squares), 1.8 (closed red triangles) and 2 (open triangle) solar masses. A universal relationship with the tidal deformability is obtained if the mass is taken into account as shown in the right plot of Fig. 2.5 where the radius is replaced by the compactness factor (M/R). As expected, the tidal deformability has an inverse power law relationship to the compactness factor

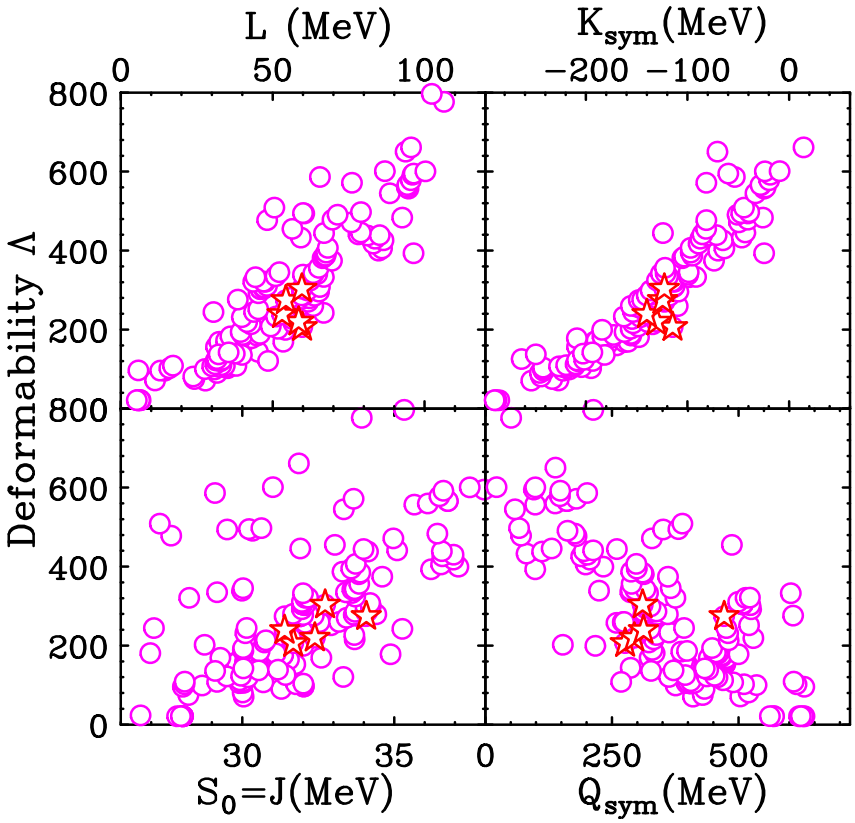

Figure 2.4: The four panels show the correlation between the neutron star deformability Λ and Taylor expansion coefficients S_0 (lower left), L (upper left), $K_{\rm sym}$ (upper right) and $Q_{\rm sym}$ defined in Eq. (1.5) for the symmetry energy and obtained for the Skyrme functionals used in the study. The symbols follow the same convention as in Figs. 2.2 and 2.3.

(M/R). For a fixed solar mass, the range of the compactness factor is limited since the radius of the neutron star mostly span a range from about 8 to 14 km. Thus it is easier to deform a smaller star giving rise to larger deformability than to deform a star with larger mass.

2.3 Neutron stars from Meta-modeling EoS

This section is a slightly modified version of Ref. [72] and reproduced here with the permission of the copyright holder.

While Skyrme EoS provides numerous advantages, it is difficult to explore new physics from the Taylor expansion parameters because they are strongly constrained by the form of the Skyrme interaction itself. It is difficult to access the functional dependencies of the Taylor expansion

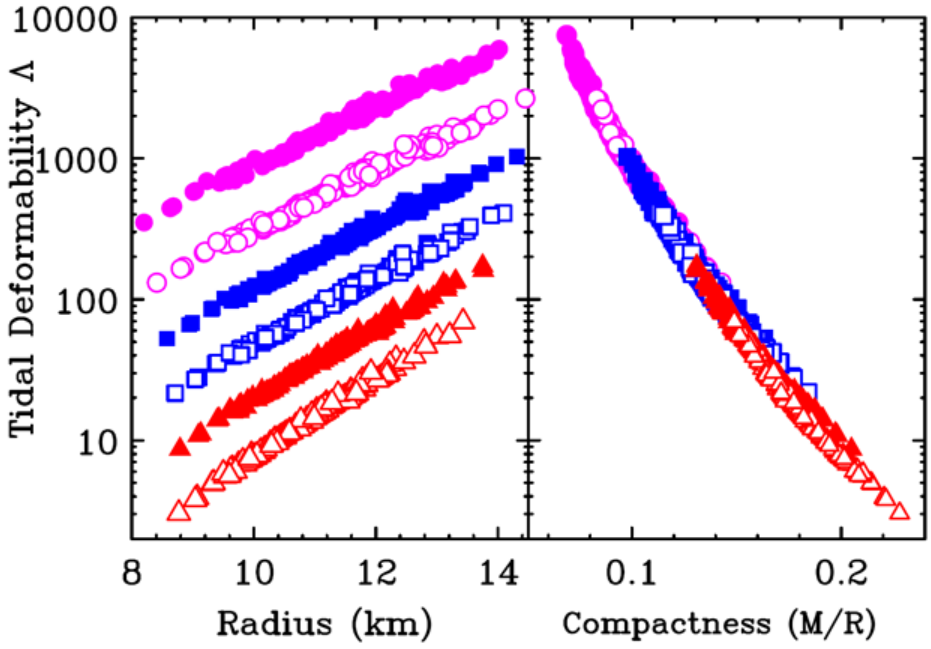

Figure 2.5: Left panel: Correlation between neutron-star tidal deformability and radius for neutron stars with different masses. From top: closed and open circles, closed and open squares, closed and open triangles represent neutron star of mass 1, 1.2, 1.4, 1.6, 1.8 and 2 solar masses. Right panel: Universal relationship between neutron-star tidal deformability and compactness (M/R) for neutron stars with different masses as plotted in the left panel.

parameters that are not contained in the original choice for the Skyrme functional form [73, 74]. This can be overcome with Meta-modeling EoS from Ref. [1]. Such metamodels for the EoS can be easily constructed with only Taylor expansion parameters and effective masses. Their derivatives of different orders are independent of each other by construction.

Four different *empirical local density functionals* (ELF) meta-models are proposed in Ref. [1]: ELFa, ELFb, ELFc and ELFd. ELFa does not produce vanishing energy as density approaches zero. ELFb does not converge to a typical Skyrme EoS even when identical Taylor parameters are used. ELFc does not have the shortcomings of ELFa and ELFb and closely resembles Skyrmes with similar Taylor parameters. Although ELFd agrees with Skyrmes better than ELFc, it relies on high density information that is not well constrained by experiments.

From the above considerations, we adopt ELFc in this study. Similar choice is also made in other recent studies [69, 75]. The formulation of ELFc is detailed in Appendix C. The following choices of parameters have been accurately constrained by nuclear experiment and are fixed in the

analysis [1]: $E_{\rm sat} = -15.8\,{\rm MeV}$, $\rho_0 = 0.155\,{\rm fm}^{-3}$.

Apart from the usual Taylor series coefficients, another important quantity that characterizes nuclear matter properties in Meta-modeling is the effective mass $m^*(\rho, \delta)$. It is used to characterize the momentum dependence of nuclear interaction and it can be different for protons $m^*_{\rm p}(\rho, \delta)$ and neutrons $m^*_{\rm n}(\rho, \delta)$ depending on the environment under which the nuclear matter is subjected to. It is generally assumed that $m^*_{\rm p} = m^*_{\rm n}$ in SNM.

Comparison of effective masses is commonly carried out through the comparison of two quantities: the nuclear effective mass in SNM at saturation $m^*_{\rm sat}$ and the splitting in neutron and proton effective masses in pure neutron matter (PNM) at saturation $\Delta m^* = m^*_{\rm n} - m^*_{\rm p}$. The choice of the two quantities mirrors the spirit of splitting EoS into isoscalar term and isovector term in Eq. (1.3) where contribution from SNM is separated from the correction factor that arises from asymmetry in numbers of protons and neutrons.

Sometimes it is more convenient to express $m^*_{\rm sat}$ and Δm^* in terms of $\kappa_{\rm sat}$, κ_{sym} and κ_v:

$$\begin{aligned} \kappa_{\rm sat} &= \frac{m}{m^*_{\rm sat}} - 1 = \kappa_s, \\ \kappa_{\rm sym} &= \frac{1}{2}\Big(\frac{m}{m^*_n} - \frac{m}{m^*_p}\Big), \\ \kappa_v &= \kappa_{\rm sat} - \kappa_{\rm sym}. \end{aligned} \tag{2.3}$$

The parameter κ_v plays the role of the enhancement factor in Thomas-Reiche-Khun sum rule and depends on the energy region of the resonance energy [76]. In this analysis, the effective masses will be expressed in terms of $m^*_{\rm sat}/m$ and κ_v.

NS EoSs are constructed from Meta-modeling EoS using procedure detailed in Section 2.1, with spline interpolation as the connection EoS in inner crust and beta-equalibrated ELFc as the EoS for outer core. The inner core is represented by the "stiffest" possible EoS where speed of sound is equal to the speed of light. The determination of transition density from outer to inner core will be outlined below.

Additional characteristics of nuclear matter can be inferred using thermodynamic equations once an EoS is specified. The pressure at various densities $P(\rho)$ is related to the derivative of the

energy:

$$P(\rho) = \rho^2 \frac{\partial E(\rho, \delta)}{\partial \rho}. \tag{2.4}$$

The adiabatic speed of sound can then be calculated [77]:

$$\left(\frac{c_s}{c}\right)^2 = \left(\frac{\partial P}{\partial \mathcal{E}}\right)_S, \tag{2.5}$$

where $\mathcal{E} = \rho(E + mc^2)$ is the energy density of the material, including mass density. This implies any thermodynamic stable EoS must satisfy $\left(\frac{\partial P}{\partial \mathcal{E}}\right)_S > 0$. Furthermore, since information cannot travel faster than the speed of light due to causality, the inequality $c_s < c$ must hold for all densities relevant to NS. This may not be always true for ELFc. To keep the EoS valid, we will switch from ELFc to an expression for the stiffest possible EoS whenever causality is violated. In terms of Eq.(2.2), ρ_c is now the density at which speed of sound from Meta-modeling EoS is equal to speed of light and $P_{\text{inner core}}$ is the stiffest EoS. The stiffest EoS is expressed as,

$$P_{\text{inner core}}(\mathcal{E}, c_s, \mathcal{E}_0, P_0) = \left(\frac{c_s}{c}\right)^2 (\mathcal{E} - \mathcal{E}_0) + P_0. \tag{2.6}$$

This equation represents a EoS with constant speed of sound c_s, with $c_s = c$ yields the stiffest possible EoS [78]. $\mathcal{E}_0$ and P_0 are reference values of energy density and pressure, respectively. The reference values can be adjusted to match the conditions at a specific density where energy density and pressure are known. The switch in EoS avoids superfluous rejection when causality is considered.

2.3.1 Bayesian inference

We use Bayesian inference to study the influence of tidal deformability constraints from LIGO on nuclear-matter EoS parameters. These parameters are sampled uniformly within reasonable ranges and are then used to construct neutron-star matter EoSs. Through solving Tolman–Oppenheimer–Volkoff (TOV) equation (see Appendix B), we are able to calculate the corresponding tidal deformabilities. By combining their prior distribution, which is our initial believe

on parameter values based on findings from literature, and likelihood, which indicates the compatibility between the calculated and the observed tidal deformability, Bayesian inference will assign probability of each EoS parameter set being the correct values with Bayes theorem:

$$P(\mathcal{M}) = \frac{1}{V_{\text{tot}}} w(\mathcal{M}) p(\Lambda(\mathcal{M})) \prod_i g_i(m_i). \tag{2.7}$$

In this equation, $\mathcal{M}$ is the set of all EoS parameters, $m_i \in \mathcal{M}$ is the i^{th} EoS parameters, V_{tot} is the normalization constant, $p(\Lambda(\mathcal{M}))$ is the likelihood of a EoS when its predicted Λ is compared to LIGO observation, g_i is the prior distribution of the i^{th} parameter and $w(\mathcal{M})$ is the filter conditions that filters out nonphysical EoSs.

The likelihood of EoS is the probability of having the observed LIGO event with the assumption that the given theoretical EoS is the ultimate true EoS. We will model the likelihood function as an asymmetric Gaussian distribution based on the extracted $\Lambda = 190^{+390}_{-120}$ [29] for 1.4-solar mass NS from GW170817 mathematically expressed as:

$$p(\Lambda) = \begin{cases} \frac{1}{V} \exp(-\frac{(\Lambda-190)^2}{2\times 120^2}), & \text{if } \Lambda \leq 190 \\ \frac{1}{V} \exp(-\frac{(\Lambda-190)^2}{2\times 390^2}), & \text{if } \Lambda > 190. \end{cases} \tag{2.8}$$

In the above equation, V is the feature scaling constant such that the likelihood function integrates to 1.

The sought function is the probability distribution of EoS parameters, so prior distribution g_i is required to convert from likelihood to posterior using Bayes theorem. A commonly used prior is the Gaussian distribution:

$$g_i(m_i) = \frac{1}{\sqrt{2\pi\sigma_i^2}} \exp\Big(- \frac{(m_i - m_{i,\text{prior}})^2}{2\sigma_i^2} \Big), \tag{2.9}$$

where $m_{i,\text{prior}}$ and σ_i are the prior mean and standard deviation of the free parameters, respectively. They should be chosen to reflect our current understanding of those free parameters. For this, we rely on Ref. [1] which summarizes the distributions of EoS parameters from three phenomenological families, Skyrme, relativistic mean field (RMF) and relativistic Hartee-Fock (RHF). The mean and

Table 2.1: Summary information of various models in Ref. [1]. The bottom half shows characteristics of the prior and posterior distribution, respectively.

	L (MeV)	$K_{\rm sym}$ (MeV)	$K_{\rm sat}$ (MeV)	$Q_{\rm sym}$ (MeV)	$Q_{\rm sat}$ (MeV)	$Z_{\rm sym}$ (MeV)	$Z_{\rm sat}$ (MeV)	$\frac{m^*_{\rm sat}}{m}$	κ_v
Skyrme Average	49.6	-132	237	370	-349	-2175	1448	0.77	0.44
Skyrme σ	21.6	89	27	188	89	1069	510	0.14	0.37
RMF Average	90.2	-5	268	271	-2	-3672	5058	0.67	0.40
RMF σ	29.6	88	34	357	393	1582	2294	0.02	0.06
RHF Average	90.0	128	248	523	389	-9956	5269	0.74	0.34
RHF σ	11.1	51	12	237	350	4156	838	0.03	0.07
Weighted Average	69.0	-45.3	248	367	-114	-3990	3310	0.712	0.42
Weighted σ	20.1	70.8	18.3	214	200	1530	989	0.06	0.17
Posterior Average	71.6	-76.9	245	436	-97	-3410	3490	0.74	0.41
Posterior σ	16.5	66.0	23	219	202	1710	970	0.07	0.25

standard deviation of the parameters for each family are tabulated in the first six rows of Table 2.1. In this study, the prior means and standard deviations are the weighted average values of the three families, with weights of 0.500, 0.333, 0.167, respectively. The weights reflect our confidence in the models. We give Skyrme EoS the most weight as it is the most heavily employed parametrization in a myriad of nuclear predictions [3]. These relative weights are chosen ad-hoc, but should cover most plausible parameter spaces. Prior means and standard deviations are listed in the seventh and eighth rows, respectively, in Table 2.1.

Some parameter sets may yield nonphysical EoSs due to various additional considerations. The filter condition $w(\mathcal{M})$ takes that into account; it is set to 1 if the following three conditions of stability, causality and maximum mass, are all satisfied and it is set to 0 otherwise.

The stability condition rejects EoSs whose pressure decreases with energy density. Above the crust-core transition density, we require the EoSs to be mechanically stable with thermodynamical compressibility greater than zero, which means that the pressure of homogeneous matter does not decrease with density. For EoSs with negative compressibilities at density above the crust-core transition densities predicted by Eq. (2.1), they will be rejected as being inconsistent with experimental information.

The requirement of causality rejects EoSs whose speed of sound is greater than the speed of light in the core region of their respective heaviest NS. The maximum mass condition rejects EoSs that fail to produce a NS of at least 2.04 solar mass in accordance with observation. [79, 80].

Using the fact that the binary NS merger GW170817 detected by LIGO did not promptly produce a black hole, the heaviest possible NS should be around 2.17 solar mass [68]. Other sources put the maximum mass at around 2.15-2.40 solar masses [81–86]. Neither of these constraints have been adopted in here but can be implemented in the future.

The calculated probability distribution from Eq. (2.7) is referred to as the posterior distribution. By comparing prior to posterior distribution, we will be able to infer the sensitivity of various EoS parameters to NS tidal deformability. By construction, priors of different free parameters in meta-modeling EoS are not correlated with each other, so any correlations in the posterior reflect the collective sensitivity of the Taylor expansion parameters to NS tidal deformability.

The EoSs are sampled uniformly within ranges of plus or minus 2σ from the mean values from the seventh and eighth rows of Table 2.1. Each EoS is weighted by the product of filter condition, prior and likelihood of Eq. (2.7). A total of 1,500,000 EoSs have been sampled and 682,652 of them satisfy all of our constraints. Only 11,711 EoSs apply to all densities without switching to the stiffest EoS.

2.3.2 Results for a 1.4-solar mass NS

After incorporating the constraint on Λ from gravitational wave observation of the merger of two 1.4-solar mass NSs by LIGO, posterior distributions of Taylor expansion parameters are shown in Fig. 2.6. The lower triangular plots show the bivariate distributions for two parameters. The diagonal plots show the prior (blue curves) and marginalized posterior distributions (red curves) for each individual parameter. The upper triangle displays the Pearson correlation coefficients for parameter pairs defined as,

$$\rho_{X,Y} = \frac{\mathbf{E}[(X - \bar{X})(Y - \bar{Y})]}{\sigma_X \sigma_Y}, \tag{2.10}$$

where $\mathbf{E}$ is the expectation value and σ_X and σ_Y are the standard deviations of the parameters distributions. The Pearson coefficient ranges from -1 to 1 and its absolute value reflects the strength of the correlation. A positive value close to 1 indicates a strong correlation, a negative value close to -1 indicates strong anti-correlation and a value close to 0 indicates lack of correlation [87]. Only bivariate distributions between L, $K_{\rm sym}$, $K_{\rm sat}$, $Z_{\rm sym}$ and $Z_{\rm sat}$ are shown because the higher order parameters do not seem to be influenced by our tidal deformability constraints. The full correlation plot is included in Appendix D. Characteristics of the probability distributions are summarized in the bottom two rows of Table 2.1.

Fig. 2.7 shows the mean and 2σ region of pressure at different densities spanned by the EoSs in the posterior. The 2σ region converge to a line for $\mathcal{E} \lesssim 20\,\mathrm{MeV/fm^3}$, which corresponds to the outer crust. Since we connect all EoSs to the crustal EoS given by Ref. [64], this convergence is expected. From around $20\,\mathrm{MeV/fm^3}$ to $70\,\mathrm{MeV/fm^3}$, the spline connection kicks in and manifests in the broadening of pressure.

The cut-offs in the lower left corner of $Z_{\rm sym}$ vs. $Z_{\rm sat}$ distribution and the upper left corner of $K_{\rm sym}$ vs. L distribution in Fig. 2.6 are the consequence of stability condition. At such extreme values, speed of sound may be imaginary when extrapolating to NS of 2.04 solar masses. This is evident in Fig. 2.8 in which 50 randomly selected EoSs from the cut-off region in $K_{\rm sym}$ vs. L are shown in the lower panel. The pressure for those EoSs do not increase monotonically with the energy density and become mechanically unstable. These EoSs are discarded.

The posterior distributions of $K_{\rm sym}$ and $Z_{\rm sym}$ differ from the prior distributions significantly. The tidal deformability constraint favors lower $K_{\rm sym}$ region. The inference also narrows the range of possible L. Parameters such as $K_{\rm sat}$ and $Z_{\rm sat}$, whose posterior distributions are not altered significantly reflect that they are not sensitive to the tidal deformability constraints.

While this Bayesian analysis is well suited to discuss the sensitivity of the deformability to the Taylor expansions parameters L, $K_{\rm sym}$, $K_{\rm sat}$, etc., it has some limitations. In particular, we note that the prior and posterior distributions of Λ as shown in Fig. D.1 (row 2 column 10 in Appendix D) are drastically different, probably as a consequence of the narrow prior distributions

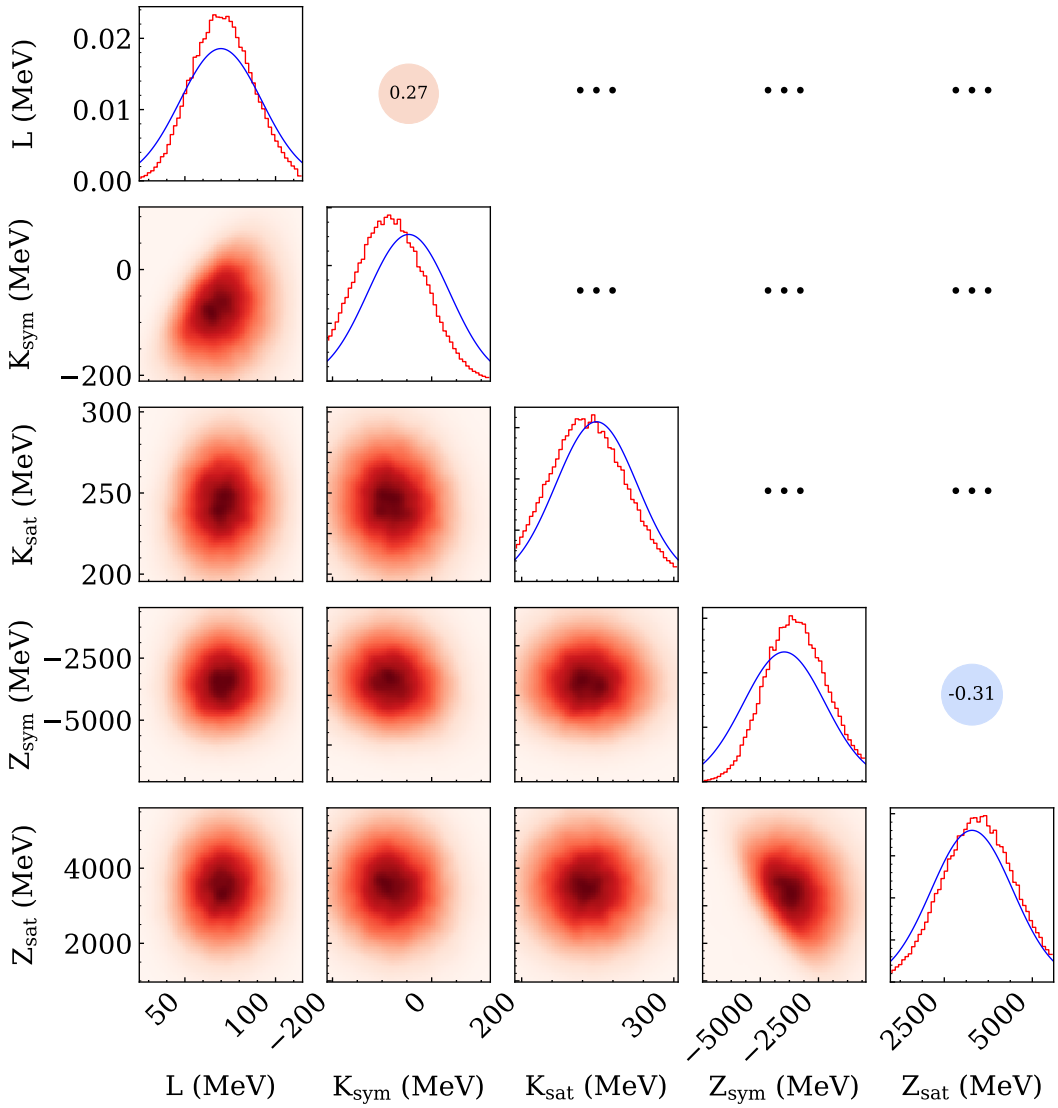

Figure 2.6: Bivariate characteristics of posterior likelihood distributions. Three regions can be distinguished. The lower triangle panels show likelihood distributions, with intensity proportional to distribution value, for pairs of Taylor parameters. The diagonal panels display prior (blue) and marginalized posterior (red) distributions for each parameter. The upper triangular region shows Pearson correlation coefficient for parameter pairs. Three dots indicate weak correlations with magnitude less than 0.1. Reprinted figure with permission from C.Y. Tsang et al., Phys. Rev. C 102, 045808. Copyright 2021 by the American Physical Society.

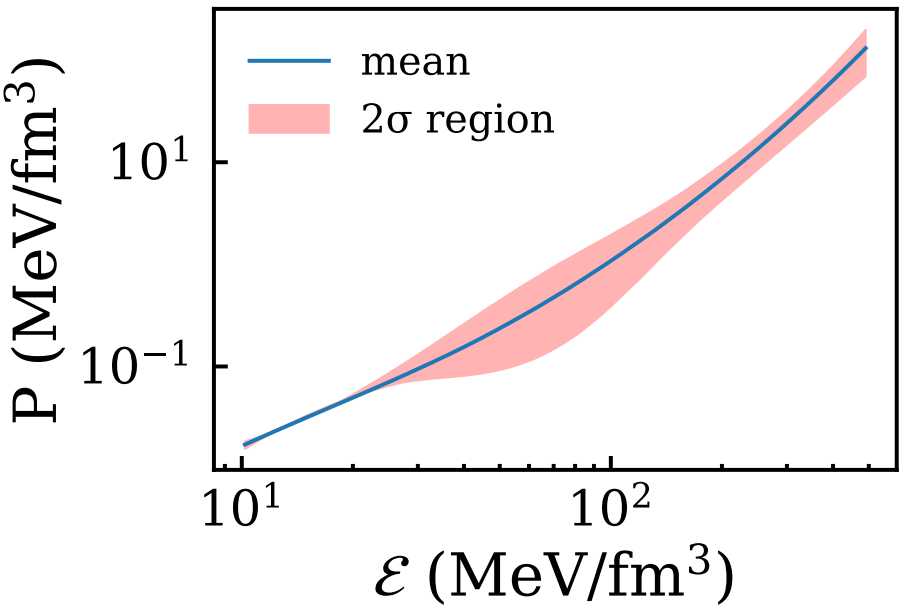

Figure 2.7: Distribution of EoSs sampled from the posterior. The divergence above energy density $\gtrsim$ 20 MeV/fm^3 coincides with the transition from outer crust to spline connection. Reprinted figure with permission from C.Y. Tsang et al., Phys. Rev. C 102, 045808. Copyright 2021 by the American Physical Society.

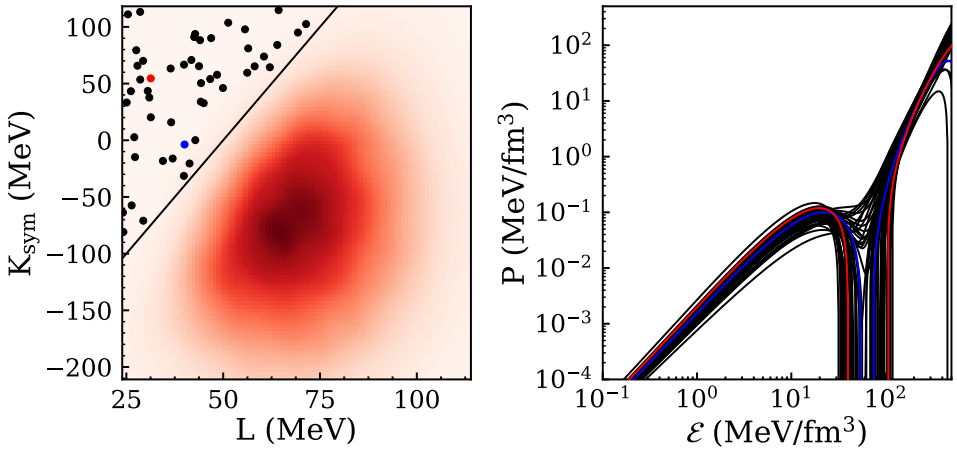

Figure 2.8: Left panel: The 50 dots in the upper left hand corner of $K_{\rm sym}$ vs. L correspond to 50 randomly chosen parameter space within the stability cut-off region. Right panel: Unstable EoSs that correspond to the 50 dots. The red and blue lines correspond to the red and blue points in the upper panel, respectively. They are highlighted to showcase how a typical EoS in the cut-off region looks like. Reprinted figure with permission from C.Y. Tsang et al., Phys. Rev. C 102, 045808. Copyright 2021 by the American Physical Society.

Table 2.2: Predicted tidal deformability for NS of different masses.

	$\Lambda(1.2)$	$\Lambda(1.4)$	$\Lambda(1.6)$	$\Lambda(1.8)$	$\Lambda(2.0)$
Posterior Average	1490	624	281	132	64
Posterior σ	310	129	61	31	17

of the Taylor expansion parameters listed in Table 2.1. This reflects the strong sensitivity of Λ to the prior distributions of the EoS. Furthermore, the posterior distribution of Λ is much sharper and peaked at 624 ± 129 which exceeds the value of 190^{+390}_{-120} from the analysis of the GW170817 [29]. While the GW constraint reflects the high density of NS core, the prior distributions of the Taylor expansion parameters do not have rigorous laboratory constraints at high density region where Λ is determined. In light of this disagreement, the ranges of Taylor parameters to be explored will be expanded to plus-or-minus four standard-deviation from the average values in Table 2.1 with uniform priors in Chapter 6.7 when we incorporate heavy-ion constraints into NS calculation.

2.3.3 Neutron star of different masses

In anticipation that more merger events involving different NS masses than the nominal NS mass of 1.4 solar mass will be observed in the future [88], we use the posterior EoS distributions to predict deformability of NS with different masses. In Table 2.2, we provide our predictions for the tidal deformabilities for NS with 1.2, 1.4, 1.6, 1.8 and 2 solar masses from the posterior distributions. To show the sensitivity of these predictions to the Taylor parameters, the bivariate distributions between the Taylor parameters from the posterior and the predicted tidal deformabilities on different stellar masses are shown in Fig. 2.9. We find that Λ is more strongly correlated with L and $K_{\rm sym}$ than it is with higher order Taylor expansion parameters. The sensitivity to $K_{\rm sym}$ increases, while the sensitivity to L decreases, with stellar mass.

To quantify this dependence of sensitivity on mass, the Pearson correlation coefficients for a few selected Taylor parameter pairs are shown in Fig. 2.10. A gradual reduction in correlation between L and tidal deformability is observed as the mass of a NS increases. This is expected as relevant

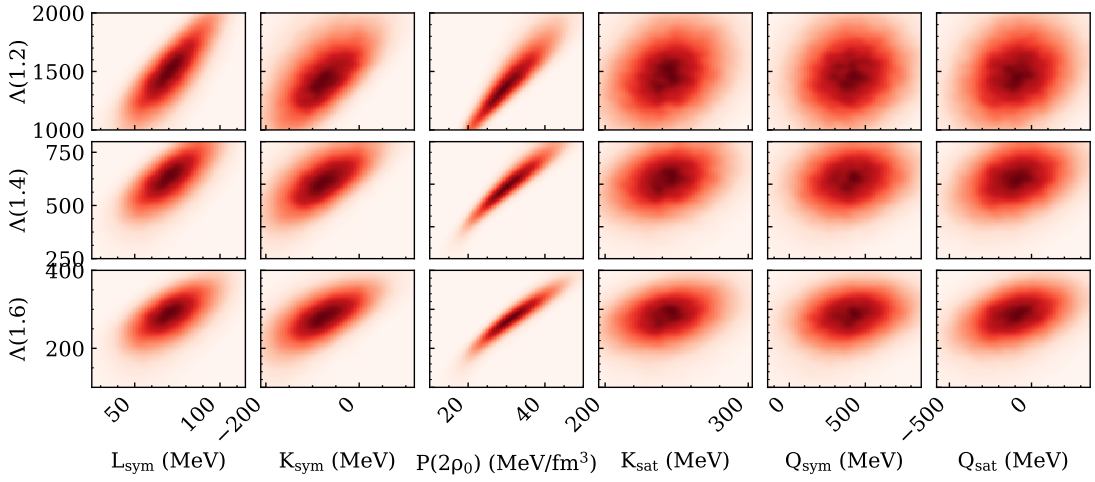

Figure 2.9: Bivariate distributions between deformabilities with NS of different masses and Taylor parameters. Correlation with tidal deformability is clearly seen with L, $K_{\rm sym}$ and $P(2\rho_0)$. Reprinted figure with permission from C.Y. Tsang et al., Phys. Rev. C 102, 045808. Copyright 2021 by the American Physical Society.

average density for more massive stars shift upward and away from those directly impacted by L. A high density parameter $P(2\rho_0)$, the pressure for pure neutron matter at twice the saturation density, is also included in Figs. 2.9 and 2.10. The strong correlation between tidal deformability and $P(2\rho_0)$ is consistent with prior works [17, 29, 38, 89]. While this strong correlation is maintained for both heavy and light NSs, the slope of the correlation becomes smaller reflecting the decrease in average values and variations of Λ with stellar mass.

Such decrease is correlated with an increase in stellar compactness. Using the posterior distributions of Taylor expansion parameters, predictions can be made on the relation between stellar mass and inverse compactness (R/M). Fig. 2.11 shows tidal deformability plotted against inverse compactness, with calculation results for 1.2, 1.4, 1.6 and 1.8 solar mass NS all combined together. It is consistent with Eq. (1.9) where $\Lambda \propto k_2(R/M)^5$. The best fitted power law has an index of 5.84 due to additional interdependence of tidal Love number k_2 and R/M. The result is consistent with Refs. [28, 90, 91].

We found that independently and in parallel, Ref. [75] conducts a very similar analysis using ELFc. Our work examines correlations between more parameters and our study extends to higher mass neutron star. Ref. [75] uses much wider priors while our prior is more restrictive and provide

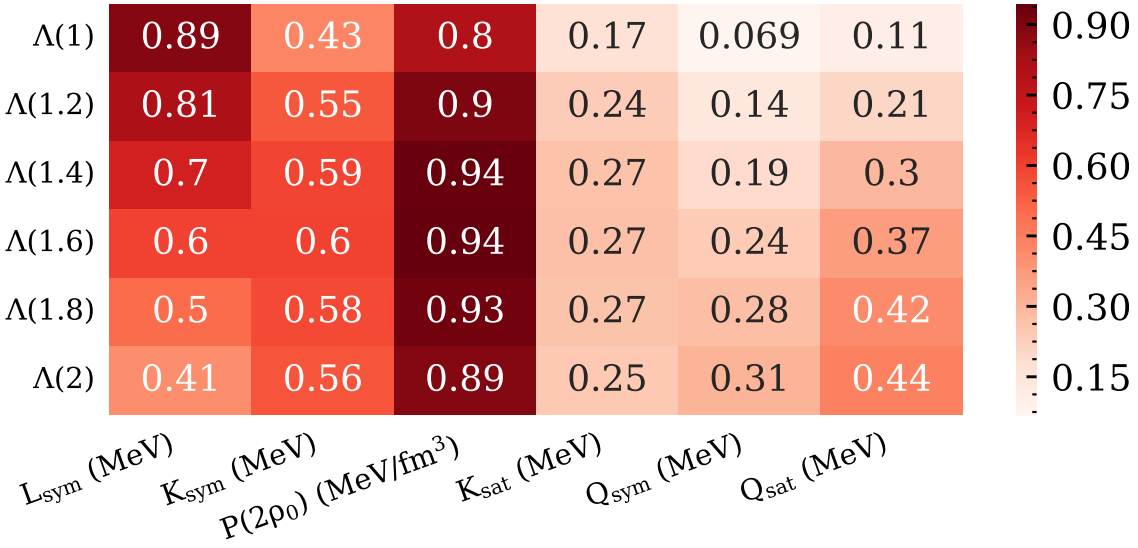

Figure 2.10: Pearson correlations for different NS masses. Reprinted figure with permission from C.Y. Tsang et al., Phys. Rev. C 102, 045808. Copyright 2021 by the American Physical Society.

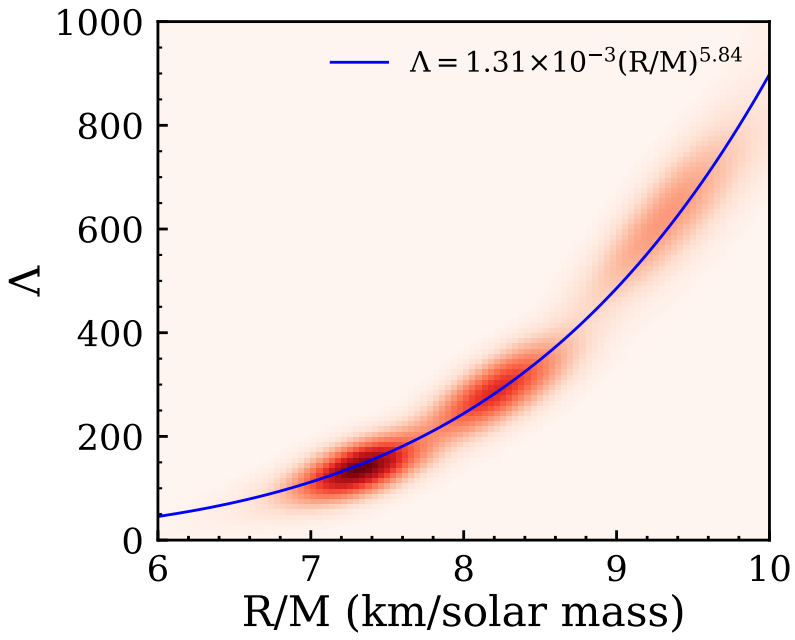

Figure 2.11: Tidal deformability vs. inverse compactness for 1.2, 1.4, 1.6, 1.8 solar mass NS. Reprinted figure with permission from C.Y. Tsang et al., Phys. Rev. C 102, 045808. Copyright 2021 by the American Physical Society.

finer details in a smaller phase-space. In addition, they apply additional constraints on the EoS using data from χEFT approach and ISGMR collective mode. Even though their extracted $Q_{\rm sat}$ and $K_{\rm sym}$ values are consistent with our extracted values, details in the correlations are not the same. The subtle differences suggest that Bayesian analysis results depend on the choice of priors and constraints applied to the EoS.

CHAPTER 3

SπRIT DATA ANALYSIS

3.1 SπRIT experiment

In the SπRIT heavy-ion experiment, the particle accelerators are provided by the Radioactive Isotope Beam Factory (RIBF) at RIKEN, JAPAN. Tin isotopes are accelerated to 270 MeV/u. The target is an isotopically highly enriched stationary Tin foils and the main particle detector is the SπRIT time projection chamber (TPC). In this chapter, the configuration and working principle of the accelerators and SπRIT TPC will be briefly described. Details can be found in Ref. [92].

3.1.1 Radioactive Isotope Beam Factory (RIBF)

RIBF produces rare Tin isotope secondary beams from relatively stable primary beams. This primary beams are created by accelerating the primary ions progressively by a linear accelerator (RILAC) and four coupled cyclotrons (RRC, fRC, IRC and SRC) to reach a beam energy of 345MeV/u. The ions are guided to hit a rotating Be target, which breaks the primary ion down to smaller fragments, and in some events one of these fragments is the desired Tin isotope. For the creation of neutron-rich ^{132}Sn and ^{124}Sn beams, ^{238}U primary ion is used and for less neutron-rich ^{112}Sn and ^{108}Sn beams, ^{124}Xe is used.

The fragments are selected by the BigRIPS spectrometer, which is a series of dipole magnets, slits and wedge degraders arranged in such a way that only particles within a narrow range of magnetic rigidity ($B\rho = p/Z$, where p is the momentum magnitude and Z is the charge) can pass through. It filters out most of the undesirable fragments, but some contaminating isotopes can still pass through. To select events from a particular isotope, scintillators and ion chambers are set-up along the beam line after the spectrometer. They measure the time-of-flight (ToF) and charge number (Z) of isotopes that reaches the SπRIT detector respectively. $B\rho$ is calculated from ToF information and magnet settings in BigRIPS. When it is used in conjunction with the charge state

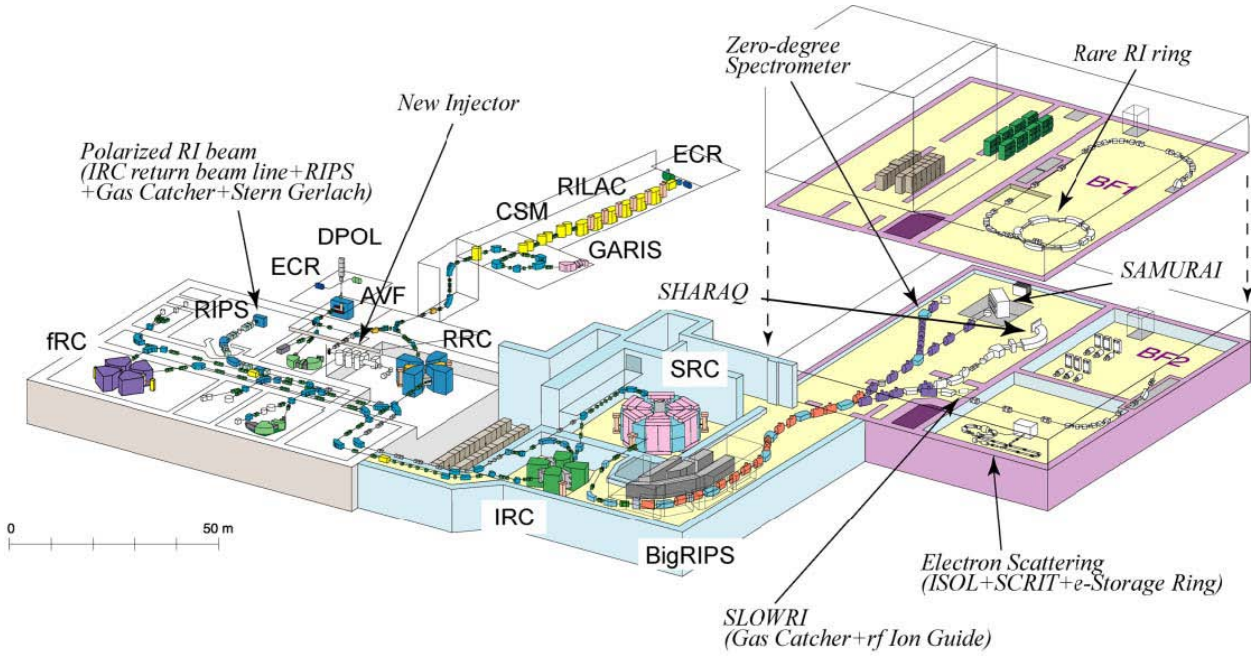

Figure 3.1: An overview of RIBF extracted from Ref. [5], with accelerators on the left, fragment separator BigRIPS in the middle and SAMURAI spectrometer on the top right.

information, we can identify the isotope that passes through BigRIPS event by event. This beam selection process is described in Ref. [2]. In this work, only events from the desired Tin isotopes are analyzed.

The configuration of RIBF is illustrated in Fig. 3.1. The BigRIPS guides the Sn beam towards SAMURAI dipole spectrometer, where the SπRIT TPC and the associated auxiliary detectors were installed inside..

3.1.2 SπRIT Time Projection Chamber (TPC)

The SπRIT TPC is a rectangular detector designed to measure momentum distributions of pions and other light fragments from fixed target collisions. It has an detection volume of dimensions 86.2 cm $\times$ 51.3 cm $\times$ 134.4 cm (width, height, length). It was surrounded by auxiliary trigger detectors on both sides and downstream. The TPC and trigger detectors are placed inside the SAMURAI dipole magnet which provides a near uniform 0.5 T magnetic field. Please refers to Ref. [93] for details of SAMURAI spectrometer.

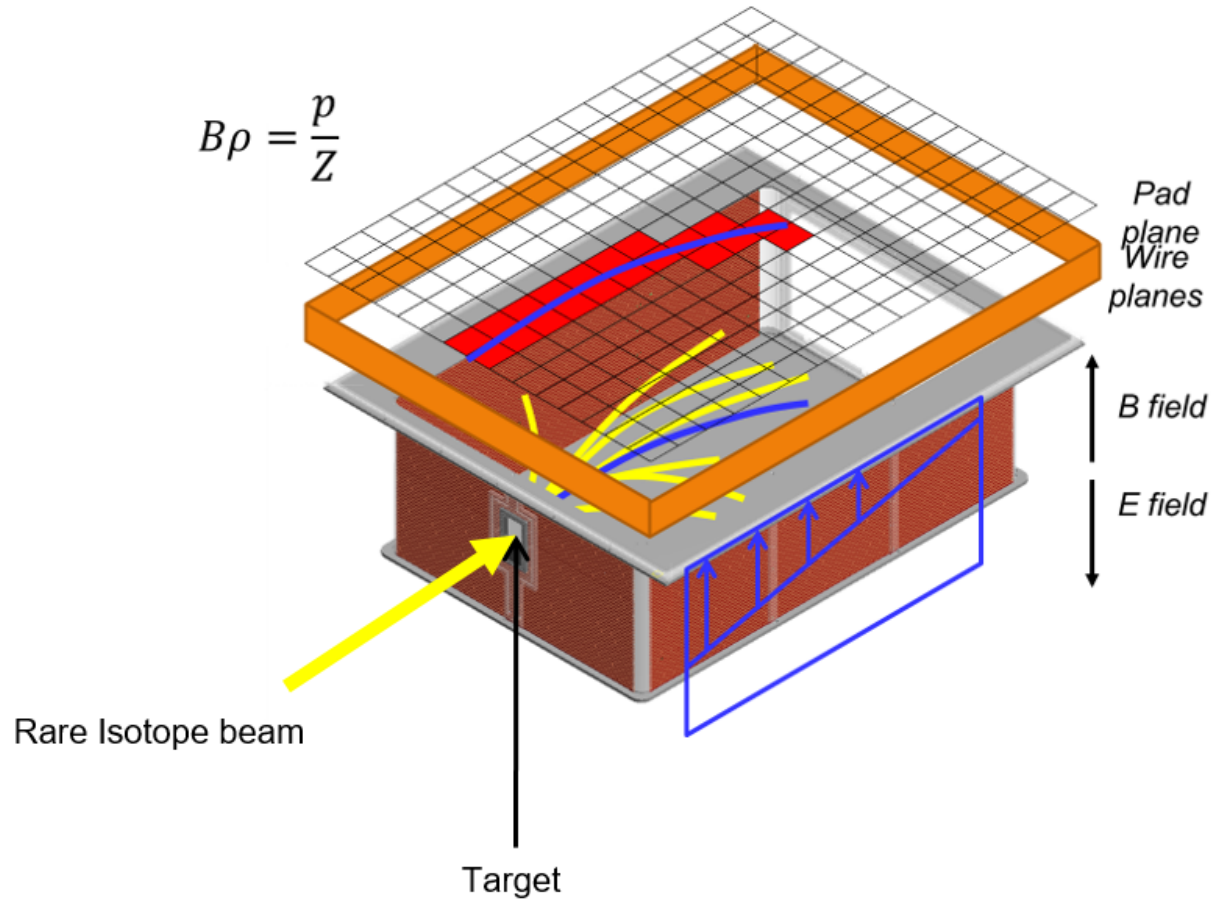

Figure 3.2: A cartoon illustration of the principal components of the SπRIT TPC. The pads are not drawn to scale as there are 12096 pads in the pad plane.

Fig. 3.2 is a simplified cartoon that illustrates the working principle of the SπRIT TPC. The detection volume called the *field cage* was filled with 90% Ar and 10% CH_4 (P10 gas) at atmospheric pressure. When charged particles pass through the detector volume, they interact with and ionize the gas molecules, leaving behind trails of free electrons and positive ions.

Magnetic and electric fields inside the detection volume force trailing electrons to drift upward and positive ions downward. The electric field is created by the walls of the field cage, which is made of PCBs and depicted as the brown vertical walls in Fig. 3.2. The field cage consists of 50 vertically stacked layers of copper strips, with each layer wraps around the detection volume horizontally and is electrically isolated from nearby layers. During operation, maximum voltage is applied to the top layer and gradually lowered voltages are applied to each successive lower layers.

This potential gradient on the boundary creates a uniform electric field.

Once the drift electrons reach the top of the TPC, they enter the *wire plane* region, which consists of three planes of *gating grid*, *anode wire* and *ground wire* from bottom to top. When drift electrons enter the volume between anode and ground wires, they are accelerated to speed high enough to ionize gas molecules by the large potential difference between these two layers. Electrons from these ionized molecules are also accelerated to create more electrons. This electron multiplying process is called *avalanche* and it amplifies the signal from the drift electrons, but a lot of unwanted positive ions are also created. They drift back into the detection volume by electrostatic force and if too many are present, the uniform electric field will be distorted. To maintain the uniformity of electric field, the gating grid is placed below anode wire to prevent excessive electrons from entering the anode in the first place [94, 95]. One of the major sources of excessive electrons is collision events that do not satisfy trigger conditions. The gating grid consists of a series of parallel wires. When trigger conditions are not met, the grid is set to "close" configuration such that the voltages of the wires are staggered. Electrons approaching the grid are pushed towards and absorbed by gating grid wires with lower voltage. When trigger condition is satisfied, the grid is set to "open" configuration such that voltages of all wires are identical. This allows electrons to move upward unimpeded. Simulation shows that average transparency is 100% in "open" position and 0% in "close" position [7], which means that the gating grid is very close to being perfect. The movement of drift electrons when gating grid is "open" and "close" are illustrated in Fig. 3.3. Despite the fact gating grid is calculated to be almost perfect in electron blocking, in practice electrons were still able to pass through wire plane at the downstream side of the detector due to the fact that gating grid do not completely cover the filed cage. Electrons and ions that leak through the gap creates subtle but noticeable effect on track recognition. The effects of incomplete gating grid coverage is the focus of Section 3.3.3.

The induced electrons from avalanche enters the *pad plane*, which consists of pads (pixels) that detect the amount of drifting electrons they come into contact with. There are 112 layers of pads along z-direction and 108 rows along x-direction, with the size of each pad being $1.2\,\text{cm} \times 0.8\,\text{cm}$

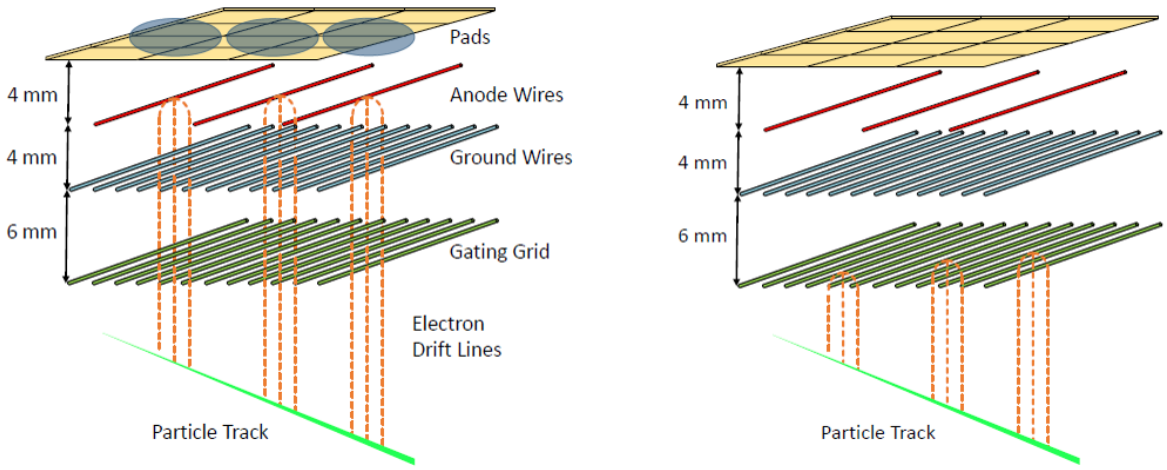

Figure 3.3: Cartoon depiction of the electric field configuration of the grating grid in "open" configuration (left) and "close" configuration (right).

(length, width). Signal from all pads can be combined to trace the two-dimension projection of the fragment trajectory along the horizontal (x-z) plane. This is illustrated in Fig. 3.2 where the red cells corresponds to pads with signal and the blue curve corresponds to the two dimension projection of a fragment track on the pad plane. Vertical information for each track can be inferred from the signal detection time on each pad relative to the start counter time-stamp. Electrons drift at a constant speed of 5.42 ns/μm in SπRIT TPC [96] so electrons that originate from lower vertical position takes longer to reach the top.

Trajectories of charged fragments inside the TPC are curved due to magnetic field. The curvature of each track is indicative of their corresponding momentum over charge (p/Z) value. With appropriate curve fitting routine, we can reconstruct momentum distributions of various fragments. Such procedures will be described in details in later chapters.

3.1.3 Beam Drift Chambers (BDC)

To boost the momentum distributions from laboratory frame to center-of-mass frame, we need to measure the angle of incidence of projectile for each event. This is achieved with a pair of Walenta-type detectors called Beam Drift Chambers (BDCs). They are placed upstream of the target along the beam pipe [2].

These chambers consist of two sets of Parallel Plate Avalanche Counters (PPACs). They are approximately 1 m apart along the beam line. PPAC is a thin rectangular box filled with methylpropane gas. The two sides of the PPAC consist of metallic strips that detects the presence of electrons from the ionization of methylpropane gas as particles move through the detector. The time difference between signals from both ends of the strips tell us the location of the beam particle as it passes through, therefore two readings from the two PPACs can be interpolated to estimate the angle of incidence. The uncertainty in BDC beam angle of the order of magnitude of 0.1 μrad [2].

3.1.4 KYOTO array and KATANA veto bars as trigger detectors

The four major triggers in the SπRIT experiment are the Scintillating Beam Trigger (SBT), Active Veto Array, KYOTO Multiplicity array and KATANA veto bars. Given that the primary objective of the experiment is to measure pions created in central collisions [97], the triggers are set-up to favor central collision events and disproportionately rejects peripheral events.

SBT is located 4.5 m upstream of the detector. It is a plastic scintillator that serves as a start counter when a beam particle registers a hit. Active veto array consists of four plastic scintillators immediately upstream of the target forming a rectangular frame with a smaller rectangular hole in the middle. The hole allows for beam particles with small angle of incidence from BigRIPS to pass through. Veto array is hit only if beam particle arrives off-center so events with a signal from veto array are rejected. Both the SBT and active veto array detectors are set-up to maintain beam quality on recorded events.

The remaining two detectors, KYOTO array and KATANA veto bars, are set-up to disproportionately reject peripheral events by selecting events with high multiplicity and low residual projectile mass. They are depicted as the transparent walls surrounding the TPC in Fig. 3.4. These conditions skew the multiplicity distribution away from what is expected from the geometric cross-section.

The KYOTO multiplicity arrays are the two arrays flanking the left and right sides of the SπRIT chamber. Each side consists of 30 tightly packed rectangular plastic scintillator bars, each with

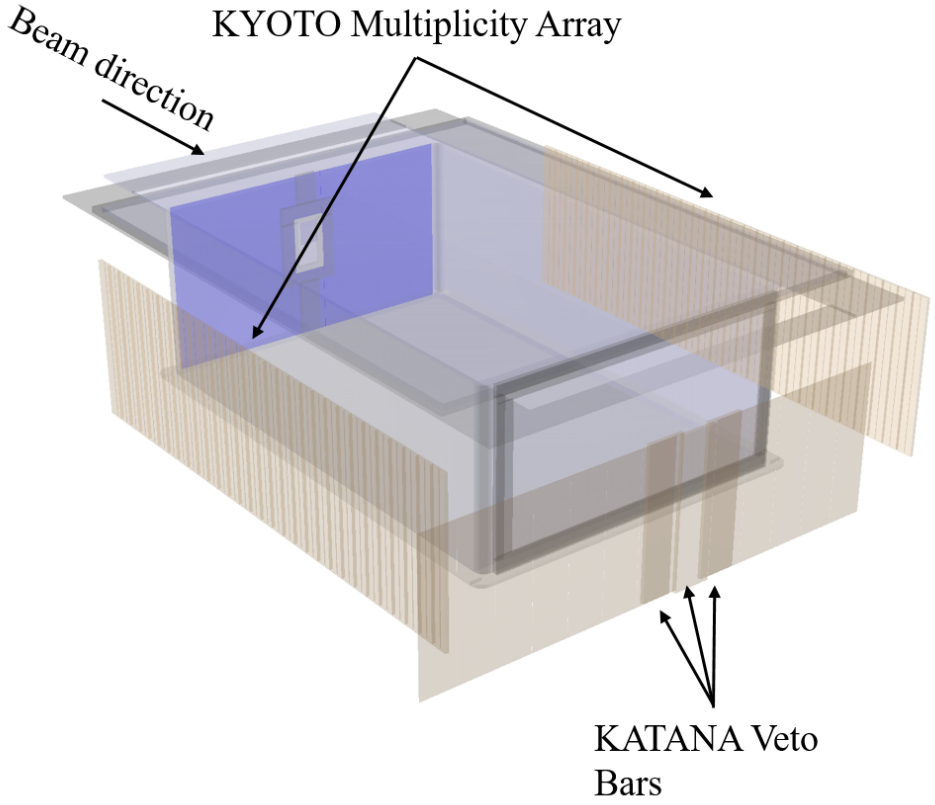

Figure 3.4: Illustration of KATANA and KYOTO arrays. KYOTO arrays surround the chamber on the left and right sides and the KATANA array is located immediately downstream. Part of the KATANA array contains the two narrow bars with deeper shade of gray and the one between them are the veto paddles used in trigger condition.

dimensions of $450 \times 50 \times 10\,\text{mm}$ (height, length, width). Scintillators are materials that emit photons when they interact with radiation, including charged particles. The photomultipliers at the ends of the bars will pick up the photons and convert it to electronic signal to record if and where charged particles hit KYOTO arrays. The hardware specifications are detailed in Ref. [98].

Krakow KATANA veto bars are three scintillating paddles at the downstream end of the SπRIT chamber, shifted slightly left of the beam axis to intercept the heavy residue traversing the magnetic field [2, 99]. The signal amplitude is proportional to the charge state Z of the residue. The trigger condition is set to only accept events where charge of heavy residue hitting KATANA is $\lesssim 20$ with at least four KYOTO bars being hit simultaneously.

3.2 Data analysis

The SπRITROOT framework is developed to analyze data from SπRIT TPC [100]. It is developed based on the FAIRROOT framework which offers modular design pattern with different tasks running sequentially to convert raw electronic signal to physical observables step-by-step. These tasks can be classified into two groups: track level tasks and particle level tasks. The former deals with recognizing tracks from pad signals and the latter deals with reconstructing observables given the fitted tracks. Track level tasks for all fragments and particle level tasks for pions are detailed in Refs. [2, 7] so they are only reviewed briefly here. Particle level tasks for light fragments are newly developed and will be discussed in more details.

3.3 Track Level analysis

This section describes analysis tasks that are required to recognize particle tracks from pad signals. Different tasks are run sequentially, in the order that they are presented below. Each task has access to output of any tasks that are executed before itself.

3.3.1 Decoder, PSA and Helix and Correction task

The *Decoder task* translates the raw data of binary files from TPC into a C++ readable data structure called the *STRawEvent* class [6]. This class contains multiple instances of *STPad* class, each corresponds to an individual pad. Each instance of STPad class encapsulates the digitized electric pulses from the corresponding pad.

The *PSA task* uses data from STRawEvent class to identify the amount and arrival time of drift electrons for all pads. Pulse of a single packet of drift electrons follows a standard shape whose height is proportional to the amount of electrons in that packet. Since it is common to have multiple tracks passing under a pad at different height, the detected pulse is often a linear combination of multiple standard pulses, each with different amplitudes and rise times. PSA Task de-convoluted the combined signal into its constituent pulses as illustrated in Fig. 3.5. We called each of these pulse a *hit*. The fitted amplitude and rise time will be stored in a data structure called the *STHit*

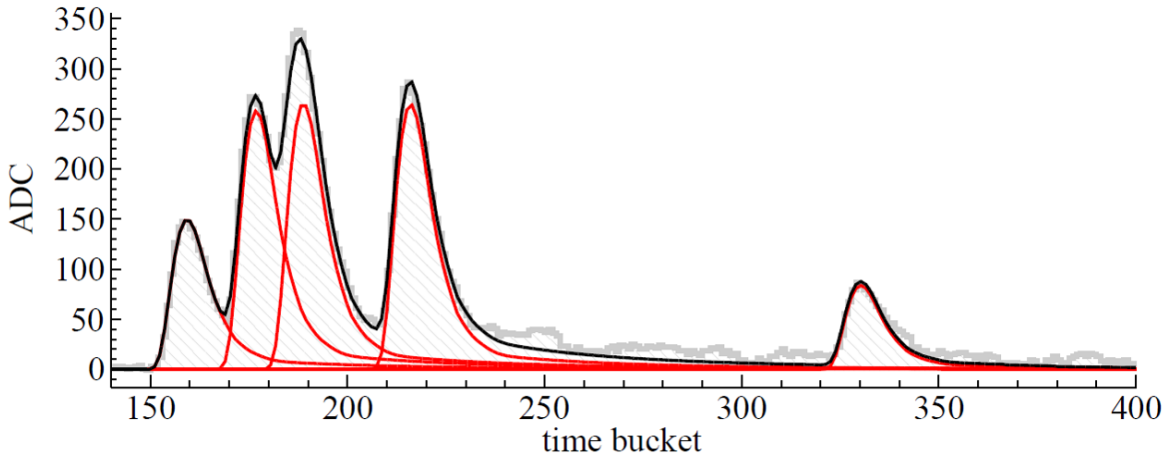

Figure 3.5: An example result from pulse analysis showing decomposition of individual pulses. Taken from Ref. [6].

class. Vertical location is then calculated by comparing the rise time of a pulse with start time of an event.

To the first order approximation, locus of charged particles under magnetic field is the arc of a circle. *Helix task* uses Riemann track finding algorithm to group hits from each event into disjoint sets such that hits from each set forms an arc [101]. The fitted arc and the grouping of hits are stored in another data structure called *STHelixTrack* class.

The next task is the *correction task* which extends the dynamic ranges of dE/dx. The signal strength in some pads are off-scale high (i.e. the digitized signal saturates at the maximum ADC channel) which renders its energy loss information unreliable, but usually such pads are surrounded by multiple pads with lower signal amplitude. Avalanche electrons spread across an area and these nearby pads detect the tails of the electron distribution. The correction task uses signals from these nearby pads to estimate the expected signal amplitude on the saturated pads [102].

3.3.2 Space Charge effect

Space charge effect is a distortion caused by the accumulation of positive ions in the detection region. Reaction cross-section of Sn + Sn collision is so small that 98% of incoming projectiles

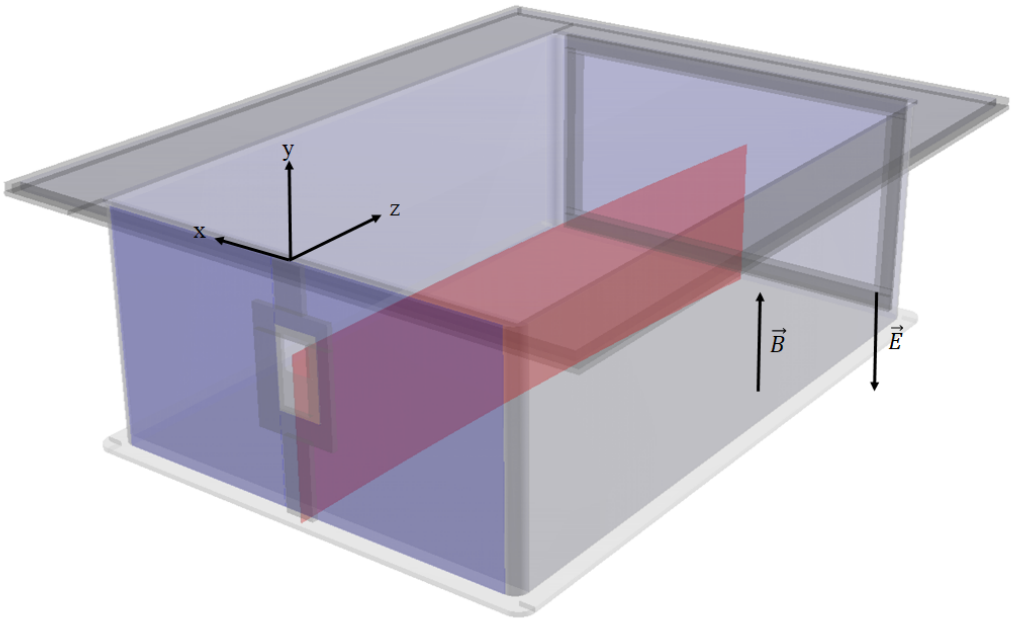

Figure 3.6: The drak red sheet illustrates the assumed shape of the positive ion distribution inside the SπRIT TPC.

pass through the target foil without a collision [96]. When these un-reacted and highly charged projectiles transverse the detector volume, they ionized a lot of gas molecules. The ionized electrons are pushed upwards by the E- and B-field. They drift relatively quickly and are promptly removed by gating grid or anode wire. The massive positive ions, however, drift downward at much slower speed. Ions from a projectile do not have time to clear the height of the TPC before the next projectile enters the detector, which causes ions to accumulate. The resultant charge configuration can be approximately described as a sheet charge extending downward from the beam track as Fig. 3.6 illustrates. The figure also shows the coordinate systems for SπRIT data, where the origin is located at middle of the front edge of the active pads and at the same height as the pad-plane. Furthermore, the $x-$ axis points towards the left when looking in the direction of beam particle to form a right handed coordinate system. The sheet charge is expected to be approximately uniform as drift velocity of ions is constant.

Their presence in the detection volume distorts the otherwise uniform E-field. This slight

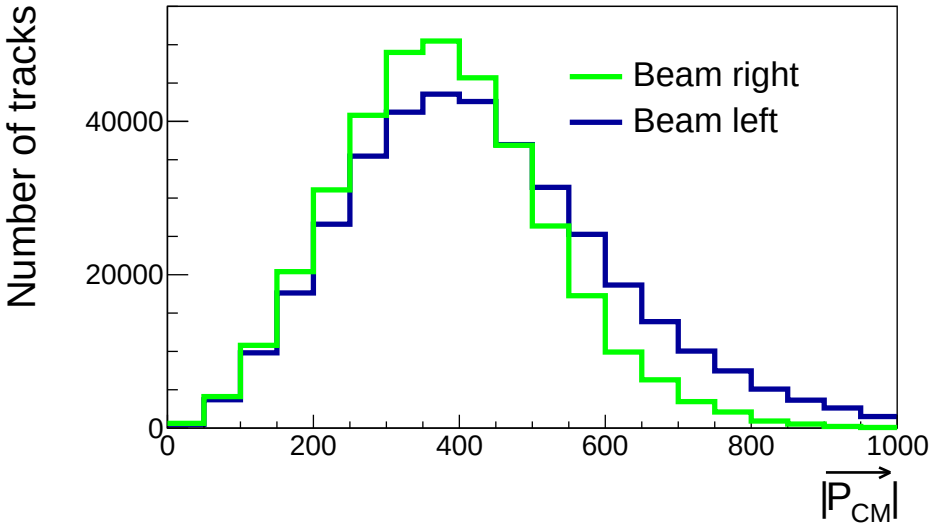

Figure 3.7: Proton momentum distribution when gated on particles with $P_x > 0$ (Beam left) and $P_x < 0$ (Beam right). The two distributions are expected to be identical due to cylindrical symmetry of the reaction.

distortion has negligible impact on trajectories of reaction fragments due to their strong inertia, but the same cannot be said for drift electrons. They acquire a "side-way" component to its drift velocity which distort the observed curvatures on pad plane. Other TPCs, like the STAR TPC, measure such distortion directly with lasers [103], but this equipment was not available during the SπRIT experimental campaign. Below are two strange features from our data that can be attributed to space charge effect.

Fig. 3.7 is the proton center of mass momentum distribution for forward emitting (i.e. $P_z > 0$ in center of mass frame) tracks. The procedure needed to identify proton, correct for detection efficiency and transform data into center of mass frame will be discussed later in Section 3.4. Only tracks with azimuth of $-30^\circ < \phi < 20^\circ$ (beam left) are selected in the blue histogram and only tracks with azimuth $160^\circ < \phi < 210^\circ$ (beam right) are selected in the green histogram. It is important to note that the x-axis is defined with respect to detector orientation instead of the reaction plane. The two distributions should be similar due to cylindrical symmetry arguments, but they are not.

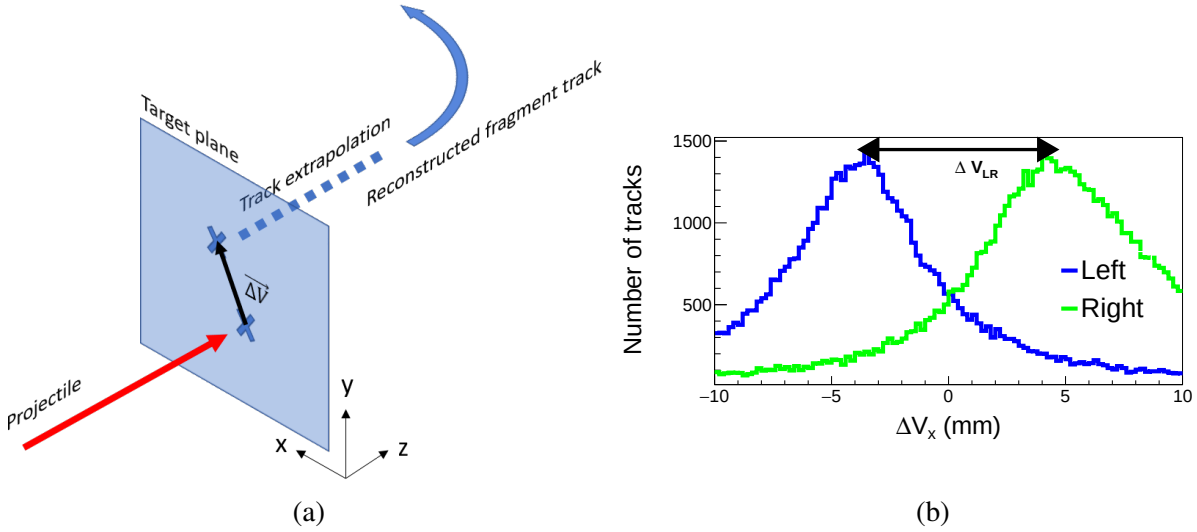

(a) (b)

Figure 3.8: (a): Cartoon illustration of the definition of $\Delta\vec{V}$. (b): The distribution of ΔV_x for particles with $\theta > 40°$. Blue histogram composes of tracks going beam left and green histogram with tracks going beam right. The definition of ΔV_{LR} is illustrated on the plot as the distance between the peak locations of blue and green histograms.

Another curious feature is found when distance to vertex distribution is examined. The reconstructed tracks can be extrapolated back to the target plane and the extrapolated point should agree with the measured vertex location from BDC. The displacement vector between the extrapolated vertex and the measured BDC vertex location is denoted as $\Delta\vec{V}$. The definition of this vector is illustrated in Fig. 3.8a.

The distribution of x-component of $\Delta\vec{V}$, denoted as ΔV_x, should be Gaussian-like with peak centered at zero. Our data, however, shows that the peak location changes with track azimuth. Fig. 3.8b shows the ΔV_x distributions of fragments going in beam left and beam right direction for tracks with polar angle $\theta > 40°$. Neither distribution peaks at 0 mm.

Evidence that supports space charge as the causative effect of these features can be found by correlating $\Delta\vec{V}$ with beam intensity. Denote ΔV_{LR} as the separation between the two peaks of ΔV_x distributions in Fig. 3.8b. It is observed that ΔV_{LR} is directly proportional to the beam intensity of the run. This correlation is shown in Fig. 3.9 and since the strength of space charge effect is also proportional to the beam intensity, it is an indication that our observed features are related to space charge.

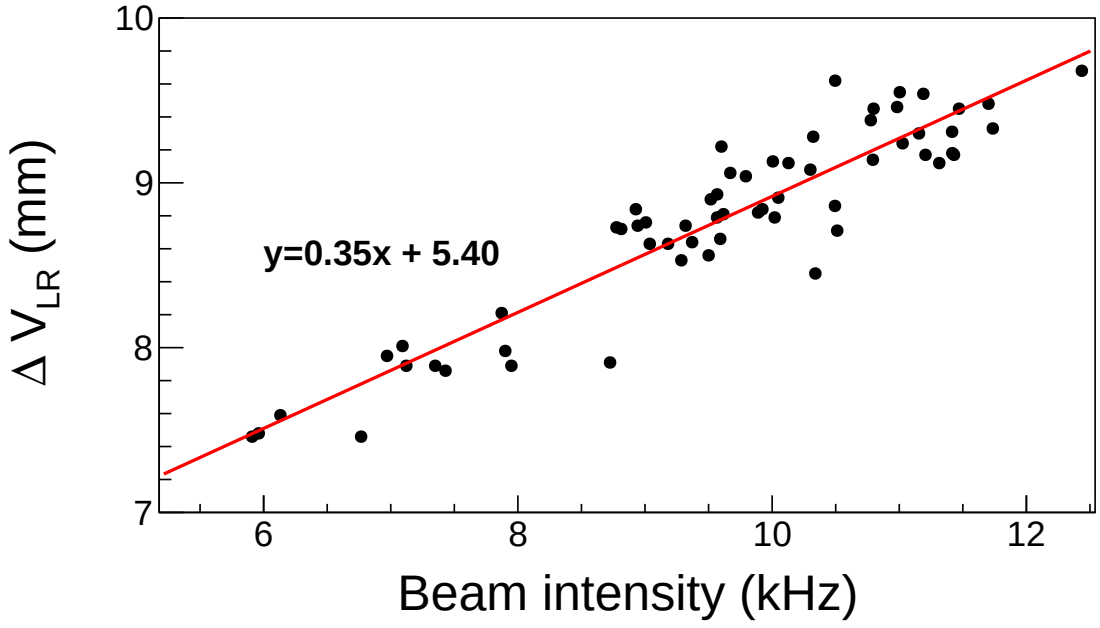

Figure 3.9: Difference in peak location ΔV_{LR} is plotted against beam intensity showing a strong positive correlation.

If space charge is indeed responsible for our observations, we should be able to correct for it as the effect of space charge is described by well established equations. To begin with we need to solve the Poisson's equation for the distorted E-field. The field follows Dirichlet boundary condition as field cage fixes potential on boundaries of the TPC. The sheet charge distribution is approximated as uniform and its magnitude is denoted as σ_{SC}, whose value will be determined later. The curvature of the sheet is easily calculated as it follows the trajectory of un-reacted Sn projectile. After that we calculate the expected lateral electron movement by solving equation of motion given by Ref. [104],

$$\frac{d\vec{x}}{dt} = \frac{\mu}{1+(\omega\tau)^2}\left(\vec{E} + \omega\tau\frac{\vec{E}\times\vec{B}}{|\vec{B}|} + \omega^2\tau^2\frac{\vec{E}\cdot\vec{B}}{|\vec{B}|^2}\vec{B}\right). \tag{3.1}$$

This equation describes the averaged motion of charged particles moving through gaseous medium under E- and B-field. $\omega = eB/m$ is the cyclotron frequency, τ is the mean free time between collisions and $\mu = e\tau/m$, where m and e are the mass and the signed electric charge of electrons/ions respectively. This equation can be solved to find the expected amount of lateral movement acquired

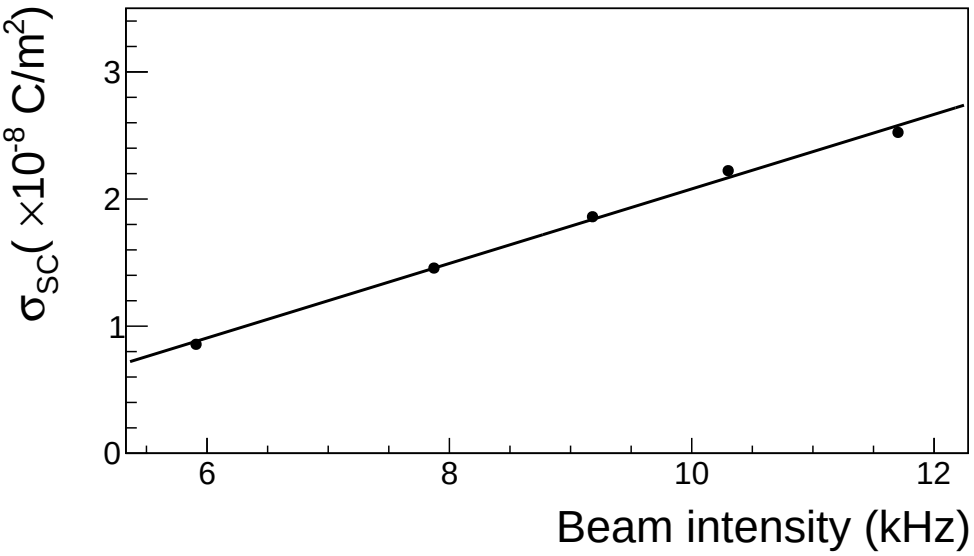

Figure 3.10: The recovered sheet charge density σ_{SC} is plotted against beam intensity for five selected runs. The fitted linear line is used to approximate the sheet charge magnitude for the other runs.

by drift electron when initial conditions are given, and during track reconstruction the measured hit points will be shifted literally in the opposite direction to compensate for space charge distortions.

The remaining loose end is the determination of σ_{SC}. Since Δ_{LR} is expected to center at zero when space charge effect is corrected, we vary σ_{SC} in track reconstruction until $\Delta_{\mathrm{LR}} = 0$. This procedure of varying σ_{SC} is computationally intensive as track reconstruction algorithms need to be run multiple times for each run, so only five selected runs with wildly different beam intensities are determined this way. The σ_{SC} for these five runs are plotted against beam intensities in Fig. 3.10. This linear relation will be used as an estimation of σ_{SC} for all other runs. When tracks are reconstructed after space charge effect correction, the proton momentum distributions of beam left and beam right particles in Fig. 3.11 now agree with each other. It is also verified that p_z and p_T distributions between beam left and right particles also agree better after the correction.

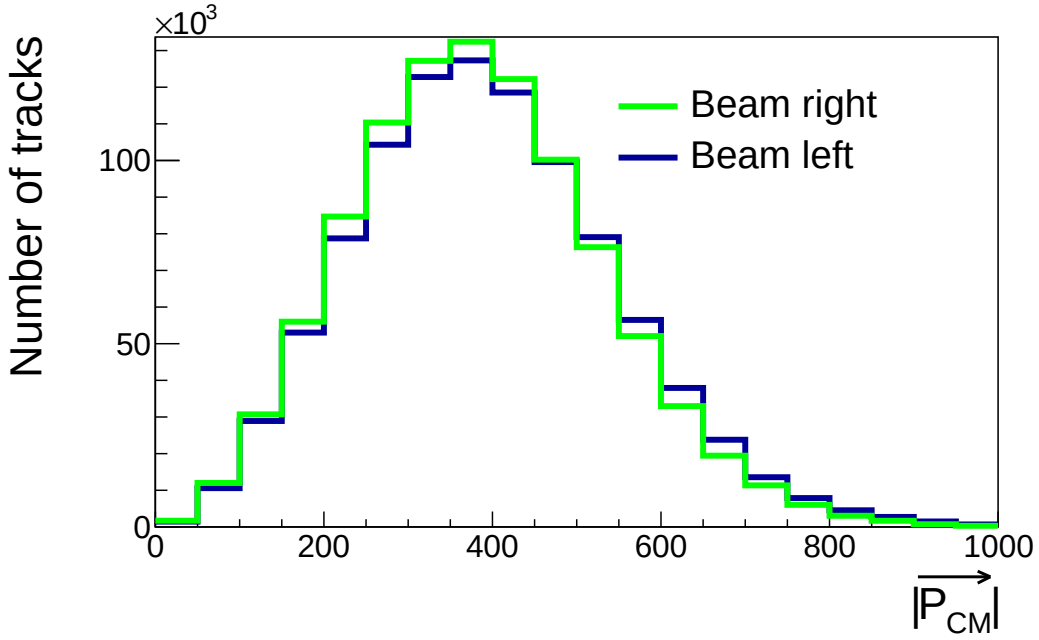

Figure 3.11: Center of mass proton momentum distribution for experimental data with $P_z > 0$ after space charge distortion is corrected. "Beam left" histogram is populated only with tracks emitted at $-30^\circ < \phi < 20^\circ$ and "Beam right" histogram is populated with tracks emitted at $160^\circ < \phi < 210^\circ$. The two histograms agree with each other much better than those obtained before space charge corrections shown in Fig. 3.7.

3.3.3 Leakage Space Charge effect

Due to design issues, the gating grid does not extend all the way to the end of the field cage. The gap of length 3.96 cm between the end of gating grid and the downstream wall of the field cage allows drift electrons from highly charged heavy residue fragment to leak into the avalanche region as Fig. 3.12 illustrates. The positive ions induced by the avalanche process in the anode wires then leak back into the field through the same gap. Ions pour out of the gap continuously as they drift steadily from the top to the bottom of the TPC, forming a sheet like positive charge configuration. This type of sheet charge will be referred to as “leakage” space charge σ_{leak} to distinguish it from the “beam” space charge described in previous section.

The presence of leakage space charge means that even after correcting for beam space charge effect, experimental momentum distributions of particles in some phase space regions with tracks that extend past the end of the grating grid should still be unreasonable. This can be demonstrated

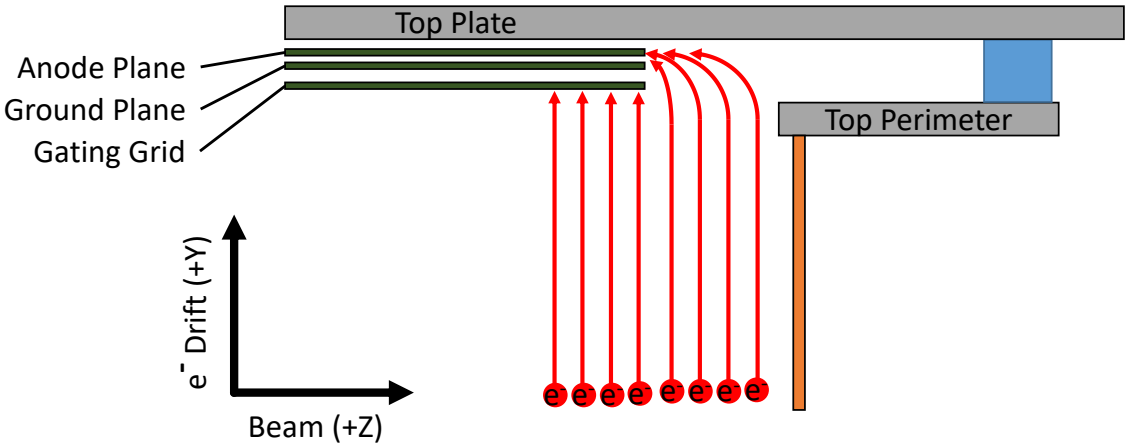

Figure 3.12: Sketch of gating grid near the rear end of SπRIT TPC, taken from Ref. [2]. Electrons, represented as the red points, leak into the anode plane from the gap between gating grid and top perimeter and induce positive ions.

by comparing momentum distributions in three different azimuth regions in Fig. 3.13a where Cut 1 corresponds to $74^\circ < \phi < 132^\circ$, cut 2 corresponds to $-29^\circ < \phi < 29^\circ$ and cut 3 corresponds to $-86^\circ < \phi < -143^\circ$.

With an ideal detector, the momentum distributions in all three cuts should be identical due to cylindrical symmetry. With SπRIT TPC, however, we expect momentum distributions to agree with each other only when polar angle cut of $6^\circ < \theta < 12^\circ$ is imposed because tracks with large polar angle suffer from geometric coverage issues.

The TPC height is shorter than its width, so large polar angle tracks with $\phi \approx \pm 90^\circ$ (moving up or down) will leave a shorter trail of ionized electrons in the field cage than those with $\phi \approx 0^\circ$ or $\phi \approx 180^\circ$ (moving sideways). Shorter tracks are reconstructed less efficiently due to the lack of available hit points. To summarize, for tracks with large polar angles, the momentum distributions in the three cuts are expected to disagree with each other due to geometric efficiencies. On the other hand, tracks with small polar angles do not escape from the sides or top or bottom. They mostly escape from the end of the TPC. The average track length in these three cuts should be similar for tracks with small polar angle. Therefore it is expected that momentum distributions in the three cuts with small polar angle condition will agree with each other. The three cuts and small polar angle condition are illustrated in Fig. 3.13b in ϕ vs. θ plots, with experimental proton distribution

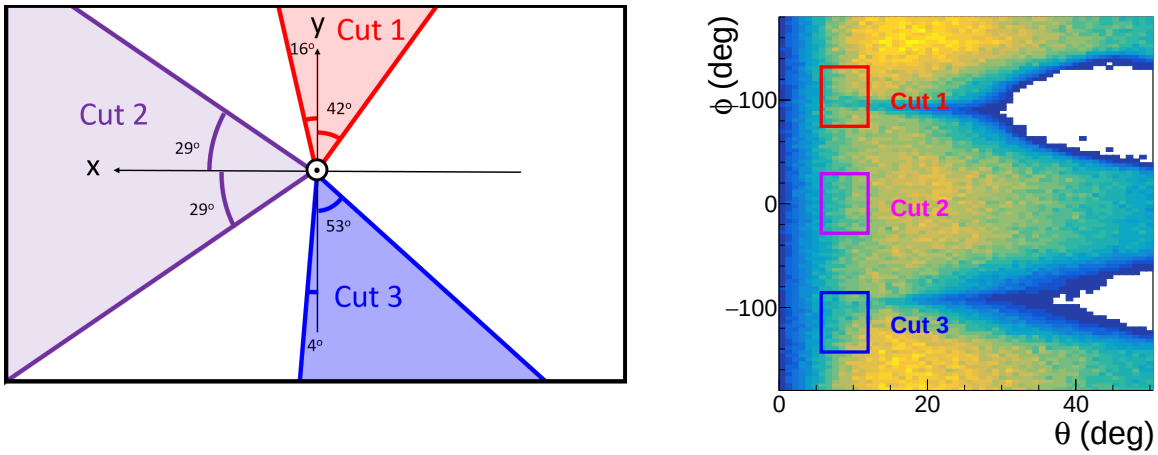

(a) (b)

Figure 3.13: (a): Not to scale illustration of the three azimuthal angle cuts when viewed along the beam axis. Beware that x-axis points toward the left in our right-handed coordinate system and z-axis points into the page, as indicated by the circle with a dot in the center of the image. (b): The three cuts are drawn as red, magenta and blue rectangle on ϕ vs. θ phase space. The colored histogram plotted behind the three cuts is the proton phase space distribution from experiment. See text for details and we will revisit this phase space plot in Fig. 3.24.

of ^{132}Sn + ^{124}Sn with number of clusters > 15 and distance to vertex < 15 (the definition of these conditions will be detailed in Section 3.3) plotted in the background.

Unfortunately, even with $6^\circ < \theta < 12^\circ$ imposed, the momentum distribution in cut 3 still looks different from that in cuts 1 and 2, contrary to our expectation. The Triton distributions in all three cuts are plotted in Fig. 3.14a. Triton is selected as it has the highest average p/Z value among all light fragments so the discrepancy is the most prominent.

Although the behavior of both leakage and beam space charge can be described by Eq. (3.1), they affect tracks in different phase space regions due to differences in their charge configuration. The expected shapes of the space charge sheets are shown in Fig. 3.15 with leakage space charge located at the rear end of the detector, therefore hit points in the forward half of the detector should not be affected by leakage charge. Furthermore, charge density of leakage space charge is much higher than beam space charge due to the magnifying effect of the avalanche. Detailed analysis in the later sections reveals that the charge density of leakage space charge is 9.8 times that of normal beam space charge.

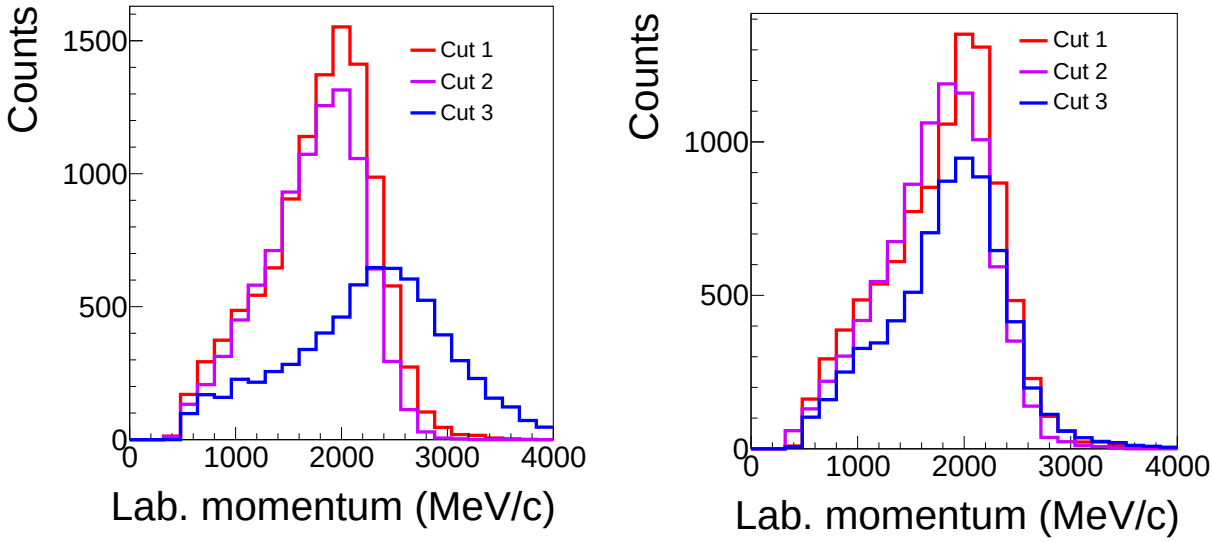

(a) (b)

Figure 3.14: Triton momentum distributions in the three azimuth cuts and $6° < \theta < 12°$ after space charge correction is applied. (a): Track reconstructed with all available hit points. (b): Track reconstructed only with hit points at $z \leq 100$ cm.

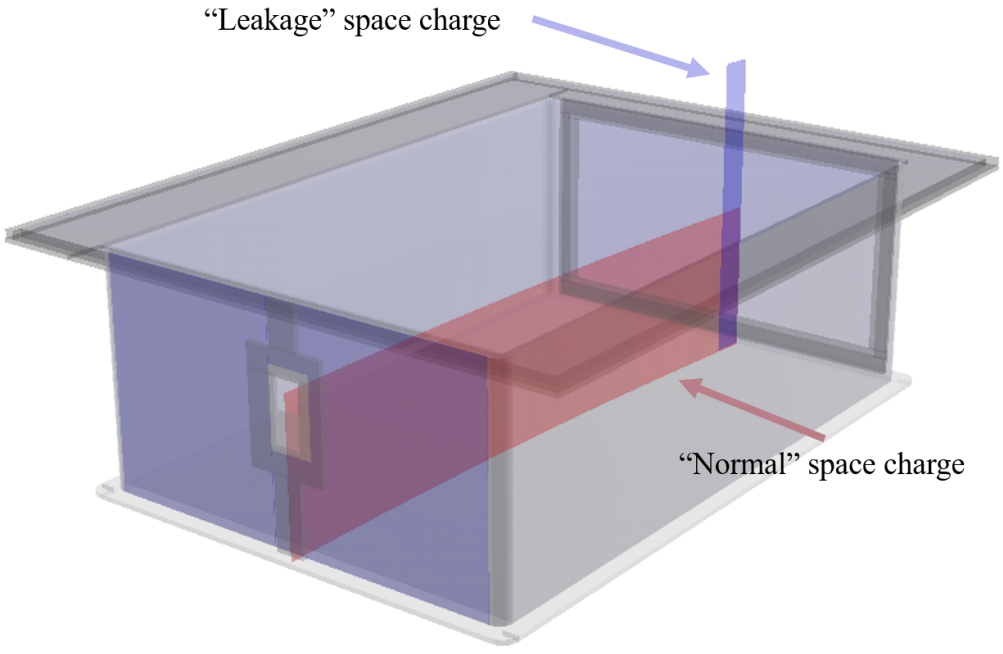

Figure 3.15: Approximate shape of the leakage and normal sheet charges. The length of the leakage space charge is only 3.96 cm and extend all the way from pad plane to the bottom of the TPC.

There are strong evidences that leakage space charge is the cause of the discrepancy in Fig. 3.14a. First and foremost, most detector distortions, such as the beam space charge and geometric inefficiencies have been corrected for or circumvented with our correction algorithms and polar angle cuts. Second, if we plot Fig. 3.14a again but with hit points beyond $z = 100\,\text{cm}$ discarded during track reconstruction, we get Fig. 3.14b where the discrepancy in momentum distributions among the three cuts are eliminated. The causative agent of the distortion must be located at the rear end of the detector. Third, if we include additional leakage sheet charge in the space charge correction algorithm, it eliminates the discrepancy without discarding any hit points.

To incorporate leakage charge into space charge correction, we need to estimate its shape and charge density. The shape, as illustrated in Fig. 3.15, is approximated as the last 3.96 cm of normal beam sheet charge but extended all the way to the top of the TPC. Charge estimation is more complicated as the procedure in Section 3.3.2 for beam space charge cannot be used here. In previous section, σ_{SC} is varied until $\Delta V_{LR} = 0$, but this cannot be done for leakage charge as it is located at the downstream side of the detector while the vertex is located at upstream. As an alternative, we will vary the leakage charge density until the reconstructed momentum remains unchanged before and after discarding downstream hit points.

The reconstructed Triton momentum in cut 3 changes as the z coordinate threshold varies, the threshold beyond which hit points are discarded. When reconstructed Triton momentum with a particular z threshold is plotted against that with another z threshold track-by-track inside cut 3, we get a two-dimensional distribution. The two dimensional plot needs to be simplified such that results with different z thresholds can be compared on a single graph. To do this, the distribution is cut into slices along x-axis and only the mean y-value for each x-slice is shown. For comparison sake, momentum reconstructed with various z thresholds are all compared to that with a standard $z < 100\,\text{cm}$ threshold, the threshold at which momentum distributions in all three cuts agree with each other. Fig. 3.16a is the comparison plot with different z thresholds, and the slope of each line will be referred to as "Triton consistency". Without leakage space charge, Triton consistency should always be one. Deviation from unity indicates distortions. Triton consistencies are plotted

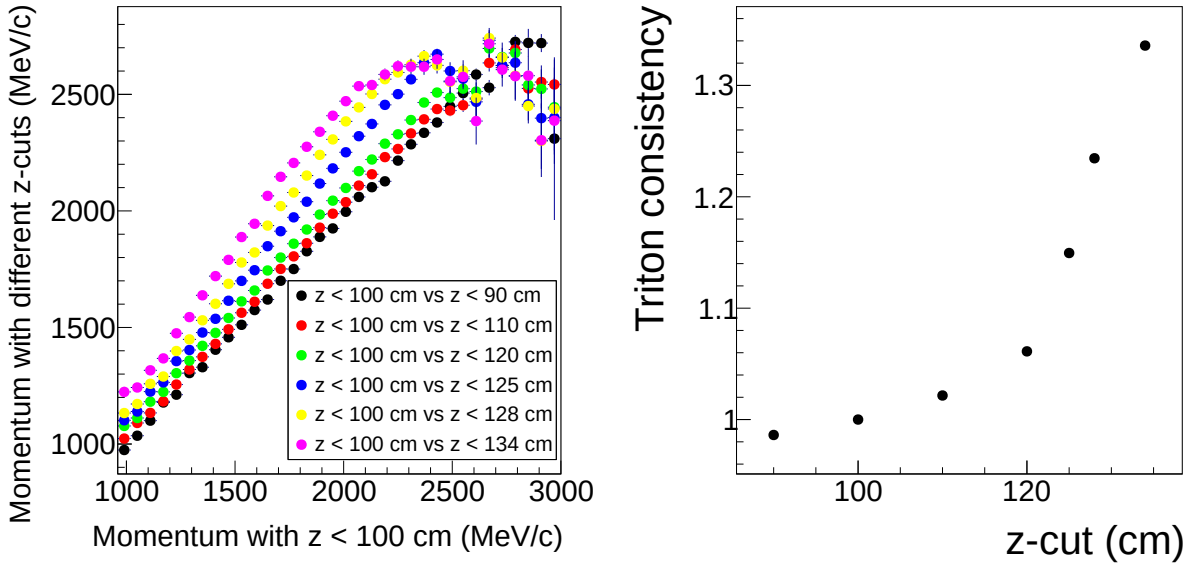

(a) (b)

Figure 3.16: (a) plots the average Triton momentum reconstructed with different z-thresholds against that with a standard z-threshold of 100 cm. (b) shows the slopes (labelled as Triton consistency) for each line in (a) as a function of their respective z-threshold.

against their respective z thresholds in Fig. 3.16b, which shows that it is monotonically increasing with z-cut value, with a sudden change in slope at z-cut equals to 120 cm.

The goal is to vary the leakage charge density in the space charge correction task until Triton consistency stays at one regardless of z threshold values. It is computationally expensive to estimate σ_{leak} for each run, so instead we assumed that $\sigma_{\text{leak}} \propto$ Beam rate and Beam rate $\propto \sigma_{\text{beam}}$. This approximation stems from the fact that leakage charge is induced by beam particles. The proportionality factor between σ_{leak} and σ_{beam}, denoted as a, is assumed to be constant across runs with different beam intensities. Fig. 3.17a demonstrates how Triton consistency vs. z-cut changes with a by scanning through multiple test values.

The desired slope and y-intercept of the fitted linear lines in Fig. 3.17a are zero and one, respectively. These two conditions allow us to determine a in two ways: 1. Interpolate slope as a function of a and find where slope = 0 corresponds to, and 2. interpolate y-intercept as a function of a and find where intercept = 1 corresponds to. The former is performed in Fig. 3.17b and the

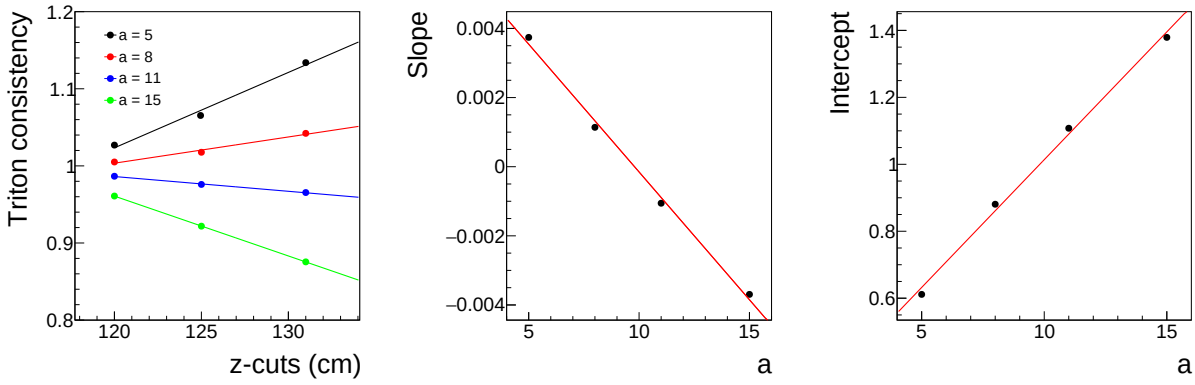

(a) (b) (c)

Figure 3.17: (a): Triton consistency vs. z-threshold when different values of a are used. Ideally we want a to be set such that Triton consistency is always one at all z-thresholds. (b) and (c): Slopes and intercepts of the linear fits of the four lines in (a), respectively.

latter is performed in Fig. 3.17c. Both methods yield $a = 9.8$. It is verified in Fig. 3.18, which is the same as Fig. 3.14a but with leakage correction performed at $a = 9.8$, that the correction is able to eliminate the discrepancy in momentum distributions.

The gating grid is modified after the last experiment such that the gap is covered with Aluminum plate [2]. It blocks electrons from entering the wire plane and leaking out into the detection volume through the gap. Future experiments involving SπRIT TPC will not suffer from leakage space charge distortion.

3.3.4 GENFIT task

The corrected hit points are passed onto the final *GENFIT task*. It uses a well established tracks fitting routine called GENFIT to reconstruct momentum for each track [105]. It offers greater reconstruction accuracy when compared to Helix task as it takes energy loss in the medium and non-uniformity of the magnetic fields into account. The grouping of hits and rough momentum estimates from Helix task are used as initial guess for GENFIT. Another function of GENFIT task is to find the location of vertex using the RAVE vertex finding package [106]. Events where vertex is located too far upstream or downstream of the target plane will be rejected from the analysis as these events most likely do not originate from the targets.

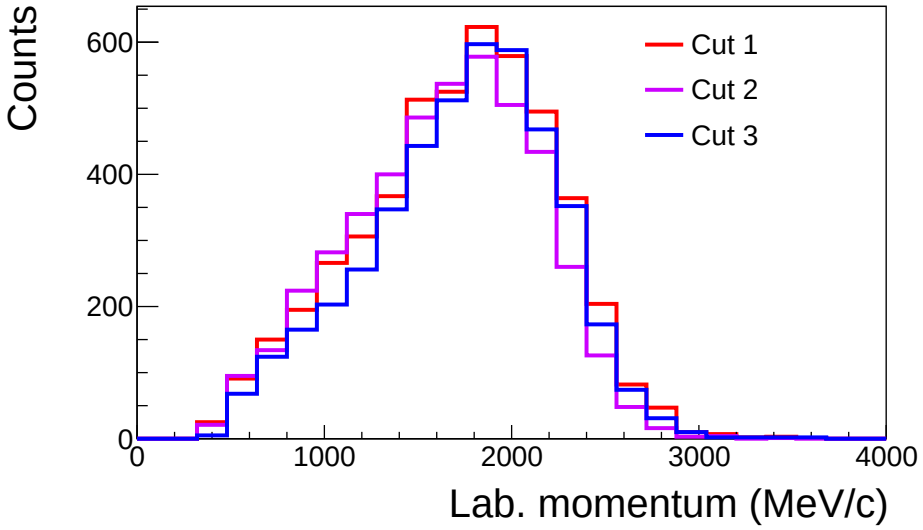

Figure 3.18: Same as Fig. 3.14 (a), but leakage space charge has been corrected with $a = 9.8$.

In general, there are too many clusters close to each other near the reaction vertex. The chances of these clusters being misidentified are high, so they are also not used in the track fitting. Hit clusters that are too close to the edges of the detector volume are not used for track recognition as well as they suffer from edge effects that render their hit locations unreliable [7]. For a hit to be used in momentum reconstruction, all of the following conditions must be satisfied,

$$|x| \leq 420\,\text{mm}, -522\,\text{mm} \leq y \leq -64\,\text{mm},$$
$$\left(\frac{x}{120\,\text{mm}}\right)^2 + \left(\frac{y - y_{\text{beam height}}}{100\,\text{mm}}\right)^2 + \left(\frac{z - z_{\text{target foil}}}{220\,\text{mm}}\right)^2 > 1.$$

The numbers are expressed using the coordinate system of Fig. 3.6. The condition on the second line represents an ellipsoid cut centers at reaction vertex. Geometric measurement of our experimental set-up shows that $y_{\text{beam height}} = -260\,\text{mm}$ and $z_{\text{target foil}} = -11.9\,\text{mm}$.

This task is executed twice. It is first run without using vertex location from BDC measurement in curve fitting, and then again with the inclusion of vertex location. The purpose of the first run is to isolate tracks that do not converge to a common vertex and the second is to improve momentum resolution by incorporating the accurately know vertex location from BDC into GENFIT routine.

3.4 Particle level analysis

This section shows steps that are needed to reconstruct accurate particle spectra from the reconstructed tracks. A short summary on the cut conditions is given in Section 3.4.5.

3.4.1 Particle identification

As particle traverse the TPC, it losses energy and ionizes the detector gas molecules. The average amount of energy loss depends on particle velocity and electric charge according to Bethe-Bloch equation (BBE) [107],

$$-\left\langle \frac{dE}{dx} \right\rangle = \frac{KZ^2}{\beta^2}\left[\ln\left(\frac{C\beta^2}{1-\beta^2}\right) - \beta^2\right]. \tag{3.2}$$

In the above equation, K and C are constants that depend only on the properties of detector gas, $\beta = v/c$ is the particle's velocity over speed of light and Z is the absolute particle electric charge in multiples of the electron charge. This allows for different particle types to be identified through a plot of average energy loss per unit length vs. momentum, commonly referred to as the PID plot. In such a plot, different elements are separated in accordance to $dE/dx \propto Z^2$. Isotopes with equal velocity lose the same amount of energy, but they have different momentum due to their difference in mass so isotopes are also separated into distinguishable lines.

PID plot for ^{132}Sn + ^{124}Sn reaction is shown in Fig. 3.19. Just from visual inspection, the boundaries between PID lines of various species are sometimes not very clear, most noticeably the Triton line and ^{3}He line are very close at $p/Z < 700\,\mathrm{MeV/c}$. To estimate the degree of cross-contamination and to classify particle type for each track, we follow the Bayesian PID method outlined in Ref. [108].

Instead of classifying each track as a single type of particle, this method tabulates the probability of a track being each type of isotope. A single track can be identified as multiple isotopes with varying probabilities in the ambiguous region of PID. For a track with observed momentum

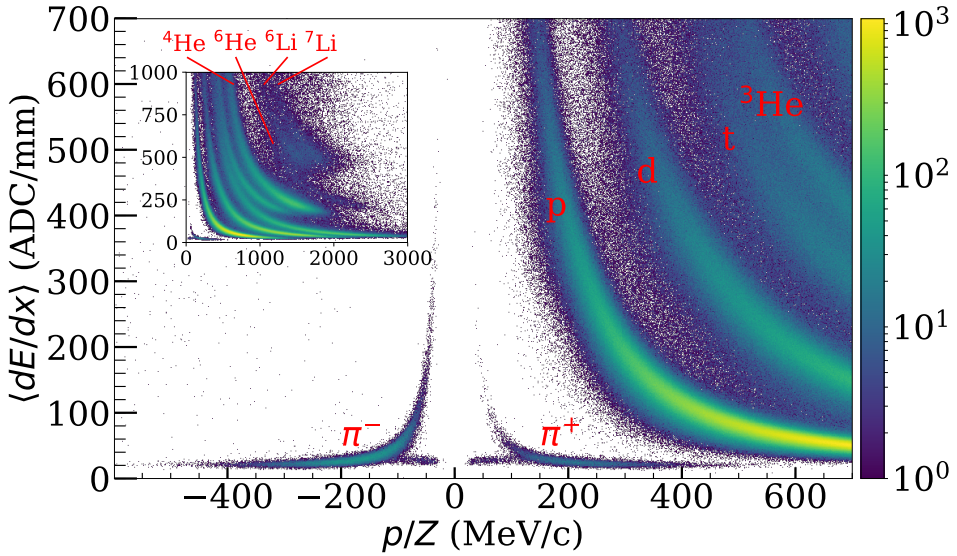

Figure 3.19: Particle identification plot with all events in ^{132}Sn + ^{124}Sn. The charged particles, p,d,t,^{3}He and ^{4}He as well as the charged pions are labelled. The horizontal appendages from the pions are electrons an positrons resulting from the decay of π^0.

magnitude p, the likelihood of detecting energy loss E given that it comes from a particle of type H_i is given by,

$$P(E|p,H_i) = \frac{1}{\sqrt{2\pi}\sigma(p,H_i)} e^{-\frac{(E-\hat{E}(p,H_i))^2}{2\sigma(p,H_i)^2}}. \tag{3.3}$$

In the equation, $\hat{E}(p,H_i)$ is the expected energy loss and $\sigma(p,H_i)$ is the measured width of PID line. The resolution in both momentum and dE/dx measurements contribute to the width of PID lines [7]. Using Bayes theorem, it can be inverted to give the probability of the track being H_i given the energy loss and momentum value,

$$P(H_i|p,E) = \frac{P(E|p,H_i)Pr(p,H_i)}{\sum_{k=P,D,T,...} P(E|p,H_i)Pr(p,H_i)}, \tag{3.4}$$

where $Pr(H_i)$ is the prior. Following Ref. [108], an iterative procedure will be used in which the priors in the first iteration are assumed to be constants. The posterior distributions from this initial run will be used as prior for the next iteration. This is repeated until the posteriors converge.

The expected energy loss $\hat{E}(p, H_i)$ and measured resolution $\sigma(p, H_i)$ are fitted empirically. To do this a crude graphical cut is made to each PID line. The measured mean and standard deviation of dE/dx inside the cut as a function of momentum will be fitted with ad-hoc functions to represent $\hat{E}(p, H_i)$ and $\sigma(p, H_i)$. Any functions that fit data good enough will work, and in this case $\hat{E}(p, H_i)$ takes the form of a modified BBE,

$$\hat{E}(p, H_i) = \frac{A_i + B_i\beta}{\beta^2}\left[\ln\left(C_i + \left(\frac{m}{\beta}\right)^{D_i}\right) - \beta^{E_i} + F_i\right]. \tag{3.5}$$

Here $\beta = p/\sqrt{p^2 + m}$ is the velocity, A_i, B_i, C_i, D_i, E_i and F_i are parameters to be fitted. The reason for the BBE to be modified is that the measured dE/dx from SπRIT is actually the truncated mean energy loss instead of the true averaged energy loss. The truncation is needed to minimize the effect of outliner energy loss data point caused by delta electrons [102]. The truncation skews the distribution to the point where the original BBE is not a good enough fit. The $\sigma(p, H_i)$ takes the following form,

$$\sigma(p, E_i) = \frac{\alpha_i}{p^{\beta_i}} + \gamma_i, \tag{3.6}$$

where α_i, β_i and γ_i are parameters to be fitted. The results fitted from ^{132}Sn + ^{124}Sn data are shown in Fig. 3.20

The classification results for ^{132}Sn + ^{124}Sn is demonstrated in Fig. 3.21, where the left panel shows dE/dx distributions within a narrow range of momentum and the right panel shows where the range of momentum is on the PID plot. Histograms on the left panel are weighted distributions of dE/dx, with each track weighted by the probability of it being a particular particle type. For instance, a track that is identified as 50% proton and 50% Deuteron is counted as 0.5 count in both proton and Deuteron distributions. The tails of the distributions overlap with each other in a way that make intuitive sense. When observables for light fragments are constructed in Chapter 4, only tracks with $P(H_i|p, E) > 0.7$ and $\sigma(p, E_i) < 2.2$ are counted. These conditions are chosen from the analysis of systematic errors from PID selection, in which fragments observables are found to not vary much within a range of P and σ thresholds that center at 0.7 and 2.2, respectively [109].

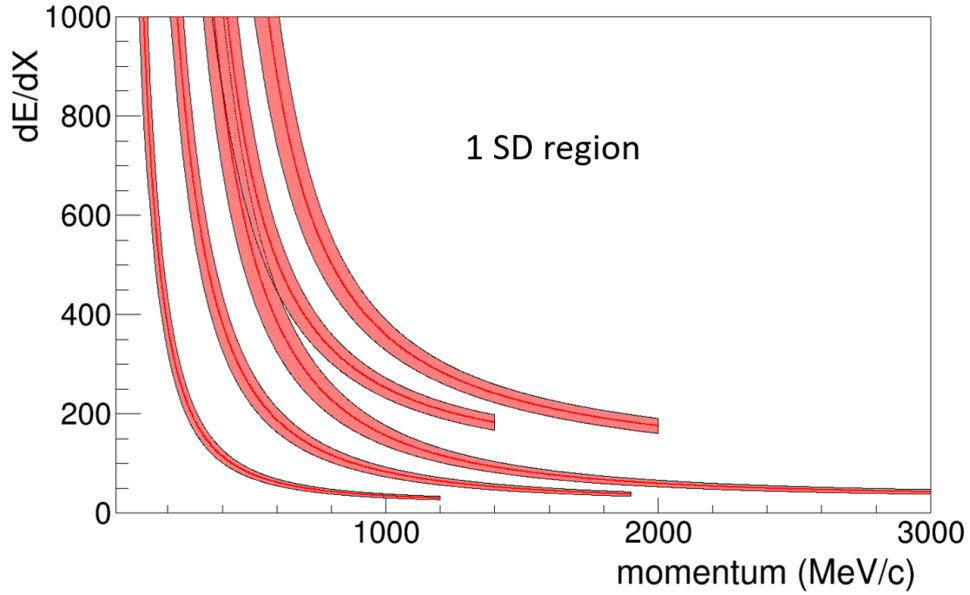

Figure 3.20: The fitted $\hat{E}(p, H_i)$ and $\sigma(p, H_i)$. The red lines in the center of the red shaded regions correspond to $\hat{E}(p, H_i)$ and the width of the shaded regions on each side the line correspond to $1\sigma(p, H_i)$.

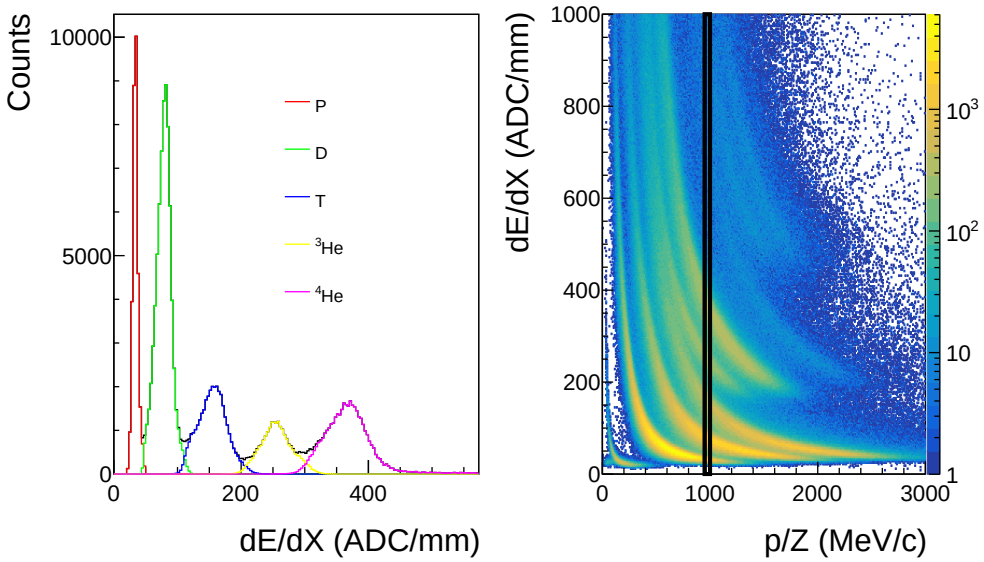

Figure 3.21: Particle selection of Bayesian PID on a selected momentum range. Left: Distributions of dE/dX, with each track weighted by the probability of it being a particular isotope. Right: PID plot with a black vertical bar indicating where the momentum cut is set in the making of dE/dX distribution on the left.

Special care must be taken in pion selection because pion PID lines are contaminated by electron and positron PID lines. The Lepton PID lines are not described well by Eq. (3.5), so a different fitting procedure is needed to estimate the amount of contamination for pions. The details on pion selection are described in Ref. [102] and the threshold is set to $P(H_i|p, E) > 0.2$. This is less stringent than for light fragments because PID lines of pions are far away from the that of other isotopes.

3.4.2 Frame transformation

Center of mass frame is the most convenient reference frame to understand nuclear dynamics. To transform measured momentum from laboratory to center of mass frame, it is first rotated such that the beam is traveling in the direction of z-axis in the rotated frame. BDC measures the angle of incidence of beam particle for each event, and this information is used to properly rotate the coordinate system. The 4-momentum vector, defined as $\mathbf{P} = (E/c, p_x, p_y, p_z)$, is constructed for each track in the rotated frame and is then boosted back to center of mass frame with Lorentz transformation.

We need to know the mass of each fragment to construct the 4-momentum because $E^2 = m^2c^4 + p^2c^2$, where m is the mass of the fragment and c is the speed of light. During particle identification, a track can be identified as multiple isotopes simultaneously with different probabilities. The mass of the most probable isotope from particle identification is used as the fragment mass of the track during frame transformation.

The initial beam energy from BigRIPS is inferred from Time-of-Flight (ToF) measurement. On average, nuclear collision are assumed to occur in the middle of the target foil along the beam axis, so the final beam energy for Lorentz transformation is the expected energy after the beam particle traverses half the thickness of the target foil, calculated from LISE++ program [110].

3.4.3 Efficiency unfolding

Particle yields are often underestimated due to inefficiencies of the detector. However, detection efficiency can be accurately estimated with Monte Carlo (MC) embedding techniques, details of which will be described later in Section 5.9.1. In this section it is sufficient to know that for a simulated particle with a given initial momentum, MC embedding returns either nothing or the reconstructed momentum. The probability of it returning nothing is equal to the probability of such particles not recognized by the software and the reconstructed momentum should follow a probability distribution that accurately reflects detector resolution.

The naive approach to correct for efficiency loss is simply to weigh each track by the inverse of the fraction of each embedded track being recognized. However, efficiency depends strongly on track momentum so it must be taken into account. To construct efficiency as a function of momentum phase space, MC embedding calculation is repeated across a range of initial momentum. The phase space can be divided into finite bins, with each bin populated by the number of detected tracks over that of initial tracks. Such seemingly innocuous procedure, however, suffers from ambiguity stemming from the fact that detected momentum is not identical to initial momentum given the finite resolution in track fitting routine, so finding efficiency from a look-up table with detected momentum may result in inaccuracies.

To demonstrate this effect, denote R_i as the number of tracks with *reconstructed* momentum and T_i as the number of tracks with *true* momentum inside the i^{th} phase space bin. In other words, R_i is the reconstructed momentum distribution and T_i is the true momentum distribution. A fraction of tracks with true momentum in bin i will end up with reconstructed momentum in bin j due to finite resolution. Denote $M_{i,j}$ as the fraction of tracks that migrate from bin i to j after track reconstruction such that,

$$\begin{aligned} R_i &= T_i M_{i,i} + \sum_{i \neq j} T_j M_{j,i} \\ &= \sum_{\forall j} T_j M_{j,i}. \end{aligned} \tag{3.7}$$

R_i is detected in the experiment and the goal of efficiency unfolding is to extract T_i from it.

Beware that some tracks are lost in reconstruction due to inefficiencies and track quality cut, so it is expected that $\sum_i M_{j,i} \leq 1$. $M_{j,i}$ can be calculated from MC embedding from the following procedure: MC embedding is performed with C amount of initial tracks in each momentum bin such that,

$$R_i^{\text{embed}} = \sum_{\forall j} T_j^{\text{embed}} M_{j,i} = C \sum_{\forall j} M_{j,i}, \tag{3.8}$$

since $T_i^{\text{embed}} \equiv C \forall i$. Note that the embedded tracks have to pass track quality conditions to be counted towards R_i^{embed}. Efficiency E_i is defined as,

$$E_i = \frac{R_i^{\text{embed}}}{T_i^{\text{embed}}} = \sum_{\forall j} M_{j,i}. \tag{3.9}$$

It is tempting to divide the number of experimentally reconstructed tracks by E_i bin-by-bin to recover the true momentum distribution, but such division does not always yield the correct distribution. Denote EC_i (stands for efficiency corrected) as the result of division for bin i,

$$EC_i = \frac{R_i}{E_i} = \frac{\sum_j T_j M_{j,i}}{\sum_j M_{j,i}}. \tag{3.10}$$

There are only two ways where EC_i equals to T_i: $M_{i,j} = A_i \delta_{i,j}$ or T_i is a constant. The former corresponds to zero bin migration, in other words perfect momentum resolution, and the latter corresponds to uniform particle distribution in momentum space. Neither is true in general, but if bin migration is small enough, EC_i will be very close to T_i. Let $M_{i,j} = A_{i,j} \delta_{i,j} + \sigma_{i,j}$ where

$\sigma_{0,0} = 0$ and $\sigma_{i,j} \ll A_{i,j}$, we have,

$$\begin{aligned} EC_i &= \frac{\sum_j T_j(A_{j,i}\delta_{j,i} + \sigma_{j,i})}{\sum_j (A_{j,i}\delta_{j,i} + \sigma_{j,i})} \\ &= \frac{A_{i,i}T_i + \sum_j \sigma_{j,i}T_j}{A_{i,i} + \sum_j \sigma_{j,i}} \\ &= A_{i,i}^{-1}(A_{i,i}T_i + \sum_j \sigma_{j,i}T_j)\left(1 + \frac{\sum_j \sigma_{j,i}}{A_{i,i}}\right)^{-1} \\ &= \left(T_i + \frac{\sum_j \sigma_{j,i}T_j}{A_{i,i}}\right)\left(1 - \frac{\sum_j \sigma_{j,i}}{A_{i,i}}\right) + O(\sigma_{j,i}^2) \\ &= T_i + \frac{\sum_j (T_j - T_i)\sigma_{j,i}}{A_{i,i}} + O(\sigma_{j,i}^2) \\ &= T_i + O(\sigma_{j,i}) \end{aligned} \tag{3.11}$$

$EC_i \approx T_i$ to the first order of σ, but the accuracy can be improved with an iterative procedure where each embedded particles are weighted by EC_i. This iterative procedure will be referred to as *unfolding* and will be repeated until the efficiency corrected histogram converges. Let $\epsilon_i = \sum_j (T_j - T_i)\sigma_{j,i}/A_{i,i}$, the embedding tracks are weighted as follows,

$$\begin{aligned} T_i^{\text{embed}(2)} &= T_i^{\text{embed}(1)} EC_i^{(1)} \\ &= C(T_i + \epsilon_i) + O(\sigma^2), \end{aligned} \tag{3.12}$$

The number in the parenthesis on superscript states the order of iteration. Following Eq. (3.8),

$$\begin{aligned} R_i^{\text{embed}(2)} &= \sum_{\forall j} T_j^{\text{embed}(2)} M_{j,i} \\ &= C \sum_j (T_j + \epsilon_j)(A_{j,i}\delta_{j,i} + \sigma_{j,i}) + O(\sigma^2) \\ &= C(A_{i,i}T_i + A_{i,i}\epsilon_i + \sum_j T_j \sigma_{j,i}) + O(\sigma^2) \end{aligned} \tag{3.13}$$

The new efficiency is,

$$\begin{aligned} E_i^{(2)} &= \frac{R_i^{\text{embed}(2)}}{T_i^{\text{embed}(2)}} \\ &= \frac{C(A_{i,i}T_i + A_{i,i}\epsilon_i + \sum_j T_j\sigma_{j,i}) + O(\sigma^2)}{C(T_i+\epsilon_i)+O(\sigma^2)} \\ &= \frac{A_{i,i}(C(T_i+\epsilon_i)) + C\sum_j T_j\sigma_{j,i} + O(\sigma^2)}{C(T_i+\epsilon_i)+O(\sigma^2)} \\ &= A_{i,i} + \frac{\sum_j T_j\sigma_{j,i} + O(\sigma^2)}{T_i+\epsilon_i+O(\sigma^2)} + O(\sigma^2). \end{aligned} \tag{3.14}$$

Make use of the fact that $\epsilon_i \sim O(\sigma)$, the efficiency becomes,

$$\begin{aligned} E_i^{(2)} &= A_{i,i} + \frac{\sum_j T_j\sigma_{j,i} + O(\sigma^2)}{T_i + O(\sigma)} + O(\sigma^2) \\ &= A_{i,i} + \frac{\sum_j T_j\sigma_{j,i} + O(\sigma^2)}{T_i}(1 - O(\sigma)) + O(\sigma^2) \\ &= A_{i,i} + \frac{\sum_j T_j\sigma_{j,i}}{T_i} + O(\sigma^2). \end{aligned} \tag{3.15}$$

The efficiency corrected histogram in the second iteration is,

$$\begin{aligned} EC_i^{(2)} &= \frac{\sum_j T_j(A_{j,i}\delta_{j,i} + \sigma_{j,i})}{A_{i,i} + \frac{\sum_j T_j\sigma_{j,i}}{T_i} + O(\sigma^2)} \\ &= \frac{T_i(A_{i,i} + \frac{\sum_j T_j\sigma_{j,i}}{T_i})}{A_{i,i} + \frac{\sum_j T_j\sigma_{j,i}}{T_i} + O(\sigma^2)} \\ &= T_i + O(\sigma^2) \end{aligned} \tag{3.16}$$

The second iteration improves the accuracy by a factor of σ. Eventually the procedure will converge to a stable EC_i. To prevent tracks with extremely small efficiency from blowing up the histogram, tracks with the unfolded efficiency smaller than 0.15 will be discarded. The efficiency is binned as 2-dimension distribution of p_T vs. y_0. This efficiency unfolding is used for reconstruction of particle yields, rapidity and p_T distribution but not for collective flow and reaction plane determination. A different type of efficiency (azimuth efficiency) is used for reaction and it will be discussed in Section 3.4.6.

3.4.4 Track and event selection task

Tracks with poor detection quality must be removed for accurate results. One of the track quality conditions used in the analysis is to remove tracks with number of clusters < 20 for pions and < 15 for other light fragments. Number of clusters of a track is defined as the sum of number of row clusters and number of layer clusters. Row refers to the pad numbering along x-direction and layer refers to pad numbering along z-direction. Number of layer clusters is the number of layers of pads that registers hits for a track when its yaw angle, defined as the angle between the projected track on x-z plane and z-axis, is less then 45° [7]. An illustration on how clusters are counted is provided in Fig. 3.22. In this example, the track spans five layers in total but the last layer is not counted because yaw of the track exceeds 45° beyond the fourth layer, therefore the number of layer clusters is equal to 4. In similar fashion, number of row clusters is the number of row of pads that register hits for a track when its yaw angle exceeds 45°. In our example figure, number of row clusters is equal to 3 and the total number of clusters is $4 + 3 = 7$. The number of clusters are the same as the number of points GENFIT used for curve fitting. Momentum resolution will be poor for tracks with inadequate points to fit. The number of clusters threshold is imposed to filter out tracks with unreliable momentum values.

The second condition is to remove tracks with distance to RAVE vertex > 20 mm for pions and > 15 mm for all other light fragments. Distance to vertex is the closest distance between reconstructed track and vertex when extrapolated back to the target, as illustrated in Fig. 3.23. If the distance to vertex is too large, then either the track does not originate from the same collision as other tracks or is badly fitted. Either way these tracks are not good enough to be counted towards the final spectrum and are removed.

The third condition is to only accept tracks with $-40° < \phi < 20°$ (beam left) or $160° < \phi < 220°$ (beam right), where ϕ is the particle azimuth in center of mass frame. The width of the SπRIT detector is greater compared to its height, so tracks that are emitted in the general upward or downward direction escape the detection volume quicker than those emitted sideways and leaves less hit points. After imposing the number of cluster cut, tracks that are emitted at $\phi \sim \pm 90°$

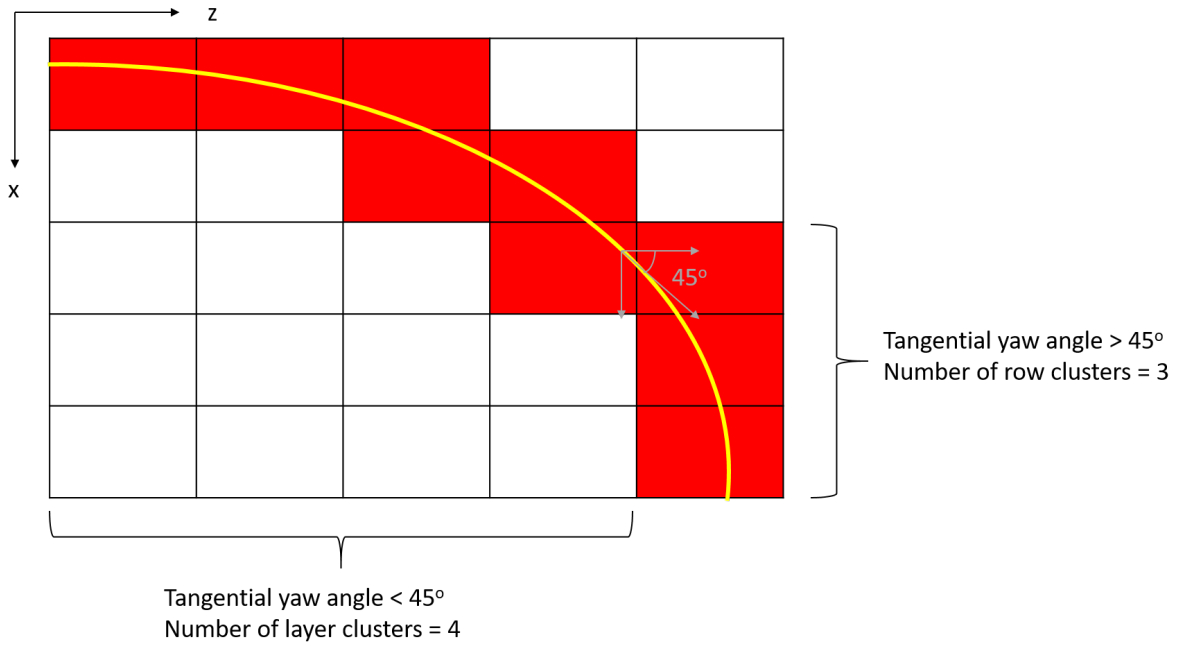

Figure 3.22: An not-to-scale illustration of how numbers of row and layer clusters are defined. The yellow line corresponds to the track trajectory projected on x-z plane and the cells that are labelled red are pads directly on top of the track.

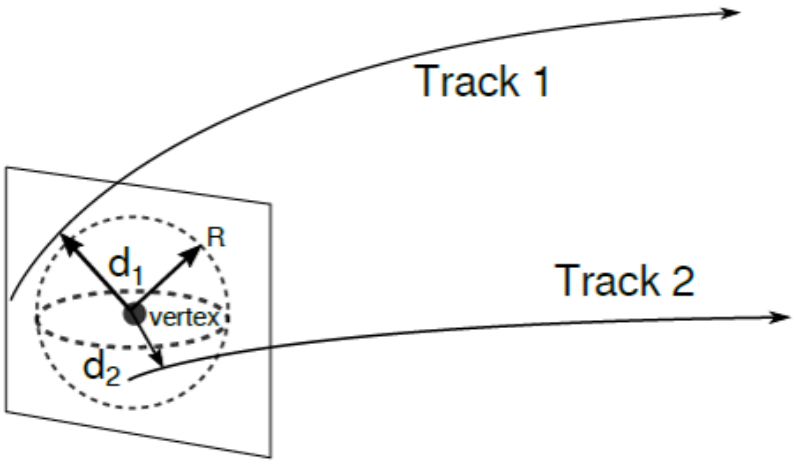

Figure 3.23: Illustration of distance to vertex, taken from Ref. [7]. Tracks 1 and 2 are example tracks with d_1 and d_2 being their corresponding distance to vertex.

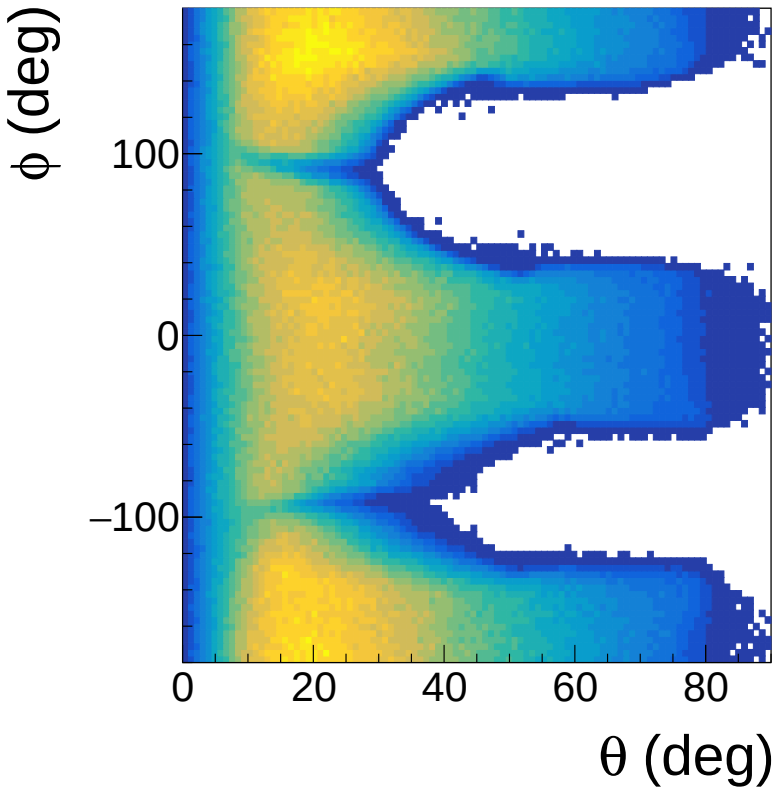

Figure 3.24: Distribution of ϕ against θ for protons with distance to vertex cut < 15 mm and number of cluster cut > 15. Data is taken from ^{132}Sn + ^{124}Sn after gating on beam purity.

are mostly be cut away. Fig. 3.24 shows the distribution of ϕ vs θ for all protons with number of clusters > 15. The cluster condition completely rejects all tracks near $\phi \sim \pm 90°$ when $\theta > 40°$. This phase-space cut-off boundary is not simple to calculate and the resultant geometric bias will be difficult to correct for. Thus we decide to only accept tracks from ϕ regions that do not suffer from such geometric efficiency problems.

The fraction of particles removed by the cut conditions must be accounted for if we want to accurately count the yield of particles. The efficiency loss due to the number of clusters and distance to vertex conditions can be accurately calculated through efficiency unfolding procedure discussed in Sections 3.4.3. For the azimuth condition we can simply multiply the result by a constant factor of $((220 - 160) + (20 + 40))/360 = 3$ since the reaction should exhibit cylindrical symmetry.

The beam particles could react with nuclei in the counter gas or other materials the beam

encounter as it travel through the beam line to the target. These events not originated from the target have to be removed from the analysis. To ensure projectile reacts with the desired Tin nucleons, cuts on vertex locations are made. A z-coordinate cut is applied to vertex fitted from tracks to make sure the reaction does not originate up-stream or down-stream of the target foil. Cuts in x- and y-coordinate are applied to BDC extrapolated vertex position to make sure the beam does not hit the frame of the target.

All of these conditions are used when we reconstruct the yields, rapidity and p_T distributions of particles. For the determination of collective flow and reaction plane, the limits in azimuth ranges are not applied and number of clusters threshold is lowered to > 7 for reasons that will be described in Section 3.4.6.

3.4.5 Summary on cut conditions

Cut conditions described in the last three sub-sections are summarized in Table 3.1. The fraction of tracks lost due to number of clusters, distance to vertex and detector inefficiencies should be corrected by efficiency unfolding. The multiplicative factor of 3 due to azimuth range cuts will be imposed after efficiency unfolding. Although Monte Carlo simulation is able to recreate the shape of particle PID to a certain extent, it is not accurate enough to be used for calculating the amount of tracks lost due to PID cuts. The performance of MC PID will be discussed in Section 5.9.2.

3.4.6 Reaction plane determination

Reaction plane is the plane that the beam axis and the displacement vector between target and projectile span. Estimation of reaction plane azimuth (Φ) is needed in the determination of *collective flow*, which was the focus of numerous previous studies [11, 111–113]. Flows are expected to shed light into the properties of nuclear matter. Collective flow indicates the degree of non-uniformity in azimuth distribution with respect to reaction plane. In this work, Q-vector method [114, 115] is used to approximate reaction plane angle, which states that the azimuth of $\vec{Q}$

Table 3.1: Cut conditions used in event and track selection for reconstruction of particle distributions.

Track conditions	Light fragments	Pions
Number of clusters	> 15	> 20
Distance to vertex	< 15 mm	< 20 mm
PID probability	> 0.7	> 0.2
PID σ	> 2.2	Not imposed
Efficiency	> 0.15	
Azimuth range	$-40^\circ < \phi < 20^\circ$ or $160^\circ < \phi < 220^\circ$	

Vertex conditions			
System	z(mm)	BDC-x(mm)	BDC-y(mm)
^{108}Sn + ^{112}Sn	-14.8 ± 3.1	0.0 ± 2.5	0.0 ± 2.4
^{108}Sn + ^{112}Sn	-14.8 ± 3.7	0.0 ± 3.0	0.0 ± 2.3
^{108}Sn + ^{112}Sn	-14.3 ± 2.6	0.0 ± 2.5	0.0 ± 3.0
^{108}Sn + ^{112}Sn	-14.8 ± 3.7	0.0 ± 2.8	0.0 ± 2.5

defined as,

$$\vec{Q} = \sum w(y_z)\vec{p_T}, \tag{3.17}$$

is a good approximation to Φ. Here $w = 1$ for $y_z > 0.4y_{\mathrm{NN}}$, $w = -1$ for $y_z < -0.4y_{\mathrm{NN}}$ and $w = 0$ otherwise, where y_{NN} is the relative rapidity of nucleons between beam and projectile. Fragments with $|y| < 0.4y_{\mathrm{NN}}$ are not used as they do not contribute to reaction plane determination [114]. When applied to SπRIT data, the number of clusters cut is relaxed to > 7 and no azimuth range cuts are applied to minimize bias in azimuth acceptance. Q-vector method work best for detectors with uniform azimuth acceptance, but given that SπRIT TPC does not exhibit cylindrical symmetry, the acceptance is non-uniform. Fragments emitted at some angles are less efficiently detected than the others, leading to under-representation of particles in those angular ranges. There are multiple ways to correct for such bias. Denote Φ_r as the approximated reaction plane angle from Q-vector method, we first weigh each track by the inverse of its empirical azimuth efficiency (when it is larger than 0.05) according to the track's θ and ϕ values in Q-vector calculation, then expand the distribution of Φ_r as a Fourier series and shifts reaction plane angles event-by-event in a way that

makes the final distribution isotropic [116]. The second step is called flattening.

The azimuth efficiency, not to be confused with embedding efficiency, can be found by plotting empirical azimuth vs. polar angle distribution as 2D histogram for each particle after beam rotation in laboratory frame. It is normalized such that maximum height of azimuth distribution along every polar angle bin is equal to one. The normalized distribution shows the relative azimuth efficiencies for particles at a fixed polar angle. Azimuth efficiency for each track is the value of this distribution at the corresponding azimuth and polar angle. To correct for azimuth efficiency, $w(y_z)$ of Eq. (3.17) is multiplied by the inverse of azimuth efficiency in Q-vector calculation. To prevent tracks with extraordinarily small efficiency from blowing up the calculation, only tracks with efficiency larger than 0.05 are counted in the calculation. The threshold is set ad-hoc, but results from simulation of detector response in Section 5.9 demonstrates that this threshold value allows us to accurately reconstruct reaction plane angle.

The flattening after correcting for azimuth efficiency is achieved by first normalizing each component of Q-vector to have zero mean and unit standard deviation,

$$\hat{Q}_i = (Q_i - \langle Q_i \rangle)/\sigma_{Q_i}, \tag{3.18}$$

where i denotes the component of Q-vector which can be either x or y. Define $\hat{\vec{Q}} = \hat{Q}_x\hat{x} + \hat{Q}_y\hat{y}$, then the n^{th} Fourier components of the azimuth distribution of $\hat{\vec{Q}}$ is,

$$\begin{aligned} a_n &= -\frac{2}{n}\langle \sin(n\phi(\hat{\vec{Q}})) \rangle, \\ b_n &= \frac{2}{n}\langle \cos(n\phi(\hat{\vec{Q}})) \rangle. \end{aligned} \tag{3.19}$$

To correct for acceptance, reaction plane angles are shifted to erase the contributions of each Fourier component by the following amount,

$$\Phi_{\text{flat}} = \phi(\hat{\vec{Q}}) + \sum_n [a_n \cos(n\phi(\hat{\vec{Q}})) + b_n \sin(n\phi(\hat{\vec{Q}}))]. \tag{3.20}$$

The effect of reaction plane angle flattening is demonstrated in Fig. 3.20 where the Q-vector azimuth distributions from ^{108}Sn + ^{112}Sn before and after azimuth efficiency correction and

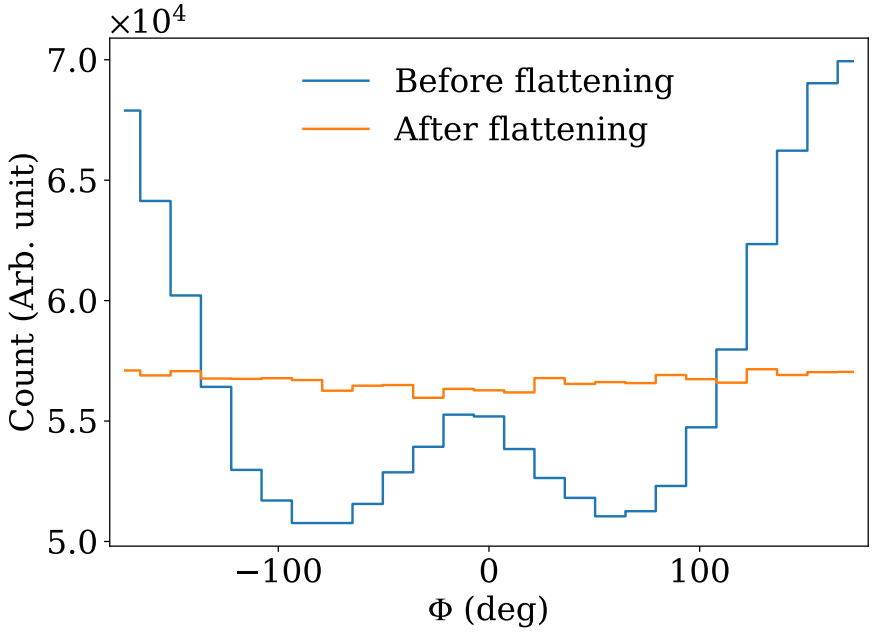

Figure 3.25: Distributions of reaction plane azimuth before (blue) and after (orange) acceptance corrections. The selected events come from ^{108}Sn + ^{112}Sn.

flattening are plotted. Even though distribution for only one reaction system is shown, acceptance corrections are verified to flatten the reaction plane distributions for all reaction systems in SπRIT experiment.

Although the flattened reaction plane angle Φ_{flat} provides a reasonable estimation of reaction plane angle Φ, they are still not identical due to stochastic nature of nuclear reaction, particle detection resolution and efficiency effects. Fortunately, as we will show in Section 4.5.4, flow observables can be accurately determined from inaccurate reaction plane angle as long as reaction plane resolution is given. It can be calculated by the *sub-event* method which quantifies the resolution as $\langle\cos(i(\Phi - \Phi_{\text{flat}}))\rangle$ for $i = 1, 2, \ldots$.

In sub-event method, fragments in each event are grouped randomly into two disjoint sub-events with equal multiplicity, which we denote as group a and b. Denote Φ^a_{flat} and Φ^b_{flat} as the reconstructed Q-vector reaction plane angle (after acceptance correction) for events in group a and b respectively and $\chi_m = \langle\cos(\Phi^a_{\text{flat}} - \Phi^b_{\text{flat}})\rangle/\sqrt{2}$, then the relation between reaction plane angle

and sub-event reaction plane angles can be approximated as,

$$\begin{aligned}\langle\cos(\Phi-\Phi_{\text{flat}})\rangle &= 0.626657\chi_m - 0.09694\chi_m^3 + 0.02754\chi_m^4 - 0.002283\chi_m^5,\\ \langle\cos(2(\Phi-\Phi_{\text{flat}}))\rangle &= 0.25\chi_m^2 - 0.011414\chi_m^3 - 0.034726\chi_m^4 + 0.006815\chi_m^5.\end{aligned} \tag{3.21}$$

These equations are then solved numerically. For full derivation of sub-event method please refers to Ref. [115].

CHAPTER 4

TRANSPORT MODELS AND EXPERIMENTAL RESULTS

4.1 Introduction

The goal of the SπRIT experiment is to study the properties of nuclear matter such that our understanding of neutron star, which is composed mostly of neutron-rich nuclear matter, can be improved. Experimental results will be compared to theoretical predictions to constrain nuclear EoS parameters. Using the SπRITROOT analysis framework, observables from spectra of pions and light fragments can be reconstructed.

Theoretical predictions are made using *transport models*, a class of semi-classical model that describes the dynamics of nuclear collisions from Fermi to relativistic energies. A review on the different transport models can be found in Ref. [117].

In this chapter, a brief summary on a few of the most commonly used many body dynamical transport models will be provided, followed by results from the SπRIT experiment.

4.2 Transport model

The idea of transport model is to extend the classical Vlasov equation for one-body phase-space distribution with a Pauli-blocked Boltzmann collision term. The resulting equation, called Boltzmann-Uehling-Uhlenbeck (BUU) equation, is formulated as,

$$\left(\frac{\partial}{\partial t} + \vec{\nabla}_p \epsilon \cdot \vec{\nabla}_r - \vec{\nabla}_r \epsilon \cdot \vec{\nabla}_p\right) f_a(\vec{r}, \vec{p}, t) = I_{\text{coll}}\left[f_a(\vec{r}, \vec{p}, t), \frac{d\sigma_{ab}^{\text{med}}}{d\Omega}\right]. \tag{4.1}$$

In this equation, $f_a(\vec{r}, \vec{p}, t)$ is the one-body phase-space distribution for particle a, $\epsilon[f_a]$ is the single-particle energy function, $I_{\text{coll}}[f_a, d\sigma_{ab}^{\text{med}}/d\Omega]$ is the two-body collision integral and $d\sigma_{ab}^{\text{med}}/d\Omega$ represents all the in-medium nucleon-nucleon differential scattering cross sections between particle a and b. ϵ and in-medium cross sections are inputs that must be provided by the

user. In particular, ϵ is governed by the mean-field potential which contains contributions from nuclear EoS. The collision term for the collision $p_a + p_b \rightarrow p'_a + p'_b$ is,

$$I_{\text{coll}}\left[f_a(\vec{r},\vec{p},t), \frac{d\sigma^{\text{med}}}{d\Omega_{ab}}\right] = \sum_b \frac{g_b}{(2\pi\hbar)^3}\int d^3p_b v_{ab}\frac{d\sigma^{\text{med}}_{ab}}{d\Omega_b}[(1-f_a)(1-f_b)f'_a f'_b - f_a f_b(1-f'_a)(1-f'_b)], \tag{4.2}$$

where v_{ab} is the relative velocity between particle a and b, g_b is the spin degeneracy and the summation over b corresponds to summation over all neutrons and protons. The collision term is solved by performing stochastic collisions of test particles. In each time step, the model first check if two test particles are close enough to incur a collision and then check if the final state of the collision is permitted by Pauli-exclusion principle.

There are two types of transport models, namely the quantum molecular dynamics (QMD) models [118–126] and the stochastic extensions of Boltzmann-Langevin type [127–132]. They mainly differ in how fluctuations and many-body correlations are introduced. Only QMD models are described and used in this thesis due to their availability in our analysis group.

QMD models approximate the many-body wave-function as a product of multiple Gaussian wave-packets with fixed width. The one-body Wigner function, which is approximately the phase space density -distribution for the corresponding many-body wave-function, is,

$$\begin{aligned} f(\vec{r},\vec{p}) &= \sum_i^A f_i(\vec{r},\vec{p}), \text{ with} \\ f_i(\vec{r},\vec{p}) &= \left(\frac{\hbar}{\Delta x \Delta p}\right)^3 \exp\left[-\frac{(\vec{r}-\vec{R}_i(t))^2}{2\Delta x^2} - \frac{(\vec{p}-\vec{P}_i(t))^2}{2\Delta p^2}\right]. \end{aligned} \tag{4.3}$$

The centroid position $\vec{R}_i(t)$ and $\vec{P}_i(t)$ are treated as variational parameters. This summarizes how QMD type models simulate nuclear dynamics, but the details in collision simulation and mean field formulation differ from code to code. We will briefly describe improved QMD (ImQMD), dcQMD and Ultra-relativistic QMD (UrQMD) in the next three subsections as these three models are used in different parts of our analysis.

4.2.1 ImQMD

ImQMD was developed at China Institute of Atomic Energy (CIAE) by the group of Prof. Zhuxia Lia based on QMD code originally imported from Frankfurt in 1989. It was improved by multiple theorists over the years, most notably by Yingxun Zhang in 2003 [126, 133–135] who incorporates the Skyrme interactions into the model. Its mean field derives from Skyrme energy density functional with explicit Skyrme-type momentum-dependent interaction [136]. Collision between nucleons is only attempted when their transverse distance is less than $\sqrt{\sigma^{\text{med}}/\pi}$, where $\sigma^{\text{med}} = (1 - \eta\rho/\rho_0)\sigma^{\text{free}}$ and η is a free parameter, and their longitudinal distance is less than $v_{ij}\gamma\delta t/2$, where v_{ij} is the relative velocity, γ is the Lorentz factor and δt is the length each time step. This model does not generate pions.

4.2.2 UrQMD

UrQMD was first developed in the mid-1990s at Frankfurt [137]. It was extended to include 50 different baryon species and 35 different meson species and is commonly used to study collisions over vast energy ranges. Different versions of UrQMD use different mean field formulations for the study of different topics in heavy-ion experiments [138–145]. The mean field of UrQMD in sections 5.8 and 5.9.3 uses Skyrme type mean field with in-medium cross-section equals to cross-section in free space [146].

4.2.3 dcQMD

dcQMD was adapted from TuQMD, which was first developed in the 90s in Tubingen, Germany [147, 148]. TuQMD includes the degrees of freedom for a lot of particle species [149]. It was extended to dcQMD for the study of asymmetric part of nuclear EoS at a few hundred MeV/u [150, 151]. The mean-field of dcQMD was formulated to introduce independent variations of compressibility or slope parameters in EoS. dcQMD allows the isospin-dependent potential of nucleon to be different from that of $\Delta(1232)$ which has a large impact on pion multiplicities [152].

Therefore this flexibility makes dcQMD suitable for the comparison of pion observables. A collision is attempted when $\pi d_{\text{min}}^2 \leq \sigma$, with σ being the scattering cross-section. A particular feature of dcQMD is that it considers the total energy balance due to in-medium potential in a collision. This condition shifts the production threshold based on differences between the initial and final potential energy [153].

4.3 Coalescence

After transport model propagates nucleons to their final positions, *clusterization* (also called *coalescence*) algorithm are normally used to group nucleons into light fragments such as, but not limited to, Deuteron and Triton. It usually involves combining neutrons and protons with small relative distance and speed into isotopes. This procedure is unreliable as the physical fragment production mechanism involves many body correlations that are not well understood [154, 155]. Such algorithms often cannot predict the binding energy of most particles especially ^{4}He.

In some models, clusterization algorithms are handled better and yield more consistent results with data. Most prominently, the Asymmetrized Molecular Dynamic (AMD) model propagate nucleons and calculate cluster formation in one unified step. Its predictions on light fragment yield was shown to agree with data to a satisfactory extent [154, 156]. It is not used in this thesis due to the limited availability of AMD code. All the QMD models used for comparison with data in this manuscript, however, use the less reliable clusterization process and therefore energy spectra of light fragments cannot be compared directly.

To overcome this difficulty, observables must be chosen carefully to minimize their sensitivity to clusterization. To be more precise, we want to construct observables whose values depend weakly on the clusterization process. This can be achieved by one of the following ways:

1. Consider particles that do not form elements or isotopes.

2. Sum up protons from all light fragments to reconstruct the primary nucleon distribution before clusterization.

3. Take ratio of the same observable between different reaction systems. Such ratios have been shown to cancel systematic errors from clusterization [157, 158].

Various observables, such as isoscaling rato [157, 158], have been constructed with these methods. In this chapter, these observables will be described and their measured values from SπRIT experiment will be shown.

4.4 Geometric coverage and impact parameter selection

SπRIT TPC has limited geometric coverage such that particles with very negative rapidity in center of mass frame are not being detected with good efficiency. Therefore for most of the results from ^{108}Sn + ^{112}Sn and ^{132}Sn + ^{124}Sn reactions, only particles at $p_z > 0$ in center of mass frame will be used. Results from particles with slightly negative rapidity are also plotted in Section 4.6.4 for the two reactions, but spectra at even lower rapidity are not usable. As for ^{112}Sn + ^{124}Sn reaction, the result can be combined with data from ^{124}Sn + ^{112}Sn to form a complete 4π solid angle coverage, so observables values for this particular reaction do not need to be conditioned on $p_z > 0$.

With the exception of Section 4.5.3, impact parameters of all observables in this chapter are selected with gates on charged multiplicity. Impact parameter cannot be measured directly, but can be inferred from other indirect observables. Traditionally, the inference is done with the help of an observable that depends on impact parameter monotonically. Examples of such observables include total charged multiplicity and ratio of total transverse kinetic energy to longitudinal kinetic energy (ERAT) [30]. With the assumption of geometric cross-section $d\sigma = 2\pi r dr$, impact parameter can be calculated from the cumulative distribution of such observable using the following formula [2],

$$b = b_{\max}\sqrt{\frac{N_{O\geq O_C}}{N_{\text{total}}}}, \tag{4.4}$$

where O_C is the current observable value, $N_{O\geq O_C}$ is number of observed events with observable value $\geq O_C$, N_{total} is the total number of observed events and $b_{\max}$ is the maximum impact parameter. $b_{\max}$ is calculated from the empirical total reaction cross-section and is measured to

be 7.13 fm for ^{108}Sn + ^{112}Sn, 7.31 fm for ^{112}Sn + ^{124}Sn and 7.52 fm for ^{132}Sn + ^{124}Sn [2]. This method is reliable for impact parameter not too close to the sharp cut-off at $b_{\max}$. Charged particles multiplicity will be used as O_C in the following sections.

Section 4.5.3 uses a Machine learning algorithm to extract pion results reliably at impact parameter near $b_{\max}$. This algorithms will be reviewed in Section 5.9.3.

4.5 Pion Observables

Since pions do not form isotopes with other particles, their yields should be independent of the clusterization process. Furthermore, pion observables are predicted to be sensitive to nuclear EoS at high density due to pion's unique production mechanism: In nucleon-nucleon collisions, some interactions are energetic enough to form excited $\Delta(1232)$ baryon resonance ($NN \leftrightarrow N\Delta$) which then promptly decay into pions and nucleons. The high production threshold of Δ resonance ($1232\,\mathrm{MeV/c^2}$) at the early stage of the reaction ensures that pions originate from high density region. SπRIT data on pion momentum spectra in central collisions have been published [33, 152] and their results will be briefly summarized here. It will be followed by data on other new pion observables.

4.5.1 Pion yield of central events

The most straight-forward pion observable to extract experimentally is their total yields. Although they are measured reliably in SπRIT experiment, comparison with theory is hard to carry out because a lot of different physical processes must be taken into account for the predicted yields to be accurate. Some of these processes are not well understood which introduce additional uncertainties in quantifying the relation between pion yields and symmetry energy. These issues can be mitigated by using the ratio of $Y(\pi^-)$ to $Y(\pi^+)$ instead. The division cancels out some contributions from physical processes that act on both π^- and π^+ in similar ways while magnifying the symmetry energy effects which act on π^- and π^+ with opposite sign.

The study of pion yields was the focus of Ref. [152]. The SπRIT experiment measured the pion

yield ratios for ^{108}Sn + ^{112}Sn, ^{112}Sn + ^{124}Sn and ^{132}Sn + ^{124}Sn systems. The total neutron to proton ratio N/Z of these three systems are 1.36, 1.2 and 1.56 respectively. Only pions with $p_z \geq 0$ in center of mass frame are measured (see Section 4.4). The effects of incomplete coverage should be minimized when ratios between yields of π^- and π^+ are taken. To impose centrality gate, only events with multiplicity larger than 50 are considered. This corresponds to an impact parameter cut of $b < 3$ fm.

With a Δ resonance model for pion production, one would expect that $Y(\pi^-)/Y(\pi^+)$ follows a $(N/Z)^2$ dependence [31, 159]. However, the measured pion ratios in Fig. 4.1 (yellow cross with circle marker) follows N/Z with a best fitted power index of 3.4 instead. The radius of the circle in the center of each cross is the uncertainty of yield measurement. The discrepancy indicates the presence of dynamical factors beyond a simple Δ resonance model. If transverse momentum cut of $p_T > 180$ MeV/c is imposed, the result (blue crosses with circle marker) still shows a $(N/Z)^{3.4}$ dependence instead of the expected $(N/Z)^2$. The effects unexplained by Δ resonance model persist even for high momentum pions and may suggest the ratios exhibit greater effects from symmetry energy.

4.5.2 Pion ratio spectra of central events

The analysis of pions momentum spectra in central collisions is the focus of Ref. [33]. Their results will be briefly summarized in this section.

dcQMD model predictions will be compared to the measured pion spectrum to constrain nuclear EoS. As described in Section 4.2.3, dcQMD is suitable for describing pion emissions due to its flexibility in adjusting Δ potential independently from that of nucleons. This is essential as it was found that if Δ potential is set equal to that of nucleons, the predicted yields of π^- and π^+ will be incorrect [152, 160]. The potential depth at saturation density is adjusted until dcQMD reproduces experimental pion yields and mean kinetic energies [160].

Only L and the scaled difference between neutron and proton effective mass $\Delta m^*_{np} = [m^*_n - m^*_p]/(m_N\delta)$ are varied to simplify the analysis. Other EoS parameters are fixed to the best extracted

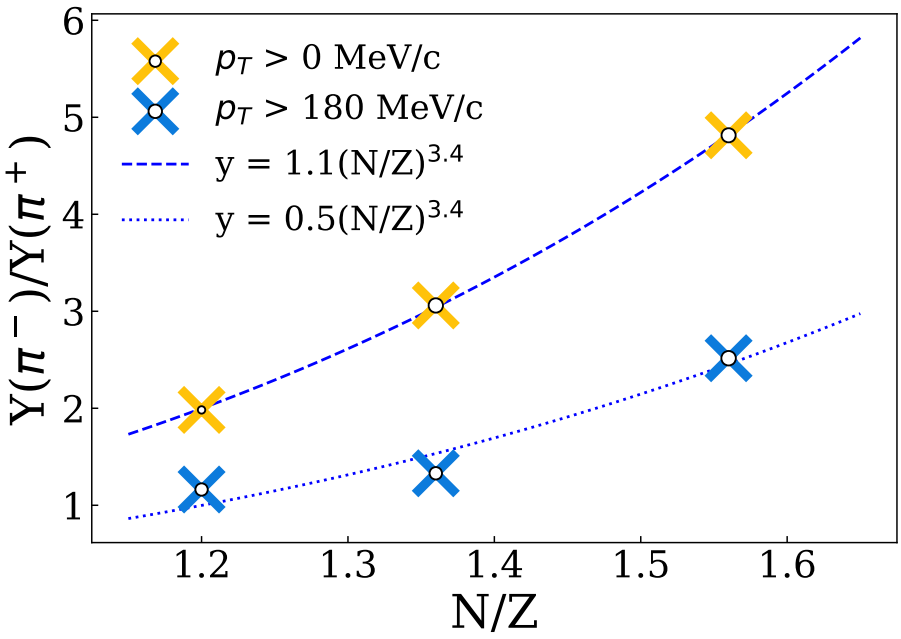

Figure 4.1: Yield of π^- over that of π^+ in $b < 3$ fm events for pions with $p_z > 0$ in center of mass frame, plotted as a function of N/Z. The yellow crosses show the yield ratios with no transverse momentum cut while the blue crosses shows that with $p_T > 180$ MeV/c. The radius of circle inside each cross represents the statistical uncertainty of the ratio. The dashed blue line and dotted blue line corresponds to best fitted power functions of N/Z for $p_T > 0$ and $p_T > 180$ MeV/c pion ratios respectively.

values from other studies. Following results in Ref. [161], K_{sat} is set to 250 MeV and Q_{sat} is set to -350 MeV. Following results from nuclear mass and radius measurements [34, 40], L will be correlated with K_{sym} via $K_{\text{sym}} = -488 + 6.728L(\text{MeV})$ and $S(\rho = 0.1\,\text{fm}^{-3})$ is fixed to 25.5 MeV.

When the measured π^+ and π^- transverse momentum (p_T) spectra for ^{108}Sn + ^{112}Sn and ^{132}Sn + ^{124}Sn reactions with impact parameter $b < 3$ fm are compared to dcQMD predictions in Fig. 4.2, it is found that pion potential is required to describe the spectra accurately. Only pions with $p_z > 0$ in center of mass frame are counted (see Section 4.4). The black markers correspond to measured spectra and both the blue and red lines correspond to dcQMD calculations with $L = 80$ MeV, $\Delta m^*_{np} = 0$ and optimized Δ potential depth. The difference between the two curves is that pion optical potential is used on the red curves but not the blue curves. Without pion potentials, the predictions under estimate production of low momentum pions. At high momentum, the two curves are nearly the same.

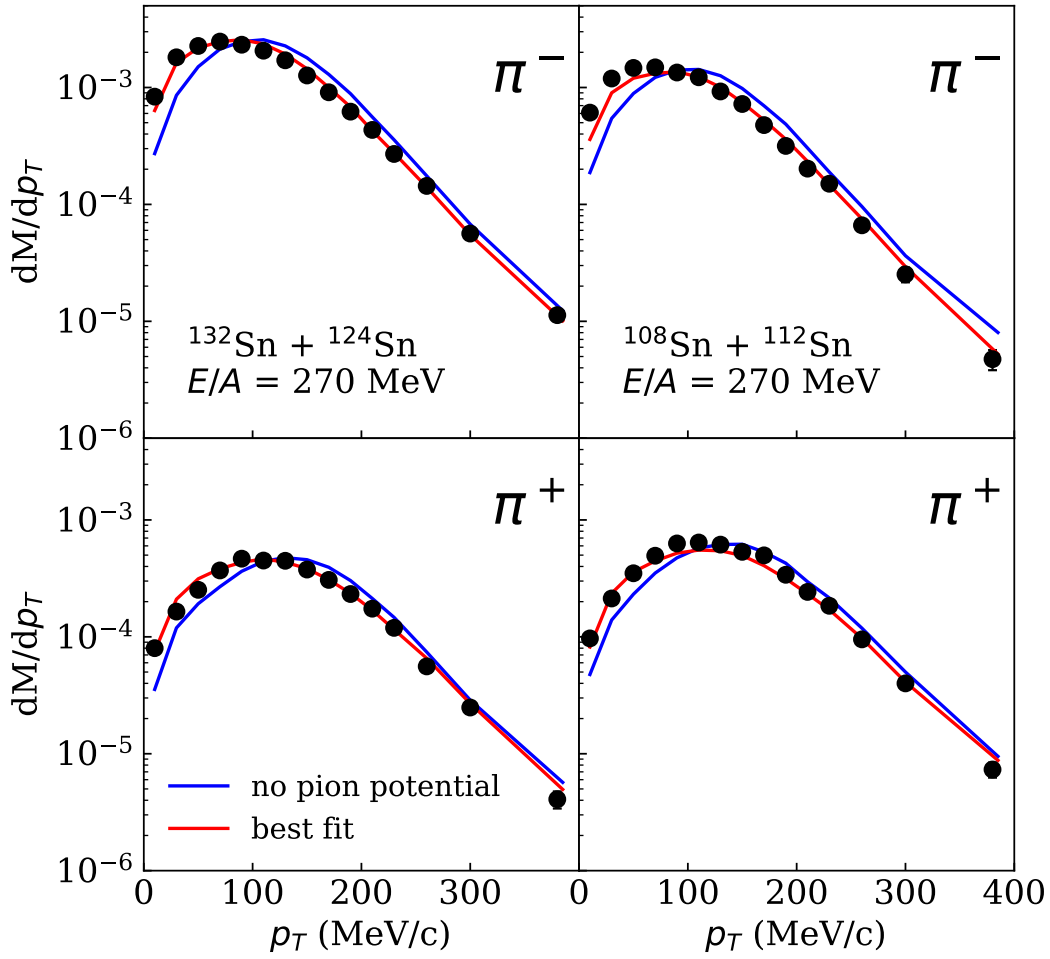

Figure 4.2: Pion spectra for $b < 3$ fm events. Red curves show dcQMD predictions with best fitted pion potential. The blue curves are identical except that no pion potential is used.

Next we focus on the single ratio spectrum $SR(\pi^-/\pi^+) = [dN(\pi^-)/dp_T]/[dN(\pi^+)/dp_T]$. This ratio magnifies symmetry energy effects as the contribution of symmetry energy to isovector mean field potential is opposite in sign for π^- and π^+, similar to our rationale for taking ratios of total yields in the previous section. We use dcQMD to predict single ratios at 12 different parameter sets in the L vs. Δm^*_{np} space, forming a regular lattice. The value of L in the lattice is either 15, 60, 106 or 151 MeV and $\Delta m^*_{np}/\delta$ is either -0.33, 0 or 0.33.

A few selected calculations and the measured single ratios are shown in Fig. 4.3. The

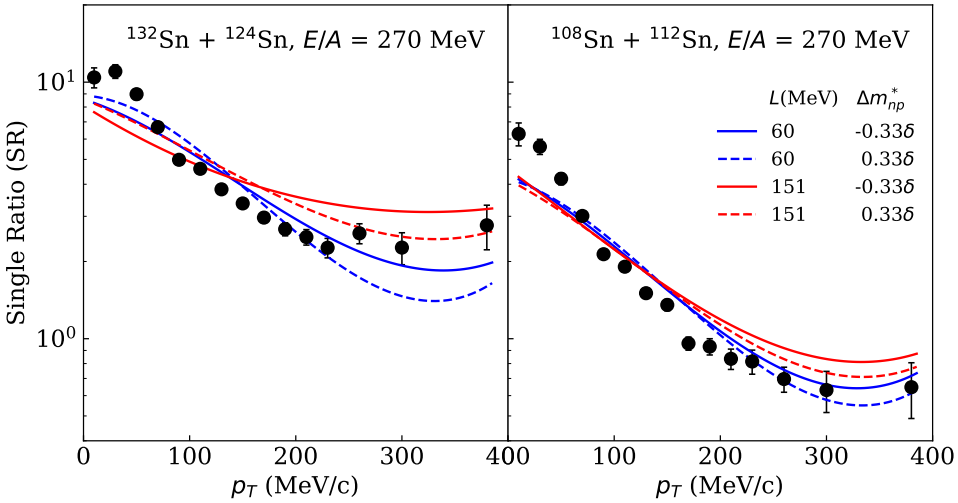

Figure 4.3: Single pion spectral ratios for ^{132}Sn + ^{124}Sn (left) and ^{108}Sn + ^{112}Sn (right) reactions with four selected dcQMD predictions overlaid. See text for details.

$(L, \Delta m^*_{np})$ values of solid blue line is $(60, -0.33\delta)$, dashed blue line is $(60, 0.33\delta)$, solid red line is $(151, -0.33\delta)$ and dashed red line is $(151, 0.33\delta)$. Coulomb effects dominate the low p_T region which cause a steep rise in measured ratios at $p_T < 200\,\mathrm{MeV/c}$. All calculations at $p_T < 200\,\mathrm{MeV/c}$ disagree with data, which could be caused by inaccuracies in the simulation of Coulomb interactions or pion optical potential above saturation density. At $p_T > 200\,\mathrm{MeV}$, the Coulomb and pion potential effects diminish and the ratios should be good probes to the symmetry energy effect.

The predicted single ratios at $p_T > 200\,\mathrm{MeV/c}$ are interpolated with 2D cubic splines over $(L, \Delta m^*_{np})$ space. The interpolated predictions are compared to experimental measurements through a chi-square analysis. The resultant multivariate constraint on L and Δm^*_{np} is shown in Fig. 4.4 where the green shaded region is the 1σ confidence interval and the area enclosed by the two blue dashed curve is the 2σ confidence interval. Without any constraints on the effective mass, the best fitted value is $L = 79.9 \pm 37.6\,\mathrm{MeV}$. The correlation between Δm^*_{np} and L suggests that tighter constraint on L can be made if Δm^*_{np} is constrained better as shown in Chapter 6.

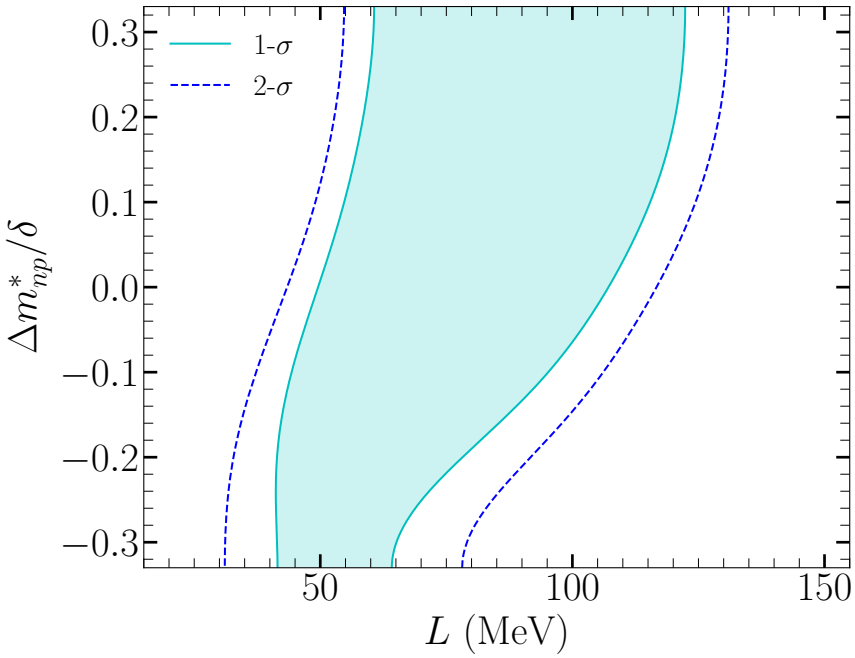

Figure 4.4: Correlation constraint between L and $\delta m^*_{np}/\delta$, extracted from pion single ratio at $p_T > 200\,\mathrm{MeV/c}$ in both the neutron deficient ^{108}Sn + ^{112}Sn and the neutron rich ^{132}Sn + ^{124}Sn systems. The light blue shaded region corresponds to 68% confidence interval while the dashed blue lines denote the contours of 95% confidence interval.

4.5.3 Pion yield dependence on impact parameter

Using machine learning algorithm described later in Section 5.9.3, events are separated into impact parameter bins from 0 to 10 fm with bin size of 1 fm. The pion yield is plotted against impact parameter for ^{132}Sn + ^{124}Sn and ^{108}Sn + ^{112}Sn systems in Fig. 4.5. Only pions with $p_z > 0$ in center of mass frame are counted (see Section 4.4). The pion yield decreases with increasing impact parameter where the overlapping zone between projectile and target (also known as the participant zone) decreases. The neutron rich system of ^{132}Sn + ^{124}Sn generates the largest difference between π^- and π^+ yields. While π^+ yields is nearly the same for both systems, the π^- yield is a near factor of 2 larger for the neutron rich systems.

The predicted pion yield may suffers from systematic errors due to incomplete description of nuclear dynamics. To minimize such effect, ratio of yields (π^-/π^+) can be used to cancel out the systematic errors. To further minimize the errors, the double ratio of π^-/π^+ of ^{132}Sn + ^{124}Sn over

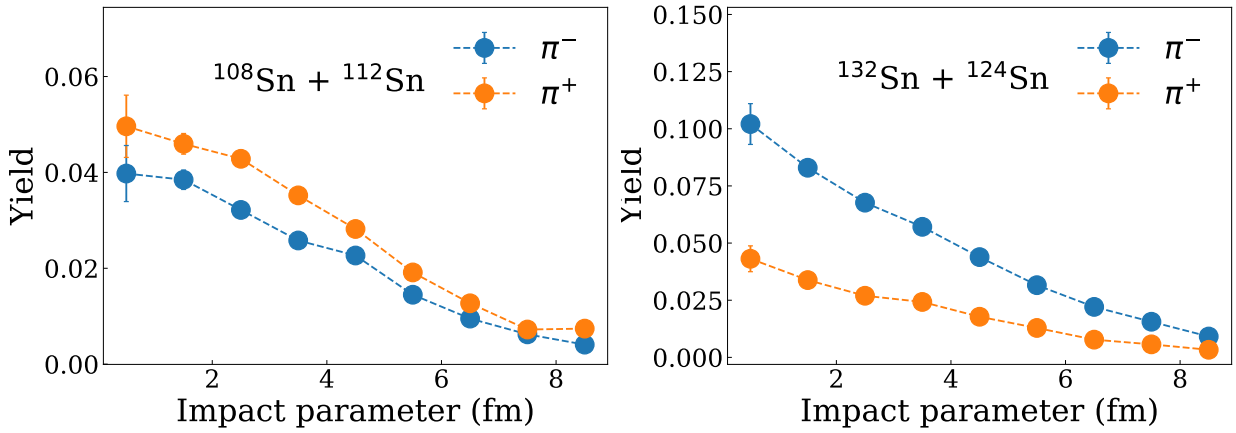

(a) (b)

Figure 4.5: Impact parameter dependence of pion yield for (Left) ^{108}Sn + ^{112}Sn and (Right) ^{132}Sn + ^{124}Sn.

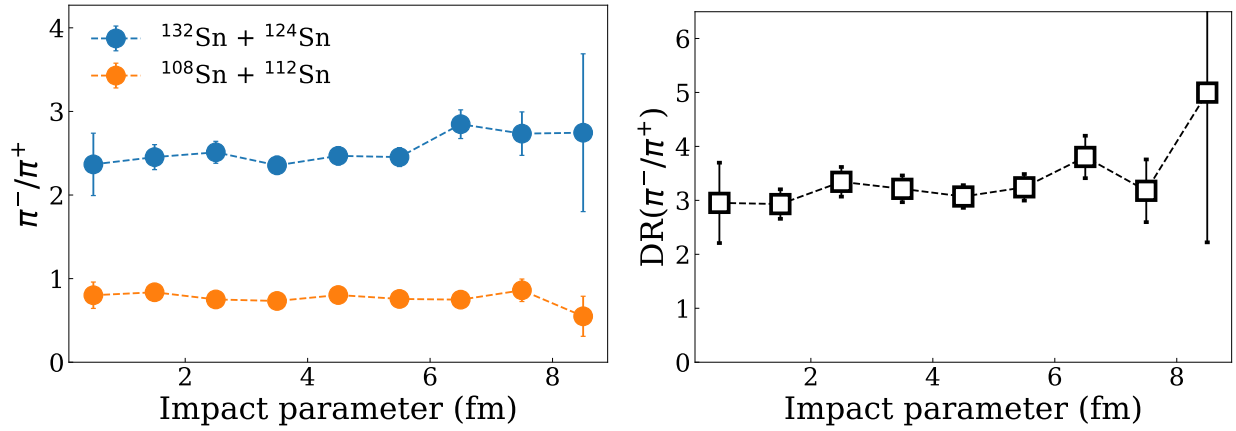

(a) (b)

Figure 4.6: (a): Single ratios of π^-/π^+ as a function of impact parameter for ^{132}Sn + ^{124}Sn (orange circles) and ^{108}Sn + ^{112}Sn (blue circles) reactions. (b): Double ratio of π^-/π^+ from ^{132}Sn + ^{124}Sn over ^{108}Sn + ^{112}Sn as a function of impact parameter.

that of ^{108}Sn + ^{112}Sn can be used for comparison with models.

These single and double ratios are shown in Fig. 4.6. It is interesting to note that the double ratio is almost constant across all impact parameters.

As described in the previous sections, pions with high transverse momentum provide a clearer signal to symmetry energy as other undesirable effects diminish such as Coulomb. The analysis is repeated, but this time only pions with $p_T > 180\,\mathrm{MeV/c}$ are counted towards particle yields. The

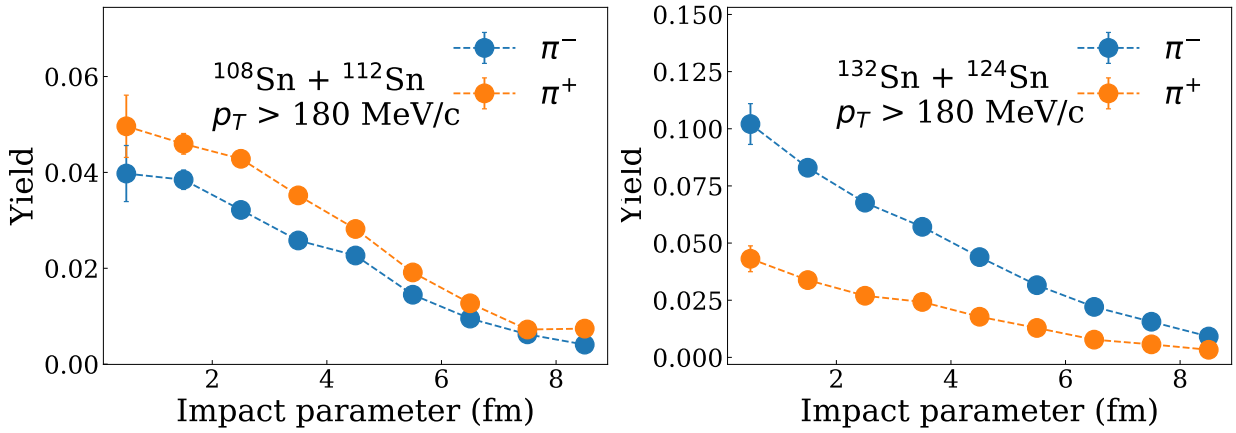

(a) (b)

Figure 4.7: Same as Fig. 4.5 except only pions with $p_T > 180\,\mathrm{MeV/c}$ are counted.

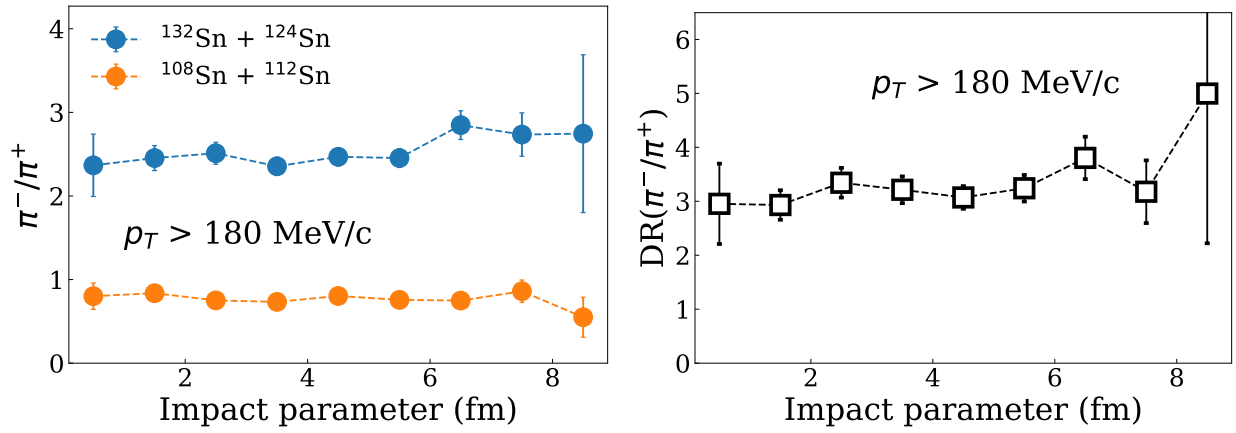

(a) (b)

Figure 4.8: Same as Fig. 4.6 except only pions with $p_T > 180\,\mathrm{MeV/c}$ are counted.

results are shown in Figs. 4.7 and 4.8. They are identical to Figs. 4.5 and 4.6 respectively except with p_T condition imposed. Within statistical errors, the impact parameter dependence of single and double ratio is still nearly flat, and the double ratio in the high p_T region is slightly higher than that without p_T cut. This suggests that the shape of the yield or ratio spectra rather than the ratios are more sensitive to the symmetry energy.

4.5.4 Pion directed flow

Collective flow in nuclear collisions have been the focus of numerous studies [11, 111–113] and was demonstrated to be a sensitive probe for nuclear EoS. It is quantified as the Fourier coefficients of the fragments' azimuthal distribution with respect to reaction plane azimuth Φ [115],

$$\frac{dN}{d(\phi - \Phi)} \propto 1 + 2v_1 \cos(\phi - \Phi) + 2v_2 \cos(2(\phi - \Phi)) + \ldots \tag{4.5}$$

Here ϕ is the fragment azimuths, v_1 is called the *directed flow* and v_2 is called the *elliptical flow*. Azimuthal distribution of nuclear fragment is not isotropic because in mid-central collisions, emissions near reaction plane are blocked by spectator nucleons. Nucleons outside of the overlapping region between projectile and target nucleus along the beam line are called *spectator nucleons* and those inside are called *participant nucleons*, first illustrated in Fig. 1.1. If the mean field is highly repulsive, participant nucleons experience higher pressure in the collision which leads to early emission. The spectator nucleons do not have time to leave and blocks the emission of particles near the reaction plane azimuth, leading to stronger flow. Vice versa when mean field is less repulsive [11].

The observed directed and elliptical flows are calculated as follows,

$$\begin{aligned} v_1^{\text{obs}} &= \langle \cos(\phi - \Phi_{\text{flat}}) \rangle \\ v_2^{\text{obs}} &= \langle \cos(2(\phi - \Phi_{\text{flat}})) \rangle \end{aligned} \tag{4.6}$$

Only particles with $-45^\circ < \phi < 45^\circ$ are being counted since geometric acceptance of SπRIT TPC for particles that move in the general direction of beam left ($\phi \sim 0^\circ$) has the most optimal geometric acceptance. The observed value v_i^{obs} is smaller than the true v_i due to non-zero resolution in the determination of reaction plane by Q-vector. Fortunately, v_i can be reconstructed using resolution information from sub-event method by the following formula,

$$v_i = v_i^{\text{obs}} / \langle \cos(i(\Phi - \Phi_{\text{flat}})) \rangle. \tag{4.7}$$

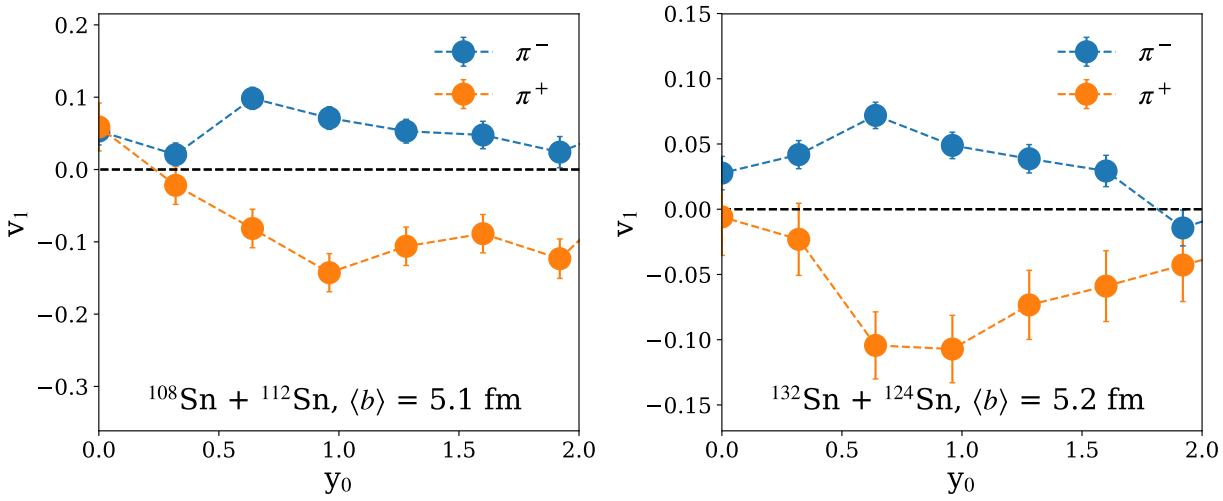

Figure 4.9: v_1 of π^+ and π^- as a function of rapidity y_0 for ^{108}Sn + ^{112}Sn (left) at $\langle b \rangle$ = 5.2 fm and ^{132}Sn + ^{124}Sn (right) reactions at $\langle b \rangle$ = 5.1 fm.

It is customary to plot observables as a function of normalized rapidity $y_0 = y_{\mathrm{CM}}/y_{\mathrm{NN}}$. Here $y_{CM} = 0.5\ln((E+p_z)/(E-p_z))$ is the center-of-mass rapidity for fragments in consideration and y_{NN} is the relative rapidity of nucleons between projectile and target. In fixed target experiment like SπRIT, target is stationary in laboratory frame so the relative nucleon rapidity is simply half of beam rapidity in laboratory frame, $y_{\mathrm{NN}} = 0.5 y_{\mathrm{Beam\ Lab}}$.

Fig. 4.9 shows pion directed flow (v_1) from SπRIT experiment for ^{108}Sn + ^{112}Sn and ^{132}Sn + ^{124}Sn reactions at mean impact parameter of 5.1 fm ($28 < M \leq 49$) and 5.2 fm ($31 < M \leq 49$) respectively. The flow of π^- is positive while that of π^+ is negative with larger magnitude. Such characteristics are not reproduced by current transport models. The directed flow of pion is expected to be sensitive to the pion potential so further studies are warranted. There are not enough statistics to extract v_2 and higher order terms with satisfactory accuracy.

4.6 Light fragments observables

4.6.1 Coalescence invariant proton spectrum

For most transport models, spectra of individual light fragments cannot be compared to model. However, when all proton contributions from light fragments are summed up, it should reproduce

the primary proton distribution before the clusterization process. Neutron-to-proton spectrum ratio constructed this way has been successfully used to constraint nuclear EoS in previous experiment [158]. By summing the rapidity distributions of light fragments, we get the *coalescence invariant proton spectrum* (CIP). In the SπRIT experiment, protons from light fragments up to ^{4}He are summed,

$$Y_{\mathrm{CIP}} = Y_{\mathrm{p}} + Y_{\mathrm{d}} + Y_{\mathrm{t}} + 2Y_{^3\mathrm{He}} + 2Y_{^4\mathrm{He}}. \tag{4.8}$$

The scaling factor of 2 in front of Helium isotopes reflects the fact that Helium consists of two protons. Isotopes heavier than ^{4}He are not counted since their yields are orders of magnitude lower. Furthermore, fragments emitted with very negative rapidity are not measured (see Section 4.4). This is problematic as we need to know how many nucleons are recovered in the summation. It is imperative that most protons are being counted in the CIP for such reconstruction of initial proton distribution to be accurate. As a result, the full CIP spectrum can only be reconstructed for ^{112}Sn + ^{124}Sn system as we have complete geometric coverage for this reaction (see Section 4.4).

Fig. 4.10 shows the complete CIP of ^{112}Sn + ^{124}Sn at $\langle b \rangle = 1.0$ fm. The impact parameter selection is done with multiplicity cut of $M > 55$. 93% of all the protons in the reaction are accounted for.

4.6.2 Stopping

Stopping refers to the degree of equilibrium between target and projectile and is sensitive to the dynamics of the reactions such as the in-medium nucleon-nucleon cross-sections used in transport models. The observable *VarXZ* is predicted by transport models to be sensitive to the *transparency*, or *stopping*, in heavy-ion collisions [32]. This observable allows us to quantify the deviation of reality from a completely stopped scenario, an assumption that were used previously in hydrodynamic models [32]. It is also useful in understanding the nuclear shear viscosity [162]. Following the convention of Ref. [32], we define *VarX* and *VarZ* as the variance of particle rapidity distributions in x-direction (transverse direction) and z-direction (longitudinal direction)

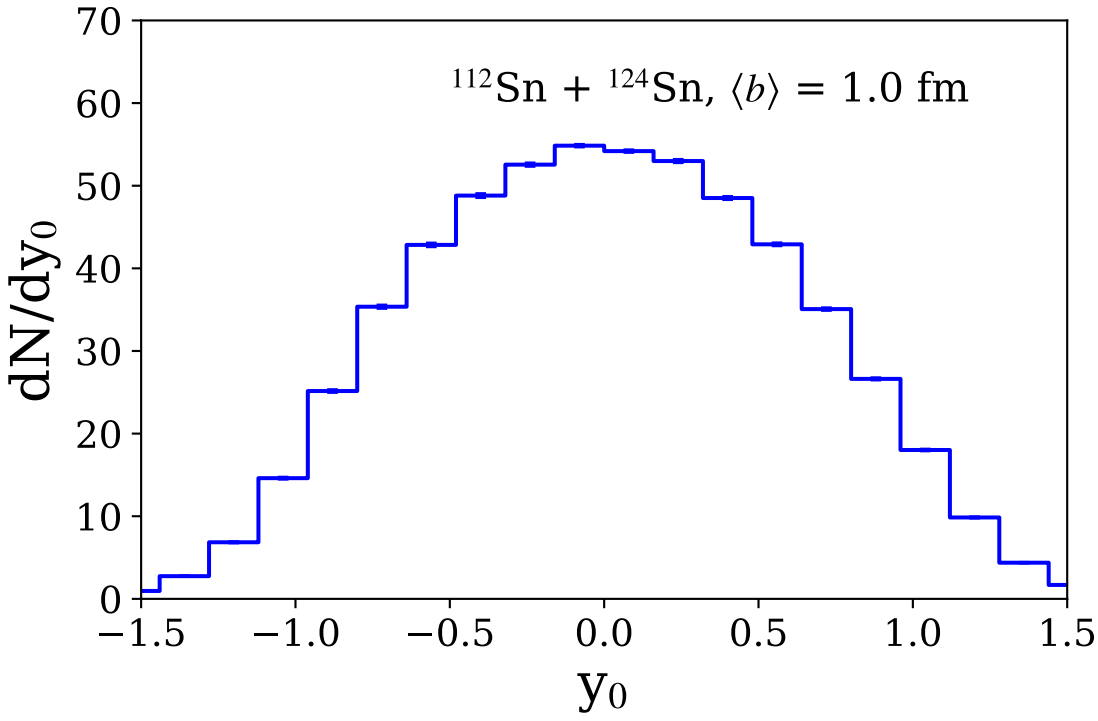

Figure 4.10: Coalescence invariant proton rapidity spectrum of ^{112}Sn + ^{124}Sn at ⟨b⟩ = 1.0 fm.

respectively, then *VarXZ* = *VarX*/*VarZ*. Note that the x-axis in VarX is an arbitrary laboratory axis and not defined with respect to reaction plane. If the target and projectile are completely equilibrated in the collision, the information on beam axis is lost and we expect the variance in x- or z-directions to be identical, thus VarXZ = 1. On the other hand, if target and projectile do not interact at all, which is the case for complete transparency, there is no collision and VarXZ should be 0.

Only VarXZ for ^{112}Sn + ^{124}Sn and ^{108}Sn + ^{112}Sn reactions are constructed. We have complete coverage for ^{112}Sn + ^{124}Sn and even-though there is no data for ^{108}Sn + ^{112}Sn at very negative rapidity (see Section 4.4), particle distributions are expected to be approximately symmetric around $y_0 = 0$ as the mass number of target and projectile are similar. The $y_0 < 0$ portion of the rapidity distribution is approximated as a mirror image of $y_0 > 0$ part of the distribution. VarXZ from ^{132}Sn + ^{124}Sn is not calculated as the mass difference between target and projectile is too large for the mirror image approximation to hold. Fig. 4.11 shows *VarXZ* of proton, Deuteron and Triton

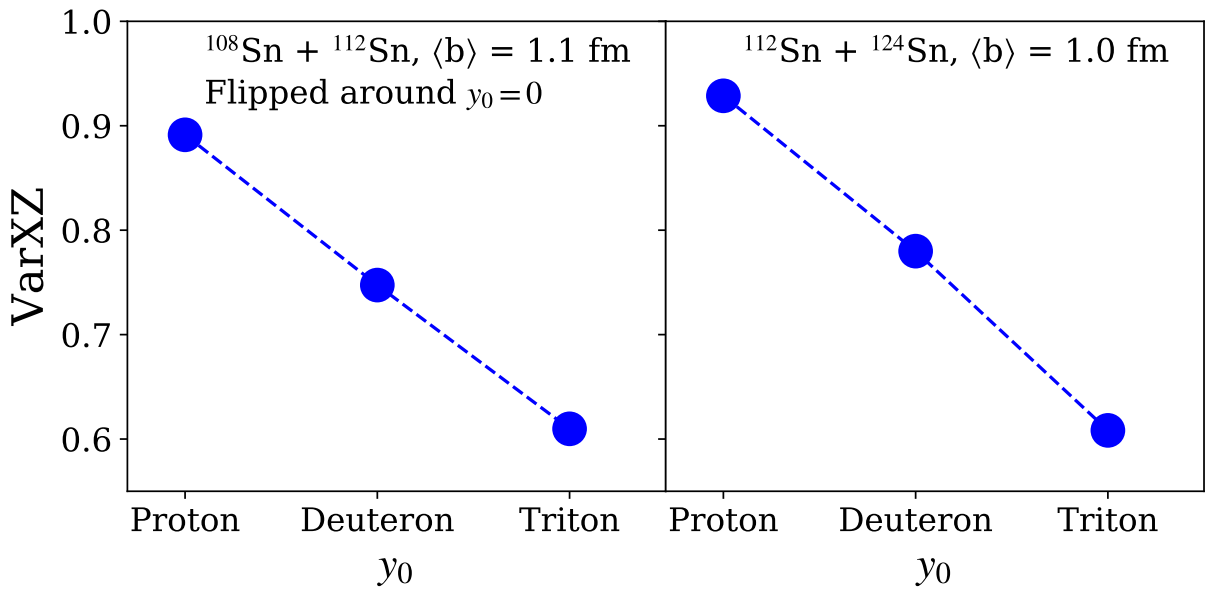

Figure 4.11: Left: *VarXZ* values for proton, Deuteron and Triton particles for ^{108}Sn + ^{112}Sn at $\langle b \rangle$ = 1.1 fm. Right: *VarXZ* for ^{112}Sn + ^{124}Sn at $\langle b \rangle$ = 1.0 fm.

for ^{108}Sn + ^{112}Sn reaction with centrality gate of $\langle b \rangle = 1.1$ fm ($M > 55$) and ^{112}Sn + ^{124}Sn at $\langle b \rangle = 1.0$ fm ($M > 55$). VarXZ decreases with increasing atomic mass on hydrogen isotopes, which is consistent with ^{197}Au + ^{197}Au results from FOPI [32] and termed this phenomena as *stopping hierarchy*.

4.6.3 Isospin Tracing

Global equilibrium is not reached in central heavy-ion collision. These non-equilibrium effects are expected to be influenced by a myriad of processes, such as in-medium effects and deflections in momentum-dependent mean fields. To quantify the extent of non-equilibrium, Isospin Tracing was proposed in Ref. [163] to constrain the magnitude of in-medium cross-section with data from the FOPI experiment. In this section, the construction of Isospin Tracing will be described and the measured values from SπRIT experiment will be presented.

Isospin Tracing R_x is a meta-observable that is defined with respect to an observable x as

follows:

$$R_x = \frac{2x^{AB} - x^A - x^B}{x^A - x^B}. \tag{4.9}$$

In this equation, x^{AB}, x^A and x^B are the observable values of x for $A + B$, $A + A$ and $B + B$ reactions, respectively. R_x takes the value of +1 if $A + B$ behaves like $A + A$ and -1 if it behaves like $B + B$. If global equilibrium is reached, it should take the value of 0 everywhere in the phase-space. R_x quantifies how well the target and projectile are "mixed".

In the case of Ref. [163], A = Ru and B = Zr. R_x is tested with x being either Triton to Helium-3 ratio (t/^{3}He) or coalescence-invariant proton spectrum (Z). $R_{\mathrm{t}/^3\mathrm{He}}$ and R_Z both increase monotonically as a function of impact parameter b. This trend agrees with the general belief that reactions are more equilibrated in central than peripheral collisions. Furthermore, when a centrality gate of $b \leq 1.3$ fm is imposed, R_Z is observed to increase with normalized rapidity $y_0 = y/y_{\mathrm{NN}}$, with $R_Z = 0$ at $y_0 = 0$. It indicates that equilibrium is reached at mid-rapidity, but not so for fragments with high rapidity. Transport model calculations showed that the slope of R_Z as a function of y_0 in central events is sensitive to in-medium cross-section [163].

4.6.3.1 Adapting Isospin Tracing for SπRIT experiment

Isospin tracing will only be calculated for ^{112}Sn + ^{124}Sn as it is the only reaction with complete geometric coverage (see Section 4.4). In this section, x in Eq. (4.9) is chosen to be coalescence-invariant proton spectrum. It is tempting to repeat the analysis of Ref. [163] simply by substituting A with ^{112}Sn and B with ^{124}Sn, but it cannot be done due to the absence of data for symmetric reactions.

The calculation of R_Z requires data for ^{112}Sn +^{112} Sn and ^{124}Sn +^{124} Sn reactions, which are not performed in the SπRIT experiment. Fortunately these distributions can be approximated by linear combinations of distributions for reaction systems performed in the experiment. Denote Z^A as CIP for $A + A$ reaction and Z^{AB} as CIP for $A + B$ reaction. To begin with, the distribution $Z^{^{112}\mathrm{Sn}} + Z^{^{124}\mathrm{Sn}}$ can be approximated as $Z^{^{112}\mathrm{Sn}^{124}\mathrm{Sn}} + Z^{^{112}\mathrm{Sn}^{124}\mathrm{Sn}}$. The two distributions are

mirror images of each other along $y_0 = 0$. The heuristic reason for the approximation is the fact that the total target mass and total projectile mass of $Z^{112}\mathrm{Sn} + Z^{124}\mathrm{Sn}$ are equal to that of $Z^{112}\mathrm{Sn}^{124}\mathrm{Sn} + Z^{112}\mathrm{Sn}^{124}\mathrm{Sn}$.

This takes care of the second and the third term on the numerator of Eq. (4.9). With data for ^{132}Sn +^{124} Sn reaction, the terms on the denominator can also be approximated. Using the mass summing heuristic, $0.5 * (Z^{132}\mathrm{Sn}^{124}\mathrm{Sn} + Z^{112}\mathrm{Sn}^{124}\mathrm{Sn}) \approx Z^{124}\mathrm{Sn}$ since the average projectile mass of L.H.S. = $0.5 * (132 + 112) = 122$, which is close to the desired projectile mass of 124. These approximated distributions will be referred to as *proxy*, as opposed to the real distributions calculated with data from the symmetric systems. The accuracy of proxy will be verified with transport model.

Lastly we scaled the amplitude of each distribution by the inverse of total system mass to eliminate any effect caused by mass differences between the symmetric and mixed systems. This step was not needed in Ref. [163] because their target and projectile are chosen to be of the same mass and the scaling amplitude can be factored out.

Using dcQMD [160], proxies and real distributions are compared in Fig. 4.12. These distributions are generated at $b = 1$ fm. From left to right, the in-medium cross-section is increased from $0.6\sigma_{\mathrm{free}}$ to σ_{free}. The distributions become flatter as σ increases. This is expected as increasing cross-section should push the reaction closer to equilibrium. For the two graphs on the bottom, only fragments with transverse momentum per nucleon $p_T/A > 300\,\mathrm{MeV/c}$ are counted in R_z. The slope of R_z at mid-rapidity increases with p_T/A threshold, which reflects an enhancement of transparency for high momentum fragments. R_Z from proxies in all four cases are very close to those from real distributions when $|y_0| < 1$.

Proxies R_z from the SπRIT experiment are shown in Fig. 4.13. As expected, the slope of R_z increases with the p_T/A threshold. When p_T/A cut is absent, data disagrees with dcQMD predictions regardless of in-medium cross-section but when $p_T/A > 300\,\mathrm{MeV/c}$ is imposed, data agrees with predictions for $\sigma = 0.6\sigma_{\mathrm{free}}$ better that for $\sigma = \sigma_{\mathrm{free}}$. This demonstrates the momentum dependence of in-medium cross-section. By varying the p_T/A slices, it may be possible to constrain

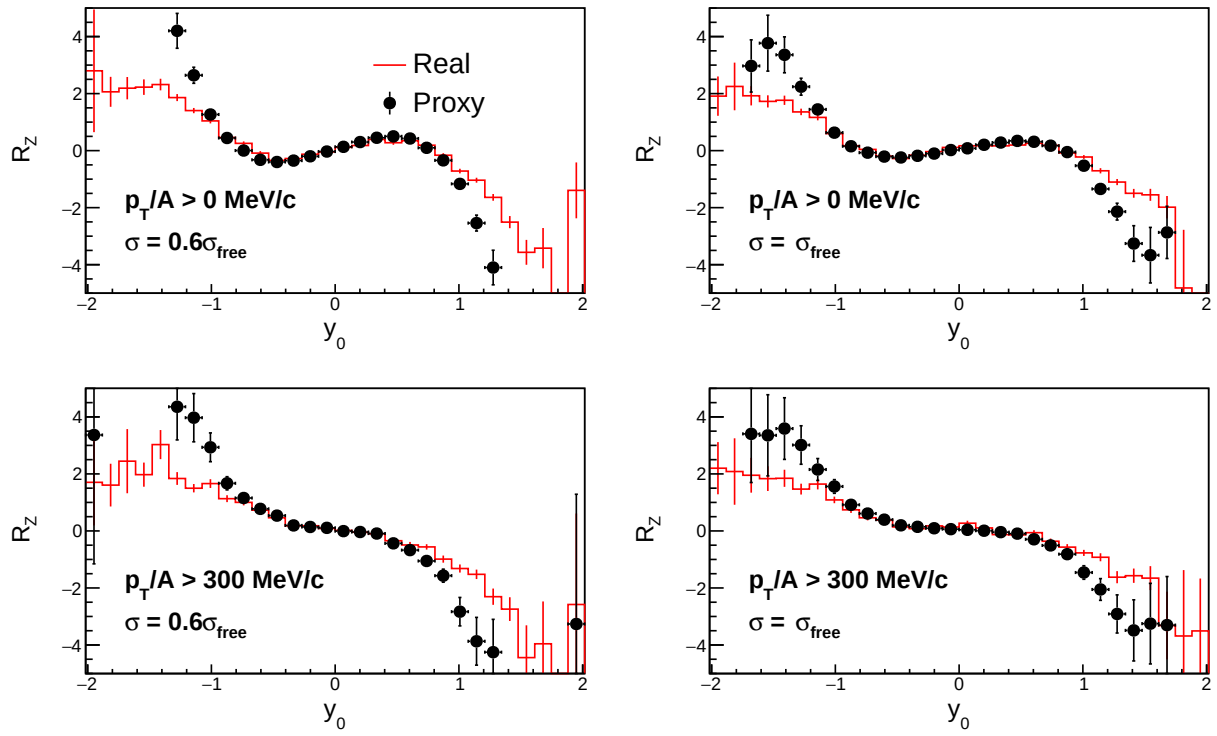

Figure 4.12: Isospin tracing from dcQMD with different parameters. Top left: $p_T/A > 0\,\mathrm{MeV/c}$ and $\sigma = 0.6\sigma_{\mathrm{free}}$. Top right: $p_T/A > 0\,\mathrm{MeV/c}$ and $\sigma = \sigma_{\mathrm{free}}$. Bottom left: $p_T/A > 300\,\mathrm{MeV/c}$ and $\sigma = 0.6\sigma_{\mathrm{free}}$. Bottom right: $p_T/A > 300\,\mathrm{MeV/c}$ and $\sigma = \sigma_{\mathrm{free}}$.

this dependence in the future.

In summary, we have demonstrated the viability of using Isospin Tracing on SπRIT data. Using proxies, R_z can be constructed despite the absence of experimental data for symmetric systems. A comparison between dcQMD predictions and experimental data reveals a possible momentum dependence of in-medium cross-section. Future studies are warranted to construct a comprehensive constraint on the in-medium effects.

4.6.4 Directed and elliptical flow

Fig. 4.14 shows the direct and elliptical flows for ^{108}Sn + ^{112}Sn and ^{132}Sn + ^{124}Sn reactions at mean impact parameter of 5.1 fm ($28 < M \leq 49$) and 5.2 fm ($31 < M \leq 49$) respectively. The methods used to determine collective flows of light fragments are identical to that of pions described in Section 4.5.4. Only $y_0 > -0.5$ are plotted due to limitations of detector acceptance. Figs. 4.14c

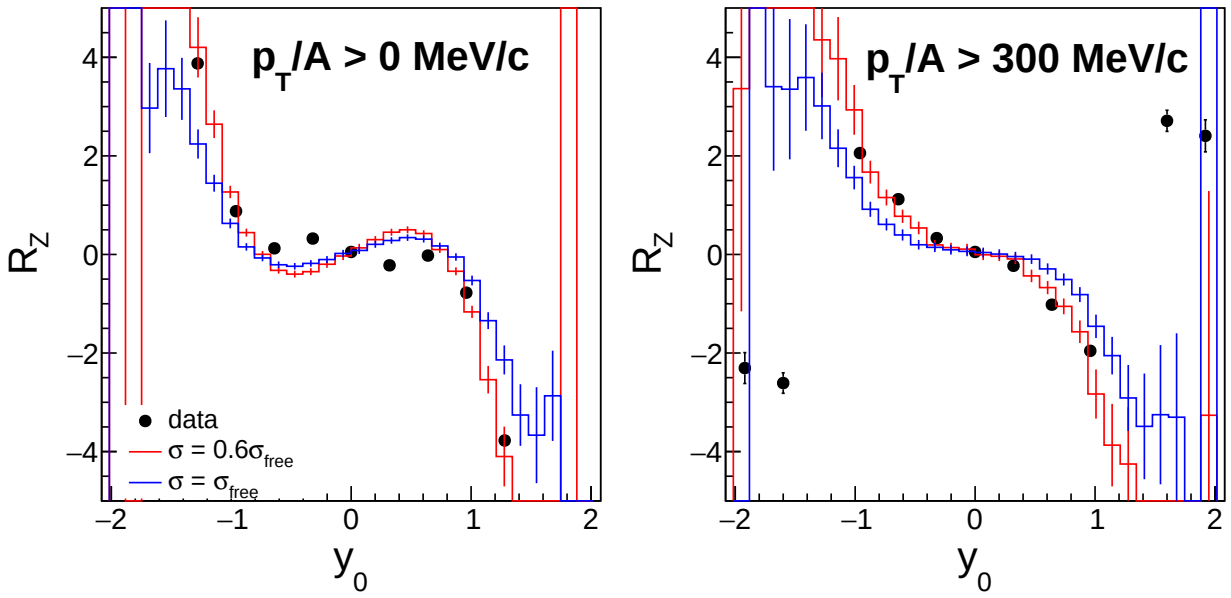

Figure 4.13: Isospin tracing from SπRIT experiment at $\langle b \rangle = 1$ fm. On the left no p_T/A cut is imposed and on the right $p_T/A > 300\,\mathrm{MeV/c}$ is imposed. The legend on the lower left hand corner on the left plot is also applicable to the right plot.

and 4.14d show v_1 as a function of p_T/A and are both gated on $0.2 < y_0 < 0.8$. The rapidity cut is imposed to increase sensitivity as it is observed that $v_1 \sim 0$ when $y_0 \sim 0$. Finally v_2 as a function of y_0 for the two systems are shown in Figs. 4.14e and 4.14f.

Direct and elliptical flows of light fragments are also influenced by the coalescence process. Similar to the construction of coalescence invariant proton spectrum, the results can be made less dependent on coalescence by summing proton contributions from all light fragments. The Coalescence invariant flow (C.I. flow) distributions are constructed by taking weighted average of cosines in Eq. (4.6) for all Hydrogen and Helium isotopes, with Helium isotopes weighted twice as much as hydrogen isotopes. Fig. 4.15 shows C.I. flow for ^{108}Sn + ^{112}Sn and ^{132}Sn + ^{124}Sn reactions.

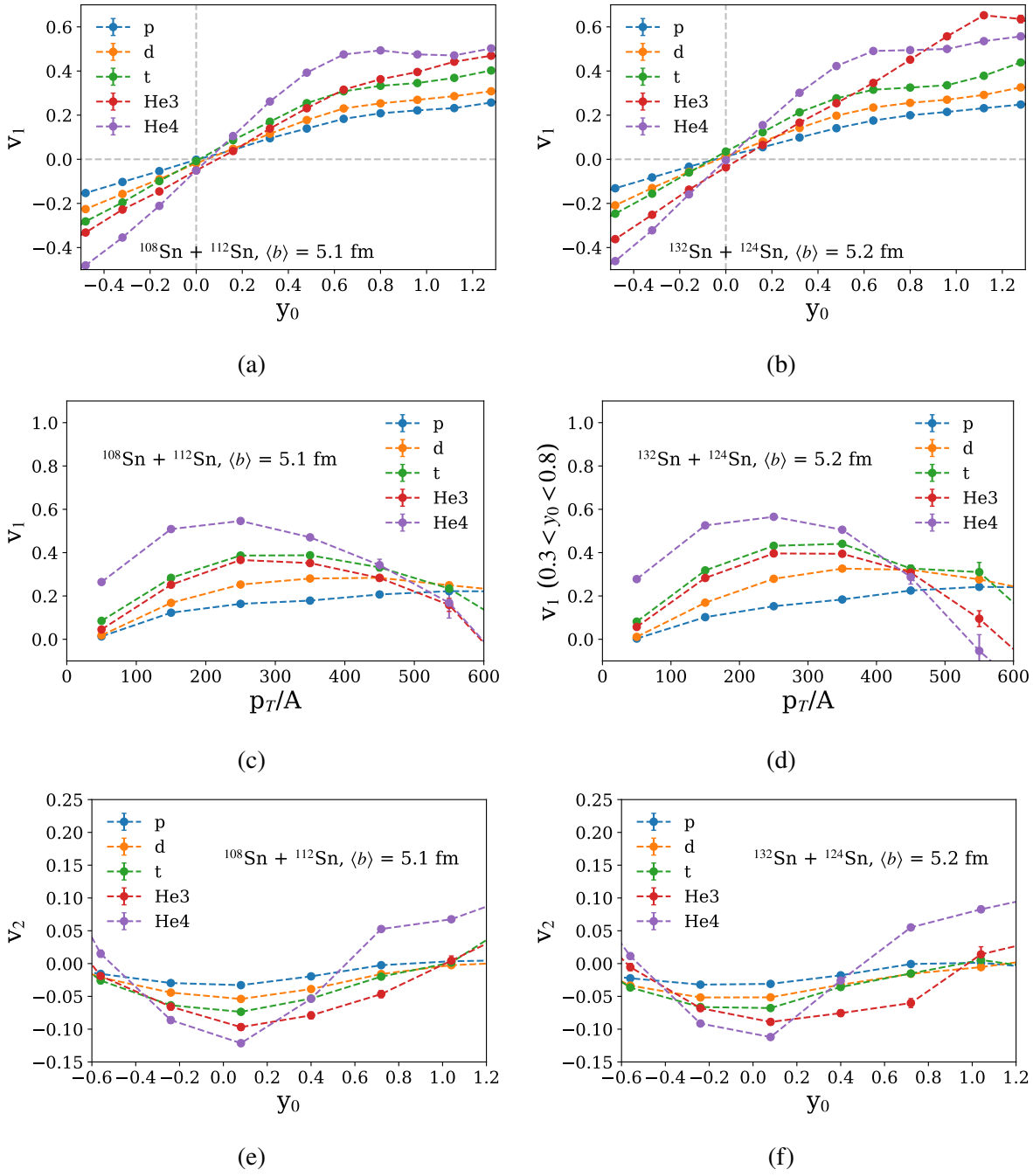

Figure 4.14: (a): Directed flow v_1 for ^{108}Sn + ^{112}Sn reaction plotted as a function of y_0 at mean impact parameter of 5.1 fm. (c): Directed flow v_1 for ^{108}Sn + ^{112}Sn is plotted as a function of p_T/A and gated on $0.3 < y_0 < 0.8$. (e): Elliptical flow v_2 as a function of y_0 for ^{108}Sn + ^{112}Sn. (b), (d) and (f) are the same as (a), (c) and (e) respectively but with results from ^{132}Sn + ^{124}Sn, all at mean impact parameter of 5.2 fm.

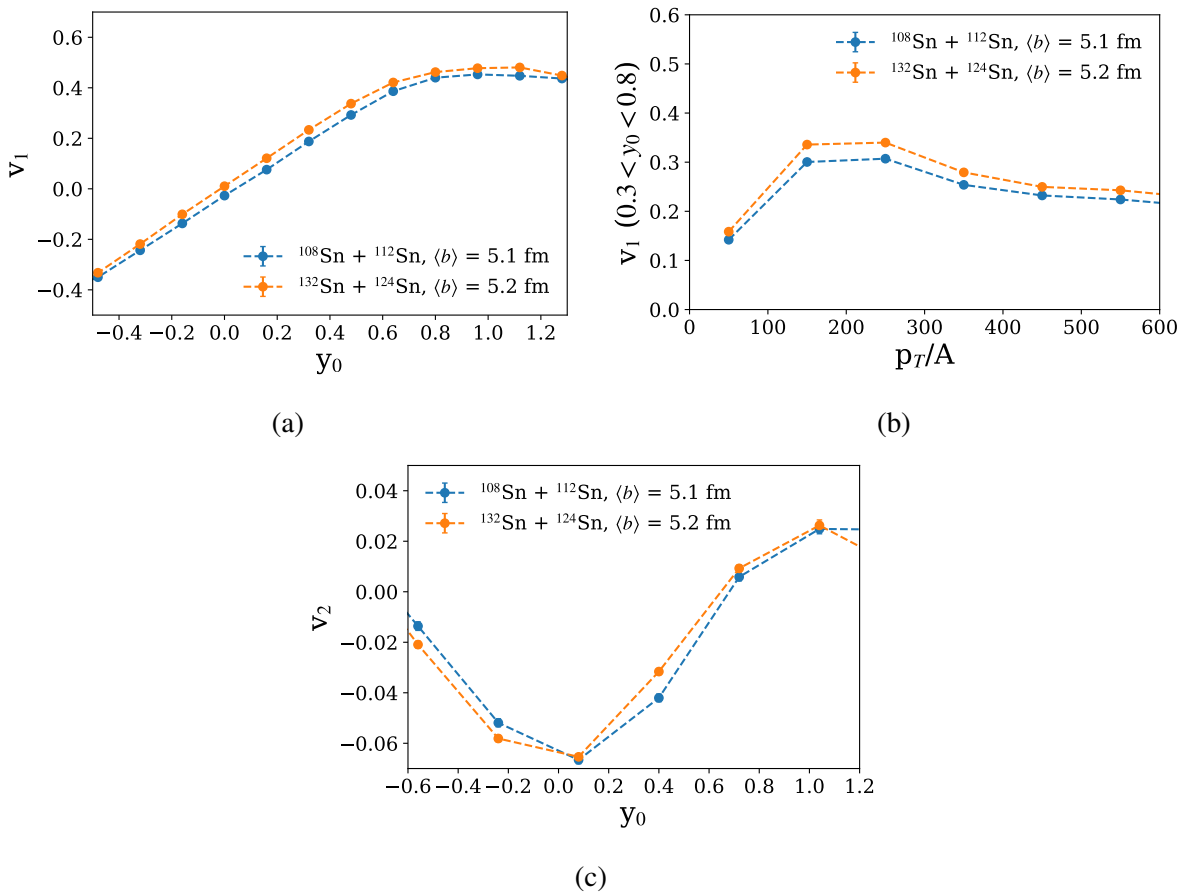

Figure 4.15: (a): Coalescence invariant directed flow v_1 as a function of rapidity. (b): Coalescence invariant directed flow v_1 as a function of transverse momentum p_T, gated on $0.3 < y_0 < 0.8$. (c): Coalescence invariant elliptical flow v_2 as a function of rapidity.

CHAPTER 5

MONTE CARLO SIMULATION

5.1 Introduction

The goal of an experiment is to extract knowledge on the physical world by comparing measured results with theoretical predictions. This comparison is complicated by the fact that detector resolutions, inefficiencies and aberrations often skew the observed results. It is imperative that the impact of detector effects be understood to ensure the validity of the reconstructed values. This can be achieved with Monte Carlo (MC) simulation.

MC simulation for SπRIT TPC is developed as a part of SπRITROOT framework. It incorporates known detector effects to generate electronic signals from event generators. The signals can be analyzed as if they are experimental data. Due to the stochastic nature of the physical processes, simulation needs to be repeated multiple times to understand the average performance of the TPC.

MC simulation routine follows a task-based sequential pipeline structure, similar to that of data analysis routine in Section 3.2. The routine consists of 7 tasks which in the order that they are presented below.

5.2 Geant4 Virtual Monte Carlo

The first task, "Geant4 Virtual Monte Carlo", uses Geant4 (version 10-02-patch-01) to simulate the interaction between detector material and the particle fragments. The geometry and material of as well as magnetic field map in SπRIT TPC are taken into consideration. Geant4 simulation covers most of the important physical processes in particle-gas interaction, like particle transport, energy loss, multiple scattering and particle decays [164]. This task outputs the amount of energy loss in keV/cm and the location of interaction (x, y, z).

5.3 Space Charge Task

In Section 3.3.2, we showed two issues in experimental data that are caused by the space charge effect. To recap briefly, the first issue is the fact that the peak location of ΔV_x distribution of beam left particles differs from that of beam right particles. The second is the fact that center of mass momentum distribution of beam left and beam right particles are not in agreement with each other when they should be due to cylindrical symmetry arguments.

Here we will try to recreate these issues by distorting the Monte Carlo hit points with space charge effect without correcting for it during track reconstruction. It serves as a confirmation that space charge effect distorts detector measurements in ways that match our observation in the experimental data.

By integrating Eq. (3.1), the expected lateral displacement for each drift electron as it drifts toward pad plane can be calculated. Each MC interaction points will be displaced accordingly. Unlike in the correction for experimental data where the sheet charge density (σ_{SC}) is a measured quantity, we are free to choose its value in simulation. All simulations in this sub-section will be performed with an ad-hoc value of $\sigma_{SC} = 4 \times 10^{-8}\,\mathrm{C/m^2}$, which is approximately the average σ_{SC} of all runs in ^{132}Sn + ^{124}Sn reaction.

As stated previously, the two main features of space charge effect are disagreement of momentum distributions in Fig. 3.7 and peak locations of ΔV_x distributions in Fig. 3.8b between left-going tracks and right-going tracks. With space charge distortion included in MC simulation and space charge correction disabled in track reconstruction, both features can be reproduced in Figs. 5.1a and Fig. 5.1b.

The space charge simulation procedure can also be used to simulate leakage space charge, first described in Section 3.3.3. The only modification needed is to include the geometry and charge density of the leakage sheet in electric field calculation. Experimental data shows that leakage sheet charge density is 9.8 times the normal beam space charge density, so the leakage charge density in the simulation is set to $9.8\sigma_{SC} = 3.92 \times 10^{-7}\,\mathrm{C/m^2}$. After the inclusion of leakage charge, results from Monte Carlo simulation exhibit inconsistencies in reconstructed Triton momentum in

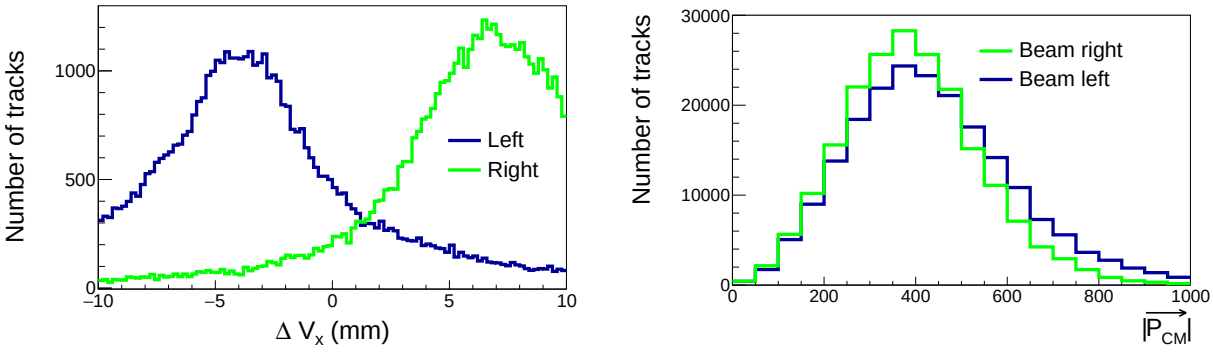

(a) (b)

Figure 5.1: (a): x-component of distance to vertex on target plane distributions. (b): Center-of-mass momentum distributions. Both distributions are populated with simulated data after the inclusion of space charge effect. Cut conditions are identical to what is being used in Fig. 3.7 and Fig. 3.8b.

ways that are similar to what is being observed in experimental data. Simulated Triton momentum distributions inside the three azimuth cuts of Fig. 3.13b are plotted in Fig. 5.2. To recap the cut conditions, cut 1 corresponds to $74^\circ < \phi < 132^\circ$, cut 2 corresponds to $-29^\circ < \phi < 29^\circ$ and cut 3 corresponds to $-86^\circ < \phi < -143^\circ$. On top of the azimuth cuts, a polar angle cut of $6^\circ < \theta < 12^\circ$ is imposed on all three cuts. Simulated results with leakage charge simulation show that the momentum distribution in cut 3 disagrees with that in cuts 1 and 2, just like results from data. The dependence of Triton consistency on z-threshold, first shown in Fig. 3.16b for experimental data, is roughly recovered in simulation in Fig. 5.3.

5.4 Drift task

The "Drift task" then converts the interaction points to secondary ionized electrons. The amount of electrons N_e- created in an interaction is described by the following equation,

$$N_e- = \frac{\Delta E}{I}, \tag{5.1}$$

where ΔE is the energy loss from Geant4 task and I is the ionization coefficient of P-10 gas, which is 26.2 eV. Electrons frequently collide with gas molecules and diffuse as they drift upward,

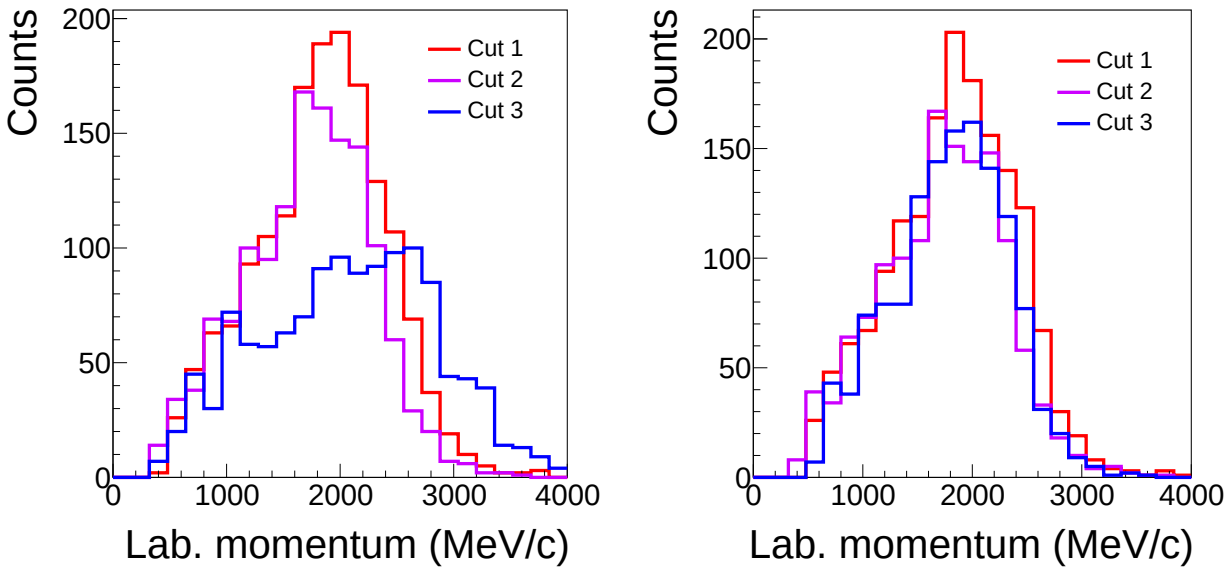

(a) (b)

Figure 5.2: Simulated Triton momentum distributions with the three azimuth cuts. (a): Momentum distributions when "leakage" space charge is simulated. (b): Momentum distributions when "leakage" space charge is not simulated.

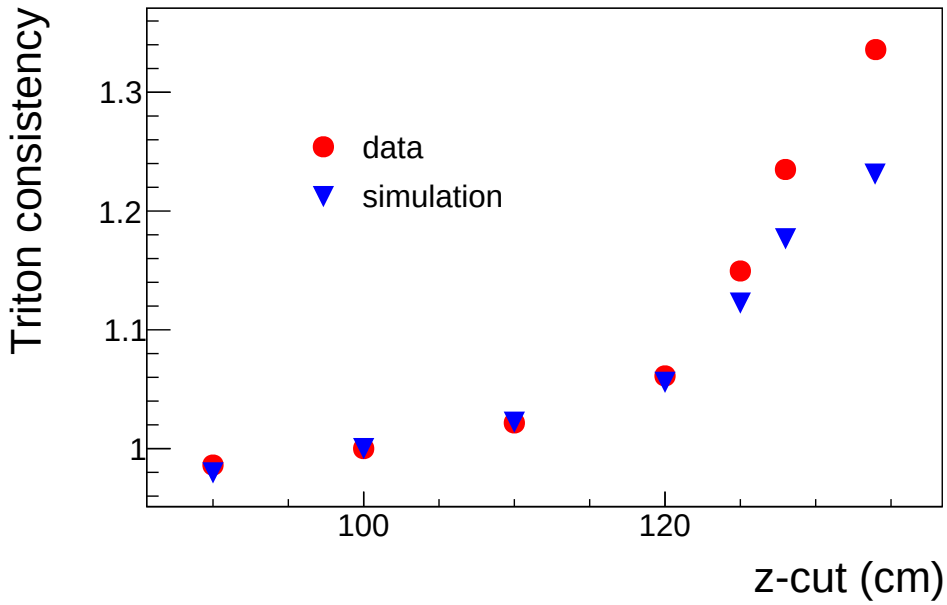

Figure 5.3: Triton consistency from Monte Carlo simulation (blue inverted triangle) that includes leakage charge effect and experimental data (red circle). Both shows a sharp increase in values beyond z-cut = 120 cm.

therefore each secondary electron is displaced by a random vector $\vec{\Delta r}$. The random vector is sampled from the following random distribution,

$$\Delta r_i \sim \text{Gauss}(0, c_i\sqrt{L}). \tag{5.2}$$

In this equation, L is the vertical distance between interaction point and the anode wires and i is the component index which can either be t, the transverse direction or l, the longitudinal direction relative to fragment trajectory. c_i represents the diffusion coefficient along the two directions, whose values are $c_t = 240\,\mu\text{m/cm}^{1/2}$ and $c_l = 340\,\mu\text{m/cm}^{1/2}$ according to Garfield++ calculation [165].

5.5 Pad Response task

The "Pad Response task" calculates the signal amplitude for each pad. Due to the spread of avalanche electrons in the anode wires, some pads that are not directly over but near the secondary electrons will also register signals with reduced amplitudes. It is found that signal amplitude depends on the horizontal displacement between electron and the pad as a two-dimension Gaussian function, whose width depends on trajectory angle. The width as a function of trajectory angle is determined empirically [102]. For each secondary electron from the drift task, this empirical function is used to distribute signals amplitude on different pads.

5.6 Beam Saturation task

Most incoming beam particles do not react with target foil and pass through the TPC detection volume unimpeded. Even when collisions occur, most of them are peripheral as geometric cross-section of peripheral event is larger than that of central event. In most peripheral collisions, projectile nucleus is not broken up effectively which results in heavy residues with high atomic number. When the highly charged particles from either un-reacted beam or heavy residues interacts with detector gas, they create large amount of electrons and saturate TPC pads when those electrons enter the wire plane. Therefore hit points directly below the projectile trajectory are not recorded. Furthermore, some pads that were saturated in previous events may not have time to recover when

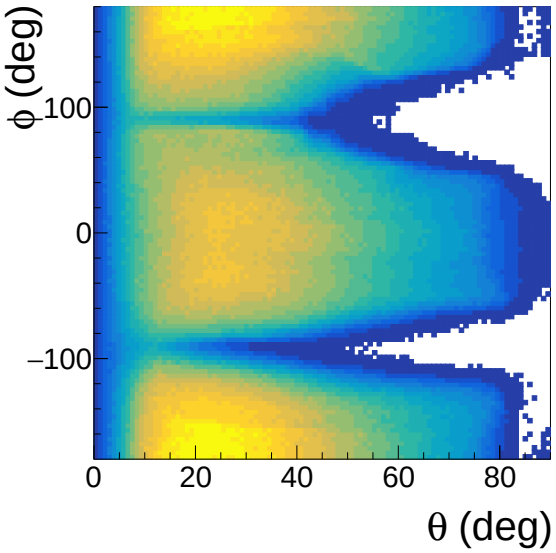

Figure 5.4: ϕ vs. θ for protons. It is similar to Fig. 3.24, but here no clusters cut are applied.

the next collision event occurs. Those pads will be unresponsive for the entire duration of some events. The purpose of Beam Saturation task is to simulate such saturation modes.

The effects of this saturation mode can be seen in Fig. 5.4 which shows the ϕ vs. θ (phase space) distribution for protons in laboratory frame. The creases at $\phi \approx \pm 90^{\circ}$ (particles that moves directly on top or below the projectile trajectory) demonstrate the inefficiencies created by the saturated of pads by heavy residues. To accentuate beam saturation at large polar angle, no cut is set on number of clusters and only distance to vertex cut of < 15 mm is applied.

The naive approach to simulate beam saturation is to include heavy-fragments in event generator. Although pad saturation is normally handled by MC simulation without needing a dedicated beam saturation task, this approach will not work for beam saturation as it suffers from performance and memory issues. Heavy-fragments spawn orders of magnitude more ionized electrons than light fragments due to its high electric charge. Since each electron is simulated individually in drift task, this approach consumes a lot of computational powers. It crashes the simulation on our available computer hardware due to excessive memory consumption.

As a result, empirical approach where pads are saturated randomly according to some given

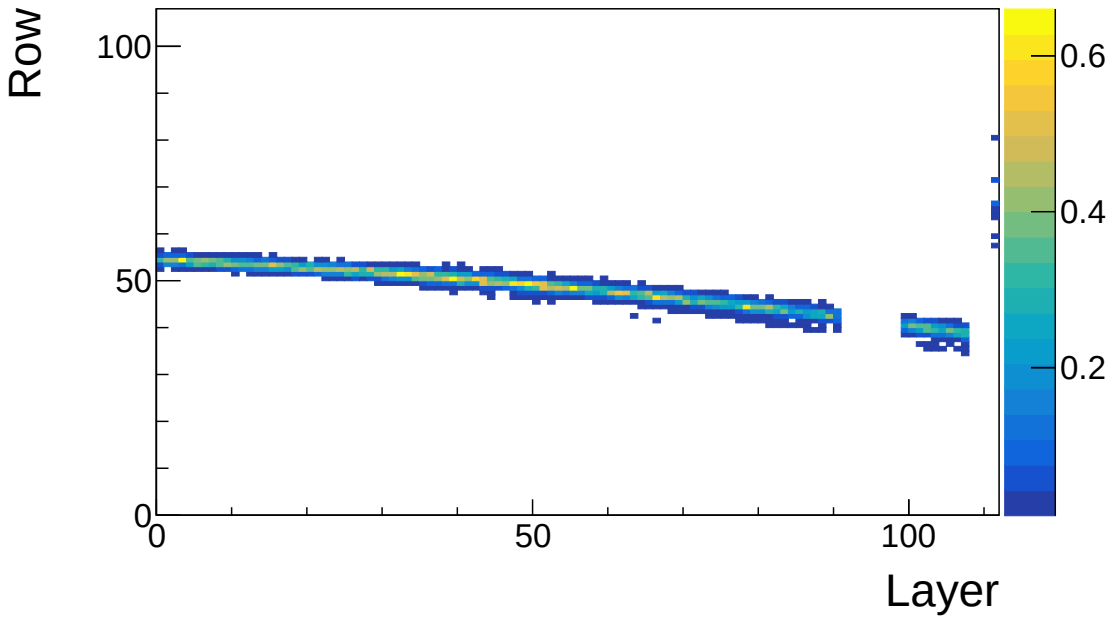

Figure 5.5: The unresponsive event fraction for each pad. It follows the beam trajectory. The color scale on each pixel corresponds to the fraction of total experimental events where the pad is completely unresponsive. White pixels represent pads that are never saturated at the beginning of any events.

probability distributions is preferred. The saturation effect of heavy-fragment is manifested in two ways which we called *complete beam saturation* and *normal beam saturation*. A pad suffers from complete beam saturation when it is unresponsive for the entire duration of an event. In normal beam saturation, the pad recovers and is responsive before secondary electrons from the heavy-fragment reach the pad plane. Both saturation modes are needed to accurately reproduce the observed creases.

To simulate complete beam saturation, we tabulate the experimental fraction of events for each pad where it is unresponsive from the beginning of an event. This unresponsive event fraction for each pad is visualized in Fig. 5.5. The empirical fraction is used as probability for each pad to be saturated randomly at the beginning of each simulation event.

To simulate normal beam saturation, we register an extraordinarily large signal amplitude to pads directly on top of the projectile track in the time bucket that corresponds to height of the

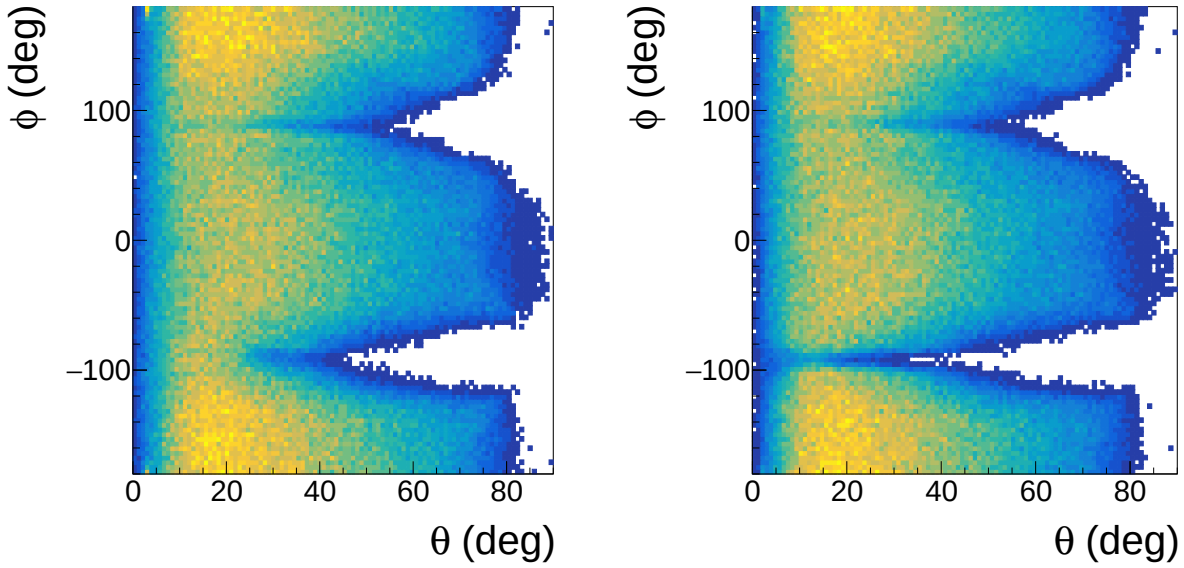

(a) (b)

Figure 5.6: ϕ vs. θ distribution of simulated protons when (a): only dead pads are simulated, (b): both dead pads and normal beam saturation are simulated.

beam. This direct injection of saturation signal circumvents the need to simulate electrons in drift task. This algorithm do not capture all the physics of heavy residues, but it is accurate enough to reproduce the creases in Fig. 5.4.

Fig. 5.6a shows phase space distribution of simulated protons when only complete beam saturation is applied. Although creases appear, the one at $\phi = -90^\circ$ is not deep enough when compared to experimental result. After normal beam saturation is also enabled, a deeper crease is observed at $\phi = -90^\circ$ in Fig. 5.6b. This indicates that both saturation modes are present in the experiment.

5.7 Electronic task

The "Electronic task" converts signal amplitudes from Pad Response tasks into electronic pulses. The pulses are stored as analogue-to-digital (ADC) readings at different time buckets. Since pulse shape does not vary significantly from pulse to pulse apart from its height, a standard template pulse shape can be extracted empirically. Electronic task takes this template pulse, scales

its height according to signal amplitude and displaces its start time bucket to give the simulated pulse [7]. If there are more than one interaction point below a pad, pulses from those interactions are superimposed to form a complete pulse. If total pulse amplitude exceeds the dynamic range of ADC, a template pulse which corresponds to saturated signal will be appended at the saturation time. All signals beyond saturation time will be discarded.

5.8 Trigger task

Trigger conditions lead to biases due to their tendency to disproportionately rejects certain type of events. Previous studies have demonstrated that event acceptance decreases with increasing impact parameter [166]. To estimate and understand the effect of trigger conditions, simulation of triggers are implemented. Here the simulated triggers will be described and simulated results will be compared to experimental data.

The geometry and material of KATANA and KYOTO trigger arrays are imported into Geant4 Virtual Monte Carlo task, which allows for the interaction between fragments and the triggers to be simulated. It is possible to convert energy loss in KATANA veto bars and KYOTO arrays into simulated electronic pulses, but since we are only interested in studying the qualitative effects of trigger bias, approximations can be made to reduce complexities in analysis and simulation. To begin with, the electric charge of heavy-residue is not calculated from energy loss amplitude in KATANA veto bars, rather the exact charge Z of fragments that passes through KATANA veto bars is saved to files. Similarly, the energy depositions in KYOTO arrays will not be converted to electric signal. Any energy deposition inside a KYOTO bar counts as a hit and the total number of KYOTO bar being hit is saved to disk. This approximation is reasonable as KYOTO efficiency is measured to be about 99% [166].

To simulate nuclear dynamics, events are generated from Ultra-relativistic Quantum Molecular Dynamic (UrQMD) for ^{132}Sn +^{124} Sn reactions at 270 MeV/u with soft EoS of Ref. [146]. This model is chosen due to availability of its result across a wide range of impact parameters in our analysis group. The same data set is re-used in Section 5.9.3 for the training of machine learning

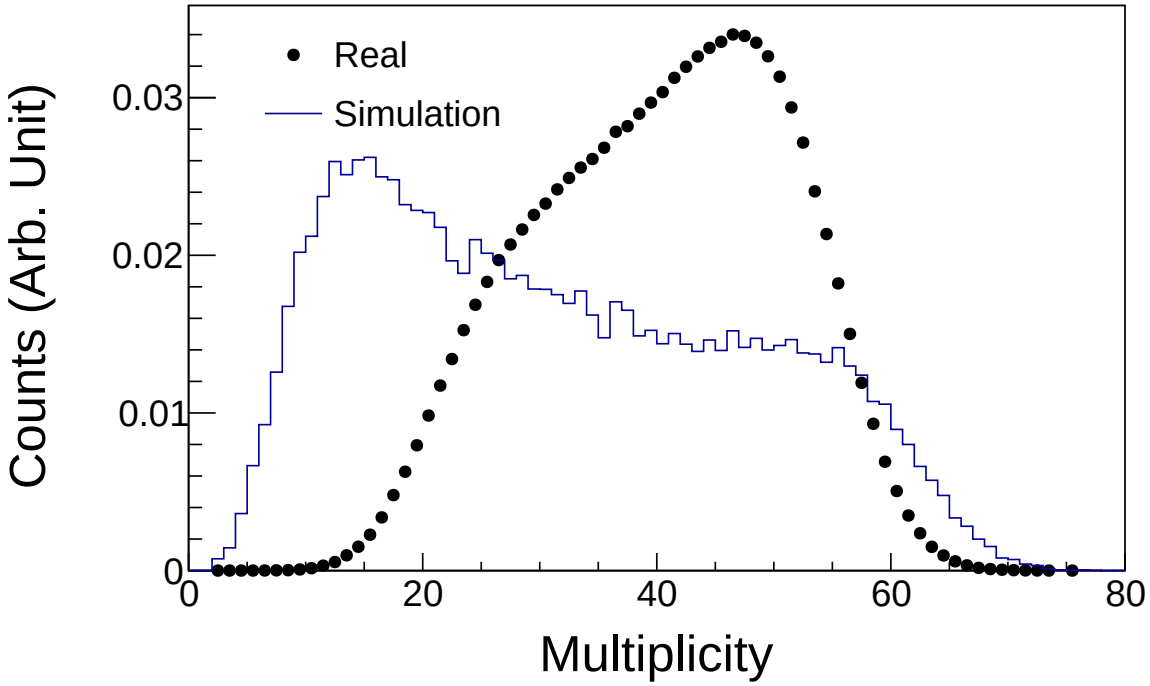

Figure 5.7: *Simulated* multiplicity distribution (blue line) and *real* multiplicity distribution (black circle points). The curves are normalized to unit area.

algorithm. The impact parameter distribution follows the geometric cross-section $d\sigma = 2\pi b db$ from $b = 0 - 10$ fm. These events are converted to electronic signals using SπRITROOT and are reconstructed with tracking algorithms, identical to what is being done with experimental data. The multiplicity distribution of the reconstructed UrQMD simulation will be referred to as *simulated* multiplicity distribution whereas that of experimental data will be referred to as *real* multiplicity distribution. For comparison, both real and simulated multiplicity distributions are normalized to unit area in the following discussions.

The simulated multiplicity distribution without any trigger conditions is plotted in Fig. 5.7 as the blue histogram. The steep rise at low multiplicity reflects the fact that cross-section increases with impact parameter. In contrast, the real distribution (black circle markers) shows a suppression of low multiplicity events due to trigger conditions.

When trigger conditions are applied, the simulated distribution resembles real distribution

better. The blue curve in Fig. 5.8 is drawn with trigger conditions set to KYOTO hits ≥ 4 and KATANA $Z \geq 20$, identical to what was used in SπRIT experiment. On the high multiplicity (≥ 50) side, there are more events in simulation than data, but that is most likely caused by inaccuracies in clusterization of UrQMD rather than problems with trigger simulation. It is well-known that UrQMD, like other similar QMD type models, over predicts light fragment yields [154]. This was discussed in Chapter 4 when transport models were introduced.

On the low multiplicity side (≤ 40), the simulated distribution underestimates the yield of peripheral events. This is also caused by inaccuracies in clusterization process: if the Z distribution of heavy residues is inaccurate, the events rejected by KATANA simulation will not reflect the event selection bias accurately. To compensate for this, the KATANA charge threshold in simulation is raised from ≤ 20 to ≤ 35. This new threshold is chosen such that low multiplicity side of the simulated multiplicity distribution matches with real distribution. The red histogram in Fig. 5.8 shows simulated multiplicity distribution after the charge threshold is raised.

To conclude, the shape of multiplicity distribution depends strongly on the trigger conditions. We have reproduced the approximate shape of multiplicity distribution with trigger simulation. The remaining differences between simulation and data can be attributed to inaccuracies in UrQMD and the rough implementation of trigger simulations. Hopefully with advancements on nuclear models, the agreement between data and simulation can be improved.

5.9 Application of Monte Carlo Simulation

One of the important applications of MC is *embedding efficiency determination*. Simulation is used to generate electric pulses of SπRIT TPC for a single particle. Those pulses will be added to pulses from experimental events in a process called *embedding*, and the embedded events will be analyzed with SπRITROOT. The fraction of events in which SπRITROOT successfully identifies the embedded particle is the efficiency of the detector. This technique is also used in STAR TPC [167].

Another application is to use Monte Carlo events for *Closure testing*, where analysis routine

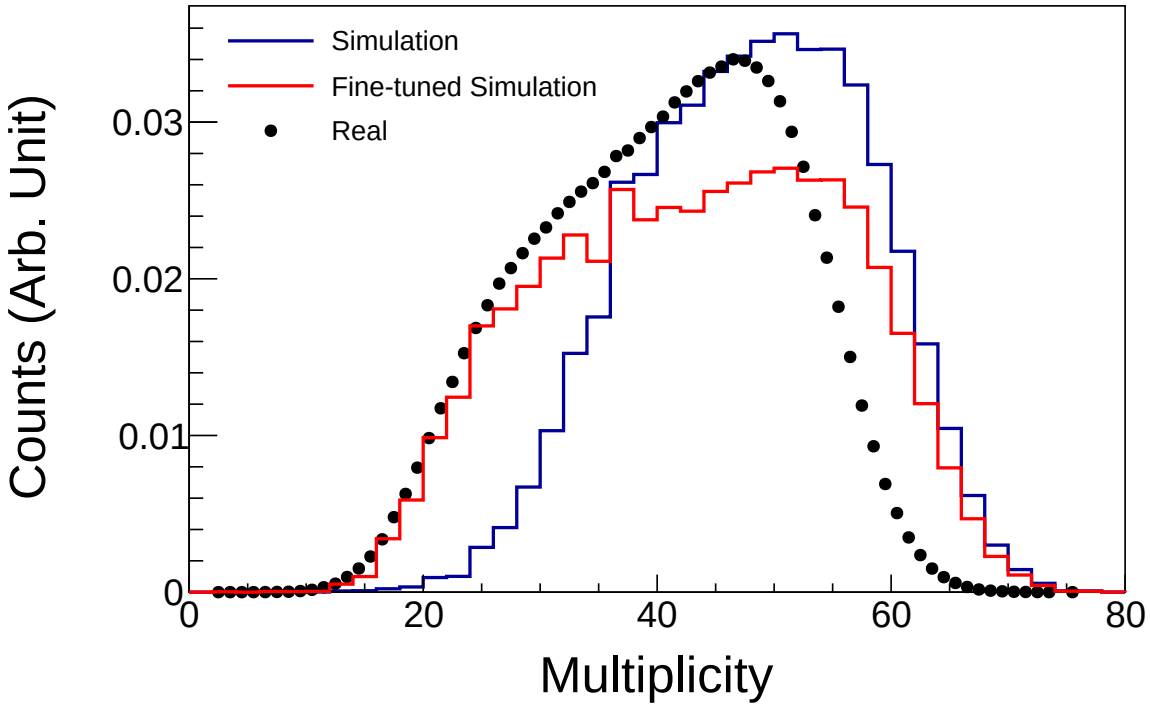

Figure 5.8: *Simulated* multiplicity distribution (blue line) and *real* multiplicity distribution (black points). The curves are normalized to unit area.

reconstructs Monte Carlo data as if it is experimental data, and the extracted observable values will be compared to the true values of event generator. This step is essential in demonstrating the validity and precision of the analysis routine, as well as revealing any potential issues the analysis may have missed.

The Monte Carlo routine was developed after the 2016 SπRIT experiment. The code will be useful for future experiment planning . The effects of any modifications to the detector can also be studied in advance. Similar strategy has been used by other experiments for *Detector Design and Optimization* and *Software and Computing Design and Testing* [168].

In this chapter, the various applications of Monte Carlo simulation in SπRIT experiment will be reviewed.

5.9.1 Efficiency calculation with track embedding

Embedding is a special type of Monte Carlo simulation, used mainly for detector efficiency calculation. If we only consider single track events, efficiency can be calculated without the need for special embedding techniques. It is simply the amount of reconstructed tracks divided by that of initial tracks.

However, real events are rarely single track events. The multiplicities of some SπRIT events are often close to 50. Detector efficiency depends on particle distributions due to varying degree of saturation or overlapping of electric pulses. If we want to calculate efficiency with ordinary Monte Carlo simulation (i.e. simulate all $\sim$ 50 tracks in an event and see how many are reconstructed), the events from event generator needs to accurately imitate real events. This is very hard to do, especially when there are many different correlations between particles that are not yet studied. On top of that, cosmic ray background which may affects the overall efficiency is also not being simulated.

Single track embedding is developed to overcome those difficulties. Instead of simulating the entire event, only one particle is simulated per event. The simulated signals will be added to signals of a real event, unless the pad it tries to embed onto is already saturated. The combined event is reconstructed and analyzed as normal event. The detector efficiency is the fraction of events where embedded tracks are correctly identified.

Special routine is developed to handle the pulse addition (embedding) and to identify the embedded tracks from all the other data tracks after track reconstruction. Fig. 5.9 shows a simplified flow diagram for the embedding procedure. For a track to be identified as the embedded track among all reconstructed tracks, it has to satisfy two conditions that quantify how similar the reconstructed track is to the initial MC track. The first condition is $N_{\mathrm{MC}} > 5$, the fitted track has to make use of at least 5 rows or columns of pad clusters from MC simulation. The second condition is $N_{\mathrm{MC}}/N_{\mathrm{total}} > 0.5$, at least half of the clusters used to reconstruct the track have to originate from MC simulation. If there are more than one track that satisfy all the similarity conditions, the one with the smallest distance to vertex is chosen.

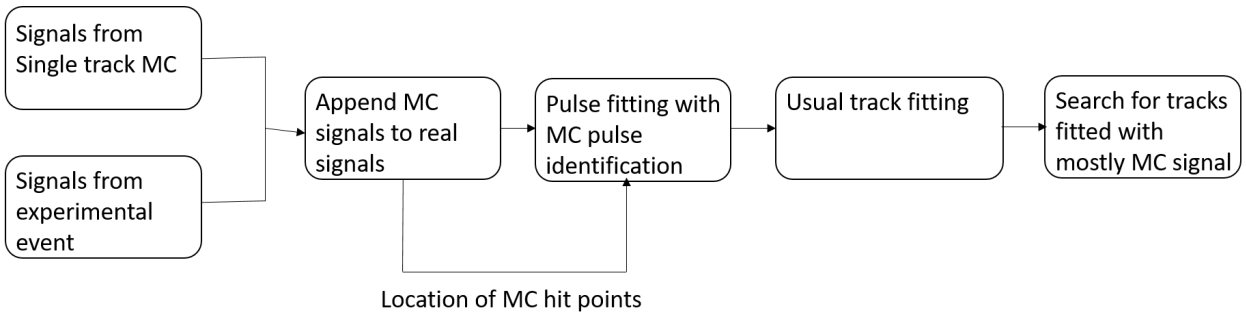

Figure 5.9: Flow diagram for the embedding software.

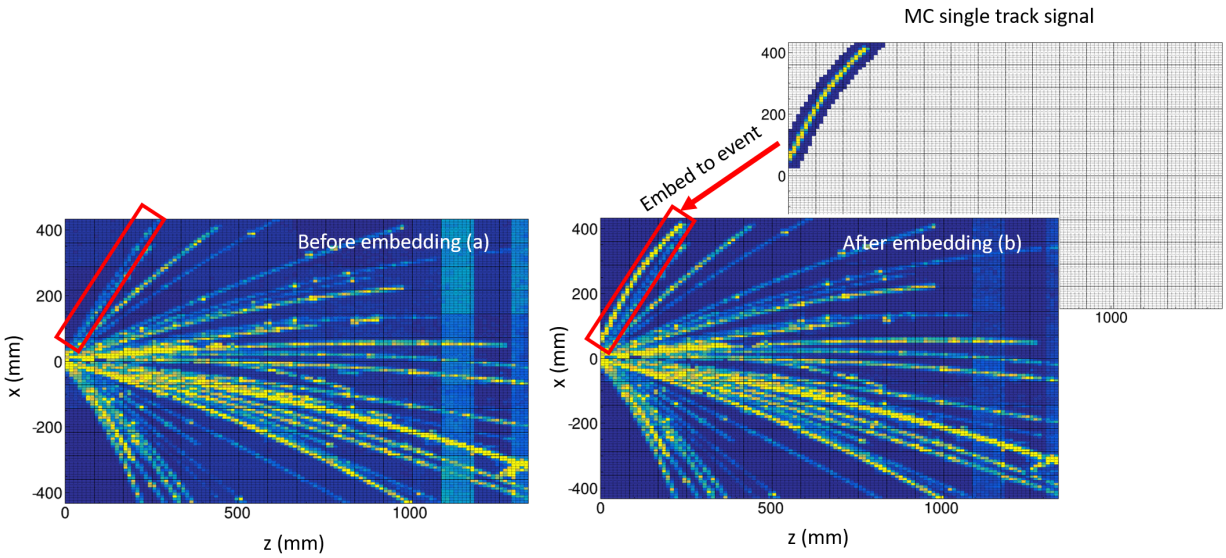

Figure 5.10: Top view of the hit pattern before (a) and after (b) embedding. The plot behind (b) shows signal generated by MC simulation.

Naturally this rises the question of how pad clusters from MC and data are differentiated. Clusters are designated as MC cluster if at least one electric pulse in a cluster originates from MC. The identification of MC pulses is done in Pulse shape analysis task in two steps: The first is to tag all pulses that satisfy following two criteria as "not MC pulse": $|(Q_{\mathrm{Exp}} - Q_{\mathrm{Exp+embed}})/Q_{\mathrm{Exp}}| < 0.05$ and $|t_{\mathrm{Exp}} - t_{\mathrm{Exp+embed}}| < 120\,\mathrm{ns}$ where Q and t represent the charge and raise time of the fitted pulse respectively. The subscript "Exp" means fitted pulses of only experimental data and "Exp + embed" means fitted pulses of the embedded data. The second is to tag the all remaining pulses that satisfy $|t_{\mathrm{Embed}} - t_{\mathrm{Exp+embed}}| < 120\,\mathrm{ns}$ as MC pulses.

The average embedding efficiency for proton, Deuteron, Triton, ^{3}He and ^{4}He as a function

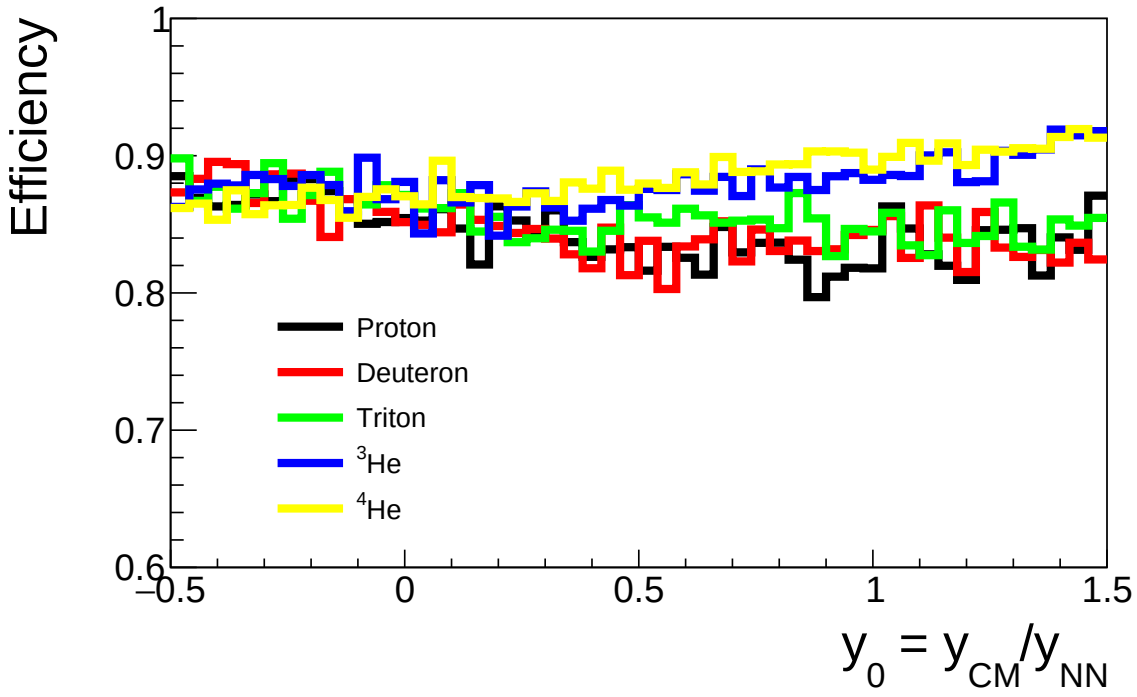

Figure 5.11: Average efficiency as a function of normalized rapidity y_0. The averaging is done over a transverse momentum values of $0 < p_T/A < 1000\,\mathrm{MeV/c}$.

of normalized rapidity $y_0 = y_{CM}/y_{NN}$ is plotted in Fig. 5.11. In the calculation of average efficiency, MC tracks are embedded onto events from ^{132}Sn + ^{124}Sn with multiplicity > 50. The averaging is done over p_T values of embedded tracks which are distributed uniformly within $0 < p_T/A < 1000\,\mathrm{MeV/c}$. The embedding tracks only occupy azimuth values within cuts in Table 3.1. It also considers track loss due to number of clusters and distance to vertex cut of Table 3.1 for light fragments. Only the dependence of efficiency on y_0 is plotted for brevity, but the dependence on both y_0 and p_T are used during efficiency unfolding in Chapter 3.4.3. The detection efficiency within the cuts are respectable as it is consistently larger than 80%. Note that efficiency loss due to PID selection is not taken into account, which contributes to further efficiency loss at negative rapidity.

5.9.2 Verification of data analysis pipeline

Although each step in our data analysis pipeline is tested vigorously, it remains to be seen if they can work in unison to reconstruct observables accurately. By analyzing data from Monte Carlo simulation of SπRIT TPC, major errors in the software could be caught by comparing the reconstructed observables with the *ground truth*, which is the expected observable values from the event generator. In this section, simulation always refers to the simulation of SπRIT TPC responses instead of QMD simulation.

Particle distributions are constructed in such a way that the expected observable values equal to some initial chosen values. These chosen values are called ground truth. Event generator will sample particles from the particle distributions, and these particles are simulated and reconstructed with SπRITROOT analysis framework. How close the reconstructed values are to the ground truth is by definition the accuracy of the analysis.

The experimental p_T vs. $y_0 = y_{CM}/y_{NN}$ distributions of proton, Deuteron, Triton, ^{3}He and ^{4}He for ^{112}Sn + ^{124}Sn reaction will be used as ground truth for event generator in the Monte Carlo simulation of SπRIT TPC to make sure that event generator imitates the behavior of real data reasonably. Heavier isotopes are not simulated because their yield is low and they are not studied in this thesis. Only distributions for ^{112}Sn + ^{124}Sn system are used because we have complete 4π solid angle coverage on that reaction (see Section 4.4). Due to computational limitations, only events with ^{112}Sn as the target and ^{124}Sn as the projectile are simulated. Since the accuracy and resolution of SπRIT TPC are intrinsic properties of the detector and do not depend strongly on reaction systems, our conclusion from ^{124}Sn + ^{112}Sn reaction can be applied to other reactions.

We first test the performance of rapidity distributions reconstruction. Accurate rapidity distributions are needed in reconstructing VarXZ and Coalescence invariant proton spectrum. The ground truth p_T vs. y_0 distributions come from data with centrality gate of $\langle b \rangle = 2.1$ fm ($M > 50$). The particle azimuth are assumed to be uniformly distributed for simplicity. It will be refined when collective flows are considered.

The simulated particles from event generator are converted to ADC pulses. These simulated

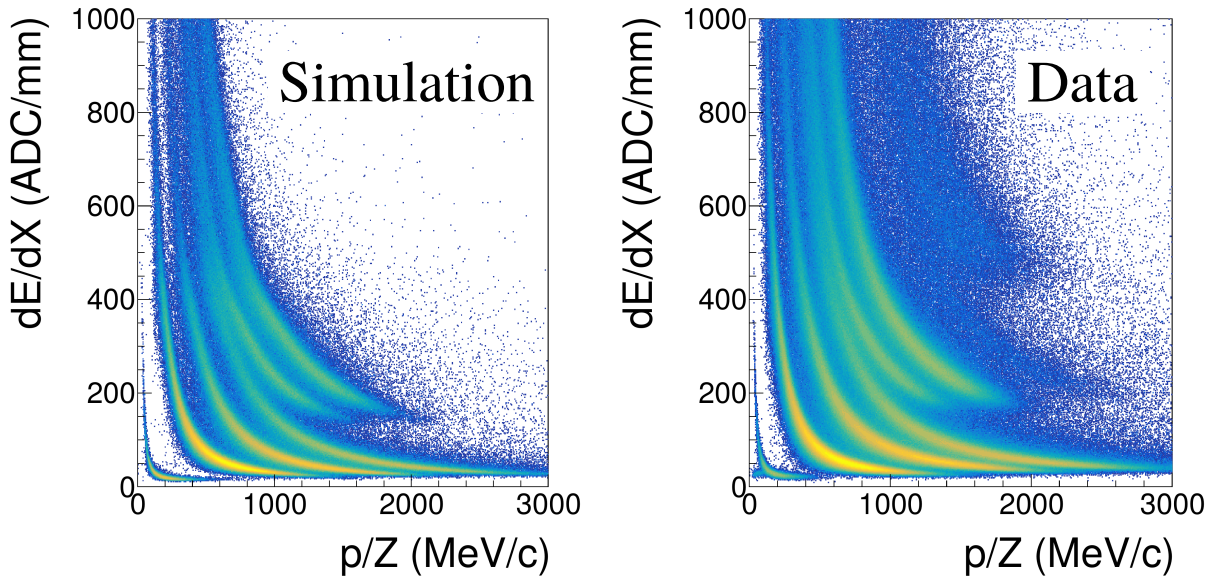

Figure 5.12: PID from simulation (left) and experimental data (right). Fragments heavier than ^{4}He are not simulated in the Monte Carlo. Aside from the missing heavy fragments in the left panel, the two look qualitatively similar.

pulses are treated as experimental data in the analysis pipeline. Cut conditions described in Table 3.1 are also used in the analysis of simulated data to keep the settings consistent. PID of simulated and experimental data are plotted side-by-side in Fig. 5.12 which shows that, at first glance, the two look very similar. However, the exact dE/dX values for each isotopes are slightly different and there are no PID lines for isotopes heavier than ^{4}He as they are not simulated in SπRITROOT. Furthermore, the amount of background junk tracks in real data differs from simulation which affects detector efficiency. The PID lines are refitted with simulated data as the shape of simulated PID lines is not identical to that of real PID lines and embedding efficiency is also recalculated with simulated event as the background for single tracks to embed onto.

The reconstructed rapidity distributions and true distributions for proton, Deuteron and Triton are plotted from left the right in that order in Fig. 5.13. Due to geometric coverage limitations of SπRIT TPC, particles with $y_0 < -0.6$ are poorly detected so only spectrum with $y_0 > -0.6$ are shown. The upper half of each subplot in Fig. 5.13 is the rapidity distribution, with red histograms being the ground truth and black solid circle being the reconstructed spectrum. The lower half is the ratio of ground truth over reconstructed spectrum, which is very close to the expected value.

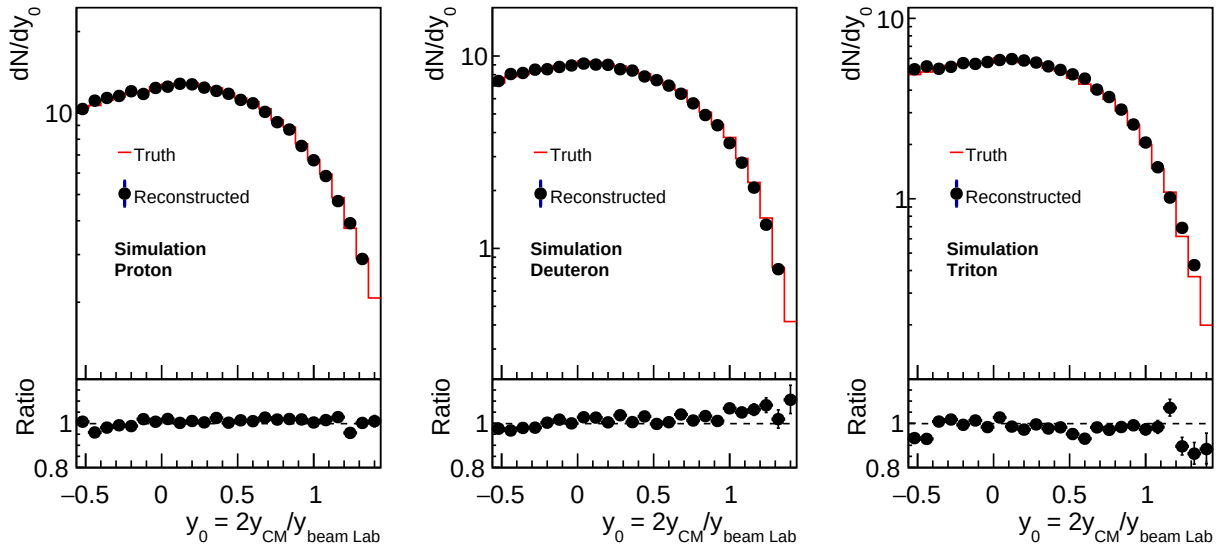

Figure 5.13: From left to right: Rapidity distributions of proton, Deuteron and Triton. The red lines correspond to the initial (true) distribution from event generator and the black points correspond to the rapidity distributions reconstructed with results from simulation of SπRIT TPC. The ratio plots on the bottom of every graphs show the ratio of the true distributions over reconstructed distributions.

This comparison verifies the data analysis procedure.

Next we test the performance of flow reconstruction. The p_T vs. y_0 distributions are extracted from data with centrality gate of $28 < M \leq 49$ which corresponds to $\langle b \rangle = 5.2$ fm. Flows are more prominent in mid-peripheral than central events. Additional steps are needed to generate collective flows from the event generator.

Let Φ be the reaction plane azimuth in laboratory frame, ϕ_i be the azimuth of the i^{th} particle in laboratory frame and v_{1i} be the ground truth directed flow value for particle i, we can define function $F(x)$ as,

$$F(x) = x + 2v_{1i} \sin x. \tag{5.3}$$

Although not explicitly stated in the formulation, v_{1i} does not need to be constant. It can be a function of y_0 or p_T of particle i. The desired flow can be generated if ϕ_i is being sampled as

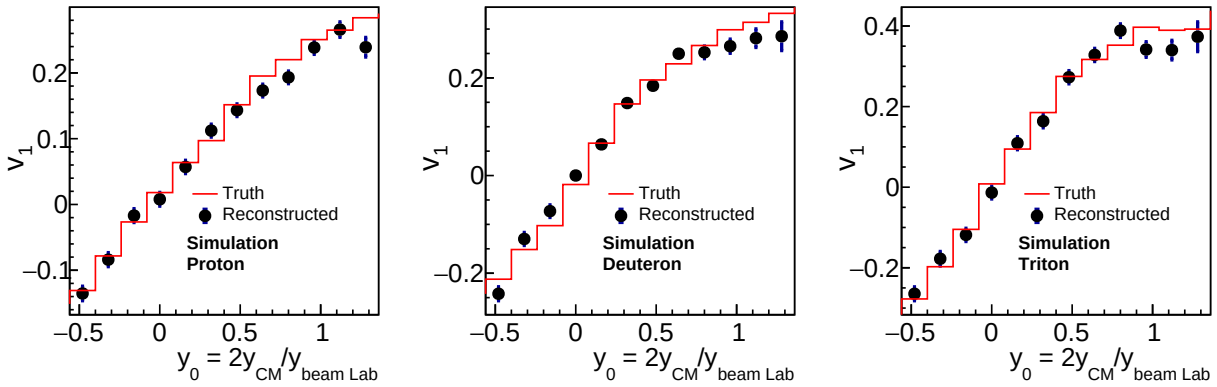

Figure 5.14: From left to right: Directed flow v_1 of proton, Deuteron and Triton as a function of y_0. The red lines correspond to the initial v_1 from event generator and the black points correspond to v_1 reconstructed with results from simulation of SπRIT TPC. The estimation of reaction plane angle with Q-vector or the estimation of reaction plane angle with sub-event method are re-calculated for simulated data.

follows,

$$\begin{gathered}\Phi \sim \mathcal{U}(0, 2\pi), \\ \phi_i = \Phi + \phi_i' + F^{-1}(\phi_i') \text{ where } \phi_i' \sim \mathcal{U}(0, 2\pi),\end{gathered} \tag{5.4}$$

where $\mathcal{U}$ is the uniform distribution and $F^{-1}(x)$ is the inverse of the function $F(x)$. In the following analysis, the ground truth v_{1i} follows the reconstructed v_1 vs. y_0 correlation from ^{112}Sn + ^{124}Sn at $\langle b \rangle = 5.2$ fm. The dependence of v_1 on p_T and any higher order flow term are not included in the ground truth for simplicity.

The simulated data is again analyzed as if it is real data. Azimuth efficiency, Fourier coefficients for acceptance correction and reaction plane resolution of real data cannot be used since flow distributions in the simulation are simplified not to include dependence on p_T and higher order terms. They need to be re-calculated "empirically" from the simulated data following the steps in Section 3.4.6. Fig. 5.14 shows that the reconstructed flow matches the true flow reasonably well.

5.9.3 Impact parameter determination with Machine Learning algorithm

The method of impact parameter determination using charged particle multiplicity in Section 4.4 will be referred to as *traditional method* in the following discussions.

Recent developments of machine learning (ML) algorithms demonstrated their potential in impact parameter determination. Ref. [146] specifically shows that with a perfect detector, algorithms based on Convolutional Neural Networks (CNN) and Light Gradient Boosting Machine (LightGBM) can be used to predict impact parameter of ^{197}Au + ^{197}Au collisions at various beam energies with simulated data generated from Ultra-relativistic Quantum Molecular Dynamics (UrQMD) model, and the prediction error is smaller than that from the traditional method.

With the development of Monte Carlo simulation for SπRIT TPC, such ML algorithms can be extended beyond perfect detector by providing realistic simulation of detector response. In this section, such algorithms will be developed and applied to real experimental data. A few key observables will be compared to gauge the quality of the impact parameter selection.

5.9.3.1 Machine Learning Algorithms

Ref. [146] shows that performance metrics of LigthGBM is slightly better than CNN with perfect detector, trained on events from UrQMD. Based on this, LightGBM is selected for this study. The training data set consists of 135,000 UrQMD ^{132}Sn +^{124} Sn events at $E/A = 270$ MeV distributed uniformly between $b = 0 - 10$ fm. The reaction is chosen to align with the experimental settings of the SπRIT experiment. UrQMD is configured to use the parameter set "SM-F", in which the compressibility $K_{\mathrm{sat}} = 200$ MeV and the nucleon-nucleon elastic scattering cross-section in free space is used as the in-medium cross-section.

Following Ref. [146], the following seven observables are chosen as features for the algorithm to infer impact parameter: (i) Total multiplicity of charged particles. (ii) Transverse kinetic energy of hydrogen and helium isotopes. (iii) Ratio of total transverse-to-longitudinal kinetic energy. (iv) Total number of hydrogen and helium isotopes. (v) Averaged transverse momentum of hydrogen and helium isotopes. (vi) Number of free protons at mid-rapidity $|y_z/y_{beam}| \leq 0.5$.

(vii) Averaged transverse momentum of free protons at mid-rapidity $|y_z/y_{beam}| \leq 0.5$.

Mean deviation (Bias) and standard deviation (S.D.) of the predicted impact parameter will be used to quantify the quality of the algorithm. Intuitively, bias and S.D. corresponds to accuracy and precision, respectively, and are defined as:

$$\begin{aligned} \text{Bias } (b^{\text{pred}}) &= \overline{b^{\text{pred}} - b^{\text{true}}} \\ \text{S.D.} &= \sqrt{\text{Var } (b^{\text{pred}} - b^{\text{true}})}. \end{aligned} \tag{5.5}$$

b^{true} is the true impact parameter used in event generation and b^{pred} is the predicted impact parameter from the LightGBM analysis. To study the performance as a function of impact parameter, events are binned according to their b^{true} values. The averaging is done over all events in the same bin.

5.9.3.2 Results on simulated events

Fig. 5.15 shows bias (left panel) and S.D. (right panel) as a function of impact parameter (b^{true}). LightGBM is used to train and test on two data sets: one includes the response of the SπRIT experiment (open red circles) and one without (blue solid stars). Both the training and the testing data sets use the same UrQMD input parameter set of SM-F. As expected both bias and S.D. worsens with the inclusion of detector response, especially in the mid-peripheral regions. Around b=3 fm, both bias and S.D. worsen by a factor of 2 when detector response is included. The worsening in bias and S.D. even when detector response is not included could be related to the physics details of transport models. In central collisions (small b), nucleon-nucleon scatterings dominate in the collision dynamics while in peripheral collisions (large b), the mean field dominates. In the mid-central or mid-peripheral regions (b=3-5 fm), accurate treatment of both the mean-field and collisions are very important but transport models may fall short.

The black inverted triangle represent results from traditional method. The cumulative multiplicity distribution for traditional method is constructed by sampling the training data set randomly with geometric cross-section $d\sigma = 2\pi b db$. In general, traditional method performs worse than

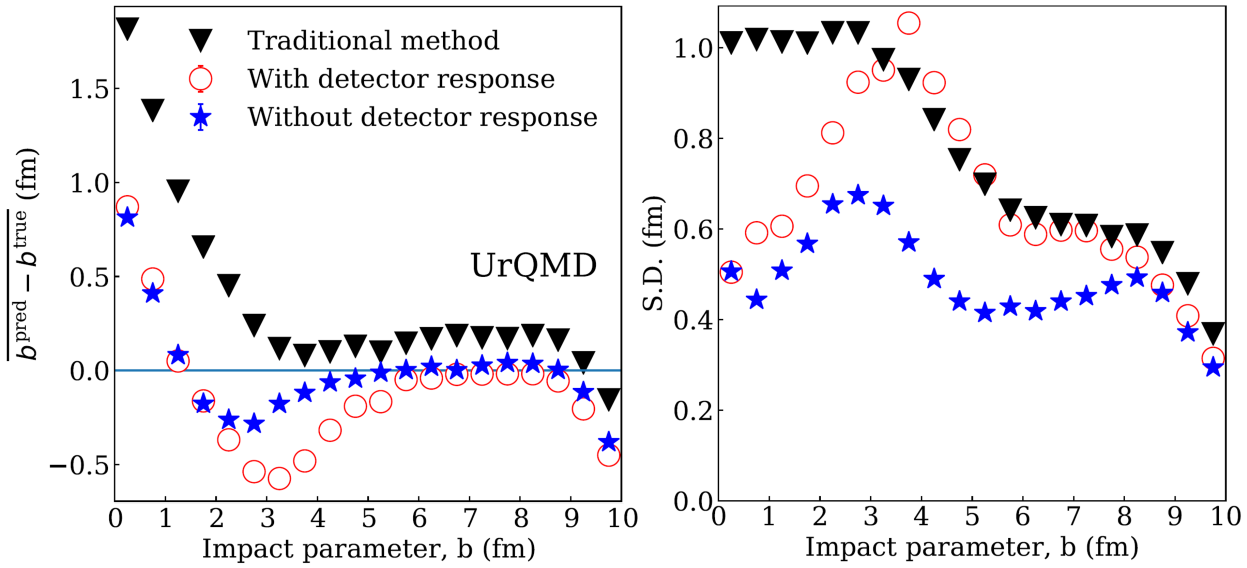

Figure 5.15: Impact parameter dependence of bias (left panel) and S.D. (right panel) predicted by LightGBM without detector response (solid stars) and with detector response (open circles). Results from traditional method are also plotted as black inverted triangles.

ML, especially for central collisions. Experimentally, we also see that ML selects central collision events better as discussed below.

If the determination of b is perfect, both bias and S.D. will be zero. That happens for the bias only in the range of b=5-8 fm. Over this region, the detector effects are minimal. S.D. never approaches zero over the range of b we investigate. The worsening of both bias and S.D. around $b \approx 0$ fm and $b \approx 10$ fm have been observed with other ML algorithms. This could be due to the inability of the LightGBM and traditional method to predict accurately near the boundaries of the observable limits.

To verify that application of the LightGBM algorithm trained on the UrQMD simulations is not restricted to only simulations from the UrQMD model and can be generalized to experimental data, we test the algorithm using simulations from four different transport models, Antisymmetrized Molecular Dynamics (AMD) model [169, 170] plus three different families of Quantum Molecular Dynamics (QMD) models, dcQMD [153, 171], IQMD [172, 173] and ImQMD [174]. All these models, including UrQMD, use different techniques and approaches to simulate the nucleus-nucleus collisions. All of them have had various success in describing different aspects of heavy ion collision

data. Their differences, underlying assumptions and performance between models are detailed in Refs. [175, 176]. In the simulations described here, default physics input parameters for each code are used. This allows us to not only gauge the discrepancy caused by different model assumptions, but also by uncertainty in input parameter values. In addition to these four different models, we also include a different input parameter set for the UrQMD model, labeled as UrQMD/SM-I. It can be considered as a different model.

Tests at $b = 3$ fm are perform to quantify the performance of ML algorithm. About 5000 events at 3 fm are generated from each code. LightGBM trained with UrQMD/SM-F data is tasked with predicting the impact parameter of these events. The bias and the corresponding S.D. values are listed in the top, middle, and bottom sections of Table 5.1. The top section contains results from the perfect detector (i.e. without the inclusion of detector response to simulated events) both for training and testing. The middle section contains results from including the detector response for both training and testing. Finally, in the bottom section, we apply the ML algorithm trained with perfect detectors to testing events that include detector response. The last option gives the largest deviation of b^{true} by predicting the mean b^{pred} as nearly 6 fm. Therefore the algorithm not including detector response in the training is unacceptable and would not be discussed any further.

AMD has the largest bias (1.09 fm), reflecting the very different approaches used in simulating HIC in AMD and other QMD-type models. As expected, both the bias and S.D. are larger than those values listed under UrQMD/SM-F column in Table 5.1 since these transport models were not used to train the events. Except for AMD, the bias and S.D. from different transport models are similar to the results of UrQMD/SM-I where the training and testing data use different input parameter sets. For AMD, while the accuracy worsens, the S.D. values are similar to the reference of UrQMD/SM-F.

As a reference, the best case scenario is LightGBM predictions on UrQMD/SM-F since training and testing data sets come from the same model. When average performance of different models is compared to it, S.D. increases by 20%. The UrQMD/SM-F under-predicts while the other models over-predict b. As expected, including the detector response worsens the bias and S.D. for all

Table 5.1: Statistical properties of b^{pred} on simulated events from various transport models. Simulated data from UrQMD/SM-F input parameter set are used for training. The bias values are plotted as absolute numbers. All values are in unit of fm.

Model	AMD	dcQMD	ImQMD	IQMD	Average	UrQMD/ SM-F	UrQMD/ SM-I
Perfect detector							
$\overline{b^{\text{pred}}}$	4.09	2.84	3.29	3.19	3.35	2.77	3.20
S.D.	0.68	1.00	0.74	0.88	0.83	0.66	0.94
|Bias|	1.09	0.16	0.29	0.43	0.49	0.23	0.20
With realistic detector response							
$\overline{b^{\text{pred}}}$	4.06	3.77	3.22	2.66	3.43	2.44	2.96
S.D.	0.91	1.22	1.02	1.03	1.04	0.94	1.05
|Bias|	1.06	0.77	0.22	0.34	0.60	0.56	0.04
Trained with perfect detector, applied to simulation with detector response							
$\overline{b^{\text{pred}}}$	6.45	6.45	6.25	6.04	6.30	5.87	5.69
S.D.	0.44	0.46	0.44	0.46	0.45	0.62	0.46
|Bias|	3.45	3.45	3.25	3.04	3.30	2.87	2.69

models. Assuming that the data could be described by the average of the models, then one could expect that the ML algorithm could determine b with a bias of 0.6 fm and S.D. of 1 fm from experimental data.

5.9.3.3 Results on experimental data

After extensive tests with transport models, we apply the ML algorithm to experimental data. Fig. 5.16 plots the correlations between b^{pred} from LightGBM and b^{pred} from traditional method. Generally, they are strongly correlated as evidenced by the overall diagonal distribution. Experimental cross-section measurements sets b_{max} of traditional method to be 7.5 fm while b^{pred} from the LightGBM extends beyond the sharp cut off limit resulting in a horizontal tail at 7.5 fm. It should be noted that the measured cross-section from which b_{max} is calculated is smaller than the true geometric cross-section due to trigger bias.

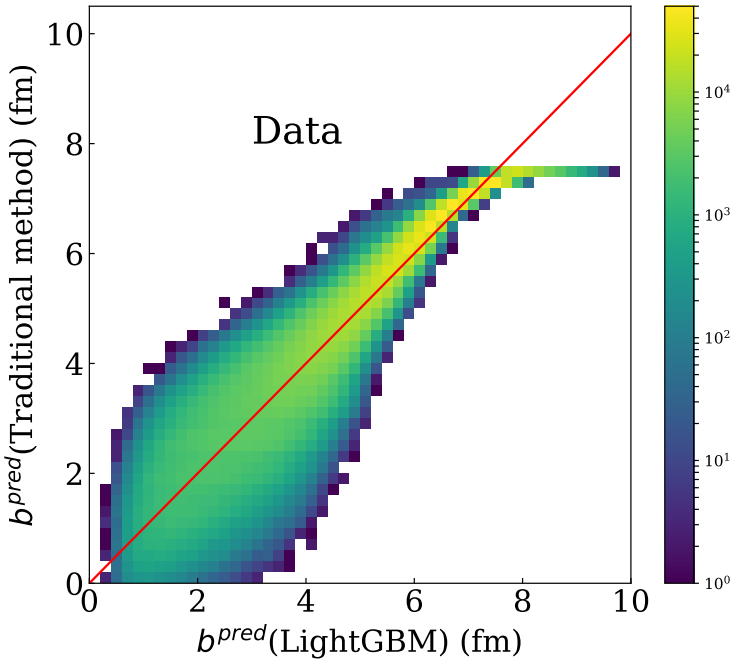

Figure 5.16: Tthe b^{pred} values from the LightGBM is plotted against that from traditional method. Color represent number of counts in each bin. The red diagonal line shows the expected correlation if impact parameters are determined perfectly.

The triangle in Fig. 5.17 shows the experimental impact parameter distributions from the sharp cut off model of eq. (4.4). The impact parameter distribution predicted by the LightGBM (open symbols) exhibits a tail that extends b^{pred} beyond 7.5 fm. It resembles smearing of the experimental impact parameter distribution which is consistent with the expectation that the experimental data should contain a range of impact parameters that would extend beyond b_{max}. In addition, one would expect the sharp cutoff model multiplicity distribution should always be equal to or higher than the realistic multiplicity distributions. Fig. 5.17 shows that from 4 to 6.5 fm, there are slightly more events from LightGBM than from traditional method. This apparent discrepancy is not understood. It could be that, not all the detector response has been accurately reproduced. It could also be that the UrQMD is not describing the experimental data accurately enough in this region as is also evidenced by the worsening of the accuracy and broadening of S.D. in Fig. 5.15. Nonetheless, the effects are small.

Unlike events from transport models, we do not have the true value of impact parameter from

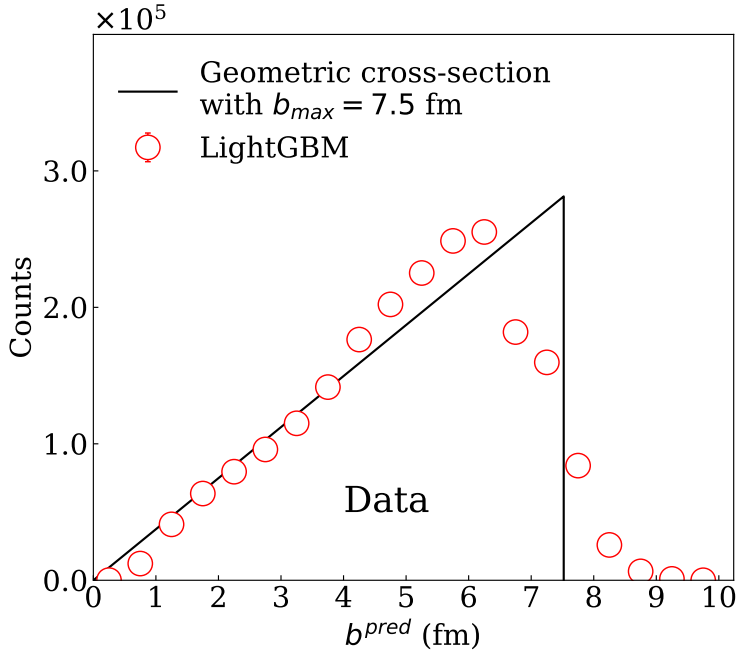

Figure 5.17: Distribution of b^{pred} made with the LightGBM (open symbols) and sharp cut off model with $b_{\text{max}} = 7.5$ fm (black line).

experimental data so we cannot evaluate the accuracy of b^{pred} values. Fig. 5.17 suggests that the LightGBM algorithm determines the impact parameter for peripheral events more accurately as it does not have the sharp cutoff limit and the impact parameter smearing occurs naturally. To evaluate the performance at central collisions, we use observables whose qualitative behavior with impact parameter is known.

One such observable is the reaction plane resolution $\langle\cos(\Phi_M - \Phi_R)\rangle$[115]. This observable was described in Section 3.4.6. Here Φ_M and Φ_R are the measured and the real azimuthal angle of the reaction plane, respectively. The reaction plane should vanish as b approaches zero due to azimuthal symmetry. In a perfect head-on collision ($b = 0$ fm), the fragment emission is isotropic and Φ_M is reduced to a random number between $0 - 2\pi$, which makes the average of cosine zero.

As shown in Fig. 5.18, the reaction plane resolution $\langle\cos(\Phi_M - \Phi_R)\rangle$ decreases with b^{pred}. However, at $b^{\text{pred}} < 3$ fm the reaction plane resolution is closer to zero if the central event selections are made with LightGBM. This finding supports the assertion that events selected by LightGBM are more central than the corresponding events selected by traditional method, although neither

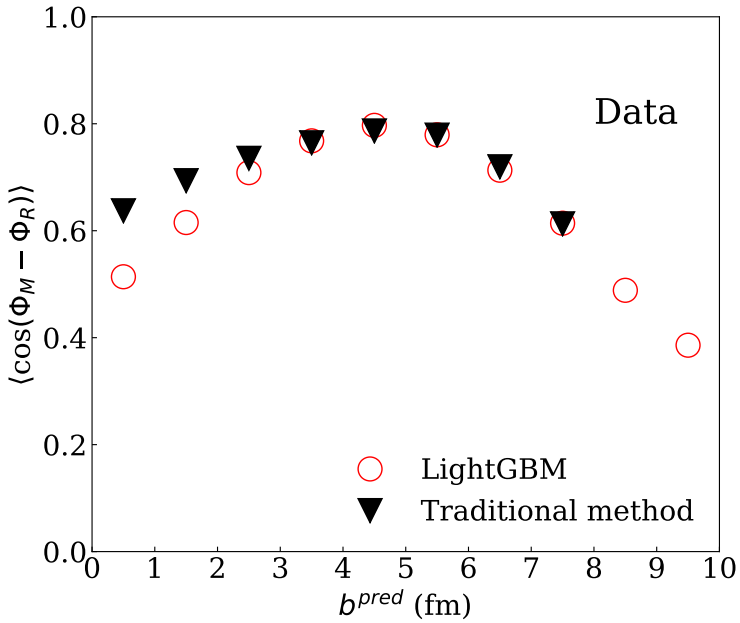

Figure 5.18: The reaction plane angle resolution, $\langle\cos(\Phi_M - \Phi_R)\rangle$ is plotted against b^{pred}. The predictions are made with traditional method (inverted black triangle) and LightGBM (red open circle).

intercepts the y-axis at zero.

CHAPTER 6

EQUATION OF STATE PARAMETER CONSTRAINTS

6.1 Introduction

We are interested in searching for the parameter space where model predictions agree with measured observables. The observables described in Chapter 4 are constructed to overcome limitations of clusterization process and should be directly comparable to model predictions. In this analysis, the Improved Quantum Molecular Dynamic (ImQMD) model will be used for constraining nuclear EoS parameters.

We will search in a multi-parameter space to explore the high dimensional correlations between different pairs of parameters. Such a high dimensional search is made with *Bayesian analysis* using *Markov Chain Monte Carlo* (MCMC) sampling. It incorporates our initial belief on parameter values (often based on results from other analysis) as *prior* and searches the high dimensional parameter space efficiently. This analysis returns the *posterior* distribution, the probability distribution in multivariate parameter space when conditioned on the measured observables. It can be easily projected onto one or two dimensional *marginal probability distribution* for visualization and interpretation.

A downside to such analysis is the intense computational requirement. MCMC sampling asks for model predictions on tens of thousands of parameter sets. Given that ImQMD typically takes roughly half an hour to make prediction on each parameter set, MCMC sampling will be prohibitively slow. To speed-up the calculations, we adopt the *Gaussian emulator* [177] and *Principal component analysis* [178]. It is a non-parametric interpolation algorithm that interpolates model predictions from a few tens of parameter sets. The emulator is robust to statistical fluctuations from finite statistics of ImQMD particle simulation, able to estimate interpolation uncertainty and fast.

In this chapter, we will describe the mathematical background of Bayesian analysis, MCMC,

Gaussian emulator and Principal component analysis. These algorithms will be tested and validated with *closure test*. A constraint on effective mass will be searched through this analysis and when it is used in conjunction with results from pion spectral yield ratios, the uncertainty on L can be reduced by 39%.

6.2 Bayesian analysis

Denote n as the number of free nuclear EoS parameters, θ^i as the i^{th} parameter, m as the number of observables, $y_P^j(\vec{\theta})$ as the predicted values for the j^{th} observable from a given parameter set $\vec{\theta} = \{\theta^1, ...\theta^n\}$, $\sigma_P^j(\vec{\theta})$ as the statistical uncertainty of $y_P^j(\vec{\theta})$, y_M^j as the measured observable value and σ_M^j as the experimental uncertainty of y_M^j. We will refer to the collection of all predicted and measured observables as $\overrightarrow{y_P}$ and $\overrightarrow{y_M}$, respectively.

From Bayes theorem, the posterior probability distribution is given by $P(\vec{\theta}|\overrightarrow{y_M}) = P(\vec{\theta})P(\overrightarrow{y_M}|\vec{\theta})$. The first term $P(\vec{\theta})$ is referred to as *Prior*, which is the assumed probability distribution of the parameters from prior knowledge. In other words, it is constraints from other experiments. The second term $P(\overrightarrow{y_M}|\vec{\theta})$ is called the *likelihood*, which is the conditional probability of having the measured observable values given $\vec{\theta}$. It is formulated as,

$$P(\overrightarrow{y_M}|\vec{\theta}) \propto \exp\left(-\sum_{i=1}^{m} \frac{(y_M^i - y_P^i(\vec{\theta}))^2}{2\sigma^{i2}(\vec{\theta})}\right). \tag{6.1}$$

In this expression, $\sigma^{i2}(\vec{\theta}) = {\sigma_M^j}^2 + \sigma_P^{j2}(\vec{\theta})$ to incorporate the uncertainty from both the experiment and model simulation.

It is hard to visualize distributions with dimensionality higher than three. To interpret the high dimensional posterior distribution, it is customary to project the distribution onto one or two dimensions such that correlation of any pairs of parameters can be examined. Such projected distributions are called *marginal distributions* and defined as

$$P(\theta_i, \theta_j) = \int \cdots \int_{-\infty}^{\infty} P(\vec{\theta}|\overrightarrow{y_M})\, d\theta_1 \ldots\, d\theta_{i-1}\, d\theta_{i+1} \ldots\, d\theta_{j-1}\, d\theta_{j+1} \ldots\, d\theta_n, \tag{6.2}$$

where θ_i and θ_j are the pair of parameters to be visualized. With conventional numerical integration technique, such integration is computationally expensive. This is mitigated by sampling the posterior with Markov Chain Monte Carlo (MCMC) which randomly walks along the parameter space according to some pre-defined conditions [179]. Those conditions are imposed such that the path of this random walk will converge to posterior distribution. Marginal distributions can be plotted efficiently by filling histograms with parameters from the samples. All posterior distributions in this study are generated with the help of python library PyMC2 [180].

6.3 Gaussian emulator

Gaussian process will be used as a surrogate model in lieu of ImQMD in MCMC sampling. It is an interpolation algorithm for arbitrary dimensional input [177]. Only calculations from ImQMD at several tens of randomly distributed parameter sets are needed for the interpolation to work accurately. Gaussian process is better than other interpolation algorithms because it is robust to fluctuations in the training samples and able to estimate interpolation uncertainty. Gaussian process is also non-parametric, meaning that the interpolation does not assume any predetermined functional forms. This is advantageous in eliminating potential sources of bias in our choice of regression functions.

Gaussian process takes the form of a high dimension Gaussian distribution, with dimensionality equals to number of training sets [177]. Denote n as the number of training sets, x_i and y_i as the set of nuclear EoS parameters and predicted observable values of the i^{th} training set, respectively. A covariance function $k(x_i, x_j)$ is specified ad-hoc to quantify the covariance between pairs of training sets. The discussion on covariance function is delayed until later sections. Consider the following $n \times 1$ column matrix f with random variable elements that follow multivariate Gaussian distribution,

$$f \sim \mathcal{N}(\mathbf{0}, K(X, X)), \tag{6.3}$$

where X represents the collection of EoS parameters x_i of all n training sets and $K(X, X)$ is a $n \times n$ matrix with elements $K_{i,j} = k(x_i, x_j)$. To predict outcome on a new parameter set x_{new},

Eq. (6.3) can be written as,

$$\begin{pmatrix} f_{\text{new}} \\ f \end{pmatrix} \sim \mathcal{N}\left(0, \begin{pmatrix} K(x_{\text{new}}, x_{\text{new}}) & K(x_{\text{new}}, X) \\ K(X, x_{\text{new}}) & K(X, X) \end{pmatrix} \right). \tag{6.4}$$

In this equation, f_{new} is a scalar random variable, $K(x_{\text{new}}, X)$ is a $1 \times n$ row matrix with elements $K_{0,i} = k(x_{\text{new}}, x_i)$, $K(X, x_{\text{new}}) = K(x_{\text{new}}, X)^T$ and $K(x_{\text{new}}, x_{\text{new}}) = k(x_{\text{new}}, x_{\text{new}})$ is a scalar. Gaussian process assumes that the prediction of ImQMD follows f_{new}, with an important twist: since the value of column matrix f is given as the training sets, the distribution of f_{new} should be conditioned on $f_i = y_i$. Denote y as a column matrix with elements y_i. After applying the formula for conditional Gaussian distribution (see Ref. [181]), the probability distribution of f_{new} becomes,

$$\begin{aligned} \mathcal{P}(f_{\text{new}}|f = y) = \mathcal{N}\big(&K(x_{\text{new}}, X)K(X, X)^{-1}y, \\ &K(x_{\text{new}}, x_{\text{new}}) - K(x_{\text{new}}, X)K(X, X)^{-1}K(X, x_{\text{new}})\big). \end{aligned} \tag{6.5}$$

y_i from ImQMD are not exact due to statistical fluctuations. Assume that such random noises follow independent and identically distributed Gaussian function with variance σ^2, they can be added to the covariance in Eq. (6.3),

$$\begin{pmatrix} f_{\text{new}} \\ f \end{pmatrix} \sim \mathcal{N}\left(0, \begin{pmatrix} K(x_{\text{new}}, x_{\text{new}}) & K(x_{\text{new}}, X) \\ K(X, x_{\text{new}}) & K(X, X) + \sigma^2 I \end{pmatrix} \right). \tag{6.6}$$

Equation (6.5) has to be modified to accommodate the additional noise,

$$\begin{aligned} \mathcal{P}(f_{\text{new}}|f = y) = \mathcal{N}\big(&K(x_{\text{new}}, X)[K(X, X) + \sigma^2 I]^{-1}y, \\ &K(x_{\text{new}}, x_{\text{new}}) - K(x_{\text{new}}, X)[K(X, X) + \sigma^2 I]^{-1}K(X, x_{\text{new}})\big). \end{aligned} \tag{6.7}$$

Covariance function is essential in the construction of Gaussian process [182]. A major assumption in interpolation is that f_{new} is similar to y_i if x_{new} is close to x_i. The covariance function encodes our assumption on the similarity between points. A commonly used covariance function is the *squared exponential* function,

$$k(x_1, x_2) = \sigma_f \exp\Big(-\sum_{i=1}^{m} \frac{(x_1^i - x_2^i)^2}{2l_i^2} \Big). \tag{6.8}$$

In the equation, m is the number of dimension of EoS parameters, x^i is the i^{th} component of x, l_i is the length-scale and σ_f is the covariance amplitude. l_i, σ_f and σ of Eq. (6.6) are free parameters that one need to adjust for optimal performance. In the context of machine learning, they are called *hyperparameters* and the problem of selecting optimal values are called *model selection*. Squared exponential function is used in this chapter.

We will use leave-one-out cross-validation (LOO-CV) for model selection [183]. The idea is to remove a particular parameter set from the training data set. The leave-one-out point, which is usually called the *validation data*, is used to quantify the predictive accuracy with log probability,

$$\log p(y_i|X_{-i}, y_{-i}, \text{hyperparameters}) = -\frac{1}{2}\log(\sigma^2_{\text{pred}}) - \frac{(y_i - y_{\text{pred}})^2}{2\sigma^2_{\text{pred}}} - \frac{1}{2}\log 2\pi. \tag{6.9}$$

(X_{-i}, y_{-i}) denotes the set of training data with i^{th} set left out and y_{pred} and σ_{pred} are the predicted values and uncertainty at x_i respectively. The hyperparameters will be adjusted until the sum of log-likelihood over all left-out sets is maximized,

$$\text{hyperparameters} = \text{argmax} \sum_{i=1}^{n} \log p(y_i|X_{-i}, y_{-i}, \text{hyperparameters}) \tag{6.10}$$

The maximization is performed with Adaptive Movement Estimation (ADAM) algorithm [184]. For a more comprehensive description and derivation of Gaussian process, readers are encouraged to read Ref. [185].

6.4 Principal Component Analysis

The output of Gaussian process is usually a scalar. Although multivariate Gaussian process has been developed [186], they are invented recently and we do not have access to such algorithms. This is problematic because our observables are spectrum with different values at different rapidity or momentum bins. The desired output should be a vector of the spectrum values instead of a scalar.

The naive approach is to emulate each bin with an independent Gaussian process, but this approach carries some major drawbacks. If the spectrum is binned finely, a lot of Gaussian

processes are needed which slows down the calculation. The inability to capture the correlated errors between nearby bins in the spectrum is also a potential concern.

Following the approach adopted by the Modeling and Data Analysis Initiative (MADAI) [187], we perform a dimension reduction on the spectrum with Principal Component Analysis (PCA) before interpolation. PCA returns the ranked orthogonal coordinate bases which satisfy the following conditions: the variance of spectrum projections on the first basis is the greatest among all possible orthogonal coordinate bases, and the variance of spectrum projections on the second basis is the greatest among all possible orthogonal coordinate bases that are orthogonal to the first one, etc. These bases are called *principal components* (PCs) and only PCs with large variance needs to be emulated. Low variance PCs can be approximated as constant without losing too much accuracy.

The formula for PCA is shown here without proof. Details of the derivation can be found in Ref. [178] for detailed derivations. Denote d as the number of bins in the spectrum and Σ as the $d \times d$ covariance matrix of all bins in spectrum on training data set, and y_i as the d-dimensional vector representing the i^{th} spectrum in the training set. If we only keep the first k components, then y_i can be transformed into a lower dimensional vector z_i by,

$$z_i = \text{eig}(\Sigma, k)(y_i - \overline{y}). \tag{6.11}$$

Here, $\text{eig}(\Sigma, k)$ is the matrix formed by stacking k row-eigenvectors of Σ with k largest eigenvalues. $\overline{y}$ is the mean y vector over all the observed data points and z_i is a k dimensional vector. It is important to note that $k \leq d$ since number of eigenvectors equals to the dimension of the covariance matrix. y_i can be approximated by z_i using the following inverse transformation,

$$\hat{y_i} \approx \overline{y} + \text{eig}(\Sigma, k)^T z_i. \tag{6.12}$$

It is guaranteed that $\hat{y_i} \approx y_i$ if k is large enough. To be precise, let λ_i be the i^{th} largest eigenvalue and we use superscript to denote the component of a vector, then $\hat{y_i}$ satisfies the following condition,

$$\frac{1}{n}\sum_{i=1}^{n}\sum_{j=1}^{d}(y_i^j - \hat{y_i}^j)^2 = \sum_{i=k+1}^{d}\lambda_i. \tag{6.13}$$

In the above equation, n is the number of training parameter sets. This means that as long as λ_i for all $i > k$ are all very small, the averaged square difference between $\hat{y_i}$ and y_i will be very small. Therefore, it is possible to approximate $d-$dimensional spectrum with just $k-$dimensional PCs, where $k \leq d$. Experience with SπRIT spectra suggests that rarely do we need more than three PCs to emulate a spectrum, even if the spectrum contains as much as fifteen points.

During MCMC, k emulators are used to interpolate k PCs independently. The interpolated PCs will be transformed back to spectrum with equation (6.12). The emulated uncertainties for each PCs are also transformed to covariance matrix of the spectrum. The truncation error of equation (6.13) is divided by d to estimate the average truncation error of each bin, which will then be added to the diagonal elements of covariance matrix for likelihood estimation.

6.5 Sensitivity of each observable

The training data for Gaussian emulator comes from ImQMD predictions on 70 parameter sets. On each parameter set, calculation is repeated for each required reaction system and impact parameter. For each calculation, 3000 events are simulated. The following three classes of observables, totaling in eight spectra, are extracted on each parameter set,

1. Coalescence Invariant Directed flow (C.I. v_1) at $b = 5$ fm
    a) C.I. v_1 as a function of y_0 for ^{108}Sn + ^{112}Sn
    b) C.I. v_1 as a function of p_T for ^{108}Sn + ^{112}Sn ($0.3 < y_0 < 0.8$)
    c) C.I. v_1 as a function of y_0 for ^{132}Sn + ^{124}Sn
    d) C.I. v_1 as a function of p_T for ^{132}Sn + ^{124}Sn ($0.3 < y_0 < 0.8$)
2. Coalescence Invariant Elliptical flow (C.I. v_2) at $b = 5$ fm
    a) C.I. v_2 as a function of y_0 for ^{108}Sn + ^{112}Sn
    b) C.I. v_2 as a function of y_0 for ^{132}Sn + ^{124}Sn
3. Stopping (VarXZ) at $b = 1$ fm

a) VarXZ of p,d and t for ^{108}Sn + ^{112}Sn (Histograms flipped along $y_0 = 0$)

b) VarXZ of p,d and t for ^{112}Sn + ^{124}Sn

The construction and physical importance of each observable are described in Chapter 4. In addition to symmetry energy term, the momentum dependence of nuclear mean-field potential also influences the properties of nuclear matter [188–194]. This dependence manifests itself as a reduction of nucleon masses. The ratio of effective mass in symmetric matter to free nucleon mass m_N is called the isoscalar effective mass m_s^*/m_N. In asymmetric matter, the contribution of isovector (symmetry) mean-field potential causes the neutron and proton effective mass to differ [188, 190, 191], which is quantified in terms of isovector effective mass m_v^*/m_N [189]. The in-medium nucleon-nucleon (NN) cross sections in ImQMD is formulated as [195],

$$\sigma_{\mathrm{QMD}}^{\mathrm{med}} = \left(1 - \frac{\eta\rho}{\rho_0}\right)\sigma^{\mathrm{free}}, \tag{6.14}$$

where σ^{free} is the NN cross-section in free space taken from Ref. [196] and η is the reduction factor to be determined. These parameters, together with S_0 and L in density dependence of symmetry energy term, strongly influence the dynamics of nuclear collision. It is expected that the predicted flow and stopping depend on the competing effect of in-medium cross-section, symmetry forces and the momentum dependence in mean-field potential.

The 70 parameter sets are sampled randomly and with Latin Hyper-cube within parameter ranges in Table 6.1.

Table 6.1: The ranges of parameters for the training of Gaussian emulator.

Parameters	Min.	Max.
S_0 (MeV)	25	50
L (MeV)	15	160
m_s^*/m_N	0.6	1
m_v^*/m_N	0.6	1.2
η	-0.25	0.25

The sensitivity of each observable group on nuclear EoS parameters can be tested with the *Closure test*, where the analysis is performed by pretending ImQMD prediction from a new parameter set, one that is not used in the training of Gaussian emulator, is the experimental data. If the marginalized posterior distributions do not show narrow peaks around the initial values, it indicates a lack of sensitivity, and vice versa.

This section can be separated into two parts: The first part examine the sensitivity of each individual observable group and the second part tests the maximal constraining power when all observables are combined in a simultaneous global fit. In the first part, Bayesian analysis will be performed three times, each by comparing only one class of observables. Pairwise marginalize probability distributions between all pairs of parameters from the Closure tests will be shown. This analysis illustrates the correlation between parameters and observables qualitatively, so the Closure test is only done on one randomly generated parameter set for brevity. The second part is a quantitative analysis that examines the average performance of the analysis across the entire parameter space. All observables are compared simultaneously for maximum performance. Closure test is repeated 18 times, each with a randomly generated set of parameters to span the entire parameter space uniformly. The one-dimensional marginalized distributions will be fitted with asymmetric Gaussian to estimate predicted averages and uncertainties, which are then compared to the true initial parameter values to gauge the accuracy of the algorithm.

6.5.1 Sensitivity of each group of observables

Through out this section, uniform priors within ranges listed in Table 6.1 are used with the true parameter values as $S_0 = 37.4\,\mathrm{MeV}$, $L = 47.3\,\mathrm{MeV}$, $m_s^*/m_N = 0.80$, $m_v^*/m_N = 1.11$ and $\eta = 0.13$. The parameter values are chosen at random, and the qualitative dependency of posterior on different groups of observables sheds light into the constraining power of the observables.

The posterior in Fig. 6.1 is the result of closure test when only the first group of observables (C.I. v_1) is being compared. It tries to simultaneously fit the spectrum of coalescence invariant proton v_1 as a function of y_0, and v_1 as a function of p_T gated on $0.3 < y_0 < 0.8$ for ^{108}Sn

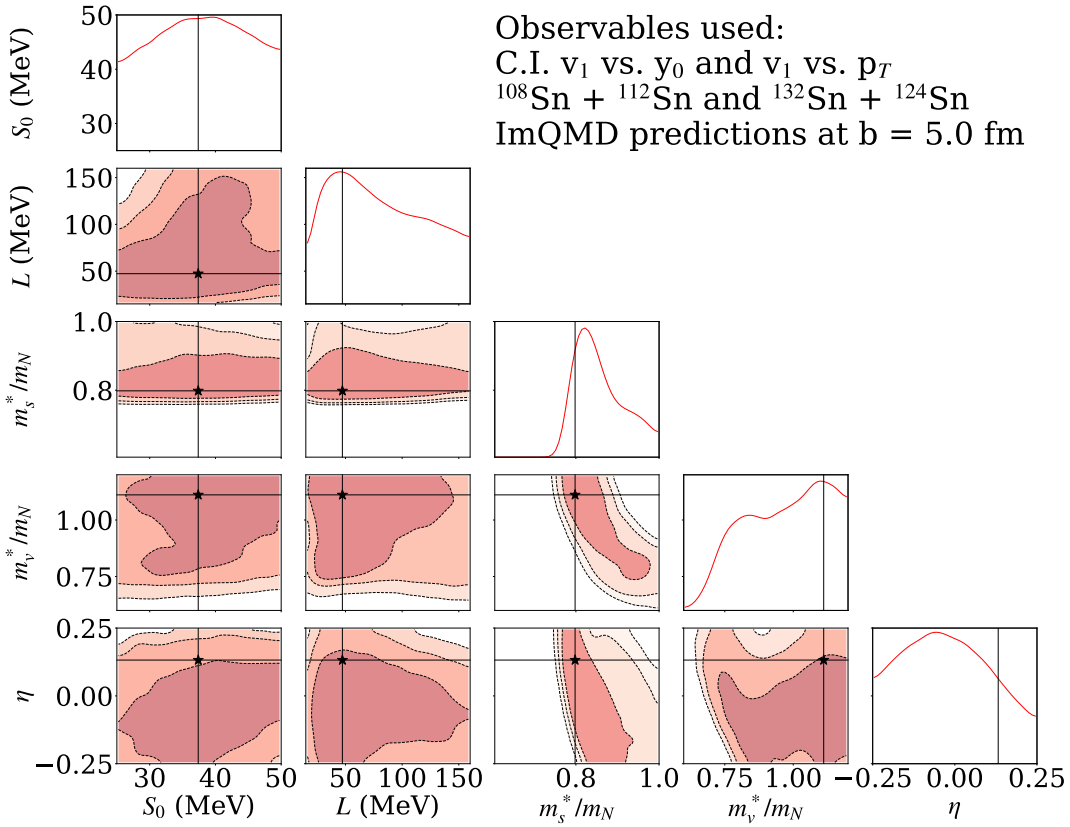

Figure 6.1: Posterior of closure test when all observables in group 1 (C.I. v_1) are compared. The black line in every plot and the black star in every off diagonal plot shows the initial true parameter values.

+ ^{112}Sn and ^{132}Sn + ^{124}Sn at $b = 5$ fm. The black vertical lines in the diagonal plots and star markers in the off-diagonal plots show the location of the true parameter values as a visual reference. The contour on off-diagonal plots shows 68% (1σ) confidence interval, 95% (2σ) and 99% (3σ) confidence interval with increasingly lighter shades. The posterior peak for m_s^*/m_N is narrow, which is consistent with the expectation that directed flow is related to the momentum dependence of nuclear mean field [11]. There is an anti-correlation between m_s^*/m_N and m_v^*/m_N which demonstrates that increasing m_s^*/m_N and m_v^*/m_N has the opposite effect on coalescence invariant directed flow.

The sensitivity of coalescence invariant elliptical flow in Fig. 6.2 is slightly different. The figure is the posterior of closure test by fitting only the coalescence invariant proton v_2 as a function of y_0 for ^{108}Sn + ^{112}Sn and ^{132}Sn + ^{124}Sn at $b = 5$ fm. It reveals a narrow peak on m_v^*/m_N as

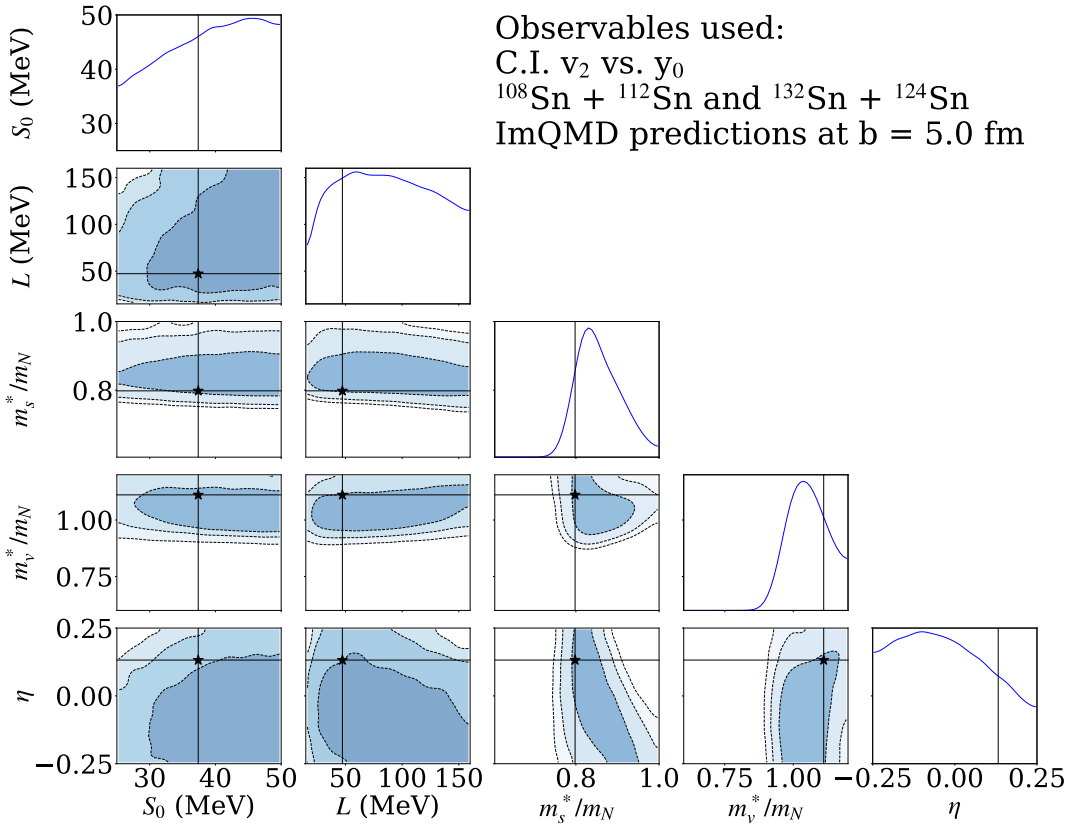

Figure 6.2: Same as Fig. 6.1 but only observables in group 2 (C.I. v_2) are being fitted.

well as m_s^*/m_N, which indicates that higher order flow terms are more sensitive to the isovector contributions to momentum dependence.

The final group of observables to be tested is VarXZ from ^{108}Sn + ^{112}Sn and ^{112}Sn + ^{124}Sn at $b = 1$ fm. Previous studies showed that VarXZ is mostly sensitive to the in-medium cross-section [32], and closure test corroborates this finding with a narrow peak on η in Fig. 6.3. The peaks of m_s^*/m_N and m_v^*/m_N are wider than those on Fig. 6.2, which indicates that the constraining power of VarXZ on effective masses is not as strong as v_2.

The maximum constraining power can be obtained by comparing all of the above observables simultaneously in one global fit. Posterior with all observables being compared are shown in Fig. 6.4. This shows that m_s^*/m_N, m_v^*/m_N and η can be recovered with reasonable accuracy while the sensitivity on S_0 and L is poor.

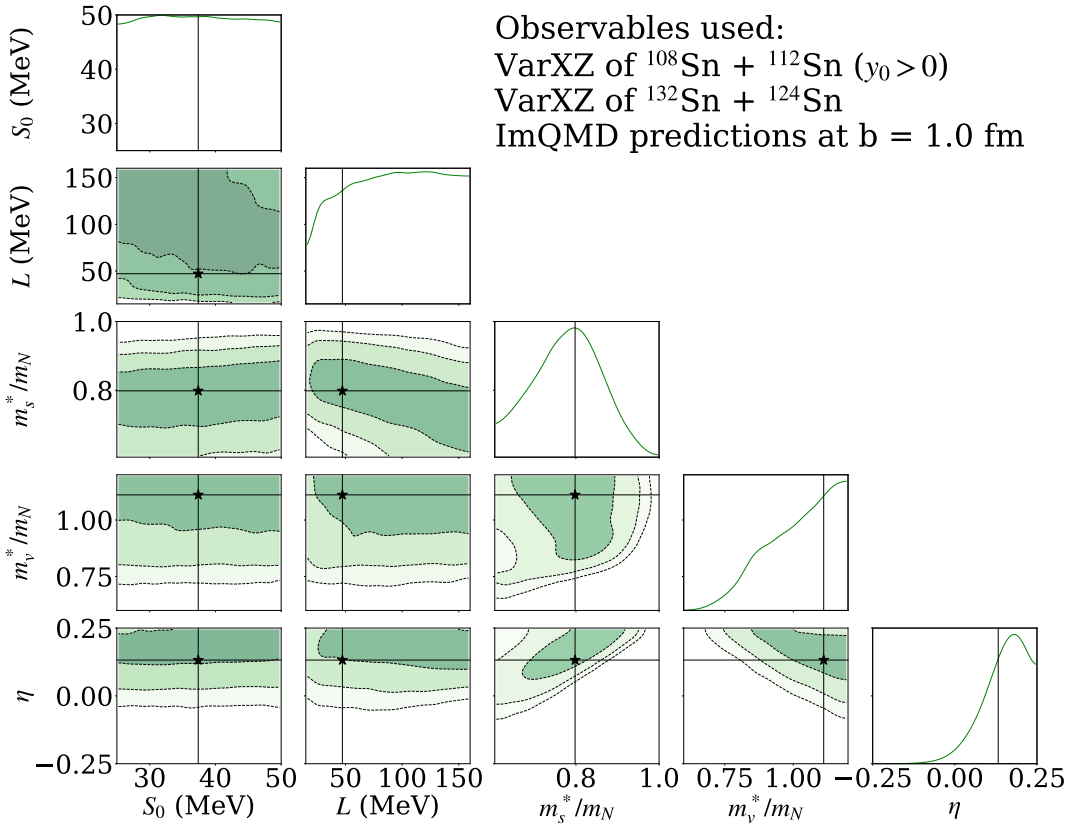

Figure 6.3: Same as Fig. 6.1 but only observables in group 3 (VarXZ) are being fitted.

6.5.2 Performance across parameter space

All posteriors in the previous section are analyzed on only one particular true parameter set, but the accuracy may change with parameter values. To understand the behavior of Bayesian analysis across the entire parameter space, closure test is repeated 18 times, each with a different randomly generated parameter set to cover the phase-space uniformly. The predicted values are plotted against the true values in Fig. 6.5. The error in the figure is the 68% confidence interval from the marginalized posterior distribution. Off-diagonal correlations between pairwise parameters are not shown for brevity. The red dotted $x = y$ line on each sub-plot represents the best possible performance where predicted values equal to true values. The sensitivities on S_0 and L is lacking throughout the parameter space, but the sensitivities on m_s^*/m_N, m_v^*/m_N and η are quite good as the analysis is able to predict the correct values.

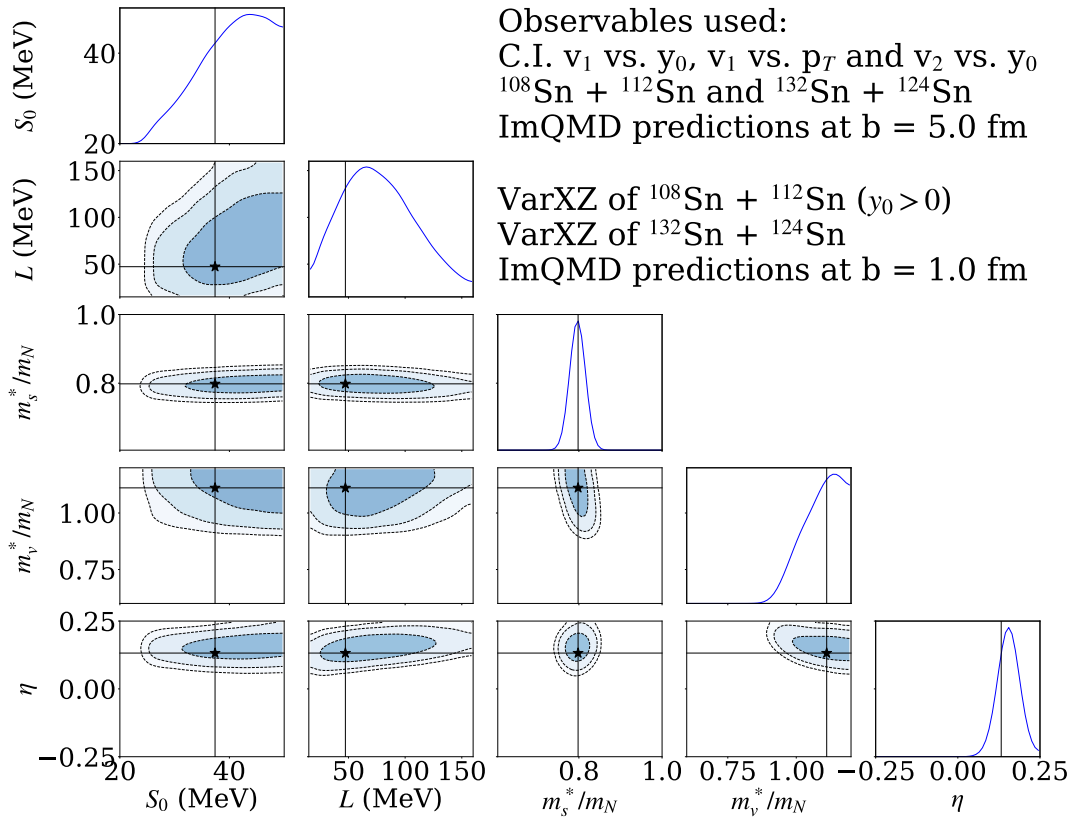

Figure 6.4: Same as Fig. 6.1, but all eight spectra across three groups of observables are used simultaneously in this analysis to demonstrate the maximal constraining power.

6.6 Constraints from experimental results

With the validity of the algorithms established, a comparison between ImQMD and experimental data can be performed to constraint nuclear EoS parameters. Unlike in previous sections where priors of all parameters are uniform, Gaussian priors are used on $S_0 \sim \text{Gauss}(\mu = 35.3, \sigma = 2.8)$ MeV and $L \sim \text{Gauss}(\mu = 80, \sigma = 38)$ MeV. These priors come from the analysis of pion spectrum ratios in Section 4.5.2.

The centrality of the experimental data are selected with multiplicity gate and the selected events spans a range of impact parameters. The ranges of multiplicities are different across reactions and observables because multiplicity distributions of different systems are not identical and centrality requirements for different observables are also different. The mean impact parameters for each observable are $\langle b \rangle = 5.1$ fm in ^{108}Sn + ^{112}Sn reaction and $\langle b \rangle = 5.2$ fm in ^{132}Sn + ^{124}Sn reaction

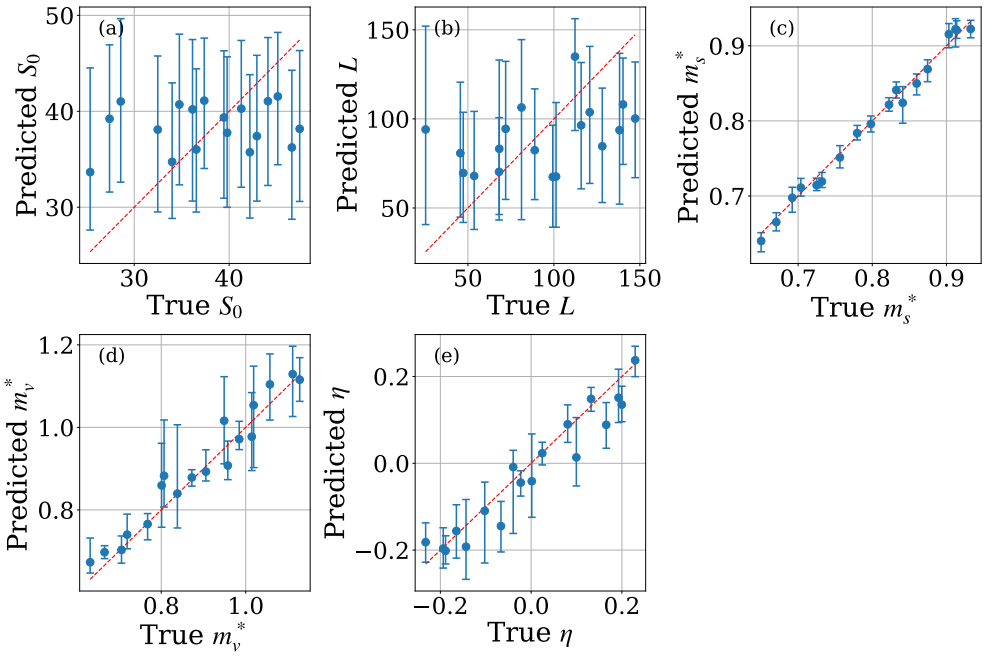

Figure 6.5: The predicted parameter values plotted against the true parameter values from the 18 closure tests. The markers and error bars indicate the medians and 68% (1σ) confidence intervals from the marginalized probability distributions respectively. The red diagonal lines on all five plots are $x = y$ to indicate where each point should be if the algorithm performs with perfect accuracy and precision.

for v_1 and v_2, and $\langle b \rangle = 1.1$ fm in ^{108}Sn + ^{112}Sn reaction and $\langle b \rangle = 1.0$ fm in ^{112}Sn + ^{124}Sn reaction for VarXZ. The ImQMD predictions that the emulator is being trained on, however, are only calculated at a single impact parameter enumerated in Section 6.5 without spanning a range. The impact parameters in ImQMD calculations differ slightly from the mean impact parameter of the selected events from the experiment, but given that the resolution of impact parameter determination with multiplicity is larger than 0.5 fm (see Section 5.9.3), this slight disagreement is negligible.

The posterior is shown in Fig. 6.6. Tight constraints on m_s^*/m_N, m_v^*/m_N and η are achieved while the uncertainty of S_0 and L remains large. The performance is consistent with our findings from closure test. The agreement between experimental spectra and emulated ImQMD predictions are shown in appendix E.

The results can be converted to a probability distribution on effective mass splitting $\Delta m_{np}^*/\delta$

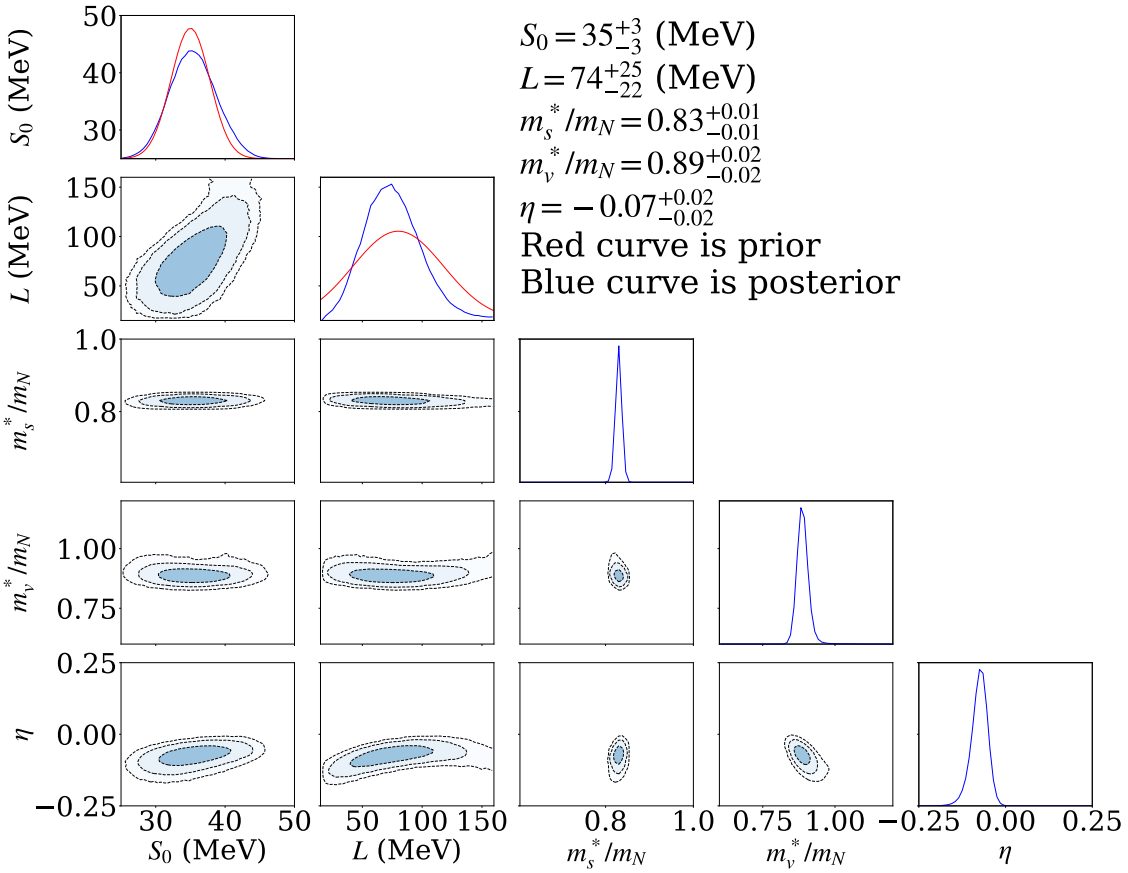

Figure 6.6: Posterior distribution when ImQMD is compared to experimental data from Chapter 4. All eight observables are used for Bayesian analysis. The values for median and 68% confidence interval of the marginalized distribution are tabulated on the upper right hand side of the figure.

with the following relation [158],

$$f_I = \frac{m_N}{m_s^*} - \frac{m_N}{m_v^*}$$
$$\frac{\Delta m_{np}^*}{\delta} \approx -2 f_I \left(\frac{m_s^*}{m_N}\right)^2 . \tag{6.15}$$

Using this equation, we find that $\Delta m_{np}^*/\delta = -0.11 \pm 0.04$. Analysis of n/p ratio using ImQMD at 120 MeV/u shows that $\delta m_{np}^*/\delta = -0.05 \pm 0.09$ [158] while analysis nuclear elastic scattering data shows that $\delta m_{np}^*/\delta = -0.25 \pm 0.27$ [197]. Previous analysis are inconclusive about the sign of effective mass splitting, but this analysis shows that $\delta m_{np}^*/\delta$ is most likely negative.

Although closure test shows that our analysis is not able to constrain L reliably, this can still be achieved indirectly by invoking previous constraint from pion ratio spectra. The pion constraint

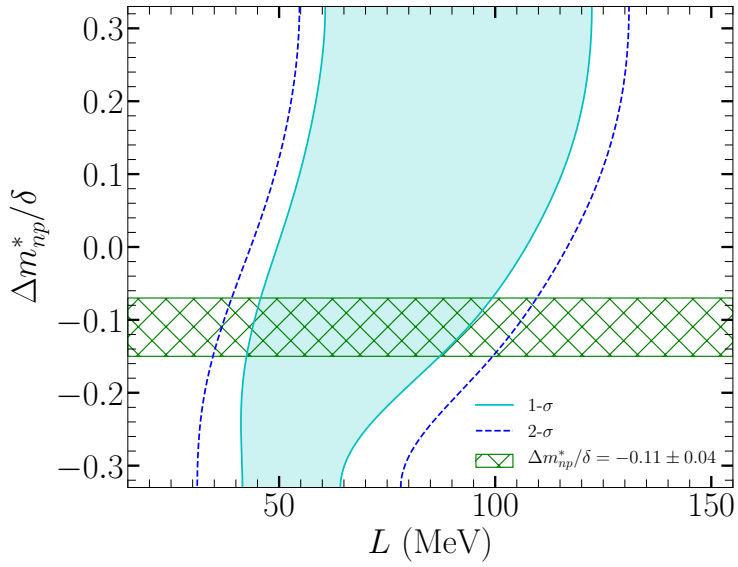

Figure 6.7: Same as Fig. 4.4, with $\delta m^*_{np}/\delta = -0.11 \pm 0.04$ overlaid as green hatch.

shows a correlation between $\Delta m^*_{np}/\delta$ and L, therefore a tighter constraint on L can be achieved with $\Delta m^*_{np}/\delta$ narrowed down, as Fig. 6.7 illustrates. The combined analysis of flows, stopping and pion ratios gives $L = 68 \pm 23$ MeV, which is 39% tighter than the previous pion ratios constraint. Since pion observables are sensitive to $\rho = 1.5\rho_0$ [143], our constraint should be placed there instead of at ρ_0. Calculation with EoS in dcQMD shows that $S(1.5\rho_0) = 46 \pm 8$ MeV and $L(1.5\rho_0) = 61 \pm 51$ MeV.

To test the predictive power of our results, ImQMD is executed with the best fitted parameters ($S_0 = 35$ MeV, $L = 68$ MeV, $m^*_s/m_N = 0.83$, $m^*_v/m_N = 0.89$ and $\eta = -0.07$) to predict VarXZ for ^{197}Au + ^{197}Au and ^{129}Xe + ^{133}Cs reactions at 250 MeV/u and $b = 1$ fm. $L = 68$ MeV comes from the analysis with pion constraints and other parameter values are set to the peak values of marginalized distributions in Fig. 6.6. Experimental results on these systems have been published by FOPI group [32]. Their results covers a wide range of beam energies, but results of 250 MeV/u is chosen as it is close to the beam energy of 270 MeV/u in SπRIT experiment. As illustrated in Fig. 6.8, the agreement between model predictions (orange points) and experimental data (blue points) are reasonable. Our constraints are applicable to reactions near 270 MeV/u.

K_0 (another name for K_{sat} in Eq. (1.4)) is known experimentally to be around 230 MeV.

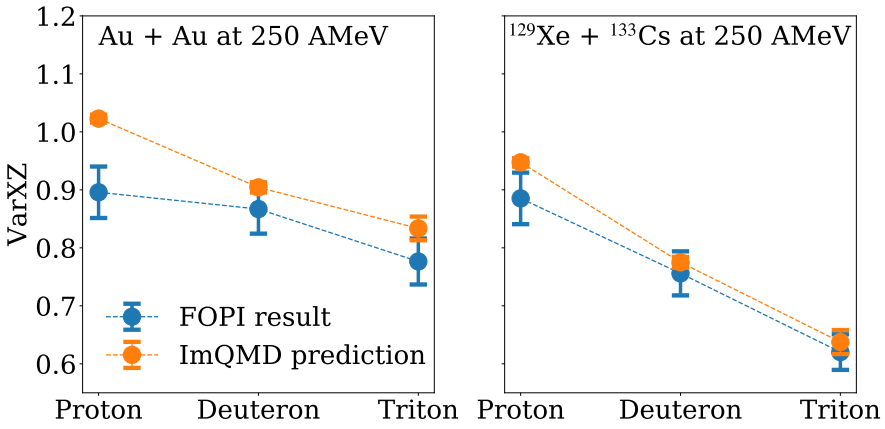

Figure 6.8: VarXZ of proton, Deuteron and Triton for ^{197}Au + ^{197}Au and ^{129}Xe + ^{133}Cs reactions at 250 MeV/u at $b = 1$ fm. The orange points show ImQMD predictions using the best fitted parameter values obtained from the SπRIT experiment. The blue points show experimental results from the FOPI data set.

Additional Bayesian analysis is done with K_0 included as a free parameter, ranging from 200 to 300 MeV. The prior for K_0 is a Gaussian distribution with mean = 237 MeV and standard deviation = 27 MeV. The values are taken from the second and third row of Table 2.1, which shows the statistics of K_{sat} for commonly used Skyrme type EoSs. The posterior in Fig. 6.9 shows that our observables are not sensitive to K_0 as the marginalized posterior distribution of K_0 is almost identical to its prior. Furthermore, posterior distributions of m_s^*/m_N and m_v^*/m_N show no correlation with K_0 and peak at around the same values as before when K_0 is not allowed to vary. Although η correlates with K_0, it does not affect our constraint on effective masses.

6.7 Implications on NS properties

With the connection between EoS parameters and NS properties established in Chapter 2, the impact of SπRIT results on NS properties will be discussed in this section.

Meta-modeling EoS from Section 2.3 is chosen for this analysis. These EoSs are randomly generated with S, L, K, Q and Z values distributed uniformly within plus or minus four standard deviation from the weighted averages of all models in row seven and eight of Table 2.1. The ranges of parameter are extended from two standard deviation in Section 2.3 to four such that a larger

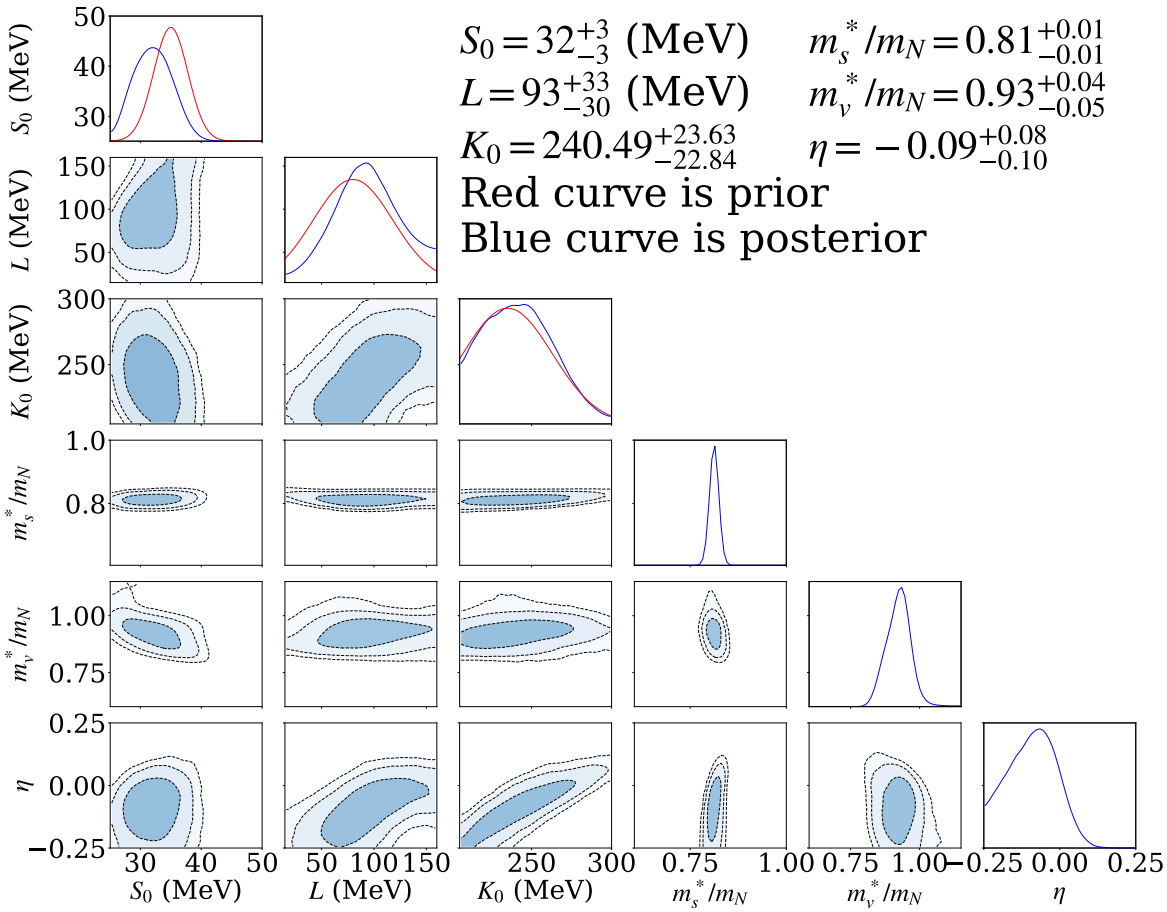

Figure 6.9: Same as Fig. 6.6, but K_0 is allowed to vary from 200 to 300 MeV.

functional space can be explored. EoSs with parameters inside the two standard deviation ranges are found to mostly outside the existing experimental constraint on symmetric matter so a wider parameter search is needed. Furthermore, we use uniform priors on S, L, K, Q, Z within the four standard deviation ranges as opposed to Gaussian priors previously used in Section 2.3 as we want to test the constraining power of just the heavy-ion results. The astronomical constraint on Λ from LIGO group is not applied here for the same reason.

We follow Eq. (2.7) to calculate posterior distributions. The EoSs that violate either maximum mass $> 2.04 M_\odot$ or causality are discarded. The remaining EoSs are weighted with the product of five Gaussian distributions with means and standard deviations given by the following constraints from heavy-ion collision: $S(1.5\rho_0) = 46 \pm 8$ MeV and $L(1.5\rho_0) = 69 \pm 51$ MeV from analysis of SπRIT data, $S(0.67\rho_0) = 25 \pm 1$ MeV from nuclear masses [34, 40], $L(0.67\rho_0) = 71 \pm 23$ MeV

from neutron skin thickness measurement of ^{208}Pb from PREX-II [198] and $P_{\rm SM}(4\rho_0) = 127 \pm 72\,{\rm MeV/fm^3}$ from the analysis of transverse flows of Au + Au at 2 AGeV [11]. Here, $P_{\rm SM}$ is the pressure of symmetric matter.

The pairwise correlations and marginal distributions of these parameters, as well as radius R and Λ of a $1.4M_\odot$ NS, are shown in Fig. 6.10. The diagonal distributions show the marginal probability distributions from only maximum mass, stability and causality conditions (red histograms), and with heavy-ion constraints included in addition to the three conditions (blue histogram). The off-diagonal pairwise correlations all show posterior with heavy-ion constraints. The table in the upper right hand corner of the figure shows parameter values and uncertainty, calculated by fitting the marginal distribution with asymmetric Gaussian. The numbers on the row labelled "Before" corresponds to the fitted values for blue histograms and "After" for red histograms. Our calculation indicates that $R = 12.7^{+0.6}_{-0.8}$ km and $\Lambda = 365^{+187}_{-118}$ for a $1.4M_\odot$ NS. For reference, analysis of GW170817 by LIGO group yields $\Lambda = 190^{+390}_{-120}$ [29] and multimessenger constraints from the survey of NICER, gravitational wave and X-ray Pulser PSR J0030 + 0740 and J0740 + 6620 yields $R = 12.56^{+1.00}_{-1.07}$ km [199]. The predicted ranges of Λ and R with heavy-ion constraints overlap significantly with that from gravitational wave and astronomical observations.

The 95% confidence interval (C.I.) of NS pressure ($\rm P_{NS}$) as a function of density is plotted in Fig. 6.11a. Solid blue region and open dashed blue region are C.I.s with and without using heavy-ion constraints, respectively. This is consistent with multimessenger constraints from the survey of NICER, gravitational wave and X-ray Pulser PSR J0030 + 0740 and J0740 + 6620 [199] whose 90% C.I. prediction on pressure is represented as a solid red region on the figure. Furthermore, symmetric matter pressure ($\rm P_{sym}$) of EoSs in the posterior also shows a good agreement with previous constraint from the analysis of transverse flow for Au + Au [11] in Fig. 6.11b. This is to be expected since the flow constraint at $4\rho_0$ is used as a likelihood condition in the calculation of posterior.

Fig. 6.12 shows the 95% C.I.s of symmetry energy term with (solid blue region) and without (dashed blue open region) heavy-ion constraints. The compiled low density data with the fitted

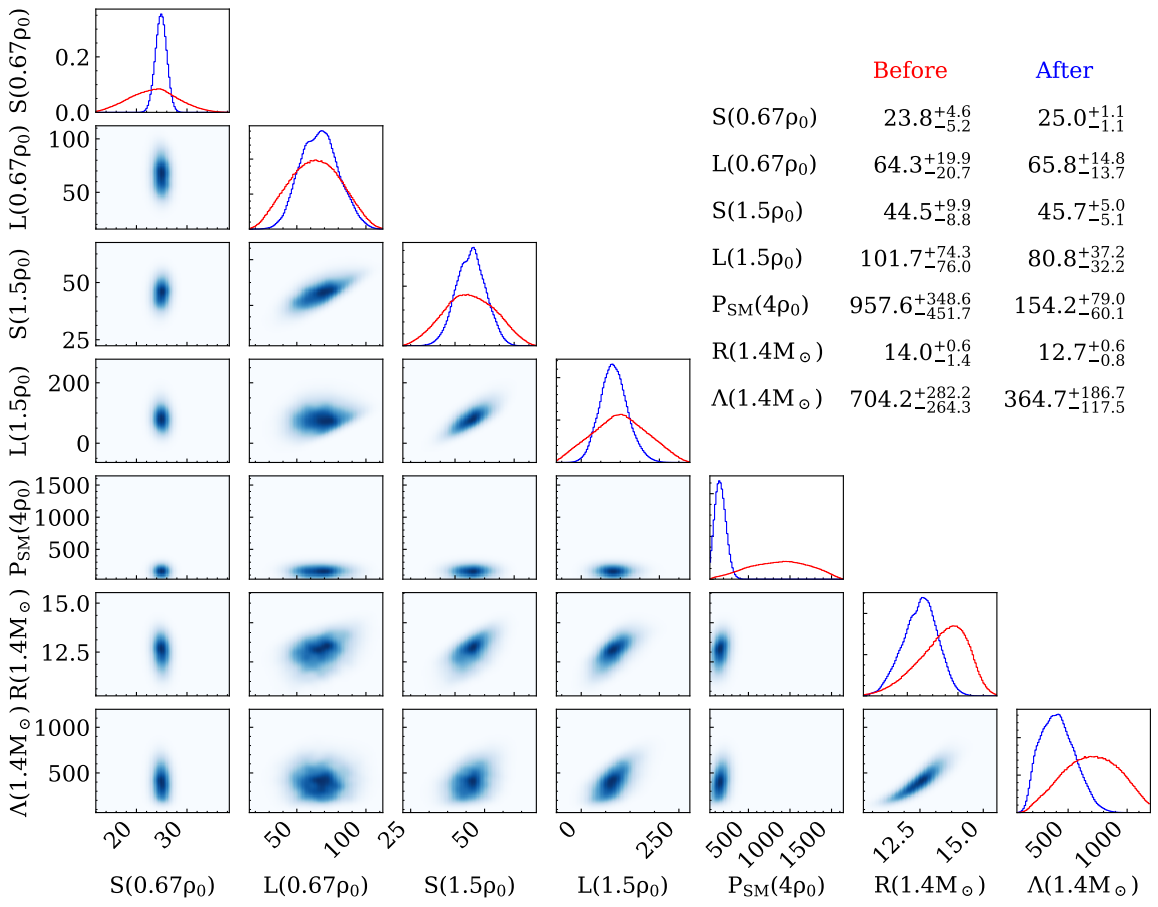

Figure 6.10: Posterior distributions for $S(0.67\rho_0)$, $L(0.67\rho_0)$, $S(1.5\rho_0)$, $L(1.5\rho_0)$, $P_{\rm SM}(4\rho_0)$, R and Λ of $1.4M_\odot$ NS. See text for details.

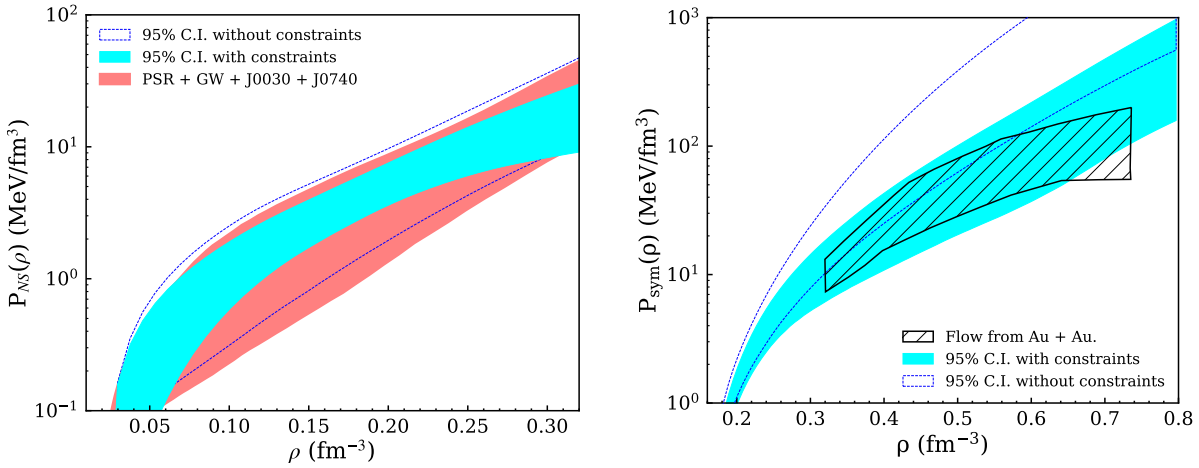

(a) (b)

Figure 6.11: (a): Dependence of NS pressure on matter density. (b): Dependence of symmetric matter pressure on matter density. See text for details.

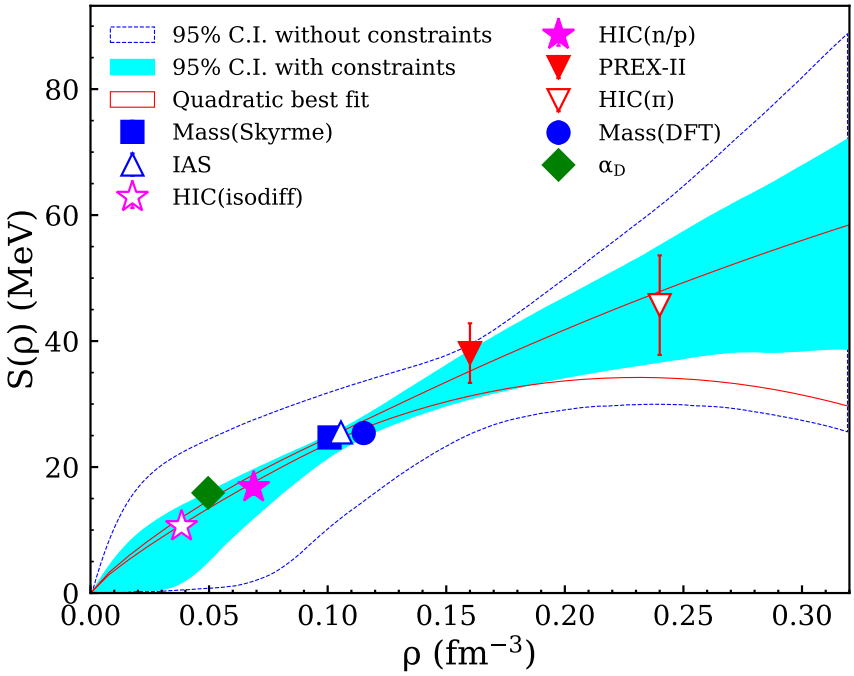

Figure 6.12: Dependence of symmetric energy on matter density with experimental constraints extracted from Ref. [8]. The blue dashed lines correspond to 95% C.I. without HIC constraints and the blue shaded region corresponds to 95% C.I. after applying HIC constraints. The open red area corresponds to best fit result from Ref. [8], fitted with all the data points except HIC(π). See text for details.

constraints from Ref. [8] are also plotted on top for comparison. These analyses are: Neutron to proton ratio (n/p) [158], isospin diffusion (isodiff) [200–202], nuclear masses (Mass(Skyrme) [40] and Mass(DFT) [203]), isobaric analog states (IAS) [39], electric dipole polarizability (α_D) [204] and neutron skin thickness of ^{208}Pb (PREX-II) [198]. The open red triangle labelled "HIC(π)" corresponds to the refined constraint on $S(1.5\rho_0)$ from SπRIT experiment. The sensitive density for each experiment is extracted in Ref. [8]. The reference also fits all of the symmetry energy constraints, excluding HIC(π), with the sum of kinetic energy term formulated as $12.7\,\mathrm{MeV}(\rho/\rho_0)^{2/3}$ and second order polynomial expended at $\rho = 0.67\rho_0$. 1σ fitted result from the reference is labelled as "Quadratic best fit" in the figure. The slight disagreement between the quadratic fit and Meta-modeling at high density could hint at the need for cubic term to make quadratic fit more stiff.

CHAPTER 7

SUMMARY

The properties of neutron stars depend strongly on high density part of symmetry energy term in nuclear equation of state (EoS). Equation of state is used as an input for Tolman–Oppenheimer–Volkoff (TOV) equation to predict neutron star properties such as radius or tidal deformability (Λ). This work demonstrates a strong correlation between Λ and the slope parameter (L) in the symmetry energy term of nuclear EoS with Skyrme type and Meta-modeling EoS.

The SπRIT TPC was constructed to the probe symmetry energy term with the main goal of measuring pion emissions from heavy-ion collisions of rare neutron-rich isotopes. Neutron star properties are sensitive to high density part of EoS and pions are predicted by transport models to originate from high density region due to its unique production mechanism. Four different reactions: ^{108}Sn + ^{112}Sn, ^{112}Sn + ^{124}Sn, ^{124}Sn + ^{112}Sn and ^{132}Sn + ^{124}Sn at 270 MeV/u are preformed during the experimental campaign. While ^{124}Sn and ^{112}Sn nuclei are stable and have been used as beams in previous studies [157, 158, 201], ^{108}Sn and ^{132}Sn beams are radioactive and can only be obtained in sufficient beam quantity in the rare isotope beam facility.

To extract useful data from SπRIT TPC, multiple analysis steps are needed to classify nuclear fragments, remove detector aberrations, and correct for detector resolution and efficiency effects. Upstream beam detectors have to be calibrated and analyzed to isolate events with the desired isotopes from beam impurities. After corrections on detector aberrations such as space charge and pad saturation are done, the hit clusters are fitted by GENFIT package to reconstruct the p/Z value for each fragment. The final step in the analysis is to correct for detector efficiency and reaction plane resolution with embedding and sub-event methods, respectively. All these steps are explained in details in different student theses [2, 7], including this work.

To verify our understanding of detector response, Monte Carlo simulation of SπRIT TPC is developed to recreate aspects of experimental data. It shows that the sudden loss of tracking efficiency for particles emitting at $\phi = \pm 90^\circ$ can be reproduced by incorporating saturation modes

of heavy residue. Discrepancies in momentum distributions between particles with positive p_x and negative p_x can be recreated by incorporating space charge effect and the shape of multiplicity distribution can be quantitatively described with the simulation of KYOTO and KATANA trigger conditions.

By comparing experimental pion ratios with transport model dcQMD, a correlated constraints on $\Delta m^*_{np}/\delta$ and L is obtained. To reduce our uncertainty on L, a tighter constraint on $\Delta m^*_{np}/\delta$ is needed. It is achieved in this work by utilizing the light fragment observables. The coalescence invariant directed and elliptical flow for ^{108}Sn + ^{112}Sn and ^{132}Sn + ^{124}Sn reactions from peripheral events, and VarXZs for ^{108}Sn + ^{112}Sn and ^{112}Sn + ^{124}Sn reactions from central events are reconstructed from SπRIT data, predictions from transport model ImQMD are then compared to constrain $\Delta m^*_{np}/\delta$.

Input parameters related to the symmetry energy in ImQMD (S_0, L, m^*_s/m_N, m^*_v/m_N and η) are fitted simultaneously through Bayesian analysis using Gaussian process with Principal Component Analysis are employed to emulate the behavior of ImQMD from calculated results with 70 parameter sets. To test the performance of such algorithms, closure test is performed on simulated data. It shows that our method is able to constraint m^*_s/m_N, m^*_v/m_N and η. S_0 and L do not show much sensitivity to the nucleonic experimental observables of VarXZ, v_1 and v_2.

The final global fit with experimental data shows a tight constraint on m^*_s/m_N, m^*_v/m_N and η. The predicting power of the constraints is verified by running ImQMD again with the best fitted parameters to predict VarXZ on ^{197}Au + ^{197}Au and ^{129}Xe + ^{133}Cs reactions at 250 MeV/u. The predictions agree reasonable well with published results from FOPI. Our preliminary values of m^*_s/m_N and m^*_v/m_N correspond to $\Delta m^*_{np}/\delta = -0.11 \pm 0.04$. When imposed together with constraint from pion ratio, the constraint on L can be tightened to $L = 68 \pm 25$ MeV, which is a 39% improvement. Our preliminary constraints on the symmetry energy term is verified to be consistent with low density constraints from previous studies of other heavy-ion collisions. Furthermore, when these heavy-ion constraints are used to predict neutron star properties with Meta-modeling type EoS, the calculated tidal deformability and radius of a $1.4M_\odot$ neutron stars are in good

agreement with astronomical observations from LIGO [22] and multimessenger analysis of pulsars and gravitational wave data [199].

Overall the SπRIT experiment have successfully constrained nuclear EoS at high density. A major source of uncertainty comes from the limited statistics of pions. We hope to increase the statistics by relaxing the cut conditions. Furthermore, collaborative efforts from theorists are underway to better understand the effect of pion potential and ensure consistent model predictions [117]. A better understanding of nuclear EoS is within reach as theories converge and data from different experiments are being finalized.

APPENDICES

APPENDIX A

SKYRME TYPE EOS

The energy density $\mathcal{E}$ of infinite nuclear matter as a function of particle number density ρ for Skyrme interaction is given by [3],

$$\begin{aligned}\frac{\mathcal{E}}{\rho} = \frac{3\hbar^2}{10M}\left(\frac{3\pi^2}{2}\right)^{2/3}\rho^{2/3}H_{5/3} + \frac{t_0}{8}\rho[2(x_0+2) - (2x_0+1)H_2] \\ + \frac{1}{48}\sum_{i=1}^{3} t_{3i}\rho^{\sigma_i+1}[2(x_{3i}+2) - (2x_{3i}+1)H_2] + \frac{3}{40}\left(\frac{3\pi^2}{40}\right)^{2/3}\rho^{5/3}(aH_{5/3} + bH_{8/3}),\end{aligned} \tag{A.1}$$

with

$$\begin{aligned} a &= t_1(x_1+2) + t_2(x_2+2), \\ b &= 0.5[t_2(2x_2+1) - t_1(2x_1+1)], \text{ and} \\ H_n(y) &= 2^{n-1}[y^n + (1-y)^n], \end{aligned} \tag{A.2}$$

where $y = Z/A$ is the proton fraction. The parameter t_0, t_1, t_2, t_{31}, t_{32}, t_{33}, x_0, x_1, x_2, x_{31}, x_{32}, x_{33}, σ_1, σ_2 and σ_3 are the free parameters. Ref. [205] introduced even more terms to Skyrme EoS to avoid the high-density ferromagnetic instability of neutron stars, but in this thesis those additional terms are never used.

APPENDIX B

TOLMAN–OPPENHEIMER–VOLKOFF EQUATION

The Tolman–Oppenheimer–Volkoff (TOV) equation set predicts the structure of a static spherical object under general relativity for any given EoS. The equations are:

$$\begin{aligned} \frac{dP(r)}{dr} &= -\frac{(\mathcal{E}(r)+P(r))(M(r)+4\pi r^3 P(r))}{r^2(1-2M(r)/r)}, \\ \frac{dM(r)}{dr} &= 4\pi r^2 \mathcal{E}(r). \end{aligned} \tag{B.1}$$

Here geometrized units $G = c = 1$ are used, $\mathcal{E}(r)$ is the energy density given by EoS, $P(r)$ is the internal pressure at given depth and $M(r)$ is the integral of gravitational mass from the core up to radius r. The surface is defined as the radial distance R at which $P(R) = 0$.

A list of equations whose solutions will lead to the value of Λ from the above structural functions will be shown without derivation. Please refer to Refs. [27, 206] for details. To begin with, an auxiliary variable $y_R = y(R)$ is calculated,

$$r\frac{dy(r)}{dr} + y(r)^2 + y(r)F(r) + r^2 Q(r) = 0. \tag{B.2}$$

where

$$F(r) = \frac{r - 4\pi r^3(\mathcal{E}(r) - P(r))}{r - 2M(r)}. \tag{B.3}$$

$$\begin{aligned} Q(r) =& \frac{4\pi r(5\mathcal{E}(r) + 9P(r) + \frac{\mathcal{E}+P(r)}{\partial P(r)/\partial \mathcal{E}} - \frac{6}{4\pi r^2}}{r - 2M(r)} \\ & - 4\Big[\frac{(M(r) + 4\pi r^3 P(r)}{r^2(1-2M(r)/r)}\Big]^2. \end{aligned} \tag{B.4}$$

The tidal Love number k_2 can then be calculated with the following expression:

$$\begin{aligned} k_2 =& \frac{1}{20}\left(\frac{R_s}{R}\right)^5\left(1-\frac{R_s}{R}\right)^2\left[2-y_R+(y_R-1)\frac{R_s}{R}\right] \\ &\times\left\{\frac{R_s}{R}\left(6-3y_R+\frac{3R_s}{2R}(5y_R-8)+\frac{1}{4}\left(\frac{R_s}{R}\right)^2\right.\right. \\ &\left.\times\left[26-22y_R+\frac{R_s(3y_R-2)}{R}+\left(\frac{R_S}{R}\right)^2(1+y_R)\right]\right) \\ &+3\left(1-\frac{R_s}{R}\right)^2\left[2-y_R+\frac{R_s(y_R-1)}{R}\right] \\ &\left.\times\ln\left(1-\frac{R_S}{R}\right)\right\}^{-1}. \end{aligned} \tag{B.5}$$

In the above equation, $R_S = 2M$ is the Schwarzschild radius. The value of Λ is then extracted with Eq. (1.9).

APPENDIX C

META-MODELING PARAMETERS AND TAYLOR PARAMETERS MAPPING

ELFc energy functional is written as a sum of kinetic energy term and potential energy term:

$$E_{ELFc}(\rho,\delta) = t^{FG*}(\rho,\delta) + v^{N}_{ELFc}(\rho,\delta), \tag{C.1}$$

where ρ is the density and δ is the asymmetry parameter. The kinetic energy term $t^{FG*}(\rho,\delta)$ in the above is written as:

$$\begin{aligned} t^{FG*}(\rho,\delta) = \frac{t^{FG}_{\text{sat}}}{2}\Big(\frac{\rho}{\rho_0}\Big)^{\frac{2}{3}}\Big[\Big(1+\frac{\kappa_{\text{sat}}\rho}{\rho_0}\Big)\Big((1+\delta)^{\frac{5}{3}}+ \\ (1-\delta)^{\frac{5}{3}}\Big) + \frac{\kappa_{\text{sym}}\rho}{\rho_0}\delta((1+\delta)^{\frac{5}{3}} - (1-\delta)^{\frac{5}{3}})\Big]. \end{aligned} \tag{C.2}$$

In the above, the parameters $t^{FG}_{\text{sat}} = 22.1\,\text{MeV}$ while κ_{sym} and κ_{sat} are effective mass parameters described in Eq. (2.3).

The potential energy term $v^{N}_{ELFc}(\rho,\delta)$ is written as:

$$\begin{aligned} v^{N}_{ELFc}(\rho,\delta) = \sum_{i=0}^{4}\frac{1}{i!}(v_i^{is} + v_i^{iv}\delta^2)(1-(-3)^{5-i}) \\ \times \exp\Big(-\frac{6.93\rho}{\rho_0}\Big)x^i. \end{aligned} \tag{C.3}$$

In the above equation, the parameters v_i^{is} and v_i^{iv} are free parameters. These 10 parameters can be uniquely mapped onto Taylor parameters using the following formulas (For a detailed derivation, please refer to Ref. [1]):

$$v_0^{is} = E_{\text{sat}} - t^{FG}_{\text{sat}}(1+\kappa_{\text{sat}}), \tag{C.4}$$

$$v_1^{is} = -t^{FG}_{\text{sat}}(2+5\kappa_{\text{sat}}), \tag{C.5}$$

$$v_2^{is} = K_{\text{sat}} - 2t^{FG}_{\text{sat}}(-1+5\kappa_{\text{sat}}), \tag{C.6}$$

$$v_3^{is} = Q_{\rm sat} - 2t_{\rm sat}^{FG}(4 - 5\kappa_{\rm sat}), \tag{C.7}$$

$$v_4^{is} = Z_{\rm sat} - 8t_{\rm sat}^{FG}(-7 + 5\kappa_{\rm sat}), \tag{C.8}$$

$$v_0^{iv} = S_0 - \frac{5}{9}t_{\rm sat}^{FG}(1 + (\kappa_{\rm sat} + 3\kappa_{\rm sym})), \tag{C.9}$$

$$v_1^{iv} = L - \frac{5}{9}t_{\rm sat}^{FG}(2 + 5(\kappa_{\rm sat} + 3\kappa_{\rm sym})), \tag{C.10}$$

$$v_2^{iv} = K_{\rm sym} - \frac{10}{9}t_{\rm sat}^{FG}(-1 + 5(\kappa_{\rm sat} + 3\kappa_{\rm sym})), \tag{C.11}$$

$$v_3^{iv} = Q_{\rm sym} - \frac{10}{9}t_{\rm sat}^{FG}(4 - 5(\kappa_{\rm sat} + 3\kappa_{\rm sym})), \tag{C.12}$$

$$v_4^{iv} = Z_{\rm sym} - \frac{40}{9}t_{\rm sat}^{FG}(-7 + 5(\kappa_{\rm sat} + 3\kappa_{\rm sym})). \tag{C.13}$$

When exploring the parameter space, Taylor parameters will be translated to Meta-modeling EoS using the above formulas and NS features will then be calculated with TOV equation. Neutron star properties will be examined to search for Taylor parameter spaces flavored by the observed tidal deformability.

APPENDIX D

FULL CORRELATION BETWEEN TIDAL DEFORMABILITY AND PARAMETERS

The correlations between L, $K_{\rm sym}$, $K_{\rm sat}$, $Q_{\rm sym}$, $Q_{\rm sat}$,$Z_{\rm sym}$, $Z_{\rm sat}$, $\left(m_{\rm sat}/m\right)$, $P(2\rho_0)$ and Λ are shown in Fig. D.1. This is an extension of Fig. 2.9 where bivariate distributions of some selected parameters are shown. The organization is similar: Lower triangles show bivariate distributions between variables and marginal distribution of each variable is shown on the diagonal. The upper triangles shows Pearson correlation coefficients between each variable pairs if it is larger than 0.1 otherwise they are omitted for simplicity and 3 dots are put in its place.

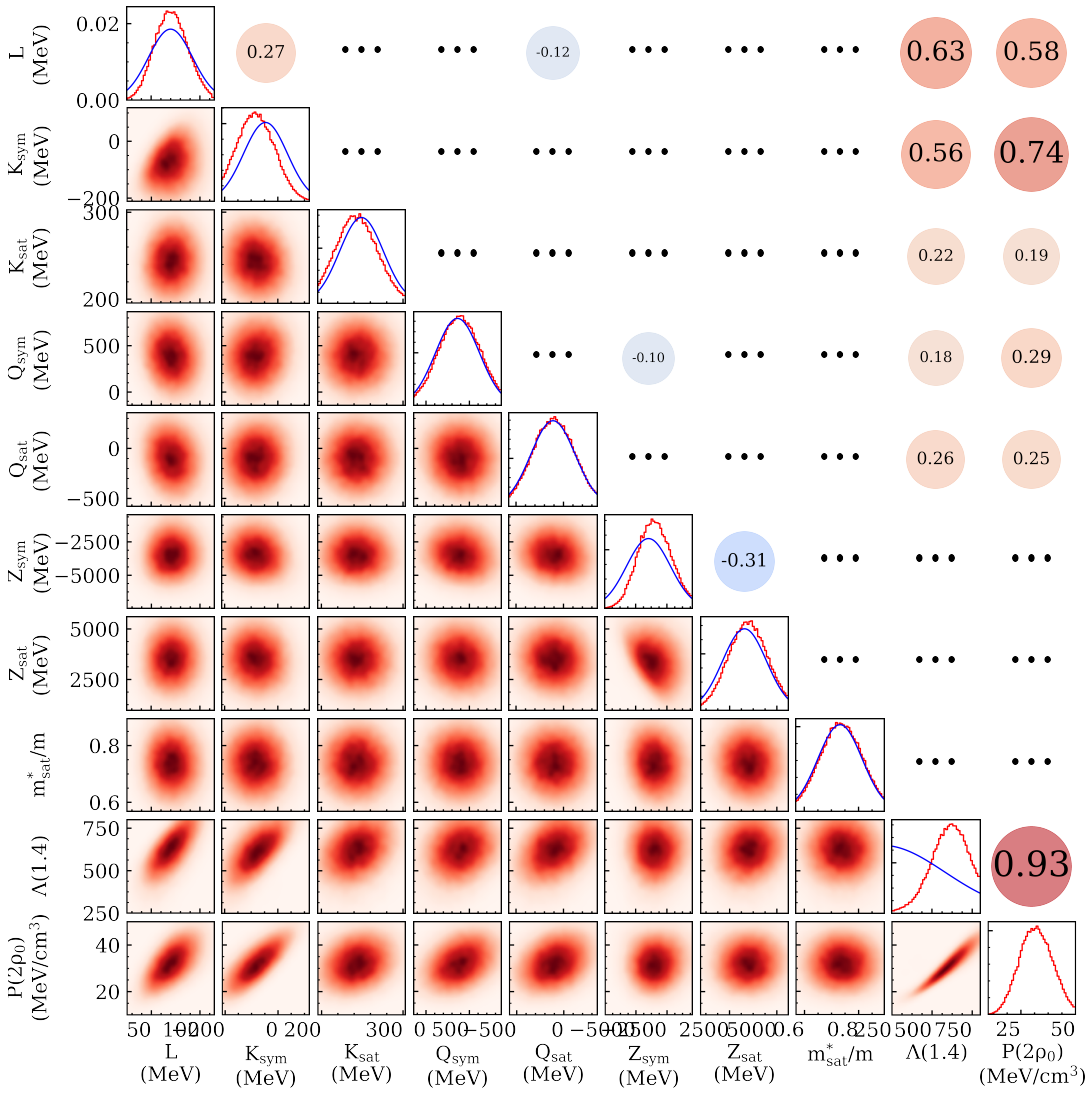

Figure D.1: Bivariate characteristics of posterior likelihood distributions. This is an extension to Fig. 2.6 and correlation pairs of all parameters pair are shown. Three regions can be distinguished. The lower triangle panels show likelihood distributions, with intensity proportional to distribution value, for pairs of Taylor parameters. The diagonal panels display marginalized distribution for each parameter. The upper triangular region shows Pearson correlation coefficient for parameter pairs, but when correlation in magnitude is less than 0.1, it is omitted and 3 dots are put in place of its value.

APPENDIX E

BEST FIT FROM IMQMD

The fitted results from Bayesian analysis are shown in Figs. E.1 and E.2.

Fig. E.1 shows results on direct and elliptical flow. Plots on the left column show results in ^{108}Sn + ^{112}Sn reaction and on the right show that of ^{132}Sn + ^{124}Sn reaction. From top to bottom, the three rows show v_1 as a function of y_0, v_1 as a function of p_T (MeV/c) and v_2 as a function of y_0.

Fig. E.2 is similar to Fig. E.1 but with results of VarXZ being shown. Beware that the reaction on the right column is now ^{112}Sn + ^{124}Sn instead of ^{132}Sn + ^{124}Sn. Using symmetry arguments in Chapter 4, rapidity distributions are reflected along $y_0 = 0$ only in ^{108}Sn + ^{112}Sn reaction when VarXZ is calculated.

ImQMD calculations are done at $b = 5$ fm for flow results and at $b = 1$ fm for stopping results, and on both Figs. E.1 and E.2 the mean impact parameter on the label of y-axis reflects the centrality gate on experimental data.

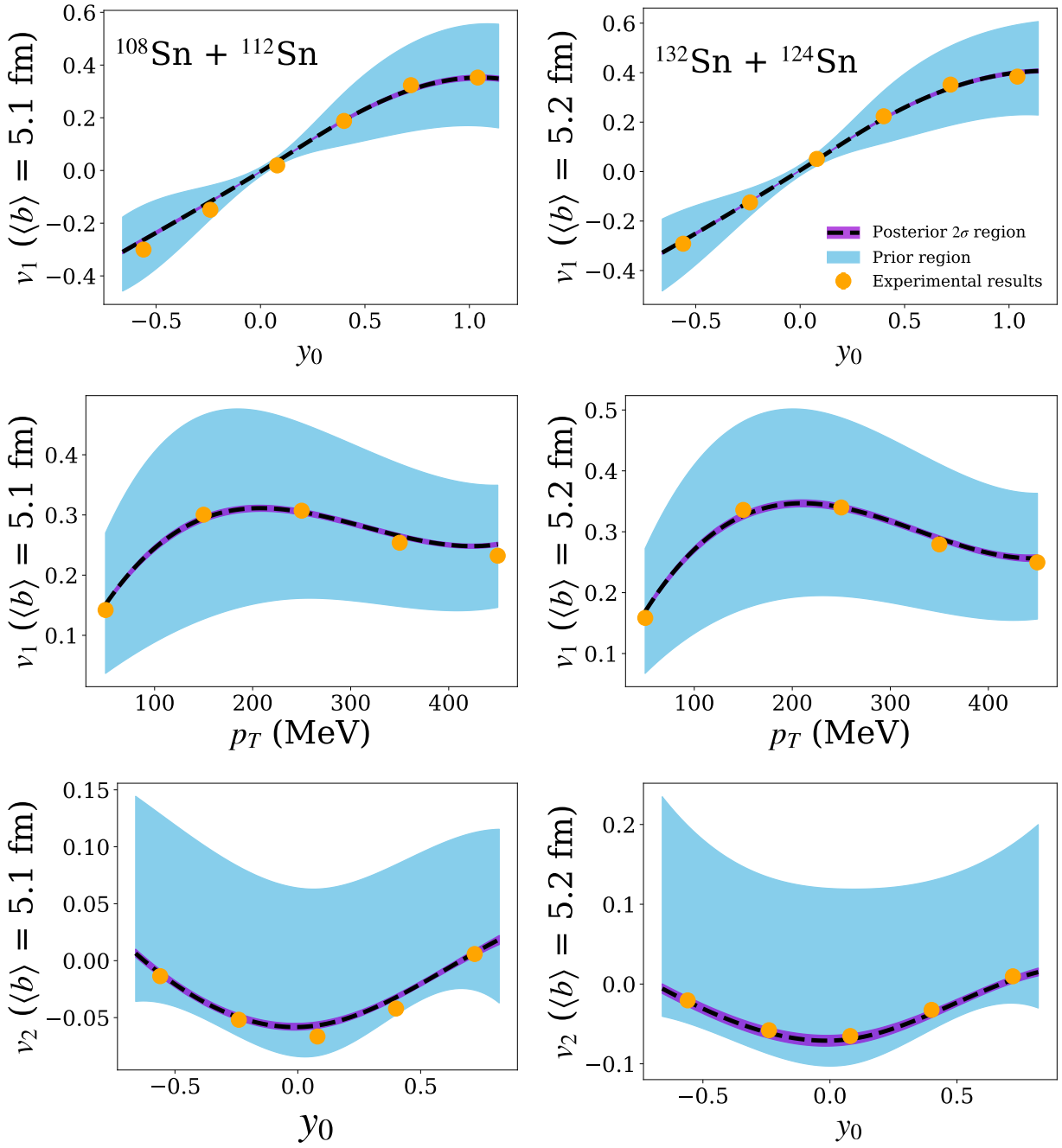

Figure E.1: Comparison of direct and elliptical flow between the best fitted ImQMD predictions and experimental results. The blue region shows the maximum range of prediction values from ImQMD with the parameter range in Table 6.1 and the purple region shows the 2σ confidence region of ImQMD's prediction after Bayesian analysis. The orange points show results from SπRIT experiment, which is identical to what is shown in Chapter 4. See text for details.

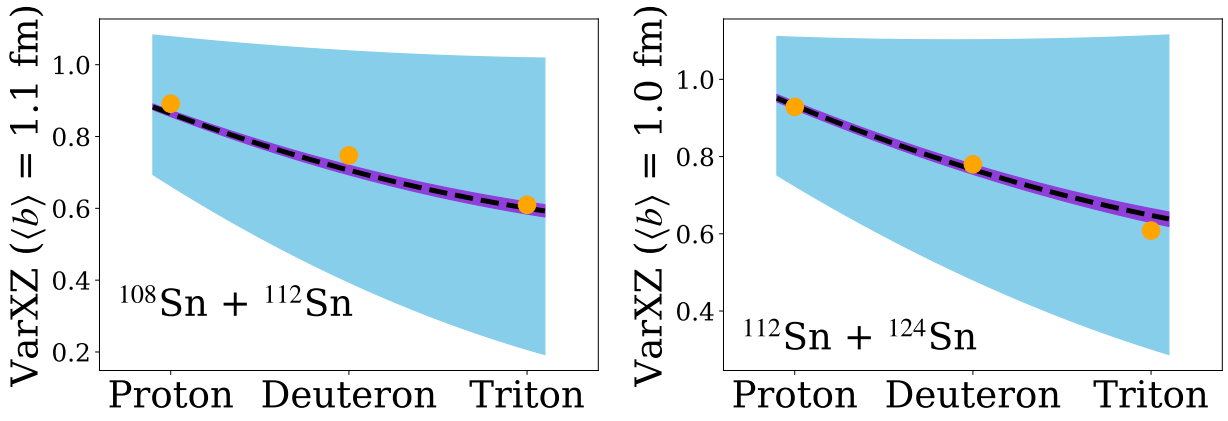

Figure E.2: Same as Fig. E.1, but with VarXZ of ^{108}Sn + ^{112}Sn on the left and that of ^{112}Sn + ^{124}Sn on the right.

BIBLIOGRAPHY

BIBLIOGRAPHY

[1] J. Margueron, R. Hoffmann Casali, and F. Gulminelli, Phys. Rev. C **97**, 025805 (2018).

[2] J. E. Barney, *Charged Pion Emission from* $^{112}Sn + ^{124}Sn$ *and* $^{124}Sn + ^{112}Sn$ *Reactions with the SπRIT Time Projection Chamber*, Ph.D. thesis.

[3] M. Dutra, O. Lourenço, J. S. Sá Martins, A. Delfino, J. R. Stone, and P. D. Stevenson, Phys. Rev. C **85**, 035201 (2012).

[4] F. J. Fattoyev, J. Piekarewicz, and C. J. Horowitz, Phys. Rev. Lett. **120**, 172702 (2018).

[5] K. Yamada, T. Dantsuka, M. Fujimaki, T. Fujinawa, N. Fukunishi, A. Goto, H. Hasebe, Y. Higurashi, E. Ikezawa, O. Kamigaito, et al., Proceedings of HIAT09 (2009).

[6] G. Jhang, *Performance of the SπRIT TPC for the nuclear physics experiment at RIBF*, Ph.D. thesis, Korea University (2016).

[7] J. Estee, *Constraining the high density nuclear symmetry energy with pions*, Ph.D. thesis, Michigan State University (2020).

[8] W. G. Lynch and M. B. Tsang, "Decoding the Density Dependence of the Nuclear Symmetry Energy," (2021), arXiv:2106.10119 [nucl-th] .

[9] C. J. Horowitz, E. F. Brown, Y. Kim, W. G. Lynch, R. Michaels, A. Ono, J. Piekarewicz, M. B. Tsang, and H. H. Wolter, Journal of Physics G: Nuclear and Particle Physics **41**, 093001 (2014).

[10] A. H. Wapstra, "Atomic masses of nuclides," in *External Properties of Atomic Nuclei / Äussere Eigenschaften der Atomkerne*, edited by S. Flügge (Springer Berlin Heidelberg, Berlin, Heidelberg, 1958) pp. 1–37.

[11] P. Danielewicz, R. Lacey, and W. G. Lynch, Science **298**, 1592 (2002).

[12] C. Fuchs, Progress in Particle and Nuclear Physics **56**, 1 (2006).

[13] W. G. Lynch, M. B. Tsang, Y. Zhang, P. Danielewicz, M. Famiano, Z. Li, and A. W. Steiner, Progress in Particle and Nuclear Physics **62**, 427 (2009), heavy-Ion Collisions from the Coulomb Barrier to the Quark-Gluon Plasma.

[14] A. L. Fèvre, Y. Leifels, W. Reisdorf, J. Aichelin, and C. Hartnack, Nuclear Physics A **945**, 112 (2016).

[15] A. W. Steiner, J. M. Lattimer, and E. F. Brown, The Astrophysical Journal **765**, L5 (2013).

[16] C. Y. Tsang, M. B. Tsang, P. Danielewicz, F. J. Fattoyev, and W. G. Lynch, Physics Letters B **796**, 1 (2019).

[17] J. M. Lattimer and M. Prakash, The Astrophysical Journal **550**, 426 (2001).

[18] B.-A. Li, P. G. Krastev, D.-H. Wen, and N.-B. Zhang, The European Physical Journal A **55**, 117 (2019).

[19] M. Baldo and G. Burgio, Progress in Particle and Nuclear Physics **91** (2016), 10.1016/j.ppnp.2016.06.006.

[20] J. M. Lattimer, Annual Review of Nuclear and Particle Science **62**, 485 (2012), https://doi.org/10.1146/annurev-nucl-102711-095018 .

[21] M. Tsang, W. Lynch, P. Danielewicz, and C. Tsang, Physics Letters B **795**, 533 (2019).

[22] B. P. Abbott et al. (LIGO Scientific Collaboration and Virgo Collaboration), Phys. Rev. Lett. **119**, 161101 (2017).

[23] T. Damour, M. Soffel, and C. Xu, Phys. Rev. D **45**, 1017 (1992).

[24] E. E. Flanagan and T. Hinderer, Phys. Rev. D **77**, 021502 (2008).

[25] T. Damour, A. Nagar, and L. Villain, Phys. Rev. D **85**, 123007 (2012).

[26] T. Binnington and E. Poisson, Phys. Rev. D **80**, 084018 (2009).

[27] S. Postnikov, M. Prakash, and J. M. Lattimer, Phys. Rev. D **82**, 024016 (2010).

[28] J. Piekarewicz and F. J. Fattoyev, Phys. Rev. C **99**, 045802 (2019).

[29] B. P. Abbott et al. (The LIGO Scientific Collaboration and the Virgo Collaboration), Phys. Rev. Lett. **121**, 161101 (2018).

[30] W. Reisdorf, D. Best, A. Gobbi, N. Herrmann, K. Hildenbrand, B. Hong, S. Jeong, Y. Leifels, C. Pinkenburg, J. Ritman, et al., Nuclear Physics A **612**, 493 (1997).

[31] W. Reisdorf, M. Stockmeier, A. Andronic, M. Benabderrahmane, O. Hartmann, N. Herrmann, K. Hildenbrand, Y. Kim, M. Kiš, P. Koczoń, et al., Nuclear Physics A **781**, 459 (2007).

[32] W. Reisdorf, A. Andronic, R. Averbeck, M. Benabderrahmane, O. Hartmann, N. Herrmann, K. Hildenbrand, T. Kang, Y. Kim, M. Kiš, et al., Nuclear Physics A **848**, 366 (2010).

[33] J. Estee, W. G. Lynch, C. Y. Tsang, J. Barney, G. Jhang, M. B. Tsang, R. Wang, M. Kaneko, J. W. Lee, T. Isobe, et al. (SπRIT Collaboration), Phys. Rev. Lett. **126**, 162701 (2021).

[34] Z. Zhang and L.-W. Chen, Phys. Lett. **B726**, 234 (2013), arXiv:1302.5327 [nucl-th] .

[35] T. Malik, N. Alam, M. Fortin, C. Providência, B. K. Agrawal, T. K. Jha, B. Kumar, and S. K. Patra, Phys. Rev. C **98**, 035804 (2018).

[36] H. Gil, Y.-M. Kim, C. H. Hyun, P. Papakonstantinou, and Y. Oh, Phys. Rev. C **100**, 014312 (2019).

[37] Z. Carson, A. W. Steiner, and K. Yagi, Phys. Rev. D **99**, 043010 (2019).

[38] Y. Lim and J. W. Holt, Phys. Rev. Lett. **121**, 062701 (2018).

[39] P. Danielewicz, P. Singh, and J. Lee, Nuclear Physics A **958**, 147 (2017).

[40] B. A. Brown, Phys. Rev. Lett. **111**, 232502 (2013).

[41] M. Bender, P.-H. Heenen, and P.-G. Reinhard, Rev. Mod. Phys. **75**, 121 (2003).

[42] J. Stone and P.-G. Reinhard, Progress in Particle and Nuclear Physics **58**, 587 (2007).

[43] P. Haensel, A. Y. Potekhin, and D. G. Yakovlev, *Neutron Stars I* (Springer, 2007).

[44] C. J. Horowitz, M. A. Pérez-García, and J. Piekarewicz, Phys. Rev. C **69**, 045804 (2004).

[45] C. J. Horowitz, M. A. Pérez-García, J. Carriere, D. K. Berry, and J. Piekarewicz, Phys. Rev. C **70**, 065806 (2004).

[46] C. J. Horowitz, M. A. Pérez-García, D. K. Berry, and J. Piekarewicz, Phys. Rev. C **72**, 035801 (2005).

[47] G. Watanabe, K. Sato, K. Yasuoka, and T. Ebisuzaki, Phys. Rev. C **68**, 035806 (2003).

[48] G. Watanabe, T. Maruyama, K. Sato, K. Yasuoka, and T. Ebisuzaki, Phys. Rev. Lett. **94**, 031101 (2005).

[49] G. Watanabe, H. Sonoda, T. Maruyama, K. Sato, K. Yasuoka, and T. Ebisuzaki, Phys. Rev. Lett. **103**, 121101 (2009).

[50] A. S. Schneider, C. J. Horowitz, J. Hughto, and D. K. Berry, Phys. Rev. C **88**, 065807 (2013).

[51] C. J. Horowitz, D. K. Berry, C. M. Briggs, M. E. Caplan, A. Cumming, and A. S. Schneider, Phys. Rev. Lett. **114**, 031102 (2015).

[52] M. E. Caplan, A. S. Schneider, C. J. Horowitz, and D. K. Berry, Phys. Rev. C **91**, 065802 (2015).

[53] P. Magierski and P.-H. Heenen, Phys. Rev. C **65**, 045804 (2002).

[54] N. Chamel, Nuclear Physics A **747**, 109 (2005).

[55] W. G. Newton and J. R. Stone, Phys. Rev. C **79**, 055801 (2009).

[56] B. Schuetrumpf and W. Nazarewicz, Phys. Rev. C **92**, 045806 (2015).

[57] F. J. Fattoyev, C. J. Horowitz, and B. Schuetrumpf, Phys. Rev. C **95**, 055804 (2017).

[58] D. G. Ravenhall, C. J. Pethick, and J. R. Wilson, Phys. Rev. Lett. **50**, 2066 (1983).

[59] M. Hashimoto, H. Seki, and M. Yamada, Prog. Theor. Phys. **71**, 320 (1984).

[60] K. Oyamatsu, M.-a. Hashimoto, and M. Yamada, Prog. Theor. Phys. **72**, 373 (1984).

[61] V. A. Ambartsumyan and G. S. Saakyan, Soviet Astronomy **4**, 187 (1960).

[62] D. Chatterjee and I. Vidaña, The European Physical Journal A **52**, 29 (2016).

[63] C. Ducoin, J. Margueron, C. Providência, and I. Vidaña, Phys. Rev. C **83**, 045810 (2011).

[64] G. Baym, C. Pethick, and P. Sutherland, Astrophys. J. **170**, 299 (1971).

[65] F. Ji, J. Hu, S. Bao, and H. Shen, Phys. Rev. C **100**, 045801 (2019).

[66] L. Perot, N. Chamel, and A. Sourie, Phys. Rev. C **101**, 015806 (2020).

[67] P. Danielewicz, P. Singh, and J. Lee, Nucl. Phys. **A958**, 147 (2017), arXiv:1611.01871 [nucl-th] .

[68] B. Margalit and B. D. Metzger, The Astrophysical Journal **850**, L19 (2017).

[69] I. Tews, J. Margueron, and S. Reddy, Phys. Rev. C **98**, 045804 (2018).

[70] H. Sotani, K. Iida, and K. Oyamatsu, Monthly Notices of the Royal Astronomical Society **470**, 4397 (2017), https://academic.oup.com/mnras/article-pdf/470/4/4397/19179395/stx1510.pdf .

[71] N.-B. Zhang, B.-A. Li, and J. Xu, The Astrophysical Journal **859**, 90 (2018).

[72] C. Y. Tsang, M. B. Tsang, P. Danielewicz, W. G. Lynch, and F. J. Fattoyev, Phys. Rev. C **102**, 045808 (2020).

[73] E. Khan, J. Margueron, and I. Vidaña, Phys. Rev. Lett. **109**, 092501 (2012).

[74] E. Khan, Physica Scripta **T152**, 014008 (2013).

[75] H. Guven, K. Bozkurt, E. Khan, and J. Margueron, (2020), arXiv:2001.10259 [nucl-th] .

[76] E. Lipparini and S. Stringari, Physics Reports **175**, 103 (1989).

[77] L. D. Landau and E. M. Lifshitz, *Fluid Mechanics* (Pergamonm Oxford, 1987) pp. 251–254.

[78] J. M. Lattimer and M. Prakash, Phys. Rep. **621**, 127 (2016), arXiv:1512.07820 [astro-ph] .

[79] P. Demorest, T. Pennucci, S. Ransom, M. Roberts, and J. Hessels, Nature **467**, 1081 (2010), arXiv:1010.5788 [astro-ph.HE] .

[80] J. Antoniadis, P. C. C. Freire, N. Wex, T. M. Tauris, R. S. Lynch, M. H. van Kerkwijk, M. Kramer, C. Bassa, V. S. Dhillon, T. Driebe, et al., Science **340** (2013), 10.1126/science.1233232.

[81] G. Baym, S. Furusawa, T. Hatsuda, T. Kojo, and H. Togashi, arXiv e-prints (2019), arXiv:1903.08963 [astro-ph.HE] .

[82] B.-A. Li, P. G. Krastev, D.-H. Wen, W.-J. Xie, and N.-B. Zhang, AIP Conference Proceedings **2127**, 020018 (2019), https://aip.scitation.org/doi/pdf/10.1063/1.5117808 .

[83] M. Shibata, S. Fujibayashi, K. Hotokezaka, K. Kiuchi, K. Kyutoku, Y. Sekiguchi, and M. Tanaka, Phys. Rev. D **96**, 123012 (2017).

[84] L. Rezzolla, E. R. Most, and L. R. Weih, The Astrophysical Journal **852**, L25 (2018).

[85] M. Ruiz, S. L. Shapiro, and A. Tsokaros, Phys. Rev. D **97**, 021501 (2018).

[86] E.-P. Zhou, X. Zhou, and A. Li, Phys. Rev. D **97**, 083015 (2018).

[87] J. Benesty, J. Chen, Y. Huang, and I. Cohen, *Pearson Correlation Coefficient. In: Noise Reduction in Speech Processing*, Vol. 2 (Springer, Berlin, Heidelberg, 2009) Chap. Pearson Correlation Coefficient.

[88] B. P. Abbott et al. (LIGO Scientific, Virgo), (2020), arXiv:2001.01761 [astro-ph.HE] .

[89] I. Tews, J. Carlson, S. Gandolfi, and S. Reddy, The Astrophysical Journal **860**, 149 (2018).

[90] A. Maselli, V. Cardoso, V. Ferrari, L. Gualtieri, and P. Pani, Phys. Rev. D **88**, 023007 (2013).

[91] J. M. Lattimer, private communication.

[92] J. Barney, J. Estee, W. G. Lynch, T. Isobe, G. Jhang, M. Kurata-Nishimura, A. B. McIntosh, T. Murakami, R. Shane, S. Tangwancharoen, et al., Review of Scientific Instruments **92** (2021), 10.1063/5.0041191.

[93] H. Sato, T. Kubo, Y. Yano, K. Kusaka, J. Ohnishi, K. Yoneda, Y. Shimizu, T. Motobayashi, H. Otsu, T. Isobe, et al., IEEE Transactions on Applied Superconductivity **23**, 4500308 (2013).

[94] S. Tangwancharoen, *Design and Construction of the SpiRIT TPC*, Ph.D. thesis, Michigan State U. (2016).

[95] S. Tangwancharoen, W. G. Lynch, J. Barney, J. Estee, R. Shane, M. B. Tsang, Y. Zhang, T. Isobe, M. Kurata-Nishimura, T. Murakami, et al., Nuclear Instruments and Methods in Physics Research. Section A, Accelerators, Spectrometers, Detectors and Associated Equipment **853** (2017), 10.1016/j.nima.2017.02.001.

[96] C. Tsang, J. Estee, R. Wang, J. Barney, G. Jhang, W. Lynch, Z. Zhang, G. Cerizza, T. Isobe, M. Kaneko, et al., Nuclear Instruments and Methods in Physics Research Section A: Accelerators, Spectrometers, Detectors and Associated Equipment **959**, 163477 (2020).

[97] R. Shane, A. B. McIntosh, T. Isobe, W. G. Lynch, H. Baba, J. Barney, Z. Chajecki, M. Chartier, J. Estee, M. Famiano, et al., Nuclear Instruments and Methods in Physics Research Section A: Accelerators, Spectrometers, Detectors and Associated Equipment **784**, 513 (2015), Symposium on Radiation Measurements and Applications 2014 (SORMA XV).

[98] M. Kaneko, T. Murakami, T. Isobe, M. Kurata-Nishimura, W. G. Lynch, M. B. Tsang, J. Barney, J. Estee, G. Cerizza, C. Santamaria, et al., RIKEN Accel. Prog. Rep. **50**, 172 (2017).

[99] P. Lasko, M. Adamczyk, J. Brzychczyk, P. Hirnyk, J. Łukasik, P. Pawłowski, K. Pelczar, A. Snoch, A. Sochocka, Z. Sosin, et al., Nuclear Instruments and Methods in Physics Research Section A: Accelerators, Spectrometers, Detectors and Associated Equipment **856**, 92 (2017).

[100] M. Al-Turany, D. Bertini, R. Karabowicz, D. Kresan, P. Malzacher, T. Stockmanns, and F. Uhlig, Journal of Physics: Conference Series **396**, 022001 (2012).

[101] J. Lee, G. Jhang, G. Cerizza, J. Barney, J. Estee, T. Isobe, M. Kaneko, M. Kurata-Nishimura, W. Lynch, T. Murakami, et al., Nuclear Instruments and Methods in Physics Research Section A: Accelerators, Spectrometers, Detectors and Associated Equipment **965**, 163840 (2020).

[102] J. Estee, W. Lynch, J. Barney, G. Cerizza, G. Jhang, J. Lee, R. Wang, T. Isobe, M. Kaneko, M. Kurata-Nishimura, et al., Nuclear Instruments and Methods in Physics Research Section A: Accelerators, Spectrometers, Detectors and Associated Equipment **944**, 162509 (2019).

[103] M. Anderson, J. Berkovitz, W. Betts, R. Bossingham, F. Bieser, R. Brown, M. Burks, M. Calderón de la Barca Sánchez, D. Cebra, M. Cherney, et al., Nuclear Instruments and Methods in Physics Research Section A: Accelerators, Spectrometers, Detectors and Associated Equipment **499**, 659 (2003), the Relativistic Heavy Ion Collider Project: RHIC and its Detectors.

[104] W. Blum and L. Rolandi, "Particle Detection with Drift Chambers," (Springer-Verlag Berlin Heidelberg, 1993) Chap. 2.1, pp. 49–97.

[105] J. Rauch and T. Schlüter, Journal of Physics: Conference Series **608**, 012042 (2015).

[106] W. Waltenberger, W. Mitaroff, F. Moser, B. Pflugfelder, and H. Riedel, Journal of Physics: Conference Series **119**, 032037 (2008).

[107] P. Sigmund, *Particle Penetration and Radiation Effect* (Springer-Verlag, 2006).

[108] J. Adam, D. Adamová, M. M. Aggarwal, G. Aglieri Rinella, M. Agnello, N. Agrawal, Z. Ahammed, S. Ahmad, S. U. Ahn, S. Aiola, et al., The European Physical Journal Plus **131**, 168 (2016).

[109] J. Lee, Private Communication (2022).

[110] O. Tarasov and D. Bazin, Nuclear Instruments and Methods in Physics Research Section B: Beam Interactions with Materials and Atoms **376**, 185 (2016), proceedings of the XVI-Ith International Conference on Electromagnetic Isotope Separators and Related Topics (EMIS2015), Grand Rapids, MI, U.S.A., 11-15 May 2015.

[111] F. Rami, P. Crochet, R. Donà, B. de Schauenburg, P. Wagner, J. Alard, A. Andronic, Z. Basrak, N. Bastid, I. Belyaev, et al., Nuclear Physics A **646**, 367 (1999).

[112] A. Andronic, W. Reisdorf, J. P. Alard, V. Barret, Z. Basrak, N. Bastid, A. Bendarag, G. Berek, R. Čaplar, P. Crochet, et al., Phys. Rev. C **64**, 041604 (2001).

[113] De Filippo, E., Russotto, P., Acosta, L., Adamczyk, M., Al-Ajlan, A., Al-Garawi, M., Al-Homaidhi, S., Amorini, F., Auditore, L., Aumann, T., et al., EPJ Web Conf. **137**, 09002 (2017).

[114] P. Danielewicz and G. Odyniec, Physics Letters B **157**, 146 (1985).

[115] A. M. Poskanzer and S. A. Voloshin, Phys. Rev. C **58**, 1671 (1998).

[116] J. Barrette, R. Bellwied, S. Bennett, R. Bersch, P. Braun-Munzinger, W. C. Chang, W. E. Cleland, M. Clemen, J. Cole, T. M. Cormier, et al., Phys. Rev. C **56**, 3254 (1997).

[117] H. Wolter, M. Colonna, D. Cozma, P. Danielewicz, C. M. Ko, R. Kumar, A. Ono, M. B. Tsang, J. Xu, Y.-X. Zhang, et al., "Transport model comparison studies of intermediate-energy heavy-ion collisions," (2022), arXiv:2202.06672 [nucl-th] .

[118] C. Hartnack, L. Zhuxia, L. Neise, G. Peilert, A. Rosenhauer, H. Sorge, J. Aichelin, H. Stöcker, and W. Greiner, Nuclear Physics A **495**, 303 (1989).

[119] J. Aichelin, Physics Reports **202**, 233 (1991).

[120] A. Ono, Phys. Rev. C **59**, 853 (1999).

[121] H. Feldmeier, Nuclear Physics A **515**, 147 (1990).

[122] M. Colonna and P. Chomaz, Physics Letters B **436**, 1 (1998).

[123] A. Ono, H. Horiuchi, T. Maruyama, and A. Ohnishi, Progress of Theoretical Physics **87**, 1185 (1992), https://academic.oup.com/ptp/article-pdf/87/5/1185/5272175/87-5-1185.pdf .

[124] A. Ono, H. Horiuchi, T. Maruyama, and A. Ohnishi, Phys. Rev. Lett. **68**, 2898 (1992).

[125] M. Papa, T. Maruyama, and A. Bonasera, Phys. Rev. C **64**, 024612 (2001).

[126] Y. Zhang and Z. Li, Phys. Rev. C **74**, 014602 (2006).

[127] S. Ayik and C. Gregoire, Physics Letters B **212**, 269 (1988).

[128] Y. Abe, S. Ayik, P.-G. Reinhard, and E. Suraud, Physics Reports **275**, 49 (1996).

[129] J. Randrup and B. Remaud, Nuclear Physics A **514**, 339 (1990).

[130] P. Chomaz, M. Colonna, and J. Randrup, Physics Reports **389**, 263 (2004).

[131] P. Napolitani and M. Colonna, Physics Letters B **726**, 382 (2013).

[132] P. Napolitani and M. Colonna, Phys. Rev. C **92**, 034607 (2015).

[133] Y. Zhang and Z. Li, Phys. Rev. C **71**, 024604 (2005).

[134] Y. Zhang, P. Danielewicz, M. Famiano, Z. Li, W. Lynch, and M. Tsang, Physics Letters B **664**, 145 (2008).

[135] Z. Yingxun, L. Zhuxia, Z. Kai, L. Hang, and T. M.B., Nuclear Science And Techniques **24**, 50503 (2019).

[136] Y. Zhang, M. Tsang, Z. Li, and H. Liu, Physics Letters B **732**, 186 (2014).

[137] S. Bass, M. Belkacem, M. Bleicher, M. Brandstetter, L. Bravina, C. Ernst, L. Gerland, M. Hofmann, S. Hofmann, J. Konopka, et al., Progress in Particle and Nuclear Physics **41**, 255 (1998).

[138] Y. Wang, C. Guo, Q. Li, H. Zhang, Z. Li, and W. Trautmann, Phys. Rev. C **89**, 034606 (2014).

[139] Q. Li, Z. Li, S. Soff, M. Bleicher, and H. Stöcker, Journal of Physics G: Nuclear and Particle Physics **32**, 151 (2005).

[140] Q. Li, M. Bleicher, and H. Stöcker, Physics Letters B **659**, 525 (2008).

[141] Y. Wang, C. Guo, Q. Li, H. Zhang, Y. Leifels, and W. Trautmann, Phys. Rev. C **89**, 044603 (2014).

[142] L. Tong, P. Li, F. Li, Y. Wang, Q. Li, and F. Liu, Chinese Physics C **44**, 074103 (2020).

[143] Y. Liu, Y. Wang, Y. Cui, C.-J. Xia, Z. Li, Y. Chen, Q. Li, and Y. Zhang, Phys. Rev. C **103**, 014616 (2021).

[144] Y.-J. Wang and Q.-F. Li, Frontiers of Physics **15**, 44302 (2020).

[145] Y.-X. Zhang, N. Wang, Q.-F. Li, L. Ou, J.-L. Tian, M. Liu, K. Zhao, X.-Z. Wu, and Z.-X. Li, Frontiers of Physics **15**, 1 (2020).

[146] F. Li, Y. Wang, H. Lü, P. Li, Q. Li, and F. Liu, Journal of Physics G: Nuclear and Particle Physics **47**, 115104 (2020).

[147] D. T. Khoa, N. Ohtsuka, M. Matin, A. Faessler, S. Huang, E. Lehmann, and R. K. Puri, Nuclear Physics A **548**, 102 (1992).

[148] C. Fuchs, L. Sehn, E. Lehmann, J. Zipprich, and A. Faessler, Physical Review C **55**, 411 (1997).

[149] K. Shekhter, C. Fuchs, A. Faessler, M. Krivoruchenko, and B. Martemyanov, Phys. Rev. C **68**, 014904 (2003).

[150] M. Cozma, Physics Letters B **700**, 139 (2011).

[151] M. Cozma, Y. Leifels, W. Trautmann, Q. Li, and P. Russotto, Physical Review C **88**, 044912 (2013).

[152] G. Jhang, J. Estee, J. Barney, G. Cerizza, M. Kaneko, J. Lee, W. Lynch, T. Isobe, M. Kurata-Nishimura, T. Murakami, et al., Physics Letters B **813**, 136016 (2021).

[153] M. Cozma, Physics Letters B **753**, 166 (2016).

[154] A. Ono, Progress in Particle and Nuclear Physics **105**, 139 (2019).

[155] B. Dönigus, The European Physical Journal A **56**, 280 (2020).

[156] M. Kaneko, T. Murakami, T. Isobe, M. Kurata-Nishimura, A. Ono, N. Ikeno, J. Barney, G. Cerizza, J. Estee, G. Jhang, et al., Physics Letters B **822**, 136681 (2021).

[157] D. Coupland, *Probing the nuclear symmetry energy with heavy ion collisions*, Ph.D. thesis, Michigan State University (2013).

[158] P. Morfouace, C. Tsang, Y. Zhang, W. Lynch, M. Tsang, D. Coupland, M. Youngs, Z. Chajecki, M. Famiano, T. Ghosh, et al., Physics Letters B **799**, 135045 (2019).

[159] B.-A. Li, Phys. Rev. Lett. **88**, 192701 (2002).

[160] M. D. Cozma and M. B. Tsang, The European Physical Journal A **57**, 309 (2021).

[161] Q. Li, C. Shen, C. Guo, Y. Wang, Z. Li, J. Lukasik, and W. Trautmann, Phys. Rev. C **83**, 044617 (2011).

[162] T. Gaitanos, C. Fuchs, and H. Wolter, Physics Letters B **609**, 241 (2005).

[163] F. Rami, Y. Leifels, B. de Schauenburg, A. Gobbi, B. Hong, J. P. Alard, A. Andronic, R. Averbeck, V. Barret, Z. Basrak, et al. (FOPI Collaboration), Phys. Rev. Lett. **84**, 1120 (2000).

[164] S. Agostinelli, J. Allison, K. Amako, J. Apostolakis, H. Araujo, P. Arce, M. Asai, D. Axen, S. Banerjee, G. Barrand, et al., Nuclear Instruments and Methods in Physics Research Section A: Accelerators, Spectrometers, Detectors and Associated Equipment **506**, 250 (2003).

[165] H. Schindler, *Garfield++ Usser Guide*, CERN.

[166] K. Masanori, *Hydrogen Isotope Productions in Sn + Sn Collisions with Radioactive Beams at 270 MeV/nucleon*, Ph.D. thesis, Kyoto University (2022).

[167] C. Adler, Z. Ahammed, C. Allgower, J. Amonett, B. D. Anderson, M. Anderson, G. S. Averichev, J. Balewski, O. Barannikova, L. S. Barnby, et al. (STAR Collaboration), Phys. Rev. Lett. **90**, 032301 (2003).

[168] V. D. Elvira, Physics Reports **695** (2017), 10.1016/j.physrep.2017.06.002.

[169] N. Ikeno, A. Ono, Y. Nara, and A. Ohnishi, Phys. Rev. C **93**, 044612 (2016).

[170] N. Ikeno, A. Ono, Y. Nara, and A. Ohnishi, Phys. Rev. C **101**, 034607 (2020).

[171] M. D. Cozma, Phys. Rev. C **95**, 014601 (2017).

[172] C. Hartnack, R. K. Puri, J. Aichelin, J. Konopka, S. Bass, H. Stoecker, and W. Greiner, Euro. Phys. J. A **1**, 151 (1998).

[173] A. Le Fevre, Y. Leifels, W. Reisdorf, J. Aichelin, and C. Hartnack, Nucl. Phys. A **945**, 112 (2016).

[174] Y. Zhang, M. Tsang, Z. Li, and H. Liu, Phys. Lett. B **732**, 186 (2014).

[175] J. Xu, L.-W. Chen, M. B. Tsang, H. Wolter, Y.-X. Zhang, J. Aichelin, M. Colonna, D. Cozma, P. Danielewicz, Z.-Q. Feng, et al., Phys. Rev. C **93**, 044609 (2016).

[176] Y.-X. Zhang, Y.-J. Wang, M. Colonna, P. Danielewicz, A. Ono, M. B. Tsang, H. Wolter, J. Xu, L.-W. Chen, D. Cozma, et al., Phys. Rev. C **97**, 034625 (2018).

[177] C. E. Rasmussen and C. K. I. Williams, in [185], Chap. 4, pp. 7–32.

[178] J. E. Jackson (Wiley-Interscience, 2003) Chap. 1.4.

[179] S. Sharma, Annual Review of Astronomy and Astrophysics **55**, 213 (2017), https://doi.org/10.1146/annurev-astro-082214-122339 .

[180] A. Patil, D. Huard, and C. J. Fonnesbeck, Journal of statistical software **35**, 1 (2010), 21603108[pmid].

[181] R. von Mises (Academic Press, 1964) Chap. 9.3.

[182] C. E. Rasmussen and C. K. I. Williams, in [185], Chap. 4, pp. 79–104.

[183] C. E. Rasmussen and C. K. I. Williams, in [185], Chap. 5, pp. 105–128.

[184] D. P. Kingma and J. Ba, "Adam: A Method for Stochastic Optimization," (2017), arXiv:1412.6980 [cs.LG] .

[185] C. E. Rasmussen and C. K. I. Williams, "Gaussian Processes for Machine Learning (Adaptive Computation and Machine Learning)," (2005).

[186] Z. Chen, J. Fan, and K. Wang, "Remarks on multivariate Gaussian Process," (2021), arXiv:2010.09830 [math.ST] .

[187] H. Petersen, C. Coleman-Smith, S. A. Bass, and R. Wolpert, Journal of Physics G: Nuclear and Particle Physics **38**, 045102 (2011).

[188] B.-A. Li, Phys. Rev. C **69**, 064602 (2004).

[189] B. Liu, V. Greco, V. Baran, M. Colonna, and M. Di Toro, Phys. Rev. C **65**, 045201 (2002).

[190] K. Brueckner, Physical Review **97**, 1353 (1955), cited By 388.

[191] C. Mahaux, P. Bortignon, R. Broglia, and C. Dasso, Physics Reports **120**, 1 (1985).

[192] F. Hofmann, C. M. Keil, and H. Lenske, Phys. Rev. C **64**, 034314 (2001).

[193] V. Greco, M. Colonna, M. Di Toro, and F. Matera, Phys. Rev. C **67**, 015203 (2003).

[194] M. Farine, J. Pearson, and F. Tondeur, Nuclear Physics A **696**, 396 (2001).

[195] X. Chen, Y. Zhang, and Z. li, Chinese Physics C (2021), 10.1088/1674-1137/abfb51.

[196] J. Cugnon, D. L'Hôte, and J. Vandermeulen, Nuclear Instruments and Methods in Physics Research, Section B: Beam Interactions with Materials and Atoms **111**, 215 (1996), cited By 95.

[197] B.-A. Li and X. Han, Physics Letters B **727**, 276 (2013).

[198] D. Adhikari, H. Albataineh, D. Androic, K. Aniol, D. S. Armstrong, T. Averett, C. Ayerbe Gayoso, S. Barcus, V. Bellini, R. S. Beminiwattha, et al. (PREX Collaboration), Phys. Rev. Lett. **126**, 172502 (2021).

[199] I. Legred, K. Chatziioannou, R. Essick, S. Han, and P. Landry, Phys. Rev. D **104**, 063003 (2021).

[200] M. B. Tsang, Y. Zhang, P. Danielewicz, M. Famiano, Z. Li, W. G. Lynch, and A. W. Steiner, Phys. Rev. Lett. **102**, 122701 (2009).

[201] M. B. Tsang, T. X. Liu, L. Shi, P. Danielewicz, C. K. Gelbke, X. D. Liu, W. G. Lynch, W. P. Tan, G. Verde, A. Wagner, et al., Phys. Rev. Lett. **92**, 062701 (2004).

[202] T. X. Liu, W. G. Lynch, M. B. Tsang, X. D. Liu, R. Shomin, W. P. Tan, G. Verde, A. Wagner, H. F. Xi, H. S. Xu, et al., Phys. Rev. C **76**, 034603 (2007).

[203] M. Kortelainen, T. Lesinski, J. Moré, W. Nazarewicz, J. Sarich, N. Schunck, M. V. Stoitsov, and S. Wild, Phys. Rev. C **82**, 024313 (2010).

[204] A. Tamii, I. Poltoratska, P. von Neumann-Cosel, Y. Fujita, T. Adachi, C. A. Bertulani, J. Carter, M. Dozono, H. Fujita, K. Fujita, et al., Phys. Rev. Lett. **107**, 062502 (2011).

[205] N. Chamel, S. Goriely, and J. M. Pearson, Phys. Rev. C **80**, 065804 (2009).

[206] F. J. Fattoyev, J. Carvajal, W. G. Newton, and B.-A. Li, Phys. Rev. C **87**, 015806 (2013).